

---

**Influence of Magnetic Structure on the Magnetic Properties  
of Compensated Substituted Compounds of  $\text{CoCr}_2\text{O}_4$**

---

A Thesis Submitted to  
Indian Institute of Technology Guwahati

*In partial fulfilment of the requirement for the award of  
the degree of*

***Doctor of Philosophy***

By

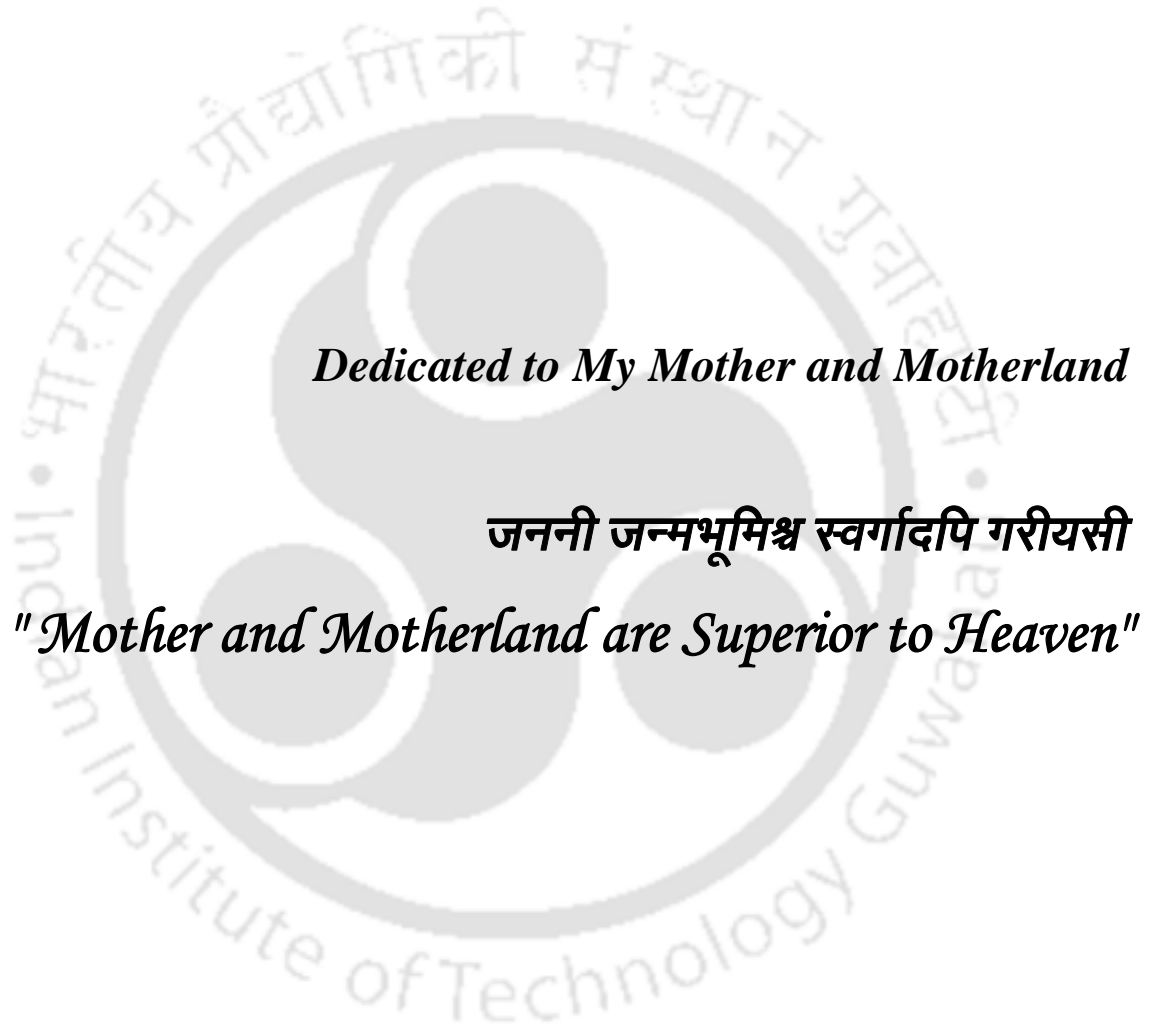
**Ram Kumar**



**Department of Physics  
Indian Institute of Technology Guwahati  
Guwahati-781039, Assam (India)**







*Dedicated to My Mother and Motherland*

*जननी जन्मभूमिश्च स्वर्गादपि गरीयसी*

*"Mother and Motherland are Superior to Heaven"*





INDIAN INSTITUTE OF TECHNOLOGY  
GUWAHATI  
Department of Physics  
Guwahati – 781039

---

### *Declaration*

I hereby declare that this thesis entitled “*Influence of Magnetic Structure on the Magnetic Properties of Compensated Substituted Compounds of  $\text{CoCr}_2\text{O}_4$* ” is the result of my own doctoral research work. This work was carried out under the supervision of Prof. Dilip Pal at the Department of Physics, Indian Institute of Technology Guwahati. To the best of my knowledge, the work presented in this thesis has not been submitted to any other Institute/University for the award of any degree.

**Ram Kumar**  
Research Scholar (Roll No: 126121028)  
Department of Physics  
Indian Institute of Technology Guwahati  
Guwahati-781039, India





INDIAN INSTITUTE OF TECHNOLOGY  
GUWAHATI  
Department of Physics  
Guwahati – 781039

---

*Certificate*

It is certified that the work described in the thesis entitled “*Influence of Magnetic Structure on the Magnetic Properties of Compensated Substituted Compounds of  $\text{CoCr}_2\text{O}_4$* ”, by Mr. Ram Kumar, a Ph.D. student of Department of Physics, Indian Institute of Technology Guwahati, for the award of degree of Doctor of Philosophy has been carried out under my supervision. This work has not been submitted elsewhere for the award of any degree.

**Dr. Dilip Pal**  
Professor  
Department of Physics  
Indian Institute of Technology Guwahati  
Guwahati-781039, India



## *Acknowledgements*

At the very onset, I offer my acknowledgement to the *Dhara* (Land) of Guwahati especially IITG, Assam, India, for having spent here a very precious time of my life.

I would like to admit my indebt gratitude to my thesis supervisor, Prof. Dilip Pal for giving me an opportunity to work under his esteemed guidance. His constant motivation, inspiration, encouragement and support have contributed to the successful completion of my Ph.D. research. I express my sincere thanks to my doctoral committee members Prof. P. K. Padmanabhan, Dr. Subhash Thota & Prof. Chandan Mukherjee for their valuable suggestions and inputs that inculcated in me- the problem solving ability and upgraded my research quality. It is my pleasure to thank all the faculty members of the Department of Physics, IIT Guwahati for their ever eager nature in explaining the concepts of physics. I express my sincere regards to the present and former heads of the Department of Physics (Prof. Subradip Ghosh, Prof. P. Poulous and Prof. Saurabh Basu), for their generous support for attending conferences and schools during Ph.D period and providing me various departmental facilities. I would like to extent my heartiest thanks to Prof. Pratima Agarwal, who considered me as her JRF student though for a short period of time, hence giving me an opportunity to continue in IIT Guwahati for my Ph.D.

I would like to thank Dr. Vasudeva Siruguri, Center Director, UGC-DAE, CSR, Mumbai Centre and Dr. Sudhindra Rayaprol for supporting collaborative research project (CRS-M-195) to carry out the neutron diffraction measurement; specially Dr. Sudhindra Rayaprol for his kind brotherly gestures. I also want to acknowledge Dr. S. D. Kaushik and Dr. S. Mukherjee for his friendly nature. My heartfelt gratitude to Prof. S. Ramakrishnan, for providing me with the golden opportunity to visit Tata Institute of Fundamental Research (TIFR), Mumbai as well as Prof. E.V Sampathkumaran and Prof. P. L. Paulose of TIFR, that was indeed very beneficial in terms of stimulating research interest and availing various instrumental facilities.

I thank Dr. Sidananda Sarma of the Department of Physics, and all other scientific officers of Central Instrumental Facilities (CIF), IITG, for smooth conduction of various experiments in the instruments. I would also like to acknowledge my department office staff members Mr. Himanku Dutta and Mrs. Leoni Choudhury. I want to thank all my seniors from IITG and scientific officers: Dr. Himanshu Sheskar Jha, Dr. Padam Rajender, Dr. Suresh Babu M, Dr. Mukesh Singh, Dr. Debashish Das, Dr. Tanveer Ahmad, Dr. Om Prakash (TIFR) along with the ones from TIFR: Dr. Ramender K. Sharma, Dr. Sanjay Uppadyay, Dr. Shidlliong Mahapattenwar, Dr. Megha Vagadia, Mr. Anil Kumar and Mr. Kartik Iyer for their enthusiastic help and advice.

It is my honour to devote special thanks to all my teachers from schooling to post graduate, Shri Yogesh Sharma, Shri Avneesh Sharma, Shri Yaspal Yadav, Shri Sanjay Varshney, Shri Todi Singh, Late Shri Radheesyam Gupta (Babu Ji), Prof. B. P Singh (AMU, Aligarh) along

with Prof. Sahid Hussain, Dr. Wasi Khan and Prof. Anchal Srivastava (BHU, Varanasi) for their instrumental efforts in encouraging me to pursue and seek academic excellence.

I thank all my lab mates and friends, Deep, Sanjib, Robin, Prativa, Prgaya, Omkar, Prahlad, Kaushik, Rahul, Nitin, Deepanjali, Ashish Singh, Anamika, Haripriya, Vinay, Vivek and all other colleagues and juniors for establishing work friendly atmosphere. My devoted gratitude to Pugal Sir, Charu Sir, Nandi Sir, Ajay Sir, Bimlesh Sir, Sisir Sir and Bhuyan Sir for their fervent attitude. My beloved friends Sharbani Kaushik, Jitendra S. Rawat, Asha Yadav, Rahul Jain, Mrinmoy Bhardwaj and Anil K. C. for sharing beautiful memories at badminton court, the early morning tea-time and the warm attachment. Sharbani and Babul for their unconditional friendship and the home-made appetizing dishes that made me feel at home, away from home!, My friends Jitendra and Kedar for the late night clever debates on politics with a cup of milk. This bonding that we share and the memories will be carried life-long, unbeaten and untainted.

I adore my amazing friends from school to post graduate, Ankush, Viswa Prakash, Sunil dutt, Ashwani, Anuj Varshney, Anuj Chandra and my well-wishers, Shri Kishan Mohan Verma, Shri Vishan Mohan Verma, Shri Sunil Varshney, Shri Alok Maheshwari, Shri Sanjeev Dixit, Shri Harish Maheshwari, Shri Sheelendra Dixit, Dr. Ashish Chauhan, Dr. Abhishek Yadav, Dr. Sugam Kumar, Dr. Kamal Kumar and Dr. Vinod Kumar for their constant motivation, love and inspiration.

I extend my acknowledgement to various software developers of FULLPROF program, Rietveld refinement technique, Origin, Vesta, and all other research analysis tools. Financial assistance from Ministry of Human Resource Development (MHRD), India and travel grants from the Department of Science and Technology (DST), India for presenting a paper at the DN-2016 conference held at Kiel, Germany and from Neutron Scattering Society of India (NSSI) for presenting a paper during ICNS-2017 South Korea are duly acknowledged.

Last but not the least, I express my fondness for my respected parents (Smt. Urmila Devi - Shri Asharam Yadav), adored sisters (Uma, Usha, Shipra, Swati, Khushboo and Shalu), brother in-laws along with other family members for making my family life so comfortable that I could balance my professional life with zeal and zest. My father is my real-life hero and I always wanted to be like him. Additionally, I have a special place in my heart for Mrs. Ranjita Sharma for her motherly affection and blessings.

*Sincerely,*  
*Ram Kumar*

## *Synopsis*

Among oxides materials, spinel oxides having structure  $AB_2O_4$ , exhibit a rich spectrum of functional responses due to their interesting magnetic, electric and multiferroic properties [1–6]. In this spinel structure, there are two different crystal-field environments: tetrahedral environment and octahedral environment. The A-site divalent cation sits in the tetrahedral environment and trivalent cation residing in the octahedral environment made by surrounding oxygen atoms [7,8]. Spinel with all sites occupied with magnetic ions, are well-established systems because of their noteworthy applications in electronic devices, magnetic recording devices, super-capacitors and phase-shifters etc. [9–11]. In the family of magnetic spinel oxides, Cobalt chromate ( $CoCr_2O_4$ ) is famous as magnetoelectric (ME) multiferroic material which exhibits a rich phase diagrams involving spin and orbital degrees of freedom, geometrical frustration and complex spiral ferrimagnetic (FIM) orderings [12–15]. The possible exchange interactions between different magnetic ions present in different crystal field environments (i.e. tetrahedral and octahedral) lead to interesting magnetic properties which result in an exotic magnetic phase diagram [12,14].  $CoCr_2O_4$  exhibits a long range collinear FIM ordering at ( $T_C$ )  $\sim 94$  K followed by another magneto-structural transition ( $T_S$ )  $\sim 24$  K below which an incommensurate conical spin-spiral order exists [8,16–18]. It is the existence of the conical spin-spiral order in this compound, which gives rise to ME coupling as predicted by the spin-current model [19]. Further, through neutron scattering experiment, another transition is also observed at  $T \sim 15$  K, known as lock-in transition ( $T_L$ ) in  $CoCr_2O_4$  [18]. Neutron scattering experiments on  $CoCr_2O_4$  have revealed that magnetic structure is quite complex in this compound where it comprises a long range FIM component around  $T_C$  and a short range spiral ordering manifests below  $T \sim 86$  K ( $T \sim 50$  K in case of single crystal) and then becomes long range at  $\sim 31$  K [8,16]. The presence of weak magnetic frustration, which is very much intangible to superexchange interactions present along different paths such as A–O–A, B–O–B and A–O–B [8,18,20] give rise to all above enthralling features.

In 1948, Néel had predicted the unusual magnetic behavior of negative magnetization (or magnetization reversal) in ferrimagnetic materials [21]. Finding of negative magnetization is fairly unconventional because it occurs without the change in the direction of the magnetic field. During the temperature variation of magnetization in the sample, net magnetization displays zero

value at a certain temperature which is known as compensation temperature ( $T_{\text{comp}}$ ). The negative magnetization is observed below this  $T_{\text{comp}}$ . The competition of different exchange interactions present in the system induces such fascinating phenomenon of negative magnetization.

Exchange bias (EB) effect attracts the interest in various magnetic materials since its discovery in 1956 by Meiklejohn and Bean due to its potential applications such as magnetic recording device, spintronics, magnetic sensors and spin valve devices [22–27]. It is demonstrated by the shift of hysteresis loops along the magnetic field or magnetization axes [28]. Recently, EB has been observed in many systems containing ferromagnetic (FM), antiferromagnetic (AFM), spin glass (SG) or cluster glass (CG) interfaces and in layer systems [29]. It is usually as a result of unidirectional anisotropy which is caused by the coupling of different components (for example: FM and AFM) at the interface below the magnetic ordering temperature [30]. Such EB effect along with the presence of negative magnetization in the compound increases the tunability for device applications by understanding the clear magnetic structures of the materials through microscopic techniques (for example: Neutron scattering).

The systematic study of crystalline and magnetic structures with substitution effect is lacking in  $\text{CoCr}_2\text{O}_4$ . This thesis presents detailed study to understand the crystalline and magnetic structure by performing neutron powder diffraction experiments and other physical properties of A and B site substituted spinel compounds;

- (i)  $\text{Co}(\text{Cr}_{1-x}\text{Fe}_x)_2\text{O}_4$  with  $x = 0.00-0.075$ ,
- (ii)  $\text{Co}(\text{Cr}_{1-x}\text{Mn}_x)_2\text{O}_4$  with  $x = 0.00-0.30$ , and
- (iii)  $\text{Co}_{1-x}\text{Cu}_x\text{Cr}_2\text{O}_4$  with  $x = 0.0-0.20$ .

This thesis is planned in 6 chapters. Brief description of each chapter is as follows:

**Chapter 1** provides an introduction to the spinel oxides, crystal structure and their applications along with some basic concepts of magnetism. Present chapter also includes current research till date on the crystalline, magnetic and dielectric properties of  $\text{CoCr}_2\text{O}_4$ . Various important concepts/topics such as crystal field environment, Jahn-Teller effect, magnetic frustration and exchange bias (EB) etc., are discussed with the underlying physics. Exciting phenomenon of negative magnetization in ferrimagnets has also been discussed in this chapter with great detailed along with some experimental findings. Further, a brief introduction to

multiferrocity was presented. This chapter concludes with the cubic spinel  $\text{CoCr}_2\text{O}_4$  that exhibits complex and rich magnetic phase diagram along with some critical issues of magnetic structure at low-temperature. Finally, a detailed description of motivation behind present research problem and its approach towards solution is illustrated in this chapter.

**Chapter 2** describes details of various experimental techniques employed in this thesis. Standard solid-state reaction method which is used for synthesis of studied compounds is discussed. The discussion regarding the working principles of various instruments are included in this chapter. The structural characterization has been performed using X-ray diffraction (XRD) technique followed by the Rietveld refinement method using Fullprof software. For the determination of magnetic structure of studied compounds, neutron scattering technique has been used and a brief introduction and working principles is included. In subsequent section, commercial superconducting quantum interference device (SQUID) based magnetometer with temperature capabilities of 2-320 K and magnetic field up to  $\pm 70$  kOe which was used to probe the dc and ac-magnetic properties, is discussed. Basic principle of temperature dependent specific-heat [ $C_p(T)$ ] measurement procedure performed by means of a physical property measurement system (PPMS) was described. Complex dielectric permittivity ( $\epsilon_r$ ) and  $\tan\delta$  (loss) as function of temperature and magnetic field was measured using Agilent E4980A LCR meter with a home-made sample holder at several frequencies (1-100 kHz) with 1V ac-bias field. These pyroelectric measurements were performed with the same sample holder by using Keithley 6517B electrometer in a columbic mode with PPMS.

**Chapter 3** presents synthesis of  $\text{Co}(\text{Cr}_{1-x}\text{Fe}_x)_2\text{O}_4$  with  $x = 0.00-0.075$  polycrystalline samples and provide a detailed structural, magnetic and magneto-dielectric properties. A systematic comparison of the structural and magnetic properties of these Fe substituted  $\text{CoCr}_2\text{O}_4$  with that of parent  $\text{CoCr}_2\text{O}_4$  has been done. The role of few percent of Fe on the global magnetic behavior of  $\text{CoCr}_2\text{O}_4$  samples was discussed in terms of dc-magnetization (M), ac-magnetic susceptibility ( $\chi_{ac}$ ) and heat capacity studies. Along with existing magnetic transitions in pristine  $\text{CoCr}_2\text{O}_4$ , temperature dependent magnetization studies reveal a fascinating phenomenon of negative magnetization in these Fe substituted samples below the respective magnetic compensation temperature ( $T_{comp}$ ) which was absent in the parent compound  $\text{CoCr}_2\text{O}_4$ . In addition to these magnetic ordering, exchange bias (EB) properties are also studied in these

compounds. Further, temperature dependent NPD experiments have been performed to study the magnetic structure which explains the finding of negative magnetization and EB in these compounds.  $\text{CoCr}_2\text{O}_4$  is well-known multiferroic materials, therefore the temperature dependent magneto-dielectric and pyroelectric studies have also been performed in these minimal Fe substituted compounds. Furthermore, the origin of all these interesting properties along with the magnetic structures of  $\text{Co}(\text{Cr}_{0.95}\text{Fe}_{0.05})_2\text{O}_4$  and  $\text{Co}(\text{Cr}_{0.925}\text{Fe}_{0.075})_2\text{O}_4$  samples were discussed in detail.

**Chapter 4** deals with the synthesis of  $\text{Co}(\text{Cr}_{1-x}\text{Mn}_x)_2\text{O}_4$  with  $x = 0.00-0.30$  polycrystalline samples and provide the evolution of temperature and magnetic field dependent magnetic properties of these compounds along with crystalline structure. Compensation temperature ( $T_{\text{comp}}$ ) and then the onset of negative magnetization at  $T = 60$  K and 83 K was noticed only for  $\text{Co}(\text{Cr}_{0.73}\text{Mn}_{0.27})_2\text{O}_4$ , i.e.  $x = 0.27$  and  $\text{Co}(\text{Cr}_{0.70}\text{Mn}_{0.30})_2\text{O}_4$  i.e.  $x=0.30$  samples which was absent in the parent compound  $\text{CoCr}_2\text{O}_4$ . For large applied fields magnetization reversal disappears but ends in field induced transition across  $T_{\text{comp}}$ . Magnetic hysteresis loops of  $\text{Co}(\text{Cr}_{0.70}\text{Mn}_{0.30})_2\text{O}_4$  exhibit gigantic coercivity at 3 K, and dramatically drops on increasing temperature. The exchange-bias-like behavior is observed below 10 K and as well as in the vicinity of compensation point,  $T_{\text{comp}}$  ( $\sim 83$  K). Compared to Fe substitution, there is no sign change in EB and a minimal amount of exchange bias field ( $H_{\text{EB}}$ ) is observed. Low temperature neutron diffraction experiments on these polycrystalline samples (i.e.  $x = 0.27$  and 0.30) are done to explore the understanding of observed negative magnetization, complex magnetic properties and correlation between chemical and magnetic structure. The reason of minimal  $H_{\text{EB}}$  observed in present chapter has also been discussed through NPD experiments. The correlation among bond-lengths, bond-angles and magnetic moments at  $T_{\text{comp}}$ , clearly indicates a magneto-elastic coupling around compensation temperature in these compounds. Through NPD experiments, we have also discussed the role of such magneto-elastic coupling which gives rise to the sign change of the magneto-caloric effect (MCE) at compensation temperature. Finally, the origin of all these interesting properties was discussed in detail.

**Chapter 5** presents a systematic study of the structural and magnetic properties of  $\text{Co}_{1-x}\text{Cu}_x\text{Cr}_2\text{O}_4$  with  $x = 0.00-0.20$  with a special emphasis on the structural transition at low temperature along with anomalous magnetic behavior such as negative magnetization, sign

change in EB across compensation temperature and large magnetic coercivity. Similar to the previous compounds, solid-state reaction method has been employed for the synthesis of these samples. Compared to previous chapters here the substitution of  $\text{Cu}^{+2}$  has been done for  $\text{Co}^{2+}$ , (i.e. A-site) in  $\text{CoCr}_2\text{O}_4$ . The role of 'Cu' substitution on A-site 'Co' of  $\text{CoCr}_2\text{O}_4$  and the corresponding changes in the crystal and magnetic structure were discussed in detail. State of magnetic compensation and then the onset of negative magnetization at  $T = 52$  K exists only for  $\text{Co}_{0.8}\text{Cu}_{0.2}\text{Cr}_2\text{O}_4$ , i.e.  $x = 0.20$  sample which was absent in the parent compound  $\text{CoCr}_2\text{O}_4$ . Neutron and x-ray diffraction, magnetic susceptibility, and specific heat measurements have been used to investigate the magneto-structural phase transitions present in the  $\text{Co}_{0.8}\text{Cu}_{0.2}\text{Cr}_2\text{O}_4$  compound which persist the state of magnetic compensation. It is noticed that Jahn-Teller active  $\text{Cu}^{2+}$  ion in the tetrahedral A-site of the spinel configuration induces the Jahn-Teller distortion slightly above the Néel temperature. It was further observed that the high temperature cubic  $Fd\bar{3}m$  structure coexists with the low temperature orthorhombic ( $Fddd$ ) structure till the lowest temperature of measurement. Furthermore, the origin of this magneto-structural correlation along with fascinating magnetic properties in  $\text{Co}_{0.8}\text{Cu}_{0.2}\text{Cr}_2\text{O}_4$  was discussed in detail.

**Chapter 6** presents a brief summary of research work carried out in this thesis. The effects of different transition metal ions substitution at both tetrahedral A-site and octahedral B-sites, which affects the exchange interaction and magnetic structures of these compounds, are studied. The present thesis also highlights the scope for the future research work, by growing single crystals and thin films of these spinel oxides for better understanding of magnetic structures as well as for application point of view.



## List of Publications:

### Peer Reviewed Journals/conf. proceedings

- [1] “Tuning of magnetic structure and its effect on magnetic properties in  $\text{Co}(\text{Cr}_{1-x}\text{Mn}_x)_2\text{O}_4$  ( $x = 0.00-0.30$ )”: **Ram Kumar**, S. Rayaprol, Y. Xiao, P.D. Babu, V. Siruguri, and D. Pal; (Under review)
- [2] “Multiferrocity across the magnetic compensation temperature in the Spinel:  $\text{Co}(\text{Cr}_{0.95}\text{Fe}_{0.05})_2\text{O}_4$  and  $\text{Co}(\text{Cr}_{0.925}\text{Fe}_{0.075})_2\text{O}_4$ ”: **Ram Kumar**, Sanjay K. Upadhyay, Y. Xiao, W. Ji and D. Pal; (Under review)
- [3] “Neutron Diffraction Study on Exotic Magnetic Properties of Mn Substituted Spinel Cobalt Chromite”; **Ram Kumar**, S. Rayaprol, V. Siruguri, and D. Pal; Physica B. 2018 (article in press).
- [4] “Magneto-structural correlation in  $\text{Co}_{0.8}\text{Cu}_{0.2}\text{Cr}_2\text{O}_4$  Cubic Spinel”; **Ram Kumar**, S. Rayaprol, V. Siruguri, Y. Xiao, W. Ji and D. Pal; Journal of Magnetism and Magnetic Materials, 454, 342-348 (2018).
- [5] “Magnetocaloric effect in Cubic Spinel  $\text{Co}(\text{Cr}_{0.95}\text{Fe}_{0.05})_2\text{O}_4$ ”; **Ram Kumar**, S. Rayaprol, Y. Xiao, W. Ji, V. Siruguri and D. Pal.; AIP Conf. Proc. (accepted) (2017).
- [6] “Room temperature neutron diffraction, optical and magnetic properties of  $\text{Co}(\text{Cr}_{1-x}\text{Mn}_x)_2\text{O}_4$  ( $x = 0.0$  and  $0.30$ )”; **Ram Kumar**, R. Padam, S. Rayaprol, V. Siruguri, and D. Pal.; AIP Conf. Proc. 1832, 130023 (2017).
- [7] “Low temperature neutron diffraction studies of  $\text{Co}(\text{Cr}_{1-x}\text{Fe}_x)_2\text{O}_4$  ( $x = 0.05$  and  $0.075$ )”; **Ram Kumar**, R. Padam, S. Rayaprol, V. Siruguri, and D. Pal; RSC Advances 4 (5), (2016) 2267-2273.
- [8] “Correlation of exchange bias with magneto-structural effects across the compensation temperature of  $\text{Co}(\text{Cr}_{1-x}\text{Fe}_x)_2\text{O}_4$  ( $x = 0.05$  and  $0.075$ )”; **Ram Kumar**, R. Padam, S. Rayaprol, V. Siruguri, and D. Pal; J. Appl. Phys. 119, 123903 (2016).
- [9] “Magnetic Structure of  $\text{Co}(\text{Cr}_{0.925}\text{Fe}_{0.075})_2\text{O}_4$ ”; **Ram Kumar**, R. Padam, S. Rayaprol, V. Siruguri, S. Ramakrishnan and D. Pal ; AIP Conf. Proc. 1731, 130025 (2016).
- [10] “Structural And Magnetic Study of  $\text{Co}(\text{Cr}_{0.925}\text{Fe}_{0.075})_2\text{O}_4$ ”; **Ram Kumar**, R. Padam, S. Rayaprol, V. Siruguri and D. Pal ; Adv. Sci. Lett. 22, 118-120 (2016).
- [11] “Magnetization reversal and giant coercivity in  $\text{Co}(\text{Cr}_{0.7}\text{Mn}_{0.3})_2\text{O}_4$ ”; R. Padam, **Ram Kumar**, A. K. Grover and D. Pal ; AIP Conf. Proc. 1591, 1648 (2014).

- [12] “Low temperature neutron diffraction studies of  $\text{Co}_{0.8}\text{Cu}_{0.2}\text{Cr}_2\text{O}_4$ ”; **Ram Kumar**, S. Rayaprol, V. Siruguri, and D. Pal; (To be communicated).
- [13] “Structural, Dielectric and magneto-dielectric studies in Jahn-teller distorted spinel  $\text{Co}_{0.8}\text{Cu}_{0.2}\text{Cr}_2\text{O}_4$ ”; **Ram Kumar** and D. Pal; (To be communicated).



### ***International and National Conference/workshop/schools presentations***

- [1] “Role of Substituents in Tailoring Magnetic Properties of Cubic  $\text{CoCr}_2\text{O}_4$  - A Neutron Diffraction Study” accepted as ***oral Presentation*** during American Conference on Neutron Scattering (ACNS2018) from June 24 - 28, 2018 in College Park, MD, at The Hotel at the University of Maryland, USA.
- [2] “Magnetocaloric effect in Cubic Spinel  $\text{Co}(\text{Cr}_{0.95}\text{Fe}_{0.05})_2\text{O}_4$ ” presented as ***oral & poster Presentation*** during 62<sup>nd</sup> DAE Solid State Physics Symposium- DAE SSPS 2017, Board of Research in Nuclear Sciences Department of Atomic Energy Government of India.
- [3] “Neutron Diffraction Study on Exotic Magnetic Properties of Mn Substituted Spinel Cobalt Chromite” presented as ***poster Presentation*** during International Conference on Neutron Scattering (ICNS-2017) held at Daejeon, South Korea.
- [4] “Room temperature neutron diffraction, optical and magnetic properties of  $\text{Co}(\text{Cr}_{1-x}\text{Mn}_x)_2\text{O}_4$  ( $x = 0.0$  and  $0.30$ )” presented as ***poster presentation*** during 61<sup>st</sup> DAE Solid State Physics Symposium- DAE SSPS 2016, Board of Research in Nuclear Sciences Department of Atomic Energy Government of India.
- [5] “Investigation on Structural And Magnetic Properties of  $\text{Co}(\text{Cr}_{1-x}\text{Fe}_x)_2\text{O}_4$  ( $x = 0.075$ )” presented as ***poster presentation*** during 6<sup>th</sup> Conference on Neutron Scattering during November 21–23, 2016 in Mumbai, India.
- [6] Attended “8<sup>th</sup> annual Asia-Oceania Neutron Scattering Association (AONSA) Neutron School organized at Bhabha Atomic Research Centre, Mumbai during 15-19 November 2016.
- [7] “Low Temperature Neutron Diffraction Studies of Fe Substituted Spinel Cobalt Chromite Systems” presented as ***poster Presentation*** during National Conference on Study of Matter Using Intense Radiation Sources and Under Extreme Conditions, (03-06 November 2016), UGC-DAE Consortium for Scientific Research (UGC-DAE CSR) University Campus, Indore.
- [8] “Neutron Diffraction Studies of Fe Substituted Spinel Cobalt Chromite” presented as ***Oral presentation*** during German Conference on Neutron Scattering 2016 (20-22<sup>nd</sup> Sep. 2016) at Kiel, Germany.
- [9] “Neutron Diffraction Study for Structure and Magnetism of  $\text{Co}(\text{Cr}_{1-x}\text{Fe}_x)_2\text{O}_4$  ( $x = 0.00, 0.05$  and  $0.075$ )” presented as ***Oral Presentation*** during Research Scholar’s Workshop On Materials Science with Neutrons (February 3-4, 2016) at BARC Mumbai.
- [10] “Magnetic Structure of  $\text{Co}(\text{Cr}_{0.925}\text{Fe}_{0.075})_2\text{O}_4$ ” presented as ***poster presentation*** during 60<sup>th</sup> DAE Solid State Physics Symposium- DAE SSPS 2015, Board of Research in Nuclear Sciences Department of Atomic Energy Government of India.

- [11] “Exchange Bias Below Compensation Temperature in  $\text{Co}(\text{Cr}_{0.7}\text{Mn}_{0.3})_2\text{O}_4$ ” presented as **poster presentation** during International conference on Magnetic materials & Applications- ICMAGMA-2015.
- [12] Attended the “14<sup>th</sup> OXFORD SCHOOL ON NEUTRON SCATTERING (OSNS-2015)” 6-18<sup>th</sup> September 2015, at Oxford, UK.
- [13] “Investigation on Structural And Magnetic Properties of  $\text{Co}(\text{Cr}_{1-x}\text{Fe}_x)_2\text{O}_4$  ( $x=0.075$ )” presented as **poster presentation** during 5<sup>th</sup> Conference on Neutron Scattering was held at the Homi Bhabha Centre for Science Education (HBCSE), Mankhurd, Mumbai, during February 2- 4, 2015.
- [14] Attended a school on “Neutrons as Probes of Condensed Matter (NPCM-2015)” from 27<sup>th</sup>-31<sup>st</sup> January 2015.
- [15] “Structural And Magnetic Study of  $\text{Co}(\text{Cr}_{0.925}\text{Fe}_{0.075})_2\text{O}_4$ ” as **poster Presentation** during The First International Conference on “Emerging Materials: Characterization & Application” (EMCA 2014, 4-6<sup>th</sup> Dec.2014) at CSIR-Central Glass and Ceramic Research Institute West Bengal, Kolkata, India
- [16] “Magnetization reversal and giant coercivity in  $\text{Co}(\text{Cr}_{0.7}\text{Mn}_{0.3})_2\text{O}_4$ ” presented as **poster Presentation** during 58<sup>th</sup> DAE Solid State Physics Symposium- DAE SSPS 2013, Board of Research in Nuclear Sciences Department of Atomic Energy Government of India.

# Contents

	<b>Page No.</b>
<b>List of Figures</b>	xxiii
<b>List of Tables</b>	xxxii
<b>List of Symbols</b>	xxxii
<hr/>	
<b>Chapter 1: Introduction</b>	<b>1 - 20</b>
1.1 Magnetism .....	1
1.2 Crystal Structure of Cobalt Chromite ( $\text{CoCr}_2\text{O}_4$ ).....	2
1.3 Magnetic Structure of $\text{CoCr}_2\text{O}_4$ .....	4
1.4 Crystal field in Spinel.....	9
1.5 Jahn-Teller Effect.....	10
1.6 Negative Magnetization (or Magnetization Reversal).....	11
1.7 Exchange Bias Effect.....	13
1.8 Multiferrocity in $\text{CoCr}_2\text{O}_4$ .....	16
1.9 Motivation.....	19
<b>Chapter 2: Experimental Techniques</b>	<b>21 - 36</b>
2.1 Sample Preparation: Solid State Reaction Method.....	21
2.2 Scattering Techniques.....	22
2.2.1 General Scattering from Matter.....	22
2.2.2 X-ray Powder Diffractometer.....	24
2.2.3 Neutron Scattering.....	25
2.2.3.1 Elastic Nuclear Scattering.....	27
2.2.3.2 Magnetic Neutron Scattering.....	28
2.2.4 High Resolution Neutron Powder Diffractometer.....	30
2.3 Physical Property Measurements.....	32
2.3.1 Superconducting Quantum Interference Device (SQUID) Magnetometer.....	33
2.3.2 Physical Property Measurement System (PPMS).....	34
2.3.2.1 AC Susceptibility Measurement .....	35
2.4 Temperature and Field dependent Dielectric and Pyroelectric Measurements.....	36

<b>Chapter 3:</b>	<b>Studies on <math>\text{Co}(\text{Cr}_{1-x}\text{Fe}_x)_2\text{O}_4</math> (<math>x = 0.00-0.075</math>)</b>	<b>37 - 74</b>
	3.1 Introduction.....	37
	3.2 Experimental Details.....	38
	3.3 Results and Discussion.....	39
	3.3.1 X-ray Diffraction.....	39
	3.3.2 Temperature and Field Dependent Magnetic Properties.....	41
	3.3.3 Exchange Bias Effect.....	44
	3.3.4 Temperature Dependent Neutron Powder Diffraction Study	44
	3.3.5 Dielectric/magneto-dielectric and Pyroelectric Properties...	63
	3.4 Summary.....	73
<b>Chapter 4:</b>	<b>Studies on <math>\text{Co}(\text{Cr}_{1-x}\text{Mn}_x)_2\text{O}_4</math> (<math>x = 0.0-0.3</math>)</b>	<b>75 - 100</b>
	4.1 Introduction.....	75
	4.2 Experimental details.....	76
	4.3 Results and Discussion.....	76
	4.3.1 X-ray Diffraction.....	76
	4.3.2 Temperature and Field Dependent Magnetic Properties...	77
	4.3.3 Exchange Bias Effect.....	84
	4.3.4 Temperature Dependent Neutron Powder Diffraction Study	86
	4.4 Summary.....	99
<b>Chapter 5:</b>	<b>Studies on <math>\text{Co}_{1-x}\text{Cu}_x\text{Cr}_2\text{O}_4</math> (<math>x = 0.00-0.20</math>)</b>	<b>101 - 129</b>
	5.1 Introduction.....	101
	5.2 Experimental Details.....	102
	5.3 Results and Discussion.....	102
	5.3.1 X-ray Diffraction.....	102
	5.3.2 Temperature and Field Dependent Magnetic Properties.....	104
	5.3.3 Exchange Bias Effect.....	110
	5.3.4 Temperature Dependent Neutron Powder Diffraction Study	112
	5.4 Summary.....	128
<b>Chapter 6:</b>	<b>Summary and Conclusions</b>	<b>130 - 133</b>
<b>References</b>		<b>134 - 139</b>

## List of Figures

Figure No.	Description	Page No.
<b>Chapter 1</b>		
1.1	Schematic representation of the different spins arrangement presenting different classes of the magnetic materials.	2
1.2	Spinel crystal structure of $\text{CoCr}_2\text{O}_4$ . The $\text{Co}^{2+}$ (green spheres) occupy the tetrahedral sites (A), the $\text{Cr}^{3+}$ (blue spheres) occupy the octahedral sites (B) and Oxygen ions are shown in the red color. The black solid lines represent a unit cell.	3
1.3	Schematic representation for the relation between the geometrical magnetic frustration along with the different magnetic configuration in different spinels.	5
1.4	Low temperature magnetic structure of spinel $\text{CoCr}_2\text{O}_4$ showing the spin-spiral ordering of $\text{Co}^{2+}$ and $\text{Cr}^{3+}$ ions for the respective sublattices (A, $B_1$ and $B_2$ ) [31].	6
1.5	(a) Field and temperature dependent phase diagram of $\text{CoCr}_2\text{O}_4$ based on magnetization and specific-heat measurements, (b) detailed spin-spiral (below $T_S$ ) phase diagram at low temperature derived from the ultrasound propagation [15,32].	7
1.6	(a) and (b) show the crystal field effect on the $3d^5$ ions in tetrahedral and octahedral environments, respectively where fivefold degeneracy is lifted and separated into two $e_g$ levels ( $d_{x^2-y^2}$ , $d_{z^2}$ ) and three $t_{2g}$ levels ( $d_{xy}$ , $d_{yz}$ and $d_{zx}$ ). (c) represents the all five different d-orbitals.	8
1.7	Schematic presentation of Jahn-Teller effect with the energy level diagram of d-orbitals showing the tetragonal distortions in case of both tetrahedral and octahedral crystal fields.	10
1.8	Temperature dependent FC ( $H = 700$ Oe) dc-magnetization curve displaying the negative magnetization in $\text{Co}_2\text{VO}_4$ [33].	12
1.9	(a) Negative ZFC magnetization due to the negative trapped field of the superconducting solenoid, and (b) a positive ZFC magnetization in the same compound with applied field of $H_A = 10$ Oe [34].	13
1.10	Schematic representation of EB effect in bilayer structure with an appearance of a pinned ferromagnetic layer at the interface with the antiferromagnetic layer having uncompensated spins (b). The hysteresis loop without shifting (a) and shifted hysteresis loop (c) presenting the exchange bias effect in the system.	14
1.11	Temperature dependence of (a) the effective coercive field ( $H_C^{\text{eff}}$ ), and (b) the EB field ( $H_{\text{EB}}$ ) of single crystalline $\text{Nd}_{0.75}\text{Ho}_{0.25}\text{Al}_2$ [26].	15
1.12	Temperature dependent FC ( $H = 0.5$ T) dc-magnetization along the [001] direction (left axis), specific heat divided by temperature in $H = 0$ T upon cooling (right axis), and dielectric constant (right axis) in $H = 0$ T at 44 kHz upon warming showing the evidence of three existing phase transitions in single crystalline $\text{CoCr}_2\text{O}_4$ [12].	17
1.13	(a) Electric polarization (P) and magnetization (M) as a function of temperature in single crystalline $\text{CoCr}_2\text{O}_4$ . (b) and (c) depict the H-dependent polarization along $[\bar{1}10]$ and magnetization along the [001] directions at 20 K and 10 K, respectively with the applied magnetic field in [001] direction [46].	18

1.14	Schematic representation of exchange bias effect around magnetically compensated state which can be achieved by tuning the different crystallographic sites of spinel $\text{CoCr}_2\text{O}_4$ .	20
------	---	----

## Chapter 2

2.1	Schematic diagram of the scattering geometry in neutron scattering experiment.	22
2.2	Schematic representation of Bragg's diffraction law with incident and diffracted waves.	23
2.3	Schematic representation of the nuclear fission reaction taking place inside the nuclear reactor for neutron production.	25
2.4	Comparison of the nuclear and magnetic form factors in neutron diffraction along with X-ray form factor plotted against scattering angle.	26
2.5	Schematic diagram presents the neutron nuclear scattering during neutron scattering experiment.	27
2.6	Schematic representation of different components of magnetic moments along with the scattering vector during magnetic scattering.	29
2.7	Block diagram of Neutron diffractometer at UGC-DAE Consortium Scientific Research, BARC, Mumbai Centre, Trombay, India.	30
2.8	Pictorial representation of neutron diffraction facility at UGC-DAE CSR, Mumbai centre [35] along with list of instrument parameters of the neutron powder diffractometer.	31
2.9	Schematic diagram of MPMS SQUID-VSM magnetometer.	32

## Chapter 3

3.1	Room temperature X-ray diffraction pattern of $\text{CoCr}_2\text{O}_4$ , along with Fe substituted compounds, i.e. $\text{Co}(\text{Cr}_{0.95}\text{Fe}_{0.05})_2\text{O}_4$ and $\text{Co}(\text{Cr}_{0.925}\text{Fe}_{0.075})_2\text{O}_4$ .	40
3.2	The temperature dependence of ZFC and FC magnetization, measured under 1 kOe field for (a) $\text{Co}(\text{Cr}_{0.95}\text{Fe}_{0.05})_2\text{O}_4$ , and (b) $\text{Co}(\text{Cr}_{0.925}\text{Fe}_{0.075})_2\text{O}_4$ . The inset of (a) shows the first order derivative plot of magnetic susceptibility for the better appearance of the magnetic transitions.	41
3.3	Temperature dependent ac-magnetic susceptibility of $\text{Co}(\text{Cr}_{0.95}\text{Fe}_{0.05})_2\text{O}_4$ measured at various frequencies under warming condition with the amplitude of dynamic magnetic-field, $h_{ac} = 3$ Oe and under zero-dc bias. Insets show the enlarged view of the magnetic transitions at different frequencies.	42
3.4	M-H loops of $\text{Co}(\text{Cr}_{0.95}\text{Fe}_{0.05})_2\text{O}_4$ and $\text{Co}(\text{Cr}_{0.925}\text{Fe}_{0.075})_2\text{O}_4$ samples in the close vicinity of respective $T_{comp}$ . Insets depict an enlarged view of respective plots to see a clear loop shifting.	43
3.5	(a-c) Rietveld refinements of the NPD patterns for $\text{Co}(\text{Cr}_{0.95}\text{Fe}_{0.05})_2\text{O}_4$ recorded in zero field at $T = 295$ K, 44 K and 20 K, respectively. Here, at 295 K, only the structural (nuclear) phase is refined and for the patterns at 44 K, both nuclear and ferrimagnetic phases are refined. For the 20 K data, incommensurate (IC) phase has also been added in the refinement where $(220)^*$ and $(002)^*$ are satellite reflections as explained in the text.	45
3.6	Temperature dependence of the bond lengths A-O and B-O along with the bond angles A-O-B and $B_1\text{-O-B}_2$ in the temperature range 2.9-90 K for both	48

Co(Cr<sub>0.95</sub>Fe<sub>0.05</sub>)<sub>2</sub>O<sub>4</sub> and Co(Cr<sub>0.925</sub>Fe<sub>0.075</sub>)<sub>2</sub>O<sub>4</sub>.

- 3.7 Schematic diagram of the crystal structure of pristine CoCr<sub>2</sub>O<sub>4</sub> for the better understanding of the different bond parameters in the compound. 49
- 3.8 Neutron diffraction patterns measured at various temperatures of (a)  $x = 0.05$  and (b)  $x = 0.075$  samples. The appearance of the (220)\* and (002)\* peaks below 35 K is evident. The insets show the temperature variation of the integrated intensity of the satellite peaks (220)\* and (002)\*. 50
- 3.9 Temperature dependence of the integrated intensity of the (111) and (220) fundamental reflections for both (a) Co(Cr<sub>0.95</sub>Fe<sub>0.05</sub>)<sub>2</sub>O<sub>4</sub>, and (b) Co(Cr<sub>0.925</sub>Fe<sub>0.075</sub>)<sub>2</sub>O<sub>4</sub>. 51
- 3.10 Diffuse signal around the (111) Bragg peak in the neutron diffraction patterns at different temperatures for (a)  $x = 0.05$ , and (b)  $x = 0.075$  (all graphs are plotted in the same scale). Temperature variation of integrated intensity of diffuse scattering are shown of both (c)  $x = 0.05$ , and (d)  $x = 0.075$  compounds.. 52
- 3.11 Temperature dependence of different site moments calculated from NPD along with EB field of Co(Cr<sub>0.095</sub>Fe<sub>0.05</sub>)<sub>2</sub>O<sub>4</sub> (a-d) and Co(Cr<sub>0.925</sub>Fe<sub>0.075</sub>)<sub>2</sub>O<sub>4</sub> (e-h) compounds. 54
- 3.12 Temperature dependence of cone angles of the different sub-lattices (A, B<sub>1</sub> and B<sub>2</sub>) of both Co(Cr<sub>0.95</sub>Fe<sub>0.05</sub>)<sub>2</sub>O<sub>4</sub> (a-c) and Co(Cr<sub>0.925</sub>Fe<sub>0.075</sub>)<sub>2</sub>O<sub>4</sub> (d-f) samples. Inset shows the ferrimagnetic spin spiral order which points to the [001] direction similar to that of the CoCr<sub>2</sub>O<sub>4</sub>. 55
- 3.13 Temperature dependent magnetization  $M(T)$  curves of Co(Cr<sub>1-x</sub>Fe<sub>x</sub>)<sub>2</sub>O<sub>4</sub> ( $x = 0.05$ , left column and  $0.075$ , right column) samples measured under the low field 0.01T [(a) and (d)], high field 5T [(b) and (e)]. (c) and (f) are the net local moments obtained from NPD data. 56
- 3.14 (a) Neutron diffraction spectra showing the modulation of the incommensurate phase for the (220)\* satellite peak which starts around 10 K. (b) depicts the  $M-T$  data at 100 Oe in the FCC and FCW modes, and (c) shows an enlarged view of the same figure for clear observation of the thermal hysteresis around 10 K. 58
- 3.15 Temperature dependent variation of different site moments from NPD data along with the Brillouin function fit of both Co(Cr<sub>0.95</sub>Fe<sub>0.05</sub>)<sub>2</sub>O<sub>4</sub> (a,b) and Co(Cr<sub>0.925</sub>Fe<sub>0.075</sub>)<sub>2</sub>O<sub>4</sub> (c,d). 60
- 3.16 Magnetic field ( $H$ ) dependence of the magnetization ( $M$ ) for Co(Cr<sub>0.95</sub>Mn<sub>0.05</sub>)<sub>2</sub>O<sub>4</sub> at different temperatures regions, (a) 34-56 K, (c) 102-120 K, (b) calculated temperature-dependent magnetic entropy change ( $-\Delta S_M$ ) around  $T_{\text{comp}}$  and (d) around FIM transition temperature  $T_C$  in the various magnetic fields changes (1 kOe-90 kOe). 61
- 3.17 The variation of the distortion ( $\Delta$ ) as a function of temperature along two different paths i.e., A-O and B-O of Co(Cr<sub>0.95</sub>Fe<sub>0.05</sub>)<sub>2</sub>O<sub>4</sub>. 62
- 3.18 Temperature dependence of (a) dielectric constant at 100 kHz (left y-axis), dc-magnetic susceptibility (right y-axis), (b) specific heat divided by temperature ( $C/T$ ) (left y-axis) and ac-magnetic susceptibility (right y-axis) with  $f = 487$  Hz of Co(Cr<sub>0.95</sub>Fe<sub>0.05</sub>)<sub>2</sub>O<sub>4</sub>. 63
- 3.19 (a) and (b) show temperature dependence of dielectric permittivity ( $\epsilon_r$ ) and  $\tan\delta$  65

- (loss) measured at the different frequencies (5kHz-100kHz) respectively for  $\text{Co}(\text{Cr}_{0.95}\text{Fe}_{0.05})_2\text{O}_4$ .
- 3.20 (a) depicts the enlarged view of temperature dependent dielectric permittivity ( $\epsilon_r$ ) at different frequencies (5kHz-100kHz) of  $\text{Co}(\text{Cr}_{0.95}\text{Fe}_{0.05})_2\text{O}_4$  and (b) shows the plot of the differences of dielectric constant ( $\Delta\epsilon_r$ ) at two extreme frequencies (5 kHz and 100 kHz) as a function of temperature in the same temperature range. 66
- 3.21 Magnetic field dependent isothermal magnetodielectric data MD, i.e.  $\Delta\epsilon_H=[(\epsilon_{H=100\text{kHz}}-\epsilon_{H=0})/\epsilon_{H=0}]$  measured at different temperatures with 100 kHz frequency of (a)  $\text{Co}(\text{Cr}_{0.95}\text{Fe}_{0.05})_2\text{O}_4$ , and (b)  $\text{Co}(\text{Cr}_{0.925}\text{Fe}_{0.075})_2\text{O}_4$ ; respective insets show the coefficient of quadratic term ( $\beta_2$ ) as a function of temperature. (For more details about fitting, see the text.) 67
- 3.22 Temperature dependence of electric polarization (P) obtained from pyroelectric current measurements for  $\text{Co}(\text{Cr}_{0.95}\text{Fe}_{0.05})_2\text{O}_4$  (a) and  $\text{Co}(\text{Cr}_{0.925}\text{Fe}_{0.075})_2\text{O}_4$  (b). The insets show the corresponding temperature dependent pyroelectric current data, which is measured with an applied voltage of 200 V in the absence of external magnetic field. 68
- 3.23 Temperature dependent magnetization of (a)  $\text{Co}(\text{Cr}_{0.95}\text{Fe}_{0.05})_2\text{O}_4$  and (b)  $\text{Co}(\text{Cr}_{0.925}\text{Fe}_{0.075})_2\text{O}_4$  samples in FC mode with two different applied magnetic field, i.e. 100 Oe and 50 kOe. Insets of both (a) and (b) show the sign change of  $\Delta M [= (M_{H=50\text{kOe}}-M_{H=100\text{Oe}})/M_{H=100\text{Oe}}]$  around compensation temperature for  $\text{Co}(\text{Cr}_{0.95}\text{Fe}_{0.05})_2\text{O}_4$  and  $\text{Co}(\text{Cr}_{0.925}\text{Fe}_{0.075})_2\text{O}_4$ , respectively. Black circles in insets represent the respective temperatures where MD effect is shown. 70
- 3.24 Plots of Inverse  $\Delta\epsilon_r$  with the square of magnetization ( $M^2$ ) of  $\text{Co}(\text{Cr}_{0.95}\text{Fe}_{0.05})_2\text{O}_4$  (a, b) and  $\text{Co}(\text{Cr}_{0.925}\text{Fe}_{0.075})_2\text{O}_4$  (c, d) at 20 K and 80 K, respectively. Respective insets show the linear variation with the square of magnetization in log scale measured at 20 K ( $T < T_{\text{comp}}$ ) and 80 K ( $T > T_{\text{comp}}$ ). 72

## Chapter 4

- 4.1 Observed and fitted powder X-ray diffraction patterns of (a)  $\text{CoCr}_2\text{O}_4$ , (b)  $\text{Co}(\text{Cr}_{0.73}\text{Mn}_{0.27})_2\text{O}_4$ , and (c)  $\text{Co}(\text{Cr}_{0.7}\text{Mn}_{0.3})_2\text{O}_4$  compounds by Rietveld refinement method using the FullProf program 77
- 4.2 (a) - (f) Temperature dependent dc-magnetization of  $\text{Co}(\text{Cr}_{1-x}\text{Mn}_x)_2\text{O}_4$  ( $x = 0.0-0.30$ ) under ZFC and FC modes with the applied field of  $H \sim 1$  kOe. 79
- 4.3 Temperature dependent magnetization of (a)  $\text{Co}(\text{Cr}_{0.73}\text{Mn}_{0.27})_2\text{O}_4$ , and (b)  $\text{Co}(\text{Cr}_{0.70}\text{Mn}_{0.30})_2\text{O}_4$  compounds measured in FC mode under various applied fields ranging from 100 Oe to 70 kOe. Here  $T_C$ ,  $T_{\text{comp}}$  and  $T_{\text{SR}}$  denote ferrimagnetic transition, compensation temperature and field induced spin reorientation transition temperatures, respectively. 80
- 4.4 Temperature dependence of ac-magnetic susceptibility measured at various frequencies under zero dc-bias field with  $h_{\text{ac}} = 3$  Oe for (a)  $\text{Co}(\text{Cr}_{0.73}\text{Mn}_{0.27})_2\text{O}_4$ , and (c)  $\text{Co}(\text{Cr}_{0.70}\text{Mn}_{0.30})_2\text{O}_4$ . (b) and (d) depict the effect of applied magnetic field for  $f = 987$  Hz for  $\text{Co}(\text{Cr}_{0.73}\text{Mn}_{0.27})_2\text{O}_4$  and  $\text{Co}(\text{Cr}_{0.70}\text{Mn}_{0.30})_2\text{O}_4$  respectively. Respective insets show the enlarged view around  $T_{\text{comp}}$ . 81

- 4.5 Main panels of (a) and (b) depict the temperature dependent specific heat  $C_p(T)$  of  $\text{Co}(\text{Cr}_{0.73}\text{Mn}_{0.27})_2\text{O}_4$  and  $\text{Co}(\text{Cr}_{0.70}\text{Mn}_{0.30})_2\text{O}_4$  samples measured in zero field, respectively. Insets of (a) and (b) show the respective  $C_p(T)/T$  vs  $T$  plot across  $T_C$  for better clarity of the transitions. 82
- 4.6 (a) FC M-H loops of  $\text{Co}(\text{Cr}_{0.7}\text{Mn}_{0.3})_2\text{O}_4$  sample at different temperatures under FC condition with  $H = 70$  kOe. (b) depicts an enlarged view of the FC M-H loop at 82 K. Inset of (a) shows the experimental and fitted initial magnetization curve at 5 K. 83
- 4.7 Temperature dependence of (a) effective coercive field  $H_c^{\text{eff}}$  and (b) EB field  $H_{\text{EB}}$  in  $\text{Co}(\text{Cr}_{0.7}\text{Mn}_{0.3})_2\text{O}_4$  compound. Inset of (a) is experimental and fitted temperature dependent  $H_c^{\text{eff}}$  plot in  $3 \text{ K} \leq T \leq 50 \text{ K}$  range. 85
- 4.8 Left panel (a-c) shows the Rietveld refinement of NPD patterns recorded in zero field at  $T = 297 \text{ K}$ ,  $59 \text{ K}$  and  $3 \text{ K}$ , respectively, for  $\text{Co}(\text{Cr}_{0.73}\text{Mn}_{0.27})_2\text{O}_4$ . Similarly, right panel (a-c) depicts NPD patterns recorded in zero field at  $T = 295 \text{ K}$ ,  $82 \text{ K}$  and  $3 \text{ K}$ , respectively for  $\text{Co}(\text{Cr}_{0.70}\text{Mn}_{0.30})_2\text{O}_4$ . NPD patterns near room temperature (297 K and 295 K) are refined using a structural phase (indicated by the first row of vertical tick marks) whereas another FM phase (second row) is also included in refinement for temperature below  $T_C$ . 87
- 4.9 Temperature dependence of the integrated intensity of the (111), (220), (400) and (331) fundamental Bragg reflections for  $\text{Co}(\text{Cr}_{0.73}\text{Mn}_{0.27})_2\text{O}_4$  (a-d) and for  $\text{Co}(\text{Cr}_{0.70}\text{Mn}_{0.30})_2\text{O}_4$  (e-h). 88
- 4.10 Diffuse signal around the (111) Bragg peak in the neutron diffraction patterns at different temperatures for  $\text{Co}(\text{Cr}_{0.73}\text{Mn}_{0.27})_2\text{O}_4$  (a-f) and  $\text{Co}(\text{Cr}_{0.70}\text{Mn}_{0.30})_2\text{O}_4$  (g-l) (all graphs are plotted in the same scale). 89
- 4.11 Temperature variation of integrated intensity of diffuse signal around (111) Bragg peak for both  $\text{Co}(\text{Cr}_{0.73}\text{Mn}_{0.27})_2\text{O}_4$  (a) and  $\text{Co}(\text{Cr}_{0.70}\text{Mn}_{0.30})_2\text{O}_4$  (b) compounds. 90
- 4.12 Temperature dependent magnetization  $M(T)$  curves of  $\text{Co}(\text{Cr}_{0.73}\text{Mn}_{0.27})_2\text{O}_4$  (Left panel) and  $\text{Co}(\text{Cr}_{0.70}\text{Mn}_{0.30})_2\text{O}_4$  (right panel) samples measured under low field (a)&(d) and under high field (b)&(e). In last (c)&(f) show the net local moments obtained from NPD data of both the samples  $\text{Co}(\text{Cr}_{0.73}\text{Mn}_{0.27})_2\text{O}_4$  and  $\text{Co}(\text{Cr}_{0.70}\text{Mn}_{0.30})_2\text{O}_4$  respectively. 91
- 4.13 Temperature dependence of different site moments (i.e.  $A$ ,  $B_1$  and  $B_2$ ) of both the compounds; (a-c)  $\text{Co}(\text{Cr}_{0.73}\text{Mn}_{0.27})_2\text{O}_4$ , and (d-f)  $\text{Co}(\text{Cr}_{0.70}\text{Mn}_{0.30})_2\text{O}_4$ . 92
- 4.14 Temperature dependence of cone angles ( $\alpha$ ), ( $\beta$ ) and ( $\gamma$ ) of sublattices  $A$ ,  $B_1$  and  $B_2$  of (a-c)  $\text{Co}(\text{Cr}_{0.73}\text{Mn}_{0.27})_2\text{O}_4$  and (d-f)  $\text{Co}(\text{Cr}_{0.70}\text{Mn}_{0.30})_2\text{O}_4$ , respectively. Insets show the cone angles representing conical spin-spiral ordering pointing to the [001] direction. 93
- 4.15 The temperature dependence of the bond lengths Co-O (A-O) and Cr/Mn-O (B-O) along with the bond angles Co-O-Cr/Mn (A-O-B) and Cr/Mn-O-Cr/Mn (B-O-B) for  $\text{Co}(\text{Cr}_{0.73}\text{Mn}_{0.27})_2\text{O}_4$  [(a) & (b)] and  $\text{Co}(\text{Cr}_{0.70}\text{Mn}_{0.30})_2\text{O}_4$  [(c) & (d)] compounds. 94
- 4.16 The variation of the distortion ( $\Delta$ ) as a function of temperature along two different path i.e. A-O and B-O of  $\text{Co}(\text{Cr}_{0.70}\text{Mn}_{0.30})_2\text{O}_4$ . 95
- 4.17 Magnetic field ( $H$ ) dependence of the magnetization ( $M$ ) for  $\text{Co}(\text{Cr}_{0.70}\text{Mn}_{0.30})_2\text{O}_4$  at different temperatures regions, 70-98 K (a) and 106-120 K (c) and calculated 97

- temperature-dependent magnetic entropy change ( $-\Delta S_M$ ) around  $T_{\text{comp}}$  (b) and around FIM transition temperature  $T_C$  (d) under various magnetic fields changes (1 kOe- 90 kOe).
- 4.18 Temperature dependent variation of different site moments along with the fit of Brillouin function for both  $\text{Co}(\text{Cr}_{0.73}\text{Mn}_{0.27})_2\text{O}_4$  (a-b) and  $\text{Co}(\text{Cr}_{0.70}\text{Mn}_{0.30})_2\text{O}_4$  (c-d). 99

## Chapter 5

- 5.1 (a) An example of the linkage of  $\text{CoO}_4/\text{CuO}_4$  tetrahedral A-site through a  $\text{CrO}_6$  octahedral B-site. Schematic representation of enlarged view of  $\text{CoO}_4$  (b) &  $\text{CuO}_4$  (c) tetrahedron and  $\text{CrO}_6$  octahedron (d) with electronic configurations of constituent  $\text{Co}^{2+}$ ,  $\text{Cu}^{2+}$  and  $\text{Cr}^{3+}$  ions, respectively. The dotted spin arrow in case of  $\text{CuO}_4$  shows the degeneracy present in the  $t_{2g}$  orbitals. Oxygen atoms are omitted for a clear view. 101
- 5.2 Room temperature X-ray diffraction patterns of  $\text{Co}_{1-x}\text{Cu}_x\text{Cr}_2\text{O}_4$  ( $x = 0.0-0.20$ ) polycrystalline compound with Rietveld refinement showing that all compounds are in single phase with cubic  $Fd\bar{3}m$  space group. 103
- 5.3 Temperature dependent dc-magnetization of  $\text{Co}_{1-x}\text{Cu}_x\text{Cr}_2\text{O}_4$  ( $x = 0.0-0.20$ ) under ZFC and FC conditions with the applied field of  $H \sim 1$  kOe. 104
- 5.4 (a) Temperature dependent magnetization for  $\text{Co}_{0.8}\text{Cu}_{0.2}\text{Cr}_2\text{O}_4$  at  $H = 100$  Oe under both the ZFC and FC conditions, and (b) shows the  $dM_{\text{ZFC}}/dT$  plot of the same sample. Insets show the enlarged portion of the plot where another transition ( $T_{\text{str}} \sim 95$  K) can be seen clearly. Arrows represent the different magnetic transitions in the sample. 105
- 5.5 Temperature dependent dc-magnetization of  $\text{Co}_{0.8}\text{Cu}_{0.2}\text{Cr}_2\text{O}_4$  sample measured in FC mode for different applied fields (1 kOe, 30 kOe and 50 kOe). 107
- 5.6 (a) Temperature dependence of ac-magnetic susceptibility of  $\text{Co}_{0.8}\text{Cu}_{0.2}\text{Cr}_2\text{O}_4$  recorded at various frequencies, 487 Hz, 987 Hz and 4797 Hz under zero dc-bias field with  $h_{\text{ac}} = 3$  Oe. (b) shows the effect of applied magnetic field for  $f = 987$  Hz of the same sample. Inset shows the enlarged view around magnetic transitions. 108
- 5.7 The magnetization ( $M$ ) versus field ( $H$ ) hysteresis loops of  $\text{Co}_{0.8}\text{Cu}_{0.2}\text{Cr}_2\text{O}_4$  are shown at selected temperatures in the vicinity of compensation temperature. The respective insets show the enlarged view of  $M$ - $H$  loops near origin showing the asymmetry in the loops. 109
- 5.8 The temperature variation of exchange bias field; (a)  $H_{\text{EB}}(T)$ , (b)  $M_{\text{EB}}(T)$ , and (c) coercive field  $H_C(T)$  in  $\text{Co}_{0.8}\text{Cu}_{0.2}\text{Cr}_2\text{O}_4$ . The lines connecting the data points are visual guides. 110
- 5.9 The main panel of (a) shows the temperature dependent specific heat  $C_p(T)$  of  $\text{Co}_{0.8}\text{Cu}_{0.2}\text{Cr}_2\text{O}_4$  sample measured with  $H = 0$  Oe and 50 kOe. Insets (I) and (II) show the enlarged view across  $T_c$  and magnetic entropy  $\Delta S_m(T)$  across the  $T_C$ , respectively. Main panel of (b) shows the  $C_p(T)/T$  with the first order derivative in the inset. 111
- 5.10 Temperature dependent NPD patterns with Rietveld refinement in zero field at (a)  $T = 300$  K, (b) 51 K and (c) 3 K of  $\text{Co}_{0.8}\text{Cu}_{0.2}\text{Cr}_2\text{O}_4$ . NPD pattern at room temperature 113

	(300 K) is refined using a structural phase (indicated by the first row of vertical tick marks) whereas for 51 K another structural phase along with FM phase (second row and third row) is also included in the refinement. NPD patterns at 3 K include additional incommensurate (IC) phase along with all these phases in the refinement.	
5.11	Temperature dependence of the integrated intensity of the fundamental reflections for $\text{Co}_{0.8}\text{Cu}_{0.2}\text{Cr}_2\text{O}_4$ .	114
5.12	Low temperature magnetic structure of $\text{Co}_{0.8}\text{Cu}_{0.2}\text{Cr}_2\text{O}_4$ at (a) 90 K, (b) 45 K, and (c) 3 K. NPD patterns of $\text{Co}_{0.8}\text{Cu}_{0.2}\text{Cr}_2\text{O}_4$ measured at 200 K (a), and at 90 K (b).	114
5.13	NPD patterns of $\text{Co}_{0.8}\text{Cu}_{0.2}\text{Cr}_2\text{O}_4$ measured at (a) 200 K, and (b) 90 K with Rietveld refinement. The enlarged view of the (8 0 0) Bragg reflections of these NPD patterns have been shown at (c) 200 K, and (d) 90 K. The stars indicate the distorted peaks in the patterns.	117
5.14	The temperature dependence of phase fraction of both the phases (cubic and orthorhombic) present in $\text{Co}_{0.8}\text{Cu}_{0.2}\text{Cr}_2\text{O}_4$ . The green dashed line at $T \sim 52$ K displays an unusual structural phase fraction around $T_{\text{comp}}$ . The inset shows an enlarged view of such unusual anomaly around $T \sim 52$ K.	120
5.15	Variation in lattice parameter as a function of temperature in $\text{Co}_{0.8}\text{Cu}_{0.2}\text{Cr}_2\text{O}_4$ . (a) Cubic lattice constant shows a dip around $T_{\text{comp}} \sim 52$ K, and (b) also depicts the non-monotonic change in lattice parameters (a, b and c) of the orthorhombic phase around same $T_{\text{comp}}$ .	121
5.16	The temperature dependence of the different Bragg peaks; (a) (400), and (b) (511) of $\text{Co}_{0.8}\text{Cu}_{0.2}\text{Cr}_2\text{O}_4$ at different temperatures.	122
5.17	Temperature dependent magnetization $M(T)$ curves of $\text{Co}_{0.8}\text{Cu}_{0.2}\text{Cr}_2\text{O}_4$ measured under low field (a) 100 Oe, and (b) high field 50 kOe. Net local moments obtained from NPD data are shown in (c).	123
5.18	(a-h) Diffuse signals around the (111) Bragg peak in the neutron diffraction patterns at different temperatures of $\text{Co}_{0.8}\text{Cu}_{0.2}\text{Cr}_2\text{O}_4$ (all graphs are plotted in the same scale). The integrated intensity of these humps is shown in (i).	124
5.19	Temperature dependence of the observed magnetic moments of A (Co/Cu) and B (Cr)-sites from the NPD data and calculated moments from the molecular field calculation (MFC) of $\text{Co}_{0.8}\text{Cu}_{0.2}\text{Cr}_2\text{O}_4$ .	125
5.20	Temperature dependent magnetic entropy change ( $-\Delta S_M$ ) around (a) $T_S$ and $T_{\text{comp}}$ , and (b) around $T_C$ for $\text{Co}_{0.8}\text{Cu}_{0.2}\text{Cr}_2\text{O}_4$ .	127
5.21	Observed distortion ( $\Delta$ ) in lattice constant of cubic phase of $\text{Co}_{0.8}\text{Cu}_{0.2}\text{Cr}_2\text{O}_4$ as a function of temperature with clear anomaly around $T_{\text{comp}}$ .	128



## List of Tables

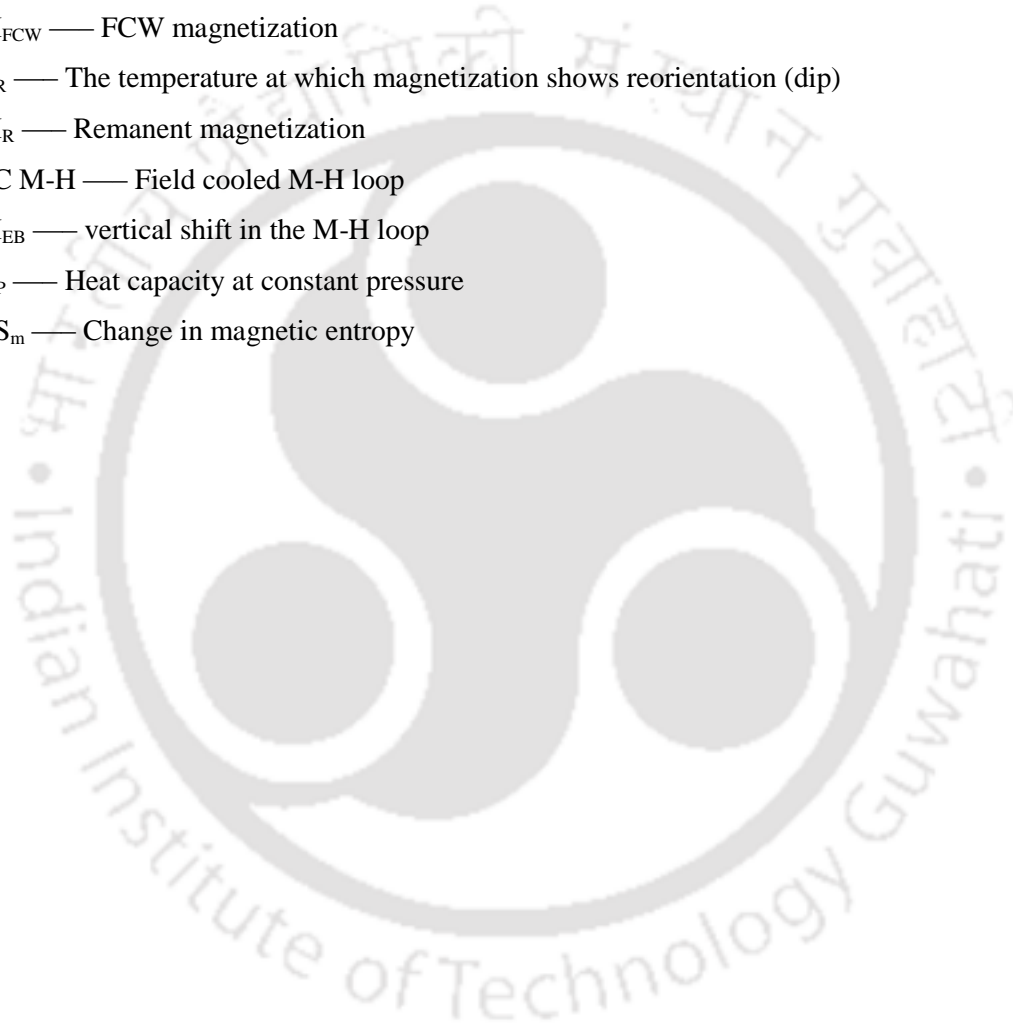
Table No.	Description	Page No.
<b>Chapter 3</b>		
3.1	Structural parameters from the Rietveld refinement of X-ray powder diffraction patterns for $\text{Co}(\text{Cr}_{1-x}\text{Fe}_x)_2\text{O}_4$ ( $x = 0.0-0.075$ ) samples at room temperature.	40
3.2	Structural and magnetic parameters like lattice constant (a), magnetic moments and agreement factors are determined from Rietveld refinement of neutron diffraction patterns measured at low temperatures for the $\text{Co}(\text{Cr}_{0.95}\text{Fe}_{0.05})_2\text{O}_4$ compound [both commensurate (CP) and incommensurate phase (ICP)].	47
3.3	Structural and magnetic parameters like lattice constant (a), magnetic moments and agreement factors are determined from Rietveld refinement of neutron diffraction patterns measured at low temperatures for the $\text{Co}(\text{Cr}_{0.95}\text{Fe}_{0.05})_2\text{O}_4$ compound [both commensurate (CP) and incommensurate phase (ICP)].	47
3.4	The calculated molecular field constants, $\lambda$ from molecular field calculations for both the compounds with $T_{\text{comp}}$ and $T_{\text{C}}$ are shown here.	59
3.5	Parameter ( $\gamma$ ) extracted from the fits in Fig. 3.23 by using equation (3) for both $\text{Co}(\text{Cr}_{0.95}\text{Fe}_{0.05})_2\text{O}_4$ and $\text{Co}(\text{Cr}_{0.925}\text{Fe}_{0.075})_2\text{O}_4$ compounds at different temperatures are given as.	73
<b>Chapter 4</b>		
4.1	Structural parameters, selected bond distances and bond angles from the Rietveld refinement of X-ray powder diffraction patterns for $\text{Co}(\text{Cr}_{1-x}\text{Mn}_x)_2\text{O}_4$ ( $x = 0.0$ and $0.30$ ) samples at room temperature.	78
<b>Chapter 5</b>		
5.1	Refined parameters of $\text{Co}_{0.8}\text{Cu}_{0.2}\text{Cr}_2\text{O}_4$ from NPD pattern at 200 K.	116
5.2	Crystallographic information and Rietveld profile reliability factors for $\text{Co}_{0.8}\text{Cu}_{0.2}\text{Cr}_2\text{O}_4$ from NPD pattern at 200 K and 90 K.	116

## List of abbreviations/Symbols

XRD	—	X-ray diffraction
d	—	Inter planar spacing
$\theta$	—	Diffraction angle
$\lambda$	—	Wavelength
Å	—	Angstrom
nm	—	Nanometer
mm	—	Millimeter
cm	—	Centimeter
$\mu\text{m}$	—	Micro-meter
T	—	Temperature
K	—	Kelvin (SI unit of temperature)
T	—	Tesla (SI unit of magnetic field)
Oe	—	Oersted (SI unit of magnetic field)
C	—	Curie constant
$T_C$	—	Curie temperature
$T_N$	—	Néel temperature
h	—	hours
FE	—	Ferroelectric
FM	—	Ferromagnetic
AFM	—	Antiferromagnetic
FIM	—	Ferrimagnetic
$\epsilon_r$	—	Relative dielectric permittivity
$\mu_{\text{eff}}$	—	Effective paramagnetic moment
$\mu_B$	—	Bohr magnetron
$\mu_A/\mu_B$	—	Net magnetic moment of A/B-sub lattice in spinel compound
P	—	Electric polarization
E	—	Electric field
H	—	Magnetic field
M	—	Magnetization
ZFC	—	Zero field cooled
FCC	—	Field cooled cooling

FC/FCW — Field cooled warming  
 A, B sites — Tetrahedral, Octahedral sites  
 M-T — Temperature dependent magnetization  
 M-H — Field dependent magnetization  
 EB — Exchange bias  
 $H_{EB}$  — EB field  
 $H_{FC}$  — Cooling field  
 $M_R$  — Remanance  
 $H_C$  — Coercivity  
 $T_{comp}$  — Compensation temperature  
 $T_{SR}$  — Spin reorientation transition  
 FWHM — Full width at half maxima  
 NPD—Neutron Powder Diffraction  
 $k$ —propagation vector  
 $Q$  — Scattering vector  
 SR — Short range  
 IC — Incommensurate  
 C — Commensurate  
 $e_{ij}$  — Position vector joining two adjacent moments in spin-spiral  
 $E$  — Magnetic exchange energy  
 $J_{ij}$  — Superexchange integral  
 $S$  — Spin moment  
 RKKY — Ruderman-Kittel-Kasuya-Yosida  
 $\chi$  — Magnetic susceptibility  
 $\chi_{ac}$  — AC Magnetic susceptibility  
 $N$  — Avagadro number ( $6.023 \times 10^{23}$ )  
 $k_B$  — Boltzman constant  
 $g$  — Lande g-factor  
 NN — Nearest neighbours  
 NNN — Next nearest neighbours  
 $T_S$  — Spin-spiral or Magneto-structural transition in  $CoCr_2O_4$   
 GMF — Geometrical magnetic frustration  
 LKDM — Lyons, Kaplan, Dwight and Menyuk (model)  
 $u$  — A parameter in LKDM model

$T_L$  — Lock-in transition in  $\text{CoCr}_2\text{O}_4$   
 $\text{CEP}$  — Conduction electron polarization  
 $\text{SQUID}$  — Superconducting Quantum Interference Device  
 $\text{PPMS}$  — Physical Property Measurement System  
 $a$  — Lattice parameter of the cubic unit-cell  
 $M_S$  — Saturation magnetization in M-H loop  
 $M_{\text{FCC}}$  — FCC magnetization  
 $M_{\text{FCW}}$  — FCW magnetization  
 $T_R$  — The temperature at which magnetization shows reorientation (dip)  
 $M_R$  — Remanent magnetization  
 $\text{FC M-H}$  — Field cooled M-H loop  
 $M_{\text{EB}}$  — vertical shift in the M-H loop  
 $C_p$  — Heat capacity at constant pressure  
 $\Delta S_m$  — Change in magnetic entropy





---

## **Introduction**

---

Nowadays our daily life is mostly dependent on magnetic materials and their applications, for example, storage of digital and analog information, in aviation industry, for the creation of strong motors and aviation sensors and in medical industry e.g. magnetic resonance imaging (MRI) etc. The field of magnetism involves several fashionable research topics, including giant magnetoresistance (GMR) effect, high  $T_C$  superconductors, magnetocaloric effect (MCE), colossal magnetoresistance (CMR) effect, magnetic exchange bias (EB) effect, spintronics, topological insulators and many more [36–41,27,42,43]. The basic motivation of the interplay between the magnetic properties and electric properties of materials opened up a field of spintronics which is believed to bring innovation in the future technology. After the discovery of EB effect, there has been a revolution in the spintronic related industry as EB plays very crucial role in devices [27,28,44]. In terms of enhancement of functionalities of these devices, one can go for the multiferroics, in which magnetic and ferroelectric ordering coexist and can be controlled by one another. Researchers in this field have renewed their interest to search for new multiferroic materials and these are indeed exciting times for material research. Strong magnetoelectric (ME) coupling in multiferroic also finds many potential applications like AC/DC magnetic field sensors, band-pass/band-stop filters, transducers and phase shifters, etc. [45–49]. Hence, one has to understand various aspects of electricity and magnetism behind such phenomena in order to adapt materials for the fundamental physics as well for technological applications point of view.

### **1.1 Magnetism**

In solids, it is the spin degree of freedom which is responsible for perceiving most of the magnetic phenomena. An ordered magnetic state exists below a characteristic temperature which is known as transition temperature  $T_C$  in magnetic compounds. Generally in solid state physics, unpaired electrons in the partially filled  $d$ -shell of transition metal ions or  $f$ -shell of rare-earth ions give rise to magnetism in the system. The magnetic exchange interaction is responsible for

giving rise to interaction among different moments of neighboring elements. This exchange interaction energy between localized moments which dominates over the thermal energy corresponds to the magnetic ordering below/at their respective transition temperature. Naively, magnetic materials are classified in to three classes (as shown in Fig. 1.1) which depends on the different microscopic arrangement of the magnetic moments,

- (i) Ferromagnetic (FM)
- (ii) Antiferromagnetic (AFM)
- (iii) Ferrimagnetic (FIM)

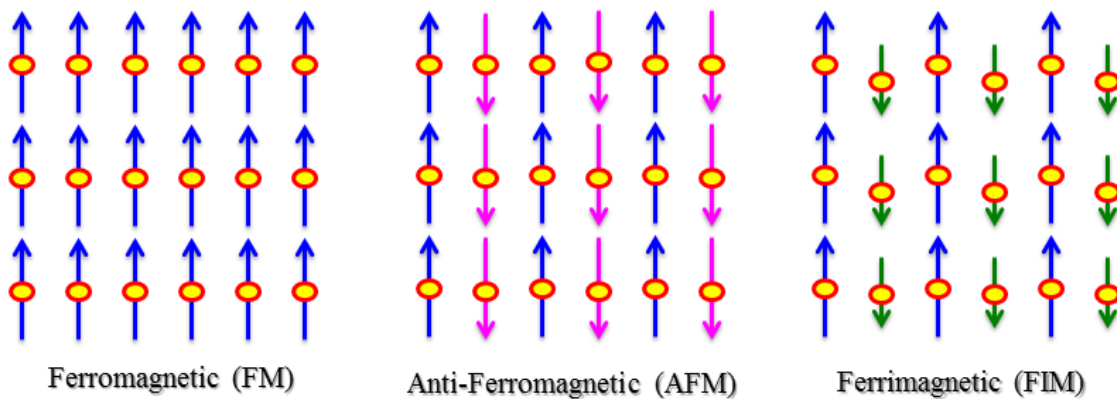


**Figure 1.1** Schematic representation of the different spins arrangement presenting different classes of the magnetic materials.

From the above figure, one can see that adjacent moment which aligns parallel to each other, even in the absence of external field, represents a FM material. These FM materials can exhibit spontaneous magnetization below the Curie temperature ( $T_C$ ). In case of AFM materials, the neighboring moments align antiparallel to each other, which results in zero net magnetic moment. In case AFM materials, the transition temperature where AFM ordering takes place is known as Néel Temperature ( $T_N$ ). Further, FIM materials are known as a special case of AFM materials having two magnetic sublattices with different magnitude of magnetic moments which give rise to net magnetization similar to the FM materials.

## 1.2 Crystal Structure of Cobalt Chromite ( $CoCr_2O_4$ )

In recent studies, due to success of technological advancement along with multiple functionalities and fascinating properties, transition metal oxides (TMO) have attracted lot of

attention [50–52]. The transition metal oxides based system with spinel ( $AB_2O_4$ ) structure have attracted many researchers due to various interesting properties such as multiferroicity, ferroelectricity, different phase-transitions, colossal magnetoresistance (CMR), metal-insulator transitions, coexistence of charge, orbital and spin ordering and magnetocaloric effect (MCE) etc. [1–4]. One should know that all these fascinating properties are very sensitive to their crystalline as well as magnetic structures and also on the application of external parameters such as temperature, pressure, electric and magnetic fields. Recently, such interesting TMO materials are under intense investigation because of their potential applications in the field of spintronic, magnetic field sensors and magnetic refrigeration etc.

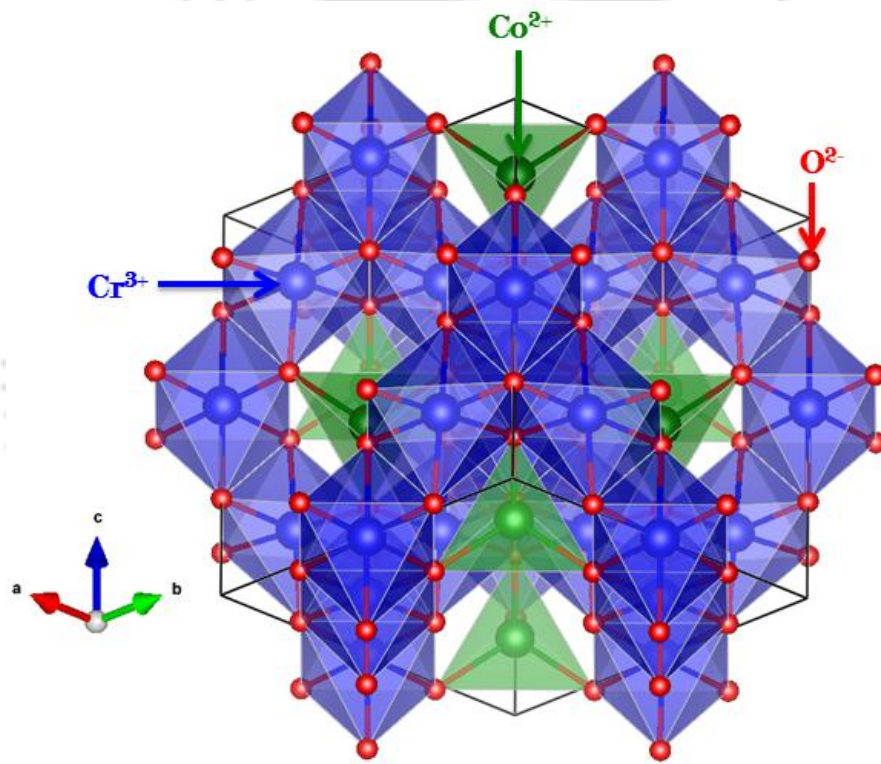


**Figure 1.2** Spinel crystal structure of  $CoCr_2O_4$ . The  $Co^{2+}$  (green spheres) occupy the tetrahedral sites (A), the  $Cr^{3+}$  (blue spheres) occupy the octahedral sites (B) and Oxygen ions are shown in the red color. The black solid lines represent a unit cell.

Spinel oxides have the same structure as that of the mineral spinel,  $MgAl_2O_4$  which have the space group  $Fd\bar{3}m$  (space group no.227). Bragg [53] and Nishikawa [54] both determined this crystal structure independently. Cobalt chromite ( $CoCr_2O_4$ ) with  $Co^{2+}$  and  $Cr^{3+}$  magnetic ions also crystallizes in this same  $AB_2O_4$  ( $MgAl_2O_4$ ) type crystalline spinel structure. Existing oxygen anions in  $CoCr_2O_4$  designed two different interstitial sites or environments which are

known as A-site (tetrahedral environment) and B-site (octahedral environment). Such atomic arrangement formed the close-packed face-centered cubic (FCC) lattice for  $\text{CoCr}_2\text{O}_4$ . A-site cations (i.e.  $\text{Co}^{2+}$ ) in the tetrahedral environment form a diamond structure whereas B-cations (i.e.  $\text{Cr}^{3+}$ ) sitting in the octahedral environment have a pyrochlore structure. There are eight formula units per unit cell of spinel structure, i.e.  $8[\text{AB}_2\text{O}_4]$  which can be represented as  $\text{A}_8\text{B}_{16}\text{O}_{32}$ . In general, there are two different sub-lattices (A and B) for spinel structure and depending on the distribution of the total present cations in the available two different sublattices, one can define the different types of spinel compounds. Generally there are three types of spinel structure: (i) Normal Spinel ( $\text{CoCr}_2\text{O}_4$ ), (ii) Inverse Spinel ( $\text{Fe}_3\text{O}_4$  [55]) and (iii) Mixed Spinel. In case of normal spinel, all tetrahedral sites are occupied by all 8 A-cations and all 16 B-cations occupy the octahedral site. For obtaining inverse spinel structure, half (i.e. 8) of the B-cations occupy tetrahedral site and remaining 8 B-cations together with all A-cations reside in the octahedral site. In case of mixed spinel, some intermediate number of total present A and B-cations occupy these tetrahedral and octahedral sites, for example  $\text{CoFe}_2\text{O}_4$  [56]. A schematic representation of normal spinel crystal structure of  $\text{CoCr}_2\text{O}_4$  is presented in Fig.1.2 where one can see that tetrahedron and octahedron are connected through the corners whereas octahedron to octahedron sharing takes place along with the edges of adjacent octahedron. Further, different angles along superexchange path in  $\text{CoCr}_2\text{O}_4$ , i.e.  $\text{Co-O-Cr}$  (A-O-B) and  $\text{Cr-O-Cr}$  (B-O-B) are around  $125^\circ$  and around  $95^\circ$ . In this cubic spinel structure, distance between the A-site ions (i.e. A-A neighbor ions) is longest followed by the A-B neighbor distance and the smallest distance exists between B-B neighbors [20].

### ***1.3 Magnetic Structure of $\text{CoCr}_2\text{O}_4$***

Depending on the existence of transition metal ions in different interstitial sites (the tetrahedral (A) and octahedral (B) of spinel structure, spinel oxides exhibit a wide range of magnetic properties. In these spinels, magnetism is mainly governed by AFM exchange interactions. Due to lattice geometry in the spinels, the existing spin interactions could not be fully satisfied which give rise to magnetic spin frustration in these compounds which is known as geometrical magnetic frustration (GMF) [57–59]. The main outcome of such frustration is the inability of the system to form collinear magnetic ground states, thus leading to emergence of

unconventional non-collinear ground states which is present in the spinel compounds as shown in Fig. 1.3 [57,60].

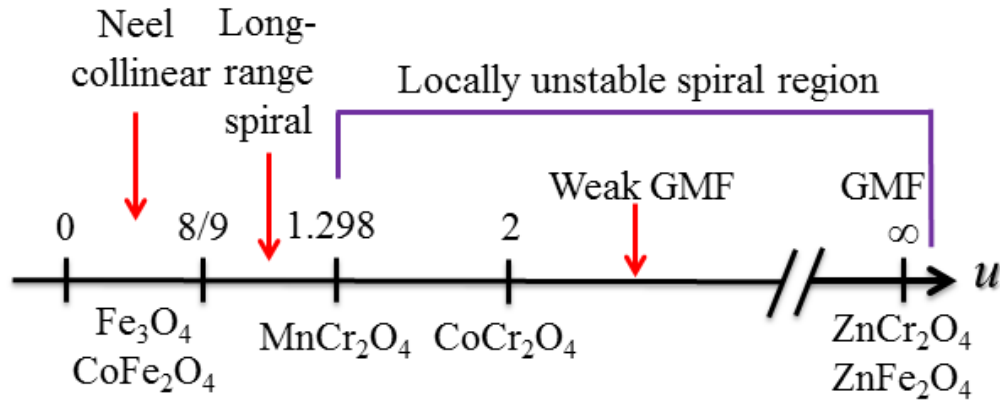


**Figure 1.3** Schematic representation for the relation between the geometrical magnetic frustration along with the different magnetic configuration in different spinels.

Having the crystallographic information of  $\text{CoCr}_2\text{O}_4$ , one should also know about the existing magnetic structure in detail. Basically, magnetic structure is not much different from chemical structure as it refers to the real arrangement of spins in the respective magnetic unit cell. One important thing to remember is that the size of magnetic unit cells can be different from the chemical one. Neutron powder diffraction (NPD) is one of best technique to find the magnetic structure of polycrystalline sample. A three dimensional orientation of magnetic spins with respect to different crystallographic directions along with their magnitude can be seen clearly through NPD experiments.

Chemical structure of  $\text{CoCr}_2\text{O}_4$  (cf. Fig.1.1) shows that magnetic ions of  $\text{Co}^{2+}$  at tetrahedral A-site is strongly coupled to the other magnetic ions of  $\text{Cr}^{3+}$  at octahedral B-site via superexchange interactions.  $\text{Co}^{2+}$ -cations in  $\text{CoCr}_2\text{O}_4$  spinels form a tetrahedrally coordinated diamond structure, which is simply looks like a chain of corner shared triangles. On the other hand, pyrochlore lattice formed by the  $\text{Cr}^{3+}$  cations represents the corner shared tetrahedra. In case of spinel where only B cations are magnetic, GMF is present due to the strong magnetic interaction in pyrochlore lattice of B-sites, and leads to evolving excitations of spin states which results in complicated non-collinear spin structures. Further, if in case A-site is also occupied with the magnetic ions (example:  $\text{CoCr}_2\text{O}_4$ ), the strength of super exchange interaction between A and B ( $J_{AB}$ ) becomes comparable to that of the strength between B-sites ( $J_{BB}$ ). This causes the

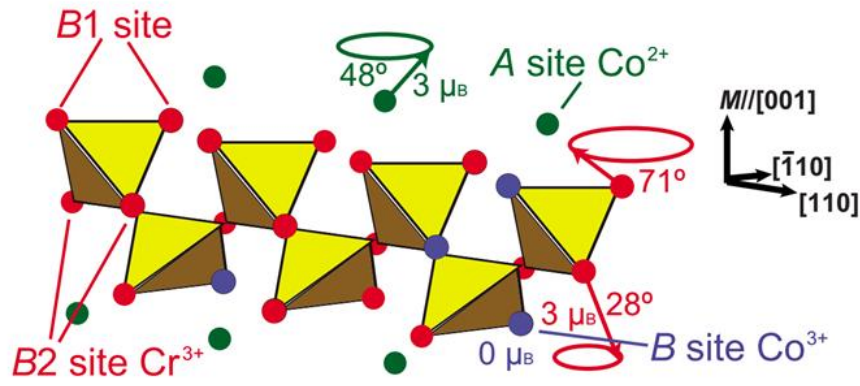
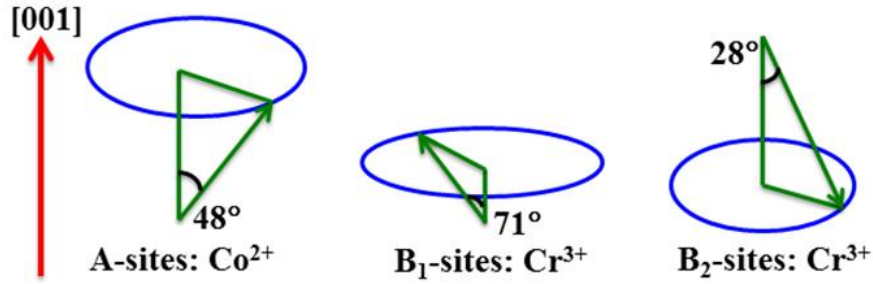


**Figure 1.4** Low temperature magnetic structure of spinel  $\text{CoCr}_2\text{O}_4$  showing the spin-spiral ordering of  $\text{Co}^{2+}$  and  $\text{Cr}^{3+}$  ions for the respective sublattices (A,  $B_1$  and  $B_2$ ) [31].

reduction in the GMF and results three different magnetic sub lattices namely Co (A),  $\text{Cr}_1(B_1)$ , and  $\text{Cr}_2(B_2)$  with complex non-collinear spin-spirals structure [33,61]. Fig. 1.4 depicts the low temperature magnetic structure of  $\text{CoCr}_2\text{O}_4$  which represents the complex non-collinear spin spiral ordering. In last case, when only the A cations are magnetic, frustration due to competing nearest neighbour (NN) and next nearest neighbour (NNN) magnetic exchange interactions lead to non-collinear magnetic ground states [62–65].

For  $\text{CoCr}_2\text{O}_4$ , neutron scattering experiment along with superexchange integrals ( $J_{AB}$  and  $J_{BB}$ ) corroborate the value of ' $u$ '  $\sim 2$  [8]. LKDM model suggests that if the value of ' $u$ ' is around 2, it will be a favourable condition for the formation of spin spirals configuration [8,33,66] which is seen in case of  $\text{CoCr}_2\text{O}_4$  at low temperature. Experimentally observed results showed that the observed FIM ordering at transition temperature  $T_C$  is mainly due to the ordering of the A-site ( $\text{Co}^{2+}$ ) moments which are parallel to  $[001]$  easy axis [33,67]. Further, neutron scattering experiments have shown that below the FIM ordering, the presence of weak GMF gives rise to

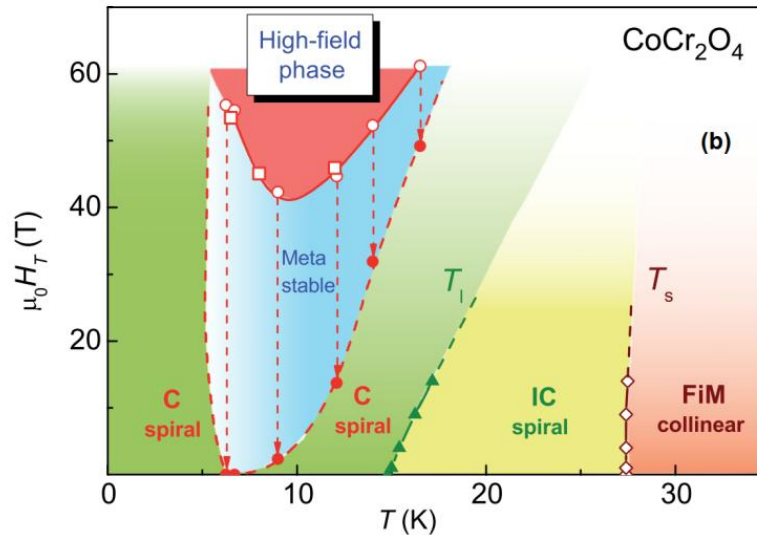
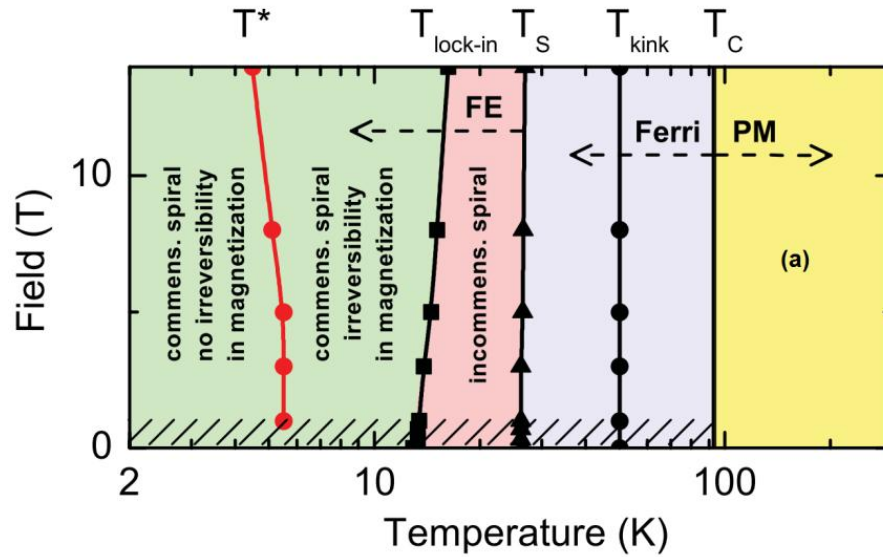


**Figure 1.5** (a) Field and temperature dependent phase diagram of  $\text{CoCr}_2\text{O}_4$  based on magnetization and specific-heat measurements, (b) detailed spin-spiral (below  $T_S$ ) phase diagram at low temperature derived from the ultrasound propagation [15,32].

the formation of short range spin-spiral ordering together with the long range ordering of A-site ( $\text{Co}^{2+}$ ) moments [8,33,67]. This short range spin-spiral ordering entirely changes into a long range incommensurate (IC) conical spin-spiral ordering at  $T_S$  which is known as the magneto-structural transition as the magnetic structure changes from collinear FIM ordering to IC conical spin-spiral ordering. Such conical spin-spiral picture of different site moments of A ( $\text{Co}^{2+}$ ),  $B_1(\text{Cr}^{3+})$  and  $B_2(\text{Cr}^{3+})$  is shown in Fig. 1.4. The cone angles for the different site moments of A,  $B_1$  and  $B_2$  are  $48^\circ$ ,  $71^\circ$  and  $28^\circ$ , respectively in pristine  $\text{CoCr}_2\text{O}_4$ . Further, one can visualize this

magnetic structure clearly as it could be seen that A-site moment is along the  $[001]$  direction along with net moment of B-site align to the  $[00\bar{1}]$  direction. The detailed magnetic ordering at  $T_S$ , which confirms the long range ordering of conical spin-spiral components with an incommensurate phase with propagation vector  $k = (0.63, 0.63, 0)$ , has been confirmed through neutron scattering experiments [8,18]. Further, another transition around 13 K had also been revealed from detailed neutron scattering experiments which was observed as step-like change in the thermomagnetic properties [12,18]. There is a further change in magnetic structure as the IC propagation vector observed at  $T_S$  adapts to a commensurate phase of conical spin order with  $k = (2/3, 2/3, 0)$  across  $T_L$  [18]. As this propagation vector of commensurate conical spin-spiral order is locked to the underlying lattice below 13 K, hence such transition at  $T_L$  is known as the lock-in transition [12]. Further, high-field magnetization and heat capacity measurements on single crystal  $\text{CoCr}_2\text{O}_4$  revealed a new transition at  $T^* = 5-6$  K [32]. Above Fig. 1.5 (a) shows a magnetic field vs. temperature (H-T) phase diagram of in single-crystalline  $\text{CoCr}_2\text{O}_4$ . Fig. 1.5 (b) also depicts the similar magnetic phase diagram with ultrasound propagation and magnetization studies [15]. Hence, with all the above phase transitions, it is very clear that  $\text{CoCr}_2\text{O}_4$  has complex magnetic phase diagram.

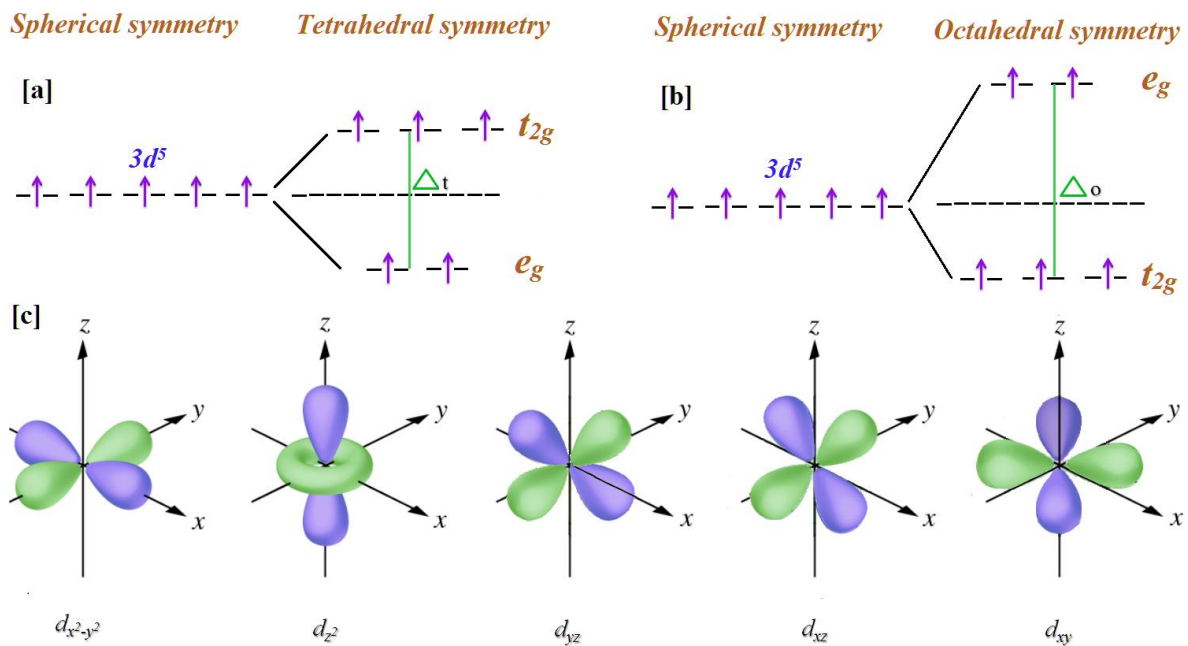


**Figure 1.6** (a) and (b) show the crystal field effect on the  $3d^5$  ions in tetrahedral and octahedral environments, respectively where fivefold degeneracy is lifted and separated into two  $e_g$  levels ( $d_{x^2-y^2}$ ,  $d_{z^2}$ ) and three  $t_{2g}$  levels ( $d_{xy}$ ,  $d_{yz}$  and  $d_{zx}$ ). (c) represents the all five different  $d$ -orbitals.

## 1.4 Crystal field in Spinel

The crystal field theory describes the effects of symmetry of the coordination environment [68,69]. In case of transition-metal oxides, where  $3d$  cations are always present in different valance state, gives rise to the degenerated  $d$  states. Due to the asymmetry of these  $3d$  orbitals in crystal, such degeneracy can be lifted up. In spinel oxides,  $3d$  transition metal cations are present in tetrahedral and octahedral coordination environments. When a transition metal cation is surrounded by four/six anions (for example: oxygen) in a tetrahedral/octahedral arrangements, the five cation  $d$ -orbitals no longer remain degenerate but split into two groups of triplet  $t_{2g}$  ( $d_{xy}$ ,  $d_{yz}$  and  $d_{zx}$ ) and doublet  $e_g$  ( $d_{x^2-y^2}$  and  $d_{z^2}$ ). The Columbic repulsion between the transition metal  $d$ -electrons and the surrounding anions is the physical basis of such splitting of energy levels. Direct overlap between  $d_{x^2-y^2}$  and  $d_{z^2}$  states of  $e_g$  orbitals with that of the surrounded oxygen  $p$  orbitals increases the energy in an octahedral environment. On the other hand,  $t_{2g}$  orbitals where  $xy$ ,  $yz$ , and  $zx$  states lies in different directions where the field is least and thus have lower energies. Consequently, octahedral coordination therefore yields lower energy triply degenerate  $t_{2g}$  states and higher energy doubly degenerate  $e_g$  states as illustrated in Fig.1.6. In case of a tetrahedral environment, the order of the triply degenerate  $t_{2g}$  states and doubly degenerate  $e_g$  states is just a reverse case of octahedral one [2,70]. The energy difference between the two sets of orbitals (i.e.  $e_g$  and  $t_{2g}$ ),  $\Delta$  is called the crystal field of respective environment [68]. The magnitude of the tetrahedral crystal field ( $\Delta_t$ ) is less than that of the octahedral crystal ( $\Delta_o$ ) field as the number of the coordinating ligands is less than to that of the number of coordinating ligands in case of tetrahedral environment.

In transition metal oxides, the understanding of electronic stabilization of various cations present at tetrahedral and octahedral sites enables significant prediction of cation distribution in these materials. It is well known that  $\text{Cr}^{3+}$  cations show a strong preference for the octahedral site where  $d^3$  electrons half fill the  $t_{2g}$  states. As a result, chromium oxide spinels typically adopt a normal spinel configuration such as in case of  $\text{CoCr}_2\text{O}_4$ . On the other hand,  $\text{Fe}^{3+}$  with  $3d^5$  shows no crystal-field stabilization on either in the tetrahedral or octahedral sites and consequently spinels with  $\text{Fe}^{3+}$  cations are typically inverse spinels.

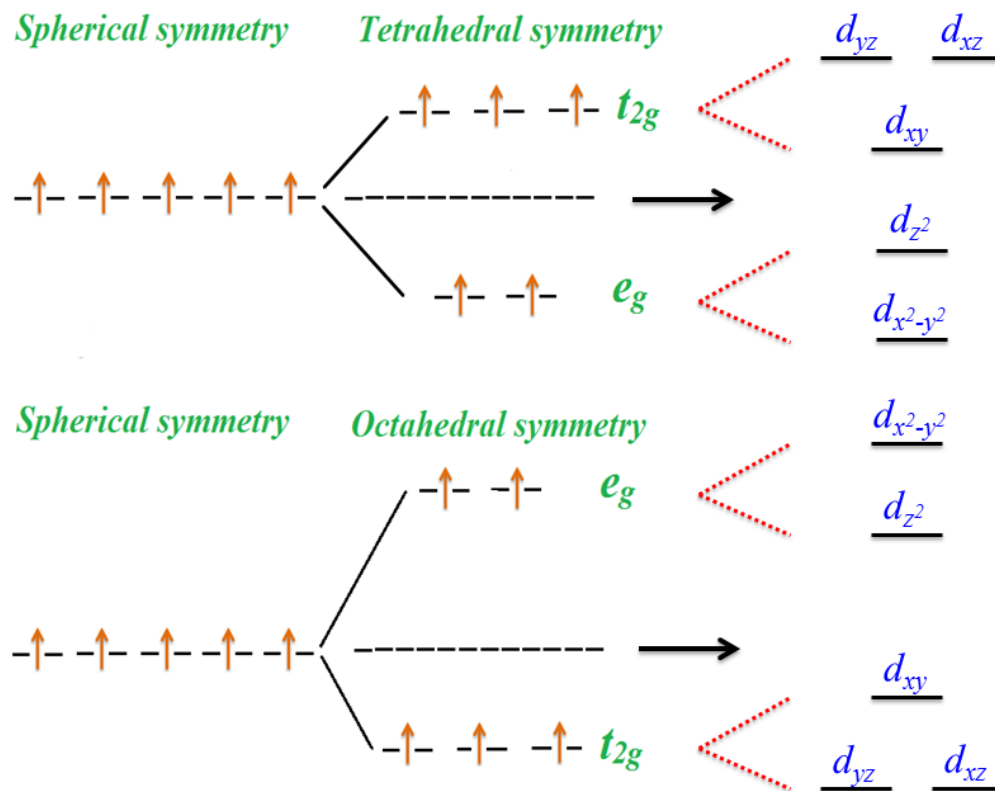


**Figure 1.7** Schematic presentation of Jahn-Teller effect with the energy level diagram of  $d$ -orbitals showing the tetragonal distortions in case of both tetrahedral and octahedral crystal fields.

## 1.5 Jahn-Teller Effect

Jahn and Teller [71] have demonstrated that if the electronic state of a non-linear molecule is orbitally degenerate then its ground state will undergo a geometrical distortion that removes orbital degeneracy in the system. Such distortion is known as Jahn-Teller distortion and the effect as Jahn-Teller effect. Earlier discussed octahedral and tetrahedral crystal fields partially lift the degeneracy of  $3d$  orbitals in transition metal oxides. The presence of any orbital degeneracy in octahedral and tetrahedral transition metal complexes gives rise to lattice instability [71]. In case of spinel oxides having orbital degeneracy, it has been found that there is strong urge to undergo lattice distortions, typically from cubic to tetragonal symmetry or much lower symmetry to lift such orbital degeneracy. Depending on the bonding and anti-bonding power of the degenerate electrons, degree of distortion could be identified. For the octahedral coordination,  $t_{2g}$  orbitals are relatively non-bonding and thus small distortions are expected from  $t_{2g}$  degenerated orbitals. On the other hand, degeneracy in the strongly anti-bonding  $e_g$  orbitals

gives rise to significant Jahn-Teller distortions. In tetrahedral coordination, it is the  $e_g$  orbitals which are non-bonding while  $t_{2g}$  orbitals are antibonding. Thus large distortions from regular tetrahedral symmetry are expected for configurations which are degenerated with respect to  $t_{2g}$  orbitals only [cf. Fig 1.7].

In general, the effect of Jahn-Teller distortion (which is not too large) in case of cubic crystal where ions are arranged in a cubic lattice, each ion will undergo a set of equivalent distortions due to its perfect symmetry. But, if the distortions are significant, the neighboring ions will influence each other and the lattice would minimize the energy by adjusting itself to a lower symmetry for example to the tetragonal one which gives rise to a new ground state. Thus Jahn-Teller mechanism is very useful to understand the structural aspects of spinel compounds [2,72–74].

### ***1.6 Negative Magnetization (or Magnetization Reversal)***

In general, magnetic material having nonzero spins such as ferromagnetic (FM), ferrimagnetic (FIM) and paramagnetic (PM) materials, show a positive magnetization with respect to the applied magnetic field direction. In 1948, Néel gave a phenomenological theory [21] according to which certain ferrimagnetic materials will exhibit spontaneous magnetization. Such spontaneous magnetization changes the sign with temperature or magnetic field due to different temperature dependence of sublattice magnetization. During the temperature dependent dc magnetization measurement a crossover of magnetization curve from a positive value to a negative value (cooled under a positive applied magnetic field), below its magnetic ordering temperature, is known as the negative magnetization or magnetization reversal. The magnetization reversal was first discovered in spinel ferrites (FIM material) where the spontaneous magnetization arises and changes sign due to uncompensated magnetic spins of two different crystallographic sites or sublattices. Various magnetic materials such as multilayers, spinel ferrites, garnets, perovskites and intermetallic alloys etc. are few examples where negative magnetization has been experimentally observed. Several intrinsic parameters for example temperature dependence of sublattice magnetization, different magnetic exchange interactions, crystalline structure and magnetic anisotropy are responsible for manifesting this phenomenon of negative magnetization. Such finding of magnetization reversal below  $T_{\text{comp}}$  was also observed in

mixed spinels [33,75], which is further extended to other FIM systems including molecular magnets, garnets along with some antiferromagnetic materials [21,76–78]. Moreover, this phenomenon of negative magnetization in the material adds another stable state of magnetization in the material can have important applications in the area of magnetic storage devices.

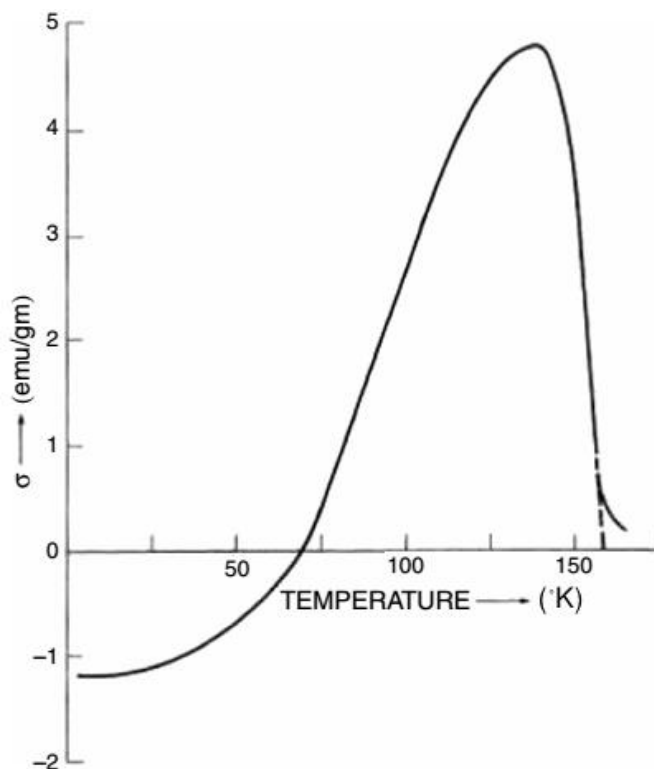


**Figure 1.8** Temperature dependent FC ( $H = 700$  Oe) dc-magnetization curve displaying the negative magnetization in  $\text{Co}_2\text{VO}_4$  [33].

During the temperature dependent dc-magnetization measurement, the net magnetization of the sample becomes zero at a particular temperature which is known as compensation temperature ( $T_{\text{comp}}$ ). The magnetization of a compound is strongly depending on the history of measurements for example cooling or heating history. Basically, there are two experimental ways of measuring dc-magnetization of a sample as a function of temperature which are known as zero-field cooled (ZFC) and field-cooled (FC) processes. The FC process represents the equilibrium magnetization whereas ZFC is known as non-equilibrium time dependent magnetization process. In general, the negative magnetization below  $T_{\text{comp}}$  is commonly observed in the FC protocol of dc-magnetization measurements. However, there exist a few reports where negative magnetization has been observed in both the ZFC and FC conditions of the magnetization measurements. Hence, one should understand that implemented experimental

conditions during the measurements of dc-magnetization in searching such phenomena of negative magnetization are playing very important role [34].

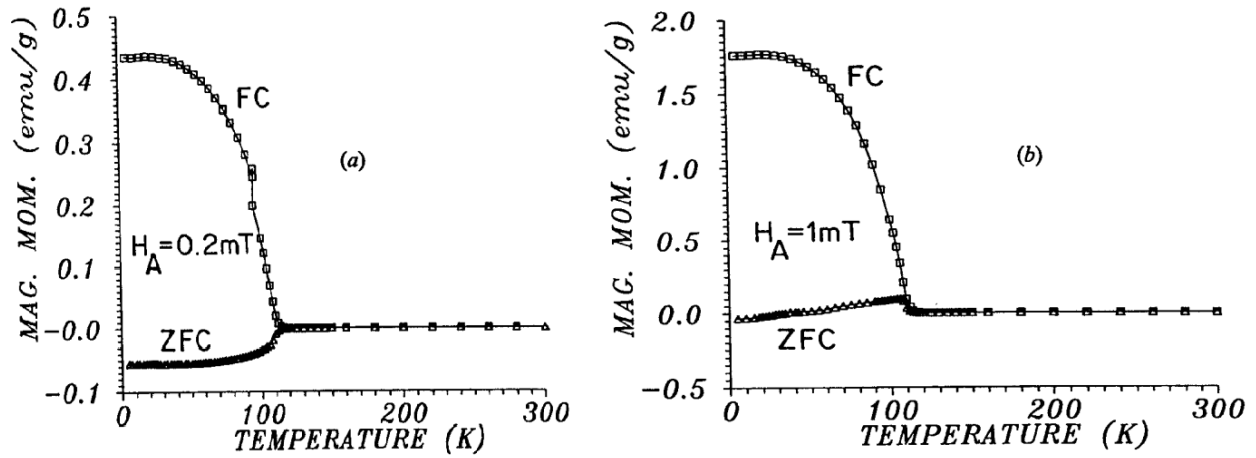


**Figure 1.9** (a) Negative ZFC magnetization due to the negative trapped field of the superconducting solenoid, and (b) a positive ZFC magnetization in the same compound with applied field of  $H_A = 10$  Oe [34].

### 1.7 Exchange Bias Effect

In 1956, Meiklejohn and Bean discovered the exchange bias (EB) effect when studying a system where Co particles were embedded in CoO [79]. In this experiment where Co is FM and CoO is AFM, the system is cooled from above the Néel temperature,  $T_N$  of AFM CoO under static applied magnetic field. They had observed a shift in M-H loops along the field axis during this experiment and discovered a new exchange anisotropy which is responsible for such shifting in M-H loops [79,80]. The EB field can be qualitatively defined in terms of the M-H loop shifting which is given as:

$$H_{EB} = -\frac{(H_{C+} + H_{C-})}{2}$$

Where  $H_{C+}$  and  $H_{C-}$  are the positive and negative coercive fields of the M-H loop, respectively. Since the discovery of EB in 1956, it was observed in various systems containing FM-AFM interfaces but still continued to be of fundamental interest with some other interface systems like AFM-FIM and FM-FIM [28]. EB effect has been observed in different bulk oxide materials [81]. Systems with EB effects have various useful technological applications for example magnetic recording devices [27,37–39,41], magnetic field sensors [28,44],

magnetostrictive random access memories (MRRAM) [82–87], and in permanent magnets [88–90].

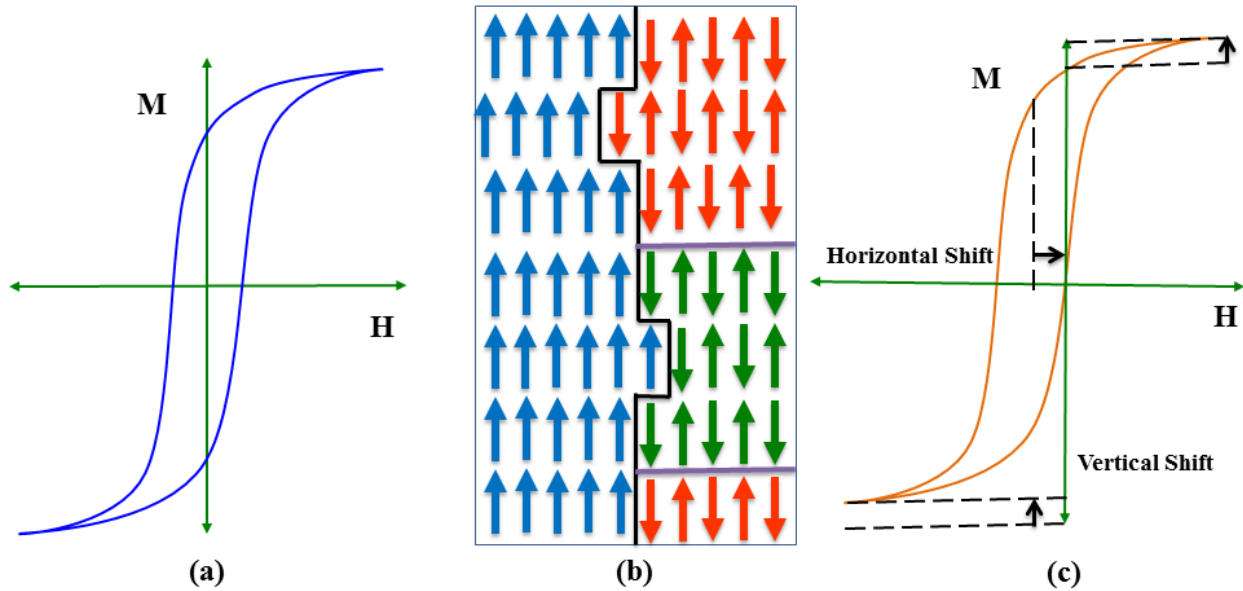


**Figure 1.10** Schematic representation of EB effect in bilayer structure with appearance of a pinned ferromagnetic layer at the interface with antiferromagnetic layer having uncompensated spins (b). The hysteresis loop without shifting (a) and shifted hysteresis loop (c) presenting the exchange bias effect in the system.

Typical EB M-H loop along with normal M-H loop is demonstrated in Fig. 1.10 where AFM interface layer has uncompensated spin and coupled to the spins at the FM interface layer via the exchange interaction. Such interactions which developed from the exchange correlations at the FM-AFM interface in the cooling process of the materials were assumed to be the origin of the EB phenomenon [91]. We can discuss the origin of EB effect with a model as shown in Fig. 1.10 where FM and AFM substances are in contact with each other having their magnetic ordering temperature  $T_C$  and  $T_N$ , respectively where  $T_C$  of FM component is greater than that of the  $T_N$  of AFM component. When a static magnetic field is applied on such system at a temperature much above of the  $T_N$  but below  $T_C$  and then cooled through  $T_N$  down to much low temperature i.e.  $T \ll T_N$ , the FM spins at the interface of the AFM spins are getting coupled to the uncompensated AFM spins of the system. In other words, the AFM spins at the interface exert a pinning force (microscopic torque) on the ordered FM spins to keep them well aligned at the interface. During this process few layers of FM spins at the interface are pinned in to the AFM spin side, hence due to this pinning there will be some difference in the energy required to

rotate the FM spins in positive and negative field directions which is responsible for shifting in the M-H loop. Depending on the depth of this FM pinning at interface which depends on the strength of anisotropy in AFM substance, one can observe an increase or decrease in the loop shifting in M-H measurements. Such existing coupling between FM and AFM substances at interface gives rise to a displacement of the M-H loop, and a  $\sin \theta$  component in the torque curve which is the typical manifestations of the EB effect [91].

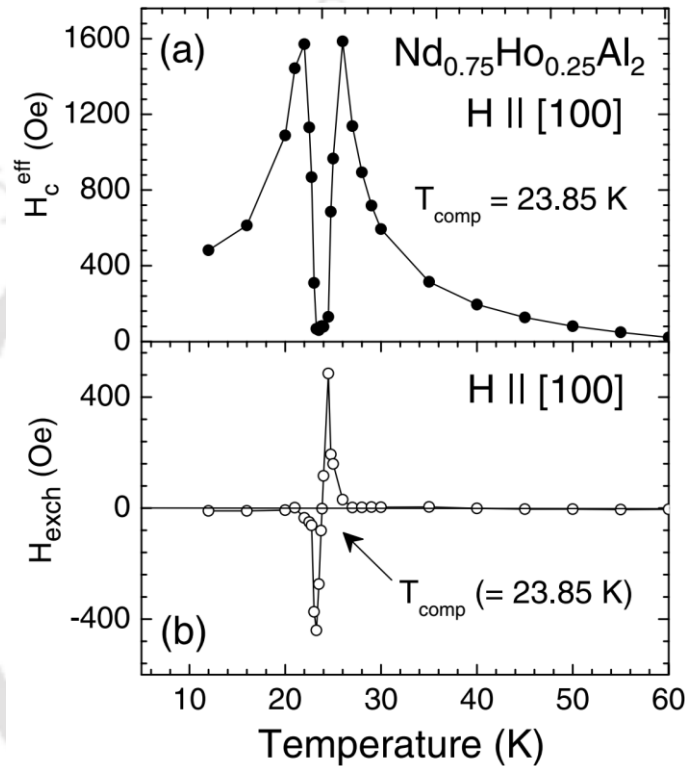


**Figure 1.11** Temperature dependence of (a) the effective coercive field ( $H_C^{\text{eff}}$ ), and (b) the EB field ( $H_{\text{EB}}$ ) of single crystalline  $\text{Nd}_{0.75}\text{Ho}_{0.25}\text{Al}_2$  [26].

Although EB effect is basically explained on the basis of interface between the FM and AFM layers and assumed to be an interfacial phenomenon, but such effect has also been observed in other materials namely, spin glasses, magnetically disordered systems, core-shell nanostructures and irregular nanostructures of metal-metal oxides etc. [92–95]. Bulk materials such as binary alloys, Heusler alloys, intermetallic compounds along with oxide materials are also known to reveal EB effect [81]. Structurally single-phase materials having the analogous structure of AFM-FM interfaces in multilayers and composites also exhibit the phenomenon of EB. Such discovery of EB effect in the single-phase alloys and compounds has renewed interest

in research community. Still there are not many reports on the investigations on the EB effects in structurally single phase materials. There are very few reports on EB effects on structurally single phase materials in charge ordered manganite having the spontaneous interfaces between short range FM clusters embedded in the AFM matrix [92].

Further, the observation of the sign change of EB with temperature across  $T_{\text{comp}}$  in an ideally homogeneous single phase system [26] is the most stunning feature of this effect. This is called the tunable EB with respect to the change in temperature. Fig. 1.11 (b) depicts the change in sign of EB effect across  $T_{\text{comp}}$ . Recently similar observation of sign reversal of both EB field and magnetization across  $T_{\text{comp}}$  is also observed in few other bulk single phase oxides [96–98]. There are a few reports where magnetic field (or cooling field,  $H_{\text{FC}}$ ) induced tunable EB is also observed for example  $\text{Sr}_2\text{YbRuO}_6$ ,  $\text{NdMnO}_3$  and in bilayer system of  $\text{FeF}_2/\text{Fe}$  etc. [97–99]. The finding of EB effect in single phase material is due to the coexistence of FM and AFM orderings which arises because of competing interactions between the transition metal ions. Origin of EB effect in these single phase materials is quite different from other interfacial systems for example multilayers etc. Further, a sign change in EB is observed across the  $T_{\text{comp}}$  which is due to both the presence of different magnetic ordering and change of exchange anisotropy between the FM and AFM spin configuration across the magnetically compensated state. Although lot of research has been done on EB effect, but the exact origin of tunable EB is under debate. Consequently, a detailed investigation is required to explore new materials, with magnetically compensated state, to observe the tunable EB effect.

## ***1.8 Multiferrocity in $\text{CoCr}_2\text{O}_4$***

Coexistence of the more than one ferroic order in a material is known as multiferroicity. In general, coexistence of ferroelectric (FE) and magnetic ordering has attracted research community as both are interesting for fundamental interest as well as for technological applications [100–107]. Such existence of these ferroic orders in material enables the mutual control of their properties. As magnetism is related to the spin degree of freedom, ferroelectricity can be observed in a material due to the presence of electric charge. Similar to the FM, a FE material exhibits electric polarization below the transition temperature ( $T_E$ ). Depending upon the mechanism of multiferrocity, there are two different types of multiferroics, i.e. Type-I and Type-

II multiferroics. The origin of the magnetism and ferroelectricity exists independently in case of type-I multiferroic, and therefore weak coupling establishes in such multiferroics. Some materials such as  $\text{BiFeO}_3$  and  $\text{YMnO}_3$  are the well-known examples of type-I multiferroics. In second case i.e. type-II multiferroics, the existing magnetic ordering gives rise to the electric polarization or ferroelectricity in the material. Materials having the non-collinear or spiral magnetic structure are basically responsible for observing the ferroelectricity. Thus ferroelectricity and magnetism are related to each other in such materials, for example  $\text{TbMnO}_3$ .

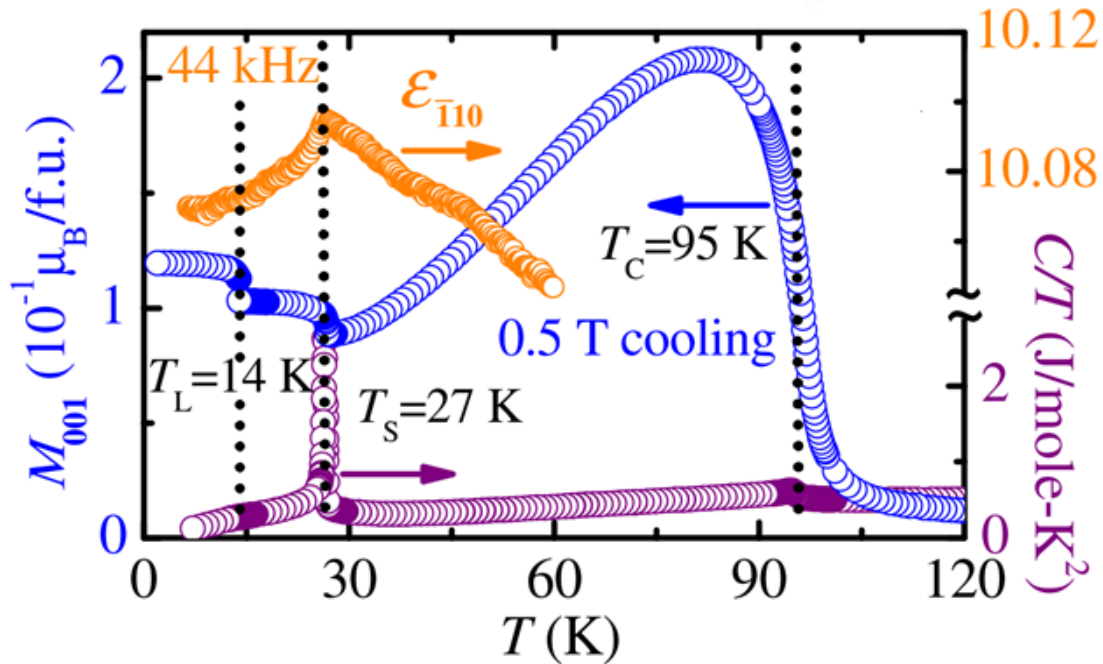


**Figure 1.12** Temperature dependent FC ( $H = 0.5 \text{ T}$ ) dc-magnetization along the  $[001]$  direction (left axis), specific heat divided by temperature in  $H = 0 \text{ T}$  upon cooling (right axis), and dielectric constant (right axis) in  $H = 0 \text{ T}$  at  $44 \text{ kHz}$  upon warming showing the evidence of three existing phase transitions in single crystalline  $\text{CoCr}_2\text{O}_4$  [12].

Interestingly, there are various well known multiferroic compounds such as  $\text{CoCr}_2\text{O}_4$ ,  $\text{RMn}_2\text{O}_5$ ,  $\text{RMnO}_3$  with  $R = \text{Tb}$ ,  $\text{Dy}$ , and  $\text{Ho}$  which persist strong ME coupling [12,13,108–111]. The observed electric polarization ( $P$ ) can be reversibly switchable by the applied magnetic field in these compounds. Among very few materials, multiferroic  $\text{CoCr}_2\text{O}_4$  is well-known for exhibiting both saturated magnetization and polarization. The non-collinear conical spin-spirals magnetic ordering observed in  $\text{CoCr}_2\text{O}_4$  [cf. Fig. 1.12] is the source of such magnetically driven electric polarization [12,13]. The spin-current model [19], which gives a relation between the polarization and the canted spins responsible for such polarization, one can express it as,

$P = ae_{ij} \times (S_i \times S_j)$ , where ‘a’ is the proportionality constant,  $e_{ij}$  is the vector connecting two adjacent spins  $S_i$  and  $S_j$  and  $P$  is the induced polarization. According to this model, all three i.e. propagation vector, spontaneous polarization and plane of spin-spiral configuration are perpendicular to each other. Earlier shown Fig. 1.4 depicts the schematic view for conical spin spiral spin configuration existed in the different sites of  $\text{CoCr}_2\text{O}_4$ . From this one can see that propagation ( $e_{ij}$ ) of the spin-spiral configuration towards  $[110]$  direction leads to a spontaneous polarization which is perpendicular to the spiral propagation direction as in  $[\bar{1}10]$  direction. Due to the change in magnetic field direction, one observes the flipping in polarization which is the results of change in the direction of spin axis [12,13].

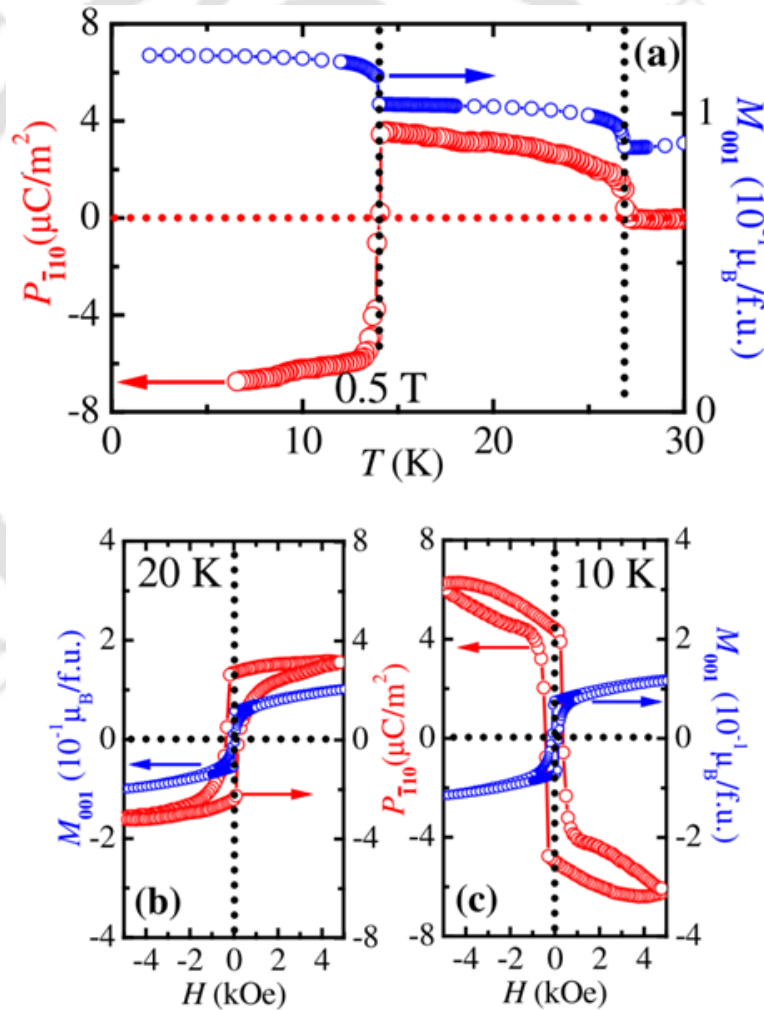


**Figure 1.13** (a) Electric polarization ( $P$ ) and magnetization ( $M$ ) as a function of temperature in single crystalline  $\text{CoCr}_2\text{O}_4$ . (b) and (c) depict the  $H$ -dependent polarization along  $[\bar{1}10]$  and magnetization along the  $[001]$  directions at  $20$  K and  $10$  K, respectively with the applied magnetic field in  $[001]$  direction [12].

In addition, Fig. 1.13 depicts a thermally (a) and magnetically (c) induced reversal of spin induced polarization below lock-in transition  $T_L$  in  $\text{CoCr}_2\text{O}_4$  [18]. Above discussed, spin-current model has failed to explain such unusual polarization behavior below  $T_L$ . Researchers have also revealed the multiferroicity in  $\text{CoCr}_2\text{O}_4$  in the temperature range of  $T_S < T < T_C$  which suggests that there exists the non-collinear or short range spin spiral ordering in this temperature region [111,112]. Previous neutron scattering experiments have already confirmed such non-collinear magnetic ordering in  $\text{CoCr}_2\text{O}_4$  [8,16]. With the motivation of finding multiferroicity in such non-collinear spin state, one can search for an existence of multiferroic order in different temperature regime.

## **1.9 Motivation**

Pristine  $\text{CoCr}_2\text{O}_4$ , which is a normal spinel with cubic crystalline structure, exhibits a complicated magnetic structure [32]. Different magnetic ordering such as long range FIM ordering with short range conical spin-spiral ordering which starts below  $T_C$  and develops in to a long range spin-spiral ordering at  $T_S$  were observed in  $\text{CoCr}_2\text{O}_4$  [8,12,13,16,19]. This magneto-structural transition  $T_S$  where magnetic structure changes, gives rise to the strong magneto-electric coupling in  $\text{CoCr}_2\text{O}_4$  [12,13,112]. Further, below  $T_S$ , more complex magnetic structure has taken place which is still controversial. The existing super-exchange interactions among different crystallographic sites in  $\text{CoCr}_2\text{O}_4$  gives rise to all exciting magnetic properties [113]. The substitution of different transition metal ions into its tetrahedral A-site and octahedral B-site of spinel structure will illustrate a different chemical and magnetic structure with new fascinating structural and magnetic properties.

Basically, the present thesis has two aims. Firstly, it attempts to study the substitution effect of different transition  $3d$ -elements having different magnetic moments into both the A (Co) and B (Cr)-sites. This will give a comprehensive understanding of the crystal and magnetic structures and observed interesting magnetic properties like negative magnetization and exchange bias which arises due to the substitution effect. Fig. 1.14 shows a schematic scheme for such plan where one can expect the magnetically compensated state with 'x' substitution in  $\text{CoCr}_2\text{O}_4$  along with the EB effect in the close vicinity of this compensated substituted compound. Therefore, we have chosen  $\text{Fe}^{3+}$ ,  $\text{Mn}^{3+}$  for B( $\text{Cr}^{3+}$ )-site substitution and  $\text{Cu}^{2+}$  for

A( $\text{Co}^{2+}$ )-site which have different magnetic moments but nearly same ionic sizes to that of the  $\text{Cr}^{3+}$  and  $\text{Co}^{2+}$  respectively. Multiferrocity is also another dimension to explore such magnetic properties having the dependency on different sublattices in spinel oxides.

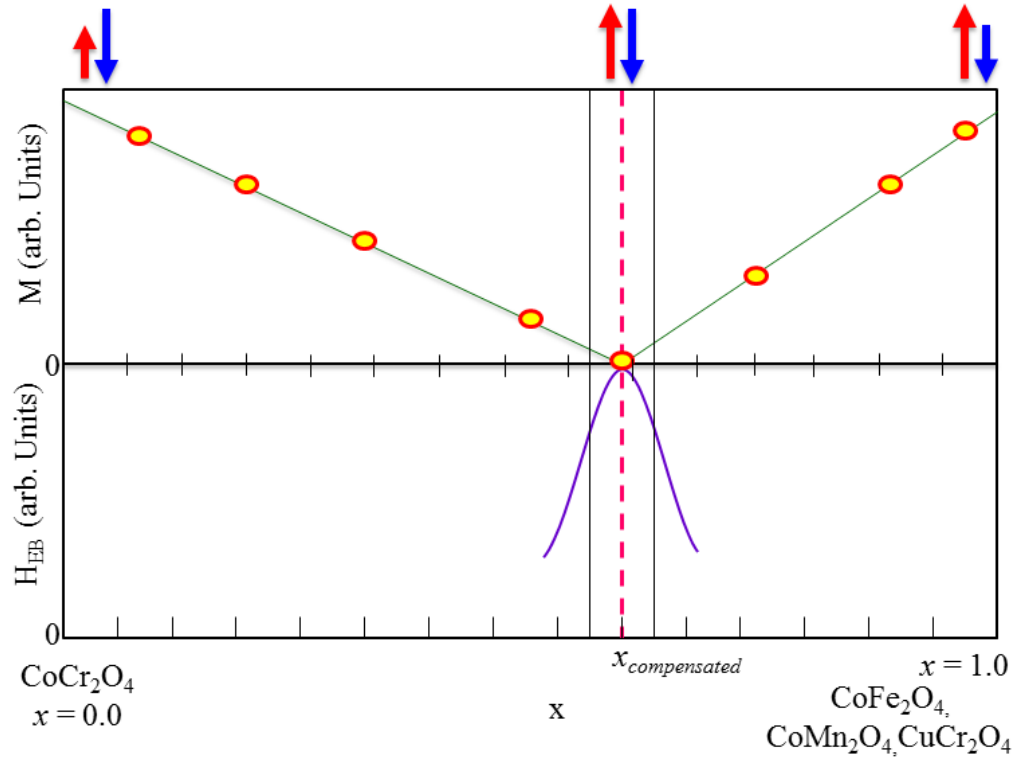


**Figure 1.14** Schematic representation of exchange bias effect around magnetically compensated state which can be achieved by tuning the different crystallographic sites of spinel  $\text{CoCr}_2\text{O}_4$ .

Secondly, we know that neutron powder diffraction experiment is the best way to understand the magnetic structure of polycrystalline compound. One can find out the exact origin of the magnetic properties like negative magnetization and exchange bias in the compounds by knowing the existing magnetic structure. Understanding of these fascinating magnetic properties of compensated substituted compounds of  $\text{CoCr}_2\text{O}_4$  requires a detailed experimental investigation of the magnetic structures.

---

### ***Experimental Techniques***

---

In the present chapter, the synthesis method of sample preparation will be discussed. This chapter also provides an insight into the basic principles of various instruments used for experimental data recording and analysis. Detailed investigation of structural and magnetic properties of the studied compounds is done for physical characterization of the samples.

After a brief discussion on the sample preparation techniques, X-ray diffraction (XRD) and neutron powder diffraction (NPD) techniques are deliberated in more detail. Further, analysis of the magnetic structure from neutron diffraction data, which is very important from the point of view of the present thesis, is also discussed. The magnetic and thermodynamical properties were investigated by carrying out temperature dependent dc and ac-magnetization, heat capacity and magnetocaloric effect (MCE). Dielectric and ferroelectric properties have also been studied by performing temperature and field dependent dielectric and piezoelectric measurements.

#### ***2.1 Sample Preparation: Solid State Reaction Method***

In the present thesis, all the experiments have been performed on the bulk-polycrystalline samples. In general, there are two basic methods for the synthesis of polycrystalline samples i.e. solid state reaction and sol-gel methods. In present thesis, solid state reaction method has been employed to synthesize the studied polycrystalline samples. Solid state reaction method is known as the versatile technique by which solid oxide materials is synthesized in bulk polycrystalline form [114]. Starting materials were mechanically mixed and the solid-state reaction among these mixed constitute powders were achieved by repeated cycles of grinding and heating at high temperatures ( $>700^{\circ}\text{C}$ ). This heating or sintering is essential for the ions to diffuse across their kinetic barrier. High temperature furnaces ( $40\text{--}1500^{\circ}\text{C}$ ) are being used for heating these mixtures of constituent oxides so that they can react with each other which are not possible at ambient temperature. Hence, such solid state reaction requires a typical reaction time from few days to few weeks which is essential to overcome the diffusion barrier. A fast reaction rate can be

achieved if there is a better contact between surfaces of the reactants. Therefore, good homogeneity as well as reduction in the particle size of reactants (i.e. increase in surface area) can be obtained by through grinding of several hours. Further, by changing the temperature rate (heating/cooling), thermodynamic kinetics of the reaction can be controlled which plays an important role for better sintering of the sample.

All samples are prepared by solid state reaction method in the present thesis. Starting with the stoichiometric equation, we weighed the required amount of starting materials using an electronic balance (accuracy of  $\pm 0.0001$  g) in the form of oxides. These weighed materials ground using an agate motor and pestle for 4-5 hours (depending on the quantity) in the organic medium (acetone/methanol) for achieving the homogeneous mixture of the final compound. This homogeneous mixture of the materials was calcined around  $600\text{--}700^\circ\text{C}$  to confiscate the remaining solvents. Further, this powder was pressed into cylindrical pellets of  $\sim 10\text{--}13$  mm and finally sintered at  $1150\text{--}1350^\circ\text{C}$  for several hours with intermediate grinding and pre-sintering to achieve pure polycrystalline compounds in single phase without any trace of impurities.

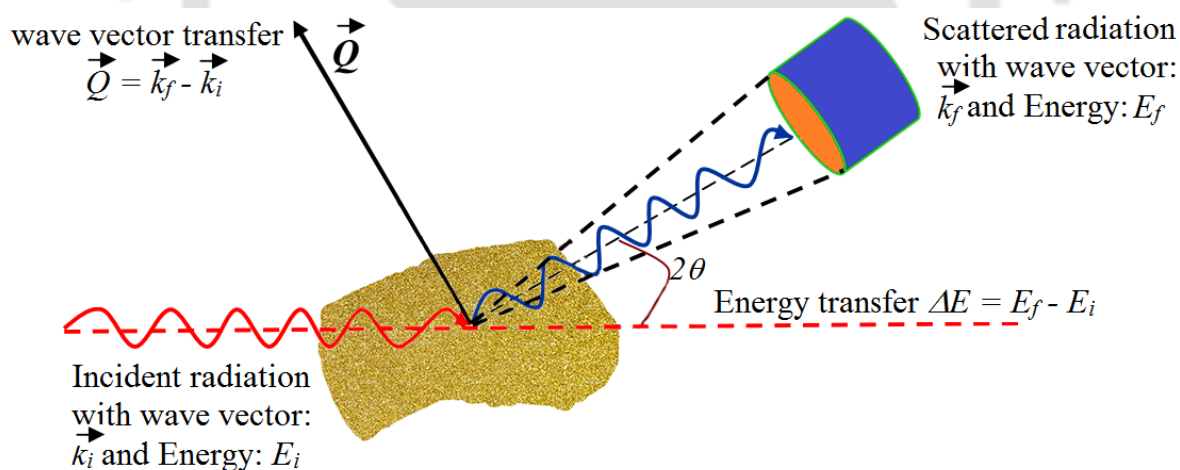


**Figure 2.1** Schematic diagram of the scattering geometry in neutron scattering experiment.

## 2.2 Scattering Techniques

### 2.2.1 General Scattering from Matter

Scattering techniques are known as the best techniques for the phase identification of a crystalline/ordered material in solid state physics. A schematic of scattering experiment is shown

in Fig. 2.1 where an incident radiation of energy  $E_i$ , with  $\mathbf{k}_i$  (wave vector) is scattered by the sample into a radiation of energy  $E_f$  and wave-vector  $\mathbf{k}_f$ . In the case of elastic scattering i.e.,  $|\mathbf{k}_f| = |\mathbf{k}_i|$  or  $E_i = E_f$ , one can analyze the scattering phenomena by knowing its important parameter of momentum transfer which is also known as the scattering vector  $\mathbf{Q} = \mathbf{k}_f - \mathbf{k}_i$ , with magnitude of  $Q = (4\pi/\lambda) \sin\theta$ . Bragg experiment is known as a very popular scattering experiment which provides all the information about the crystalline structure of the sample. In this experiment, Bragg scattering/diffraction of the incident radiation takes place from the existing lattice planes of the sample. According to Bragg's condition, once the wavelength of the incident radiation is of the order of interatomic spacing of the lattice plane, diffraction pattern will be obtained. Further, one can measure the intensity of the diffracted radiation as a function of the magnitude of the scattering vector ( $\mathbf{Q}$ ) or in terms of the angle ( $\theta$ ) which provides the information about the crystal structure of the sample. The following figure depicts the necessary geometrical condition for achieving Bragg's diffraction.

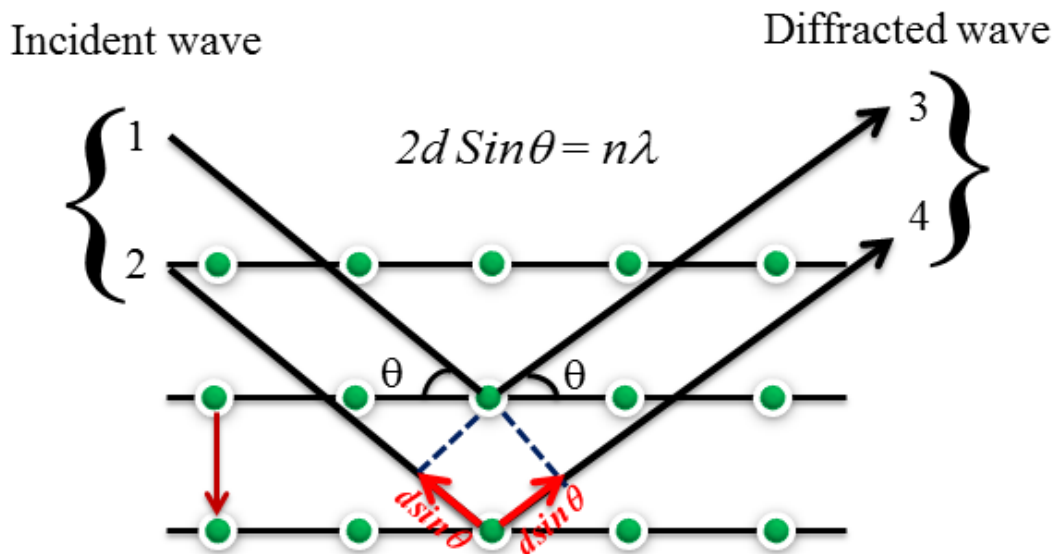


**Figure 2.2** Schematic representation of Bragg's diffraction law with incident and diffracted waves.

In his experiment of scattering, Bragg considered that the diffraction of crystals is nothing but a reflection from atomic lattice planes of the sample. According to him, the scattering centers can be represented by a set of parallel atomic planes from which incident rays of radiation reflect. One observes the peaks in diffraction pattern when scattered radiation from these planes is in 'phase' or the path difference of the scattered waves is an integral multiple of

the radiation wavelength. From here, one can write this condition which is shown in Fig. 2.2 with path difference ' $2d \sin \theta$ ', i.e.

$$2d \sin \theta = n \lambda \quad (2.1)$$

Where,  $d$  is spacing between these parallel planes,  $2\theta$  is angle of diffraction and  $\lambda$  is the wavelength of radiation. Above equation represents the Bragg's law. Nowadays, many different radiations are being used for diffraction experiments such as x-ray, electrons and neutrons. From the point of view of the present thesis, we have used x-ray and neutron scattering techniques which we will discuss in detail in the following section.

### **2.2.2 X-ray Powder Diffractometer**

A powder x-ray diffraction experiment is known to be a primary technique to characterize a polycrystalline sample. One can determine the crystal structure, atomic spacing along with the phase purity of a particular compound through x-ray diffraction technique. Present thesis has employed the powder x-ray diffraction method for determining the very first chemical structure of the studied sample. As shown in schematic diagram (Fig. 2.2), in x-ray diffraction experiment, incident monochromatic x-rays are scattered by the different atomic planes of the sample and gives rise to a diffraction pattern due to the interference of scattered rays. From the basic principle of diffraction, one observes a diffraction pattern just because of comparable order of inter-atomic spacing and the wave length of x-rays. These diffracted rays must undergo a constructive interference for the validation of Bragg's law. A detector is used to collect these diffracted/scattered x-rays and a diffraction pattern is produced during the scanning through a certain range of angle. RIGAKU diffractometer (TTRAX III) of 18 kW power with rotating anode in the Bragg-Brentano geometry having Cu- $K_{\alpha}$  radiation ( $\lambda = 1.5406 \text{ \AA}$ ) is used to perform powder x-ray diffractions of all the samples synthesized for this thesis. Studied polycrystalline samples were scanned in the angle range of  $2\theta = 10^{\circ}$ – $90^{\circ}$  at a step of  $0.02^{\circ}$ . All obtained XRD patterns are fitted by Rietveld refinement technique using the FULLPROF program [115–117]. Through such refinement analysis, one can calculate all the information about the crystalline structure for example, lattice parameter, atomic positions, site occupancies and different bond parameters such as bond lengths and respective bond angles etc.

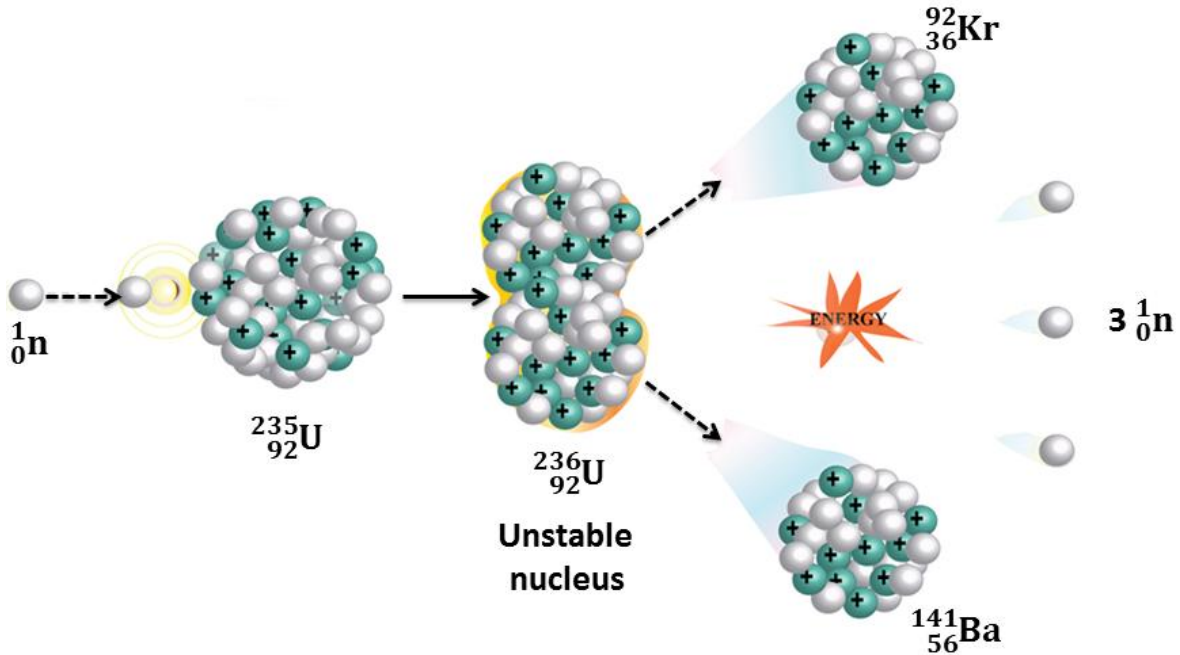


**Figure 2.3** Schematic representation of nuclear fission reaction taking place inside the nuclear reactor for neutron production.

### 2.2.3 Neutron Scattering

For performing neutron scattering experiments, one needs to produce the neutrons. In general, there are two best techniques are known for neutron production which are (i) nuclear fission reaction and (ii) spallation source. Fig. 2.3 presents a schematic presentation of the nuclear fission reaction where single neutron gives rise to three another neutrons. This reaction will continue like a chain reaction if the produced neutron involves in the further fission. In case of neutron production through spallation source, a high intensity proton beam having energy of  $\sim 1$  GeV strikes on a heavy metal target of W or Ta. Different particles like neutron, proton etc. are emitted during the returning of excited nucleus (happens due to interaction between high energy proton and target nucleus) to ground state. If these emitted neutrons again interact with the other nuclei, a neutron shower takes place similar to the case of fission reaction. Compare to fission reaction, spallation source produces more high energy neutrons; therefore the energy spectra of produced neutrons from these methods are also different.

As neutron is a neutral (chargeless) particle, it penetrates deep into materials with short range interaction. In contrast to x-ray atomic form factor which strongly depends on atomic

number ( $Z$ ), neutron atomic scattering factor is not following any trend. Another important thing is the neutron scattering length which is different for different isotopes of the same element which is essential for different isotopes study.

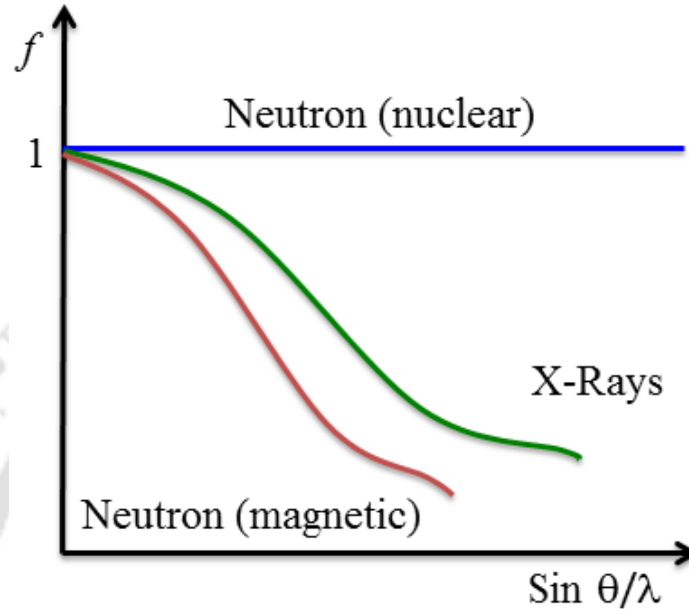


**Figure 2.4** Comparison of the nuclear and magnetic form factors in neutron diffraction along with X-ray form factor plotted against scattering angle.

In comparison to X-rays which is generally used for investigation of chemical structure, neutron is an excellent probe to investigate both chemical and magnetic structures of the solids. As neutron has a magnetic moment which interacts via a long range dipole-dipole interaction with the atomic magnetic moments of sample, one can investigate the magnetic structure of the sample. Fig. 2.4 shows a comparative plot between the nuclear as well as magnetic form factors in neutron diffraction and X-ray form factor plotted against scattering angle. Unlike, the nuclear scattering form factor, magnetic form factor  $f(Q)$  has  $Q$  dependence and decreases rapidly with  $Q$ , therefore magnetic scattering can be observed up to the low- $Q$  region. In addition, one can also investigate the energy dynamics of sample as thermal neutrons have the energy of the order of few meV which matches with the excitation energy of the solids.

In the present thesis, NPD has been used to study the crystal and magnetic structures of the prepared oxide compounds. Before going further, one should understand the concept of the scattering cross-section as it is the main quantity which is measured in the diffraction

experiment. In the NPD experiment, one measures the differential scattering cross-section, which is defined as [118,119],

$$\frac{d\sigma}{d\Omega} = \frac{\text{total number of neutron scattered into a solid angle } d\Omega \text{ per unit time}}{\phi d\Omega} \quad (2.2)$$

Where,  $\phi$  is the incident flux and  $d\Omega$  is the solid angle in the  $\theta, \phi$  direction.

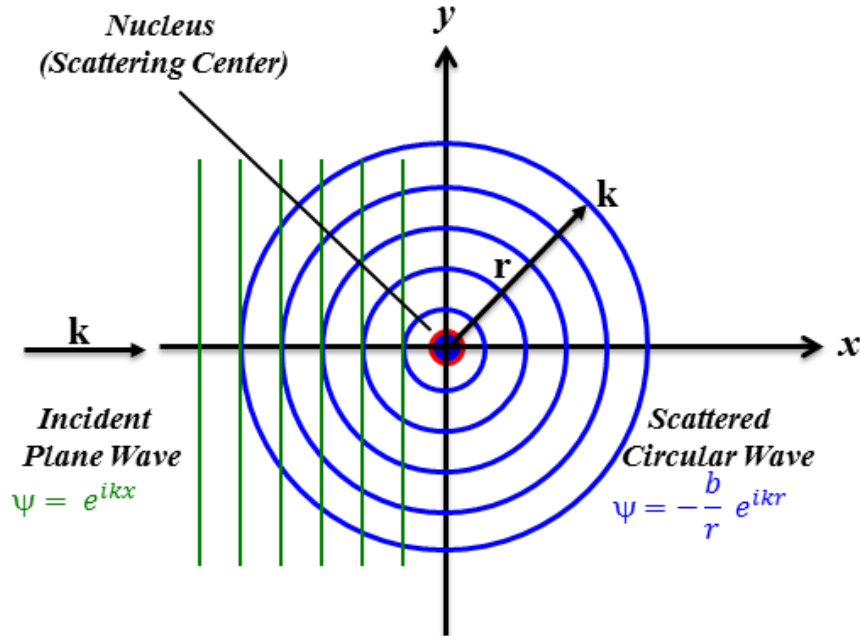


**Figure 2.5** Schematic diagram presents the neutron nuclear scattering during neutron scattering experiment.

### 2.2.3.1 Elastic Nuclear Scattering

As we know that neutron has both nuclear as well as magnetic scattering from the sample, we first discuss the scattering of the neutrons with a fix nucleus (nuclear scattering) in the present section. In case of neutron scattering experiments, neutron is supposed as a plane wave ( $\psi_i = e^{ikz}$  where  $k$  is the wave vector  $= 2\pi/\lambda$ ). In elastic neutron scattering,  $|k_i| = |k_f|$ , i.e.  $\Delta E = 0$  and  $Q$  (scattering vector) has to be equal to a reciprocal lattice vector ( $G$ ) of the sample. As compare to neutron wavelength ( $\lambda$ ), the range of nuclear force ( $\sim 1$  fm) is very small which gives rise to a point like scattering. This elastic nuclear scattering is isotropic in nature as shown in Fig. 2.5.

In case of nuclear scattering, both coherent and incoherent scattering arises from a nucleus. Coherent scattering is the one which is of interest during crystal structure determination of a material. Along with coherent scattering, incident neutron can also scatter incoherently and such scattering can be seen as background in the data.

The total nuclear elastic differential cross-section is given by,

$$\frac{d\sigma}{d\Omega} = \left(\frac{d\sigma}{d\Omega}\right)_{coh} + \left(\frac{d\sigma}{d\Omega}\right)_{inc} \quad (2.3)$$

For the crystal structures, having more than one atom per unit cell, the coherent scattering cross-section is given by,

$$\left(\frac{d\sigma}{d\Omega}\right)_{coh} = N \frac{(2\pi)^3}{V} \langle b \rangle^2 \sum_{\mathbf{G}} \delta(\mathbf{Q} - \mathbf{G}) |F_N(\mathbf{G})|^2 \quad (2.4)$$

Here  $N$  is the total number of unit cells, and  $V$  is the volume of the unit cell. The  $\delta$ -function in coherent scattering cross-section implies that coherent scattering cross-section is finite when  $\mathbf{Q} = \mathbf{G}$ , otherwise it is zero. We know that reciprocal lattice vector  $|\mathbf{G}| = 2\pi/d_{hkl}$  and scattering vector  $|\mathbf{Q}| = 4\pi \sin\theta/\lambda$ , then the condition  $\mathbf{Q} = \mathbf{G}$  yields, Bragg's law.

With nuclear structure factor,

$$F_N(\mathbf{Q} = \mathbf{G}) = \sum_j e^{i\mathbf{Q}\cdot\mathbf{r}_j} b_j e^{-W_j(\mathbf{Q},T)} \quad (2.5)$$

For the elastic neutron scattering at finite temperature, the Debye-waller factor  $e^{-W_j(\mathbf{Q},T)}$  of the atom as a function of scattering vector and temperature must be included. It takes into account the small thermal fluctuation of the atom.

### 2.2.3.2 Magnetic Neutron Scattering

Neutron possesses a magnetic moment of  $-1.913\mu_N$  ( $\mu_N$  is nuclear Bohr magneton) which is responsible for the magnetic scattering in the material. This magnetic moment of a neutron can interact with the existing magnetic moment of the unpaired electron in the sample via dipole-dipole interaction. The main difference between nuclear and magnetic cross-sections is that magnetic moment arising from the electron cloud of unpaired electrons has a large special distribution of its scattering potential whereas nuclear scattering taking place when the neutron is

very close to it and has a small range of scattering potential. A necessary condition for magnetic scattering to occur is that an incident neutron only scatters from a magnetic moment of a material when the present moment is perpendicular to the scattering vector  $\mathbf{Q}$ .

The differential cross-section for elastic magnetic scattering is given as,

$$\left(\frac{d\sigma}{d\Omega}\right)_{coh} = N_M \frac{(2\pi)^3}{V_M} \sum_{\mathbf{G}_M} \delta(\mathbf{Q} - \mathbf{G}_M) |F_{M\perp}(\mathbf{G}_M)|^2 \quad (2.6)$$

Where  $N_M$  is the number of magnetic unit cells,  $V_M$  the volume of the magnetic cell and  $\mathbf{G}_M$  is the reciprocal lattice vector in the same magnetic unit cell.

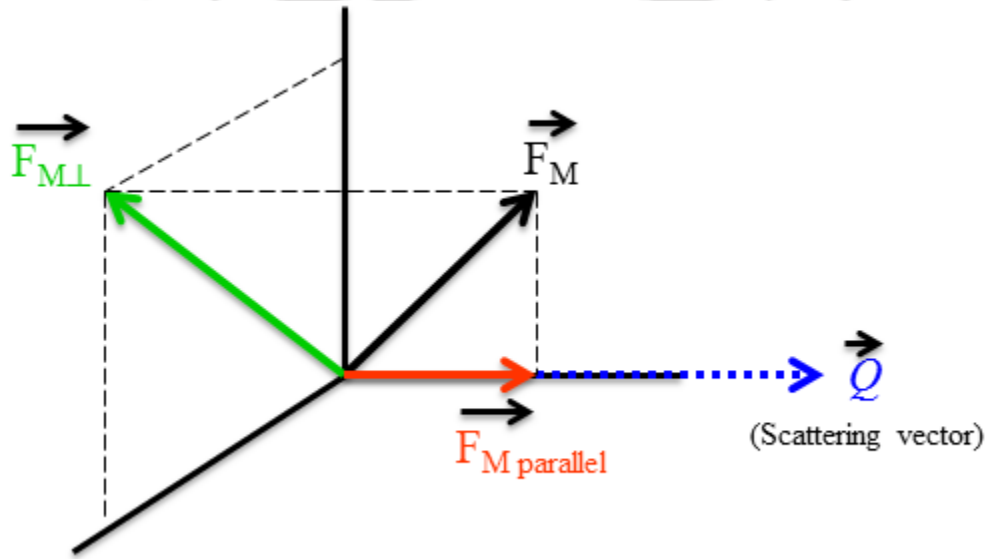


**Figure 2.6** Schematic representation of different components of magnetic moments along with the scattering vector during magnetic scattering.

Next,

$$F_{M\perp} = \hat{Q} \times F_M \times \hat{Q} \quad (2.7)$$

Here,  $F_m$  is known as the magnetic structure factor and is defined as:

$$F_M(\mathbf{Q}) = \gamma r_0 \sum_j f_j(\mathbf{Q}) \mu_j e^{i\mathbf{Q} \cdot \mathbf{r}_j} e^{-W_j(\mathbf{Q}, T)} \quad (2.8)$$

Where  $\gamma = 1.9132$  is the gyromagnetic ratio,  $r_0 = 2.8 \times 10^{-15}$  m (classical radius of the electron), and  $\mu_j$  the magnetic moment of the  $j^{\text{th}}$  ion. Here  $f(\mathbf{Q})$  magnetic form factor which is given by:

$$f(\mathbf{Q}) = \int \mathbf{M}(\mathbf{r}) e^{i\mathbf{Q}\cdot\mathbf{r}} d^3\mathbf{r} \quad (2.9)$$

Where  $\mathbf{M}(\mathbf{r})$  is the magnetization density. This  $f(\mathbf{Q})$  arises because of the finite spatial extent of electron cloud of unpaired electrons in the atom.

Detailed mathematical derivations and equations used in above sections are given in many books on neutron scattering [118–123].

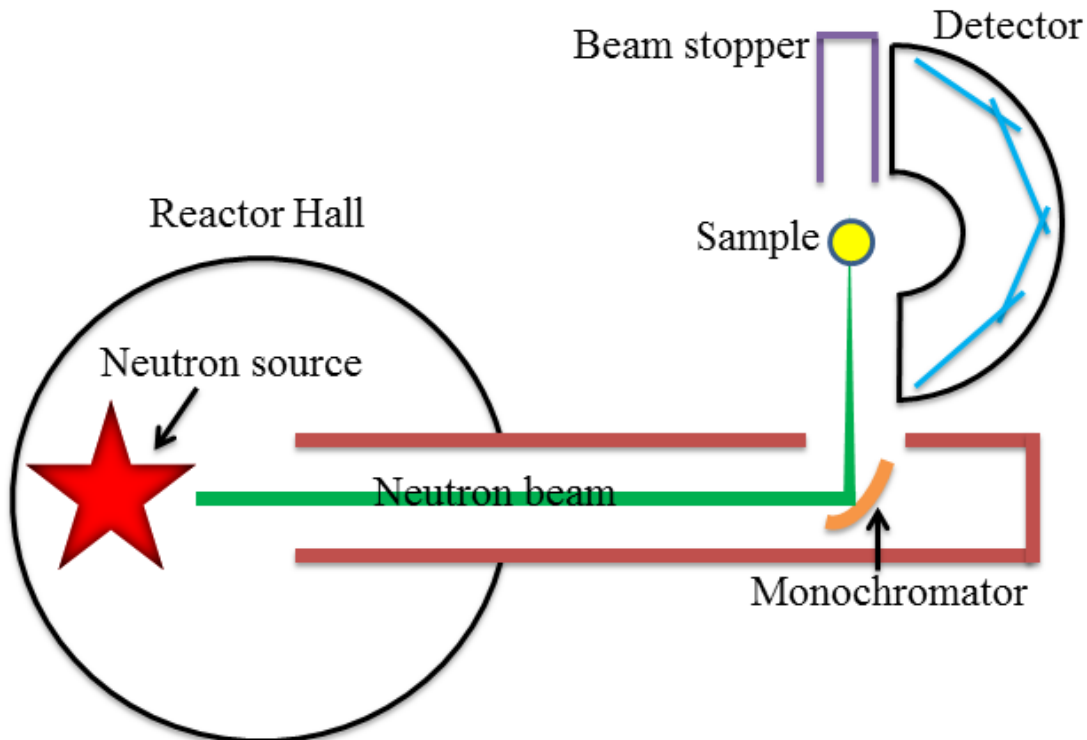


**Figure 2.7** Block diagram of Neutron diffractometer at UGC-DAE Consortium Scientific Research, BARC, Mumbai Centre, Trombay, India.

### 2.2.4 High Resolution Neutron Powder Diffractometer

Neutron powder diffractometer has been extensively used for performing neutron powder diffraction (NPD) experiments in the present thesis work to get a deep understanding into the crystalline and magnetic structures. All NPD experiments were carried out using position-sensitive detector based focusing crystal high resolution neutron powder diffractometer (PD-3) (as shown in Fig. 2.7) designed and developed [124] by UGC-DAE CSR Mumbai Centre, at Dhruva reactor, Trombay India. During these NPD experiments, a collimated monochromatic neutron beam is incident on the polycrystalline sample which is in powder form. A bent Si single

crystal behaving as a crystal monochromator at a take-off angle of  $90^\circ$ , is employed to enable high flux at the sample position along with high resolution ( $\Delta d/d \sim 0.3\%$ ). A desired wavelength out of the operational ones i.e.  $\lambda = 1.10 \text{ \AA}$ ,  $1.48 \text{ \AA}$ ,  $1.76 \text{ \AA}$  &  $2.31 \text{ \AA}$  of monochromatic beam can be achieved by rotating or flipping the crystal monochromator. In the present thesis, a standard wavelength of  $1.48 \text{ \AA}$  is used for all the neutron diffraction measurements.



### Instrument Parameters

Beam hole No.	TT-1015
Monochromator	Bent Si
Wavelength	$1.48 \text{ \AA}$ (standard)
Beam size	$15 \times 25 \text{ mm}^2$
Flux at sample	$7 \times 10^7 \text{ n/cm}^2/\text{s}$
Scattering angle	$6-123^\circ$
Q-range	$0.4 - 7.4 \text{ \AA}^{-1}$
$\Delta d/d$	$< 0.3 \%$
Detector	12 Linear $^3\text{He}$ PSDs

**Figure 2.8** Pictorial representation of neutron diffraction facility at UGC-DAE CSR, Mumbai centre [35] along with list of instrument parameters of the neutron powder diffractometer.

In a polycrystalline sample, the diffracted beam of neutron lies on the surface of several cones (Debye-Scherrer cones) which satisfy the Bragg's condition. Multi-position sensitive detectors (PSDs) with large angular range are being used for the detection of these cones. The neutron powder diffraction measurements were carried out at the different temperature between 2.9 K to 300 K in the  $2\theta$  range of  $6^\circ$  to  $120^\circ$ . NPD data were refined by again Rietveld refinement method using the Fullprof suite programs.

### 2.3 Physical Property Measurements

After the structural analysis, the high quality polycrystalline samples with single phase are subjected to study further. Hence, to investigate different physical properties of all these single phase compounds, many experiments such as dc-magnetization, ac-magnetization and heat-capacity measurements were performed which are discussed in details in the next few subsections.

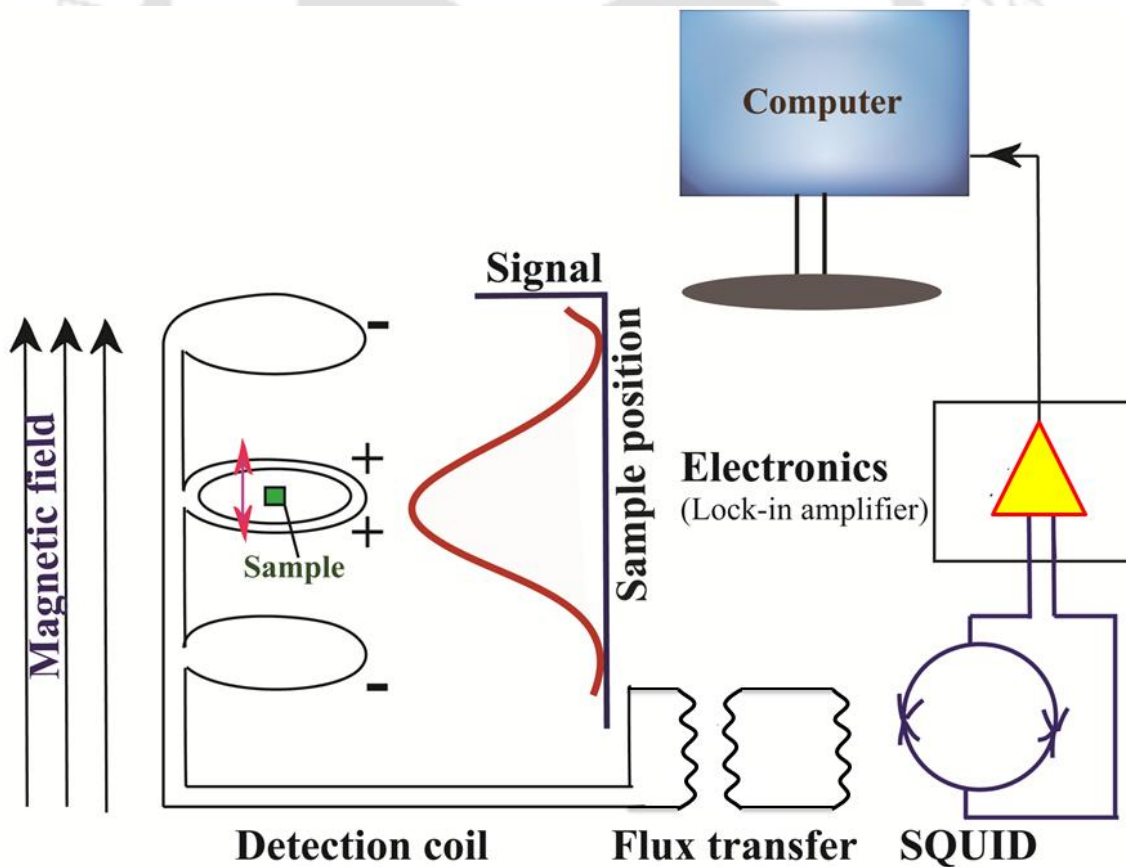


Figure 2.9 Schematic diagram of MPMS SQUID-VSM magnetometer.

### ***2.3.1 Superconducting Quantum Interference Device (SQUID) Magnetometer***

All temperature and magnetic field dependent magnetization measurements were performed in Quantum Design MPMS SQUID-VSM and PPMS VSM magnetometer. Both instruments can measure over a wide range of temperature between 1.8 to 400 K and isothermal magnetization measurements in fields up to 7 and 9 T respectively.

In recent times, superconducting quantum interference device (SQUID) is the most delicate device for magnetization measurement of a material. The simplified block diagram of a SQUID-VSM magnetometer is shown in Fig. 2.9. The basic principle of SQUID is based on two parallel Josephson junctions in a loop. Extremely small magnetic field (for example  $10^{-15}$  Tesla) can be measured by using SQUID as it has a very high sensitivity. Sensitivity of SQUID magnetometer is connected with the concept of flux quantization. A SQUID device is a closed superconducting loop which includes one/two Josephson junctions in the current path. The main detection coil in SQUID is consisted of superconducting pick-up coils. Such superconducting detection coils are configured as a second-order gradiometer. With respect to the central windings in the coils, two center-windings are in the same sense whereas the outmost two are in counter-wound. With such arrangements, the set of coil becomes non-responsive to uniform magnetic fields and linear magnetic field gradients. Hence, the detection coils generate a current in response to local magnetic field disturbances. Besides, the sensor itself is shielded properly from the fluctuation of the ambient magnetic field of the laboratory and the magnetic field produced by the superconducting magnet. During magnetization measurement in SQUID magnetometer, sample is allowed to vibrate through the superconducting detection coils where the change in magnetic moment of the sample induces an electric field in the pick-up coils. Such generated electric field gives rise to a change in persistent current in the detection circuit which is proportional to the change in magnetic flux. The SQUID functions as a highly linear current-to-voltage convertor, so that variation of the current in the detection coils results in a variation in output voltage proportional to the magnetic moment of the sample. Hence, SQUID directly determines the magnetic moment of the sample by measuring the output voltage of the detection coil as the sample moves through the coil. The vibration frequency of the sample in case of SQUID VSM is 14 Hz. The sensitivity of SQUID VSM is very high (of the order of  $10^{-8}$  emu moment) with one second averaging time.

To perform temperature dependent dc-magnetization measurements different modes were used which are described below.

(i) **Zero-field-cooling (ZFC):** In this mode, sample was cooled from room temperature/paramagnetic region to lowest temperature of measurement in zero magnetic field. Data were recorded in the heating cycle after switching on a constant magnetic field for this measurement.

(ii) **Field-cooled cooling (FCC):** In this mode, sample was cooled from room temperature or paramagnetic region to lowest temperature of measurement in presence of constant applied magnetic field and data were also reordered in the same cooling cycle.

(iii) **Field-cooled warming (FCW):** Similar to FCC mode, here also sample was cooled from room temperature or paramagnetic region to lowest temperature of measurement in presence of constant applied magnetic field (same field as of FCC case) but data were reordered in the heating cycle of the measurement. In general FCW is commonly written as 'FC'.

### 2.3.2 Physical Property Measurement System (PPMS)

Physical Property Measurement System (PPMS, Model P 650) is utilized for performing the heat capacity measurements of different prepared samples in present thesis. Here Quantum Design heat capacity option in PPMS uses a conventional relaxation technique [125] to measure the heat capacity at constant pressure,

$$C_P = \left(\frac{dQ}{dT}\right)_P \quad (2.10)$$

Such relaxation technique controls the heat added to and removed from a sample while monitoring the resulting change in temperature. For Heat Capacity measurements, a known amount of heat is applied to the sample for a certain time with constant power and then this heating period is followed by a cooling period (when heat is removed) of the same duration. Heat capacity measurement provides significant information about the phase transitions, lattice, electronic, and magnetic properties of the samples. A very thin layer of grease works as a thermal connector between sample and platform. Samples are mounted on the platform using adhesive such as Apiezon N or H Grease (addenda). In general the mass of the sample must be at

least of ~10 mg for precise measurement. Typically a single heat capacity measurement involves of several distinct stages. To start the measurement, first the temperatures of sample platform and puck are stabilized at some initial temperature and then by applying power, once can increase sample platform temperature to a particular temperature. Subsequently, the temperature of the sample platform decreases to match the puck temperature. One can monitor the sample platform temperature during both cooling and heating cycles of the experiment which provides the raw data of the heat capacity calculation. Further, a well-known two-tau model is used to analyse the heat capacity data of the compound [126,127]. This model simulates the effect of heat flowing between the sample platform and puck as well as the effect of heat flowing between the sample platform and the sample.

One can determine the values of the heat capacity by optimizing the agreement between the measured data and the two-tau method. Such two-tau model has two different time constants where the first time constant ( $\tau_1$ ) represents the relaxation time between the sample platform and the puck and second time constant ( $\tau_2$ ) represents the relaxation time between the sample platform and the sample itself. Sample heat capacity ( $C_P$ ) is calculated by subtracting addenda heat capacity from total heat capacity.

### ***2.3.2.1 AC Susceptibility Measurement***

The Quantum Design AC Measurement System (ACMS) option for the Physical Property Measurement System (PPMS) is a versatile technique for AC susceptibility measurements. By being connected to the automated temperature and field control systems of the PPMS, the ACMS provides a highly powerful, fully automated magnetic workstation for sample characterization. Magnetization measurements performed through ac-susceptibility are different from that of the magnetic moment measurements in case of dc-magnetization. One can measure the response of magnetic moment present in the sample by adding a small alternating field to the large field of PPMS superconducting magnet through ACMS. Both the amplitude and phase of this response are reported. One should remember that the output amplitude from ACMS measurement is the amplitude of the change in magnetic moment, i.e.  $dM$  which is different from the susceptibility ( $dM/dH$ ). Hence, one can obtain the ac-susceptibility by simply dividing the change in amplitude  $dM$  by the amplitude of the alternating field  $dH$  which gives  $\chi_{ac} = dM/dH$ . Remember that this is only the local slope of the sample's magnetization curve  $M(H)$  which is different from

the 'true' susceptibility  $\chi = M/H$ . During an AC susceptibility measurement, an alternating magnetic field is applied to the measurement region by itself or in addition to the constant field applied by the PPMS superconducting magnet. The signals are stored as waveform blocks in the data buffer. The real and imaginary components of each response waveform are obtained by again fitting the data and comparing it to the driving signal. The two calibration readings are subtracted to yield a calibration vector in the complex plane. Subtracting the two calibration readings subtracts out the sample signal, leaving only environmental and instrumental factors that affect the reading. The true values of interest for the sample are then reported, either as moment amplitude and phase (magnitude and angle of the sample vector) or as in-phase and out-of-phase (or quadrature) components of the moment (real and imaginary components of the sample vector.) Notice that in-phase components of the response signal are *in phase* with the *ideal* response signal, which is  $90^\circ$  *out of phase* with the *driving* signal. This is due to the nature of Faraday's law.

### ***2.3.3 Temperature and Field dependent Dielectric and Pyroelectric Measurements***

Temperature and field dependent dielectric and pyroelectric studies of Fe substituted  $\text{CoCr}_2\text{O}_4$ , i.e.  $\text{Co}(\text{Cr}_{0.95}\text{Fe}_{0.05})_2\text{O}_4$  and  $\text{Co}(\text{Cr}_{0.925}\text{Fe}_{0.075})_2\text{O}_4$  were done in the temperature range of 5 K and 300 K. Complex dielectric permittivity ( $\epsilon_r$ ) and  $\tan\delta$  (loss) as function of temperature and magnetic field were measured using Agilent E4980A LCR meter with a home-made sample holder at several frequencies (1-100 kHz) with 1V ac-bias field where the control of the sample temperature and external magnetic field was ensured by using PPMS. The electric polarization was measured using pyroelectric current measurements for both the samples. These pyroelectric measurements were performed with the same sample holder by using Keithley 6517B electrometer in a columbic mode with PPMS.

---

### *Studies on $\text{Co}(\text{Cr}_{1-x}\text{Fe}_x)_2\text{O}_4$ ( $x = 0.00-0.075$ )*

---

#### **3.1 Introduction**

Cobalt chromite ( $\text{CoCr}_2\text{O}_4$ ) is a well-known multiferroic material having fascinating temperature and magnetic field dependent magnetoelectric (ME) properties [12,13,111].  $\text{CoCr}_2\text{O}_4$  has spinel structure in which  $\text{Co}^{2+}$ -ions ( $3d^7$ ,  $S=3/2$ ) occupy the tetrahedral sites (A) and the  $\text{Cr}^{3+}$ -ions ( $3d^3$ ,  $S= 3/2$ ) are at the octahedral sites (B). Theoretical calculations with the nearest-neighbor and isotropic antiferromagnetic exchange interactions ( $J_{AB}$  and  $J_{BB}$ ) reveal that the arrangement of the magnetic moments in this compound will be like “*ferrimagnetic conical spiral*”[33,66]. In this structure, the axes of the cones are along the [001] crystallographic direction and the magnetic moments lie on their respective conical surfaces. This *spin spiral* configuration has repeated modulation along the [110] direction [8,33]. Hence, this configuration produces a finite magnetization along the [001] direction. The competition between the exchange interactions of magnetic ions located at the A and B sites leads to an exotic magnetic phase diagram [12,14,15]. Even though the  $\text{CoCr}_2\text{O}_4$  shows a FIM ordering below  $T_C \sim 94-97$  K, we do not observe a sign change in the magnetization across the compensation temperature, as seen in most of the traditional FIM compounds. Also, it is reported that the magnetic structure changes below 26 K which may be hindering the magnetization reversal [33]. Some homogeneous rare-earth intermetallic compounds have demonstrated exchange bias across the compensation temperature in single phase compounds [96,128,129]. Such investigations were extended to compensated FIM Heusler alloys along with some other oxides, where a similar effect was observed [130,131]. In all the above alloys, the EB is observed because of the presence of the ferromagnetic clusters created due to anti-site disorder in the fully compensated host.

In recent years, investigations of magnetoelectric (ME) multiferroic materials which have coexistence of ferroelectricity and ferromagnetism, have attracted attention due to their potential applications such as dual read-write memory devices, spintronic devices and sensitive magnetic field sensors [102,103,107]. In general, a strong magnetoelectric coupling is observed in multiferroics; that is, the induction of magnetization (M) by external electric field (E) and/or electrical polarization (P) tuned by applied magnetic fields (H) [100,132–134]. In such ME

multiferroics, the dielectric constant is affected by the applied magnetic field through the intrinsic spin arrangements. Such coupling of the dielectric constant to the applied magnetic field is called the magnetodielectric (MD) coupling, which is commonly observed in oxide materials [135–140]. From literature, it has been found that due to inverse Dzyloshinskii-Moriya (DM) interaction, the breaking of inversion symmetry at neighboring sites of non-collinear spins at spiral magnetic transition produces ferroelectricity [45,141,142].

This chapter deals with the synthesis of  $\text{Co}(\text{Cr}_{1-x}\text{Fe}_x)_2\text{O}_4$  for  $x = 0.00\text{--}0.075$ , and study of their structural, temperature and magnetic field dependent magnetic, dielectric, ferroelectric and magnetodielectric properties. As it is well known that all these fascinating properties are dependent on the existing complex crystalline and magnetic structures of the compounds, therefore to understand the microscopic origin of these novel properties, we have reported the magnetic structures of these compounds by performing the temperature dependent NPD experiments.

### ***3.2 Experimental Details***

The phase pure polycrystalline samples of  $\text{Co}(\text{Cr}_{1-x}\text{Fe}_x)_2\text{O}_4$  for  $x = 0.00\text{--}0.075$  were synthesized by standard solid state reaction methods. Stoichiometric amounts of the constituent oxides ( $\text{Co}_3\text{O}_4$ ,  $\text{Cr}_2\text{O}_3$ , and  $\text{Fe}_2\text{O}_3$ ) with purity ( $\geq 99.6$ ) were initially mixed using an agate mortar pestle. These mixed powders were pressed into cylindrical pellets of a diameter of  $\sim 10$  mm using a hydraulic press with a maximum load of  $5 \text{ tons/cm}^2$  and placed in a platinum crucible. In order to enrich the homogeneity throughout the sample, pellets were reground and pelletized 2/3 times and finally sintered at  $1300\text{--}1350$  °C for 24 hours. The structural characterization and phase formation of the samples were investigated by room temperature XRD patterns on powdered samples by utilizing  $\text{Cu-K}\alpha$  ( $\lambda = 1.5406$  Å) radiation using a Rigaku X-ray diffractometer (model:TTRAX-III). NPD measurements were carried out on finely ground powders of the  $\text{Co}(\text{Cr}_{1-x}\text{Fe}_x)_2\text{O}_4$  for  $x = 0.05, 0.075$  samples packed in a vanadium container in the temperature range of  $2.9\text{--}295$  K at the UGC-DAE CSR beam line at the Dhruva reactor using a focusing crystal based powder diffractometer (FCD-PD3). Patterns covering the  $2\theta$ -range  $6\text{--}120^\circ$  were recorded at all temperatures using a closed cycle refrigerator (AS Scientific make). Neutrons at a wavelength of  $1.48$  Å were used in the measurements [124]. Temperature and magnetic field

dependent magnetic measurements were performed with a Magnetic Property Measurements System (MPMS), Quantum design, USA. Specific heat ( $C_p$ ) and ac-susceptibility measurements were carried with a commercial Physical Properties Measurements System (Quantum Design, USA). Complex dielectric permittivity ( $\epsilon_r$ ) and  $\tan\delta$  (loss) as function of temperature and the magnetic field were measured using Agilent E4980A LCR meter with a home-made sample holder at several frequencies (1 kHz-100 kHz) with 1V ac-bias field where the control of the sample temperature and external magnetic field was ensured by using PPMS. The electric polarization was measured using pyroelectric current measurements for both the samples. These pyroelectric measurements were performed with the same sample holder by using Keithley 6517B electrometer in a coulombic mode with PPMS. A poling static electric field of  $\sim 3$  kV/cm for both the samples, i.e.  $\text{Co}(\text{Cr}_{0.95}\text{Fe}_{0.05})_2\text{O}_4$  and  $\text{Co}(\text{Cr}_{0.925}\text{Fe}_{0.075})_2\text{O}_4$  was applied at 150 K (which is above the transition temperatures) during cooling to align electric dipoles. At 8 K, the poling electric field (E) was switched-off and the polarization vs time was recorded for the 2000s before measuring polarization (P) vs temperature during warming (5 K/min) under zero electric field. To test the effect of the magnetic field upon polarization, the sample was also cooled with a magnetic field ( $H = 9$  T) always applied at 150 K.

### **3.3 Results and Discussions**

#### **3.3.1 X-ray Diffraction**

X-ray diffractograms of pristine and Fe-substituted  $\text{CoCr}_2\text{O}_4$  compounds are compared in Fig. 3.1. It can be clearly seen that all the Bragg peaks of  $\text{CoCr}_2\text{O}_4$  can be indexed using a cubic spinel structure in space group  $Fd\bar{3}m$ . The cell parameters were calculated on the basis of the Miller indices and their corresponding d-values using the least squares method. Cell parameters calculated from above XRD experiment are found to be in good agreement with earlier reports [32]. Comparison of XRD patterns of Fe substituted  $\text{CoCr}_2\text{O}_4$  samples with that of the pristine  $\text{CoCr}_2\text{O}_4$  shows that all the Bragg peaks can be accounted for the same space group and no extra peaks are seen which indicates that Fe is indeed substituted for Cr. The slight variation of cell parameters further confirms this. For qualitative analysis of the XRD data, Rietveld analysis of the powder XRD data was carried out using the reported  $\text{CoCr}_2\text{O}_4$  structure as the starting model. The results of the XRD investigations are given in Table 3.1. We have noticed an increase in the

lattice parameter with Fe substitution which is due to the difference in the ionic sizes of  $\text{Fe}^{+3}$  (~0.785 Å) to that of the  $\text{Cr}^{+3}$  (~0.755 Å) in the octahedral crystal field [143].

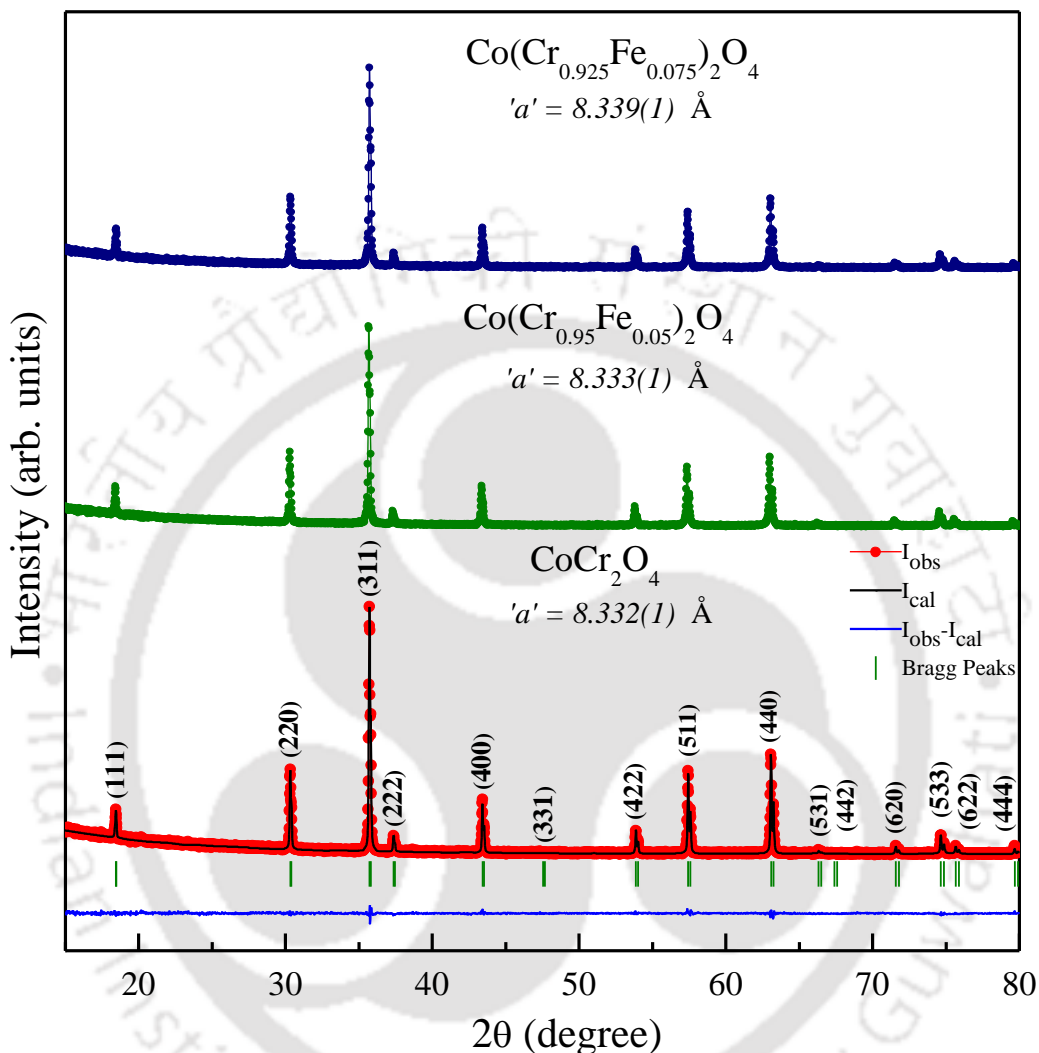


**Figure 3.1** Room temperature X-ray diffraction pattern of  $\text{CoCr}_2\text{O}_4$ , along with Fe substituted compounds, i.e.  $\text{Co}(\text{Cr}_{0.95}\text{Fe}_{0.05})_2\text{O}_4$  and  $\text{Co}(\text{Cr}_{0.925}\text{Fe}_{0.075})_2\text{O}_4$ .

Table 3.1 Structural parameters from the Rietveld refinement of X-ray powder diffraction patterns for  $\text{Co}(\text{Cr}_{1-x}\text{Fe}_x)_2\text{O}_4$  ( $x = 0.0-0.075$ ) samples at room temperature.

Parameters	$x = 0.00$	$x = 0.05$	$x = 0.075$
Crystal Symmetry	Cubic	Cubic	Cubic
Space Group	$Fd\bar{3}m$	$Fd\bar{3}m$	$Fd\bar{3}m$
$a = b = c$ (Å)	8.332(1)	8.333(1)	8.339(1)
$V$ (Å <sup>3</sup> )	578.43(1)	578.63(2)	578.89(1)
Oxygen position	0.263(2)	0.261(2)	0.260(2)
GOF ( $\chi^2$ )	2.4	2.1	2.8

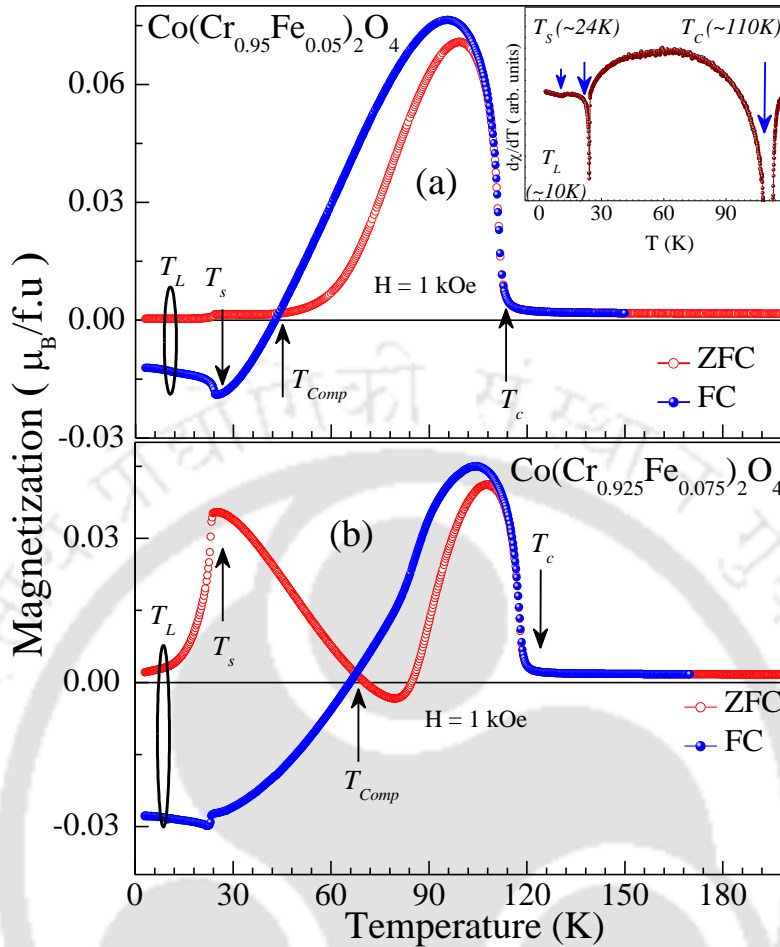


**Figure 3.2** The temperature dependence of ZFC and FC magnetization, measured under 1 kOe field for (a)  $\text{Co}(\text{Cr}_{0.95}\text{Fe}_{0.05})_2\text{O}_4$ , and (b)  $\text{Co}(\text{Cr}_{0.925}\text{Fe}_{0.075})_2\text{O}_4$ . The inset of (a) shows the first order derivative plot of magnetic susceptibility for the better appearance of the magnetic transitions.

### 3.3.2 Temperature and Field Dependent Magnetic Properties

Temperature dependent ZFC and FC magnetization measurements were carried out in the temperature range of 2–180 K under an external applied magnetic field of 1 kOe. Fig. 3.2 (a) and (b) depict the temperature dependent magnetization (M–T) curves of the  $\text{Co}(\text{Cr}_{0.95}\text{Fe}_{0.05})_2\text{O}_4$  and  $\text{Co}(\text{Cr}_{0.925}\text{Fe}_{0.075})_2\text{O}_4$  compounds, respectively, under two different conditions, namely, ZFC and FC under the external magnetic field of 1 kOe. It is observed that 5% and 7.5% Fe substituted samples exhibit the ferrimagnetic transition at  $T_C \sim 110$  K and  $\sim 118$  K, respectively. One can see clearly that there is an increase in  $T_C$  with Fe substitution. In the case of FC measurements, upon field cooling the sample from a paramagnetic state, the spin configuration goes to a stable state. But in the case of the ZFC measurements, because of the absence of an applied external field

during cooling, the spin configuration attains the metastable configuration. It is possible that complete reorientation of the spins does not take place when the field is applied in the ferrimagnetic state. However, for the FC case, the spin configuration attains the stable state because of slow field cooling with temperature. Hence, we have considered using this FC mode of measurement to identify different magnetic transitions. With lowering the temperature below  $T_C$ , the FC curves of both the samples exhibit a reversal in the magnetization across  $T_{\text{comp}} \sim 43.8$  K and 67.8 K respectively. Further, below  $T_{\text{comp}}$ , the samples show another transition around  $T_S \sim 24$  K which could be due to the accompanied magneto-structural transition into the non-collinear phase similar to the parent compound. This transition temperature,  $T_S$  is unaffected by Fe substitution. The inset of Fig. 3.2 (a) shows the first derivative plots of magnetic susceptibility, where we can see clear evidence of all these transitions. Furthermore, the lock-in transition around  $T_L \sim 10$  K, which is not that clear in the M–T curves, is also clearly seen in this inset of the plot.

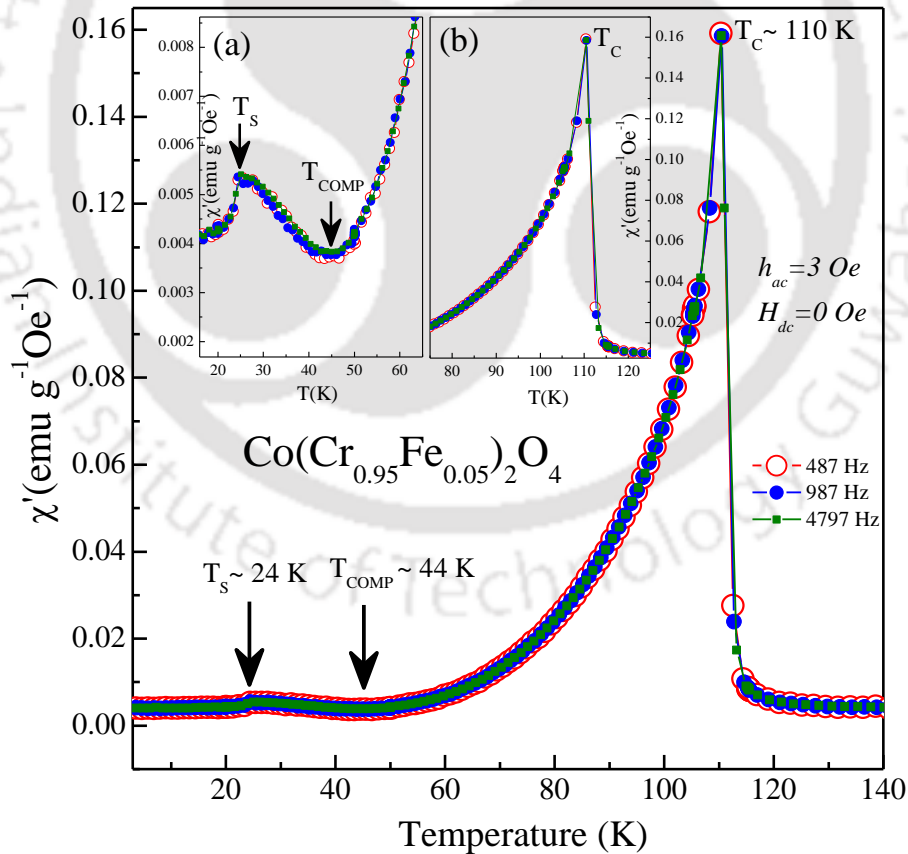


**Figure 3.3** Temperature dependent ac-magnetic susceptibility of  $\text{Co}(\text{Cr}_{0.95}\text{Fe}_{0.05})_2\text{O}_4$  measured at various frequencies under warming condition with the amplitude of dynamic magnetic-field,  $h_{ac} = 3$  Oe and under zero-dc bias. Insets show the enlarged view of the magnetic transitions at different frequencies.

Fig. 3.3 shows the temperature dependence of ac-magnetic susceptibility ( $\chi_{ac}$ ) measured under warming condition using different frequencies for  $\text{Co}(\text{Cr}_{0.95}\text{Fe}_{0.05})_2\text{O}_4$  with  $h_{ac} = 3$  Oe and  $H_{dc} = 0$  Oe. It is observed that there is a sharp peak at  $T_C = 110$  K confirming the long range FIM ordering and another peak is at  $T_S \sim 24$  K showing the signature of magneto-structural transition which validates with dc-magnetization measurements presented in Fig. 3.2. In addition, a clear anomaly around  $\sim 44$  K confirms the presence of  $T_{comp}$  as shown in inset (a) for the clear view. Further, inset (b) does not show any frequency dependence of  $T_C$ . From these susceptibility measurements at different frequencies, we ruled out the possibility of glassy nature of the sample.

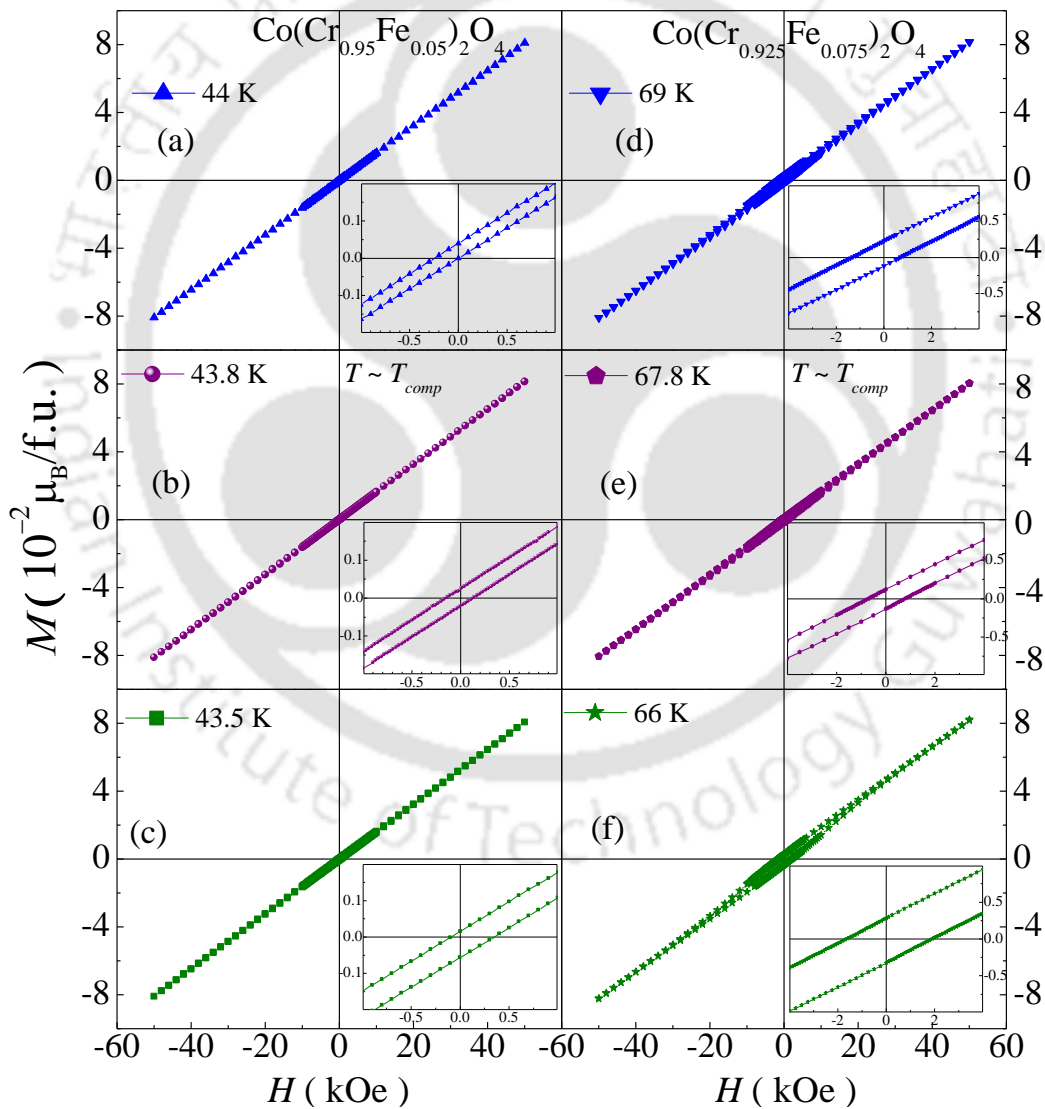


**Figure 3.4**  $M$ - $H$  loops of  $\text{Co}(\text{Cr}_{0.95}\text{Fe}_{0.05})_2\text{O}_4$  and  $\text{Co}(\text{Cr}_{0.925}\text{Fe}_{0.075})_2\text{O}_4$  samples in the close vicinity of respective  $T_{comp}$ . Insets depict an enlarged view of respective plots to see a clear loop shifting.

### 3.3.3 Exchange Bias Effect

Recently, it has been found that the materials having negative magnetization are likely to exhibit the sign change in the EB across the  $T_{\text{comp}}$  [26,98,144–146]. The study of EB effect in these compensated samples may reveal new features in these  $\text{Co}(\text{Cr}_{1-x}\text{Fe}_x)_2\text{O}_4$  compounds. A set of six panels in Fig. 3.4 shows the distinct and detailed information on the hysteretic behavior of 70 kOe FC M-H loops for 5% and 7.5% Fe substituted compounds, i.e.  $\text{Co}(\text{Cr}_{0.95}\text{Fe}_{0.05})_2\text{O}_4$  and  $\text{Co}(\text{Cr}_{0.925}\text{Fe}_{0.075})_2\text{O}_4$  in the vicinity of the  $T_{\text{comp}} \sim 43.8$  K and  $\sim 67.8$  K, respectively. The small left shift in the origin of M-H loop observed above the  $T_{\text{comp}}$  of the respective sample becomes right shift below  $T_{\text{comp}}$ . Temperature dependence of EB effect is studied by recording field cooled (FC) M-H loops by following the given protocol. First, the sample was cooled in 70 kOe from room temperature (i.e. paramagnetic range) to the temperature of interest in the close vicinity of  $T_{\text{comp}}$  for recording M-H loop, and thereafter the field was cycled between  $H = \pm 50$  kOe to complete the M-H loop at that particular temperature. Importantly one should notice that it is very important to repeat the same procedure for each and every temperature in order to avoid the possibility of the sample history on the M-H loop measurements. Linear behaviour of M-H loop is observed in the close vicinity of respective  $T_{\text{comp}}$  reveals the fact of compensated moments of the two sublattices at  $T_{\text{comp}}$ . We will further discuss it in detail in next section with NPD results.

### 3.3.4 Temperature Dependent Neutron Powder Diffraction Studies

For the microscopic magnetic structure study of the above observed fascinating properties such as negative magnetization, sign change in exchange bias along with the temperature dependency of crystalline and magnetic structure, NPD experiments have been performed at various temperatures ranging from a paramagnetic state to magnetically ordered states across  $T_C$ ,  $T_{\text{comp}}$ ,  $T_S$ , and  $T_L$  till  $\sim 3$  K. Fig. 3.5 (a)–(c) shows the Rietveld refinement of the NPD patterns recorded in the full range, i.e.  $2\theta = 6\text{--}118^\circ$ , at 295 K (paramagnetic state), at 44 K ( $T_{\text{comp}}$ ) and at 20 K (below  $T_S$ ) for the  $\text{Co}(\text{Cr}_{0.95}\text{Fe}_{0.05})_2\text{O}_4$  using the FULLPROF program [147]. Magnetic symmetry analysis using the program BasIreps was used to obtain the irreducible representations (IR) and their basis vectors (BV) for the magnetic atoms on different sites for  $k = [\delta \delta 0]$  and  $\delta = 0.62$  has given the best fitted values for low temperature magnetic structures ( $T =$

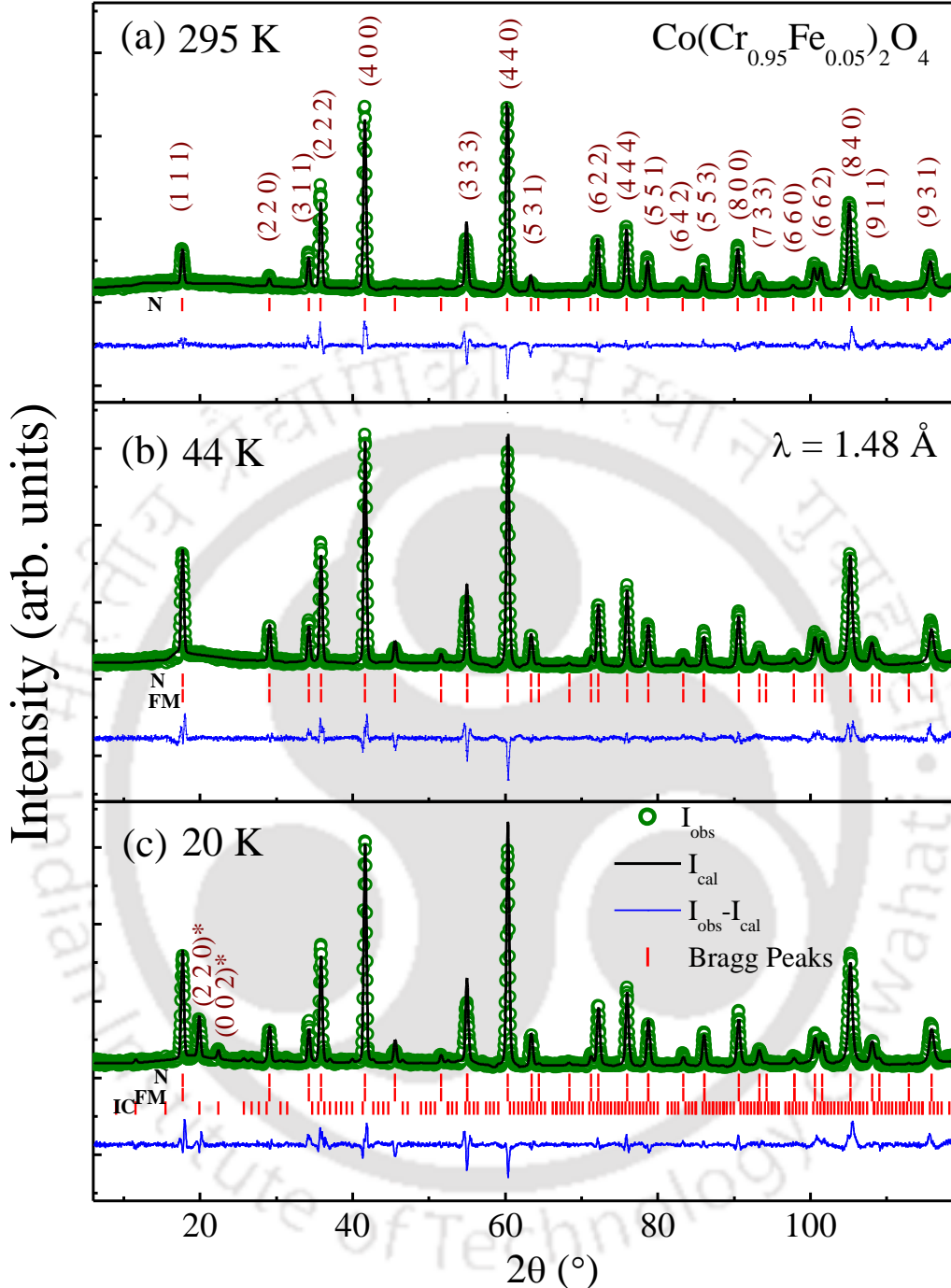


**Figure 3.5** (a–c) Rietveld refinements of the NPD patterns for  $\text{Co}(\text{Cr}_{0.95}\text{Fe}_{0.05})_2\text{O}_4$  recorded in zero field at  $T = 295 \text{ K}$ ,  $44 \text{ K}$  and  $20 \text{ K}$ , respectively. Here, at  $295 \text{ K}$ , only the structural (nuclear) phase is refined, and for the patterns at  $44 \text{ K}$ , both nuclear and ferrimagnetic phases are refined. For the  $20 \text{ K}$  data, the incommensurate (IC) phase has also been added in the refinement where  $(220)^*$  and  $(002)^*$  are satellite reflections as explained in the text.

2.9–20 K). But above these temperatures, we have  $k = [0 \ 0 \ 0]$  for  $T = 35\text{--}90 \text{ K}$ . Here, refinement converged with reasonable values of profile fitting parameters such as Bragg-R factor,  $R_f$ -factor,

$R_p$ -factor,  $R_{wp}$ -factor and goodness of fit (GOF-index) throughout the temperature range, similar to the values represented in Tables 3.2 and 3.3. These numbers are good enough to show the goodness of the fit [148]. From the magnetization measurements, it is clearly established that these compounds are paramagnetic at room temperature, hence only the nuclear (crystallographic) structure was refined for the room temperature NPD data. It can be seen from the NPD pattern that the nuclear reflections at 295 K are well fitted to the cubic spinel structure. The structure is characterized by the positions of cations on the A (tetrahedral) and B (octahedral) sites of the  $AB_2O_4$  type spinel structure. Here, the A-sites are occupied by Co ions, whereas the B-sites are occupied by Cr and substituted Fe, indicating that there is no mixing of the Fe cation on the A and B sites up to the given percentage of Fe substitution. The Wyckoff position for the Co ions is  $8a$ , for the Cr/Fe atoms it is  $16d$ , and oxygen atoms are at the  $32e$  ( $u \sim 0.26$ ) site having the  $Fd\bar{3}m$  space group, where  $u$  represents the oxygen coordinates. The lattice parameters of the  $Co(Cr_{0.95}Fe_{0.05})_2O_4$  and  $Co(Cr_{0.925}Fe_{0.075})_2O_4$  samples at room temperature (295 K) are found to increase similar to XRD. There is also a minimal change in the lattice parameter upon lowering the temperature from 295 K for both the compounds. As shown in Fig. 3.5 (b) and (c), the NPD patterns near to the compensation temperature ( $T_{comp} \sim 44$  K) and below the magneto-structural transition temperature ( $T_S \sim 24$  K), the magnetic structure has also been refined with the nuclear (crystallographic) structure for low temperature NPD patterns. At 44 K, the magnetic structure has been refined by assuming two phases (i.e. the nuclear phase along with the commensurate (C) FM/FIM phase). Below  $T_S$  (i.e.  $T = 20$  K), we have further added, an incommensurate (IC) antiferromagnetic phase in the refinement. The magnetic reflections have been refined based on symmetry operators given in the numeric form, generated for the propagation vector,  $k = [0\ 0\ 0]$  using BasIreps with  $Fd\bar{3}m$  space group for the temperature above  $T_S$  (i.e. for 44 K).

As depicted in Fig. 3.5 (c), at 20 K (below  $T_S$ ), two additional magnetic reflections [i.e.  $(220)^*$  and  $(002)^*$ ] are observed compared to the patterns above  $T_S$  which are similar to that of the parent compound. The observation of these reflections may indicate the persistence of the conical spirals as reported by Menyuk et al. [33]. These additional peaks have been fitted to the IC spin-spiral component with an IC propagation vector of  $(0.62, 0.62, 0)$  which is different from the  $T = 44$  K NPD data. Such  $(220)^*$  is the satellite reflection for the  $(220)$  Bragg peak as

Table 3.2 Structural and magnetic parameters like lattice constant (a), magnetic moments and agreement factors are determined from Rietveld refinement of neutron diffraction patterns measured at low temperatures for the  $\text{Co}(\text{Cr}_{0.95}\text{Fe}_{0.05})_2\text{O}_4$  compound [both commensurate (CP) and incommensurate phase (ICP)]

T(K)	a (Å)	A ( $\mu_B$ )	B ( $\mu_B$ )	Net moment	A ( $\mu_B$ )	B ( $\mu_B$ )	Net moment	R <sub>p</sub>	R <sub>wp</sub>	R <sub>f</sub>	R <sub>B</sub>	GOF index
	$\pm 0.002$	$\pm 0.01$	$\pm 0.01$	$(\mu_B) \pm 0.02$	$\pm 0.01$	$\pm 0.01$	$(\mu_B) \pm 0.02$					
		(CP)	(CP)		(ICP)	(ICP)						
2.9	8.329	1.53	1.61	0.08	3.07	2.85	0.22	8	11	4	8	4.2
10	8.330	1.50	1.53	0.03	2.75	2.84	0.09	8	10	4	7	4.1
20	8.330	1.50	1.74	0.24	2.54	2.36	0.18	8	10	4	7	4.0

Table 3.3 Structural and magnetic parameters like lattice constant (a), magnetic moments and agreement factors are determined from Rietveld refinement of neutron diffraction patterns measured at low temperatures for the  $\text{Co}(\text{Cr}_{0.925}\text{Fe}_{0.075})_2\text{O}_4$  compound [both commensurate (CP) and incommensurate phase (ICP)]

T(K)	a (Å)	A ( $\mu_B$ )	B ( $\mu_B$ )	Net moment	A ( $\mu_B$ )	B ( $\mu_B$ )	Net moment	R <sub>p</sub>	R <sub>wp</sub>	R <sub>f</sub>	R <sub>B</sub>	GOF index
	$\pm 0.002$	$\pm 0.01$	$\pm 0.01$	$(\mu_B) \pm 0.02$	$\pm 0.01$	$\pm 0.01$	$(\mu_B) \pm 0.02$					
		(CP)	(CP)		(ICP)	(ICP)						
2.9	8.331	1.62	1.67	0.05	3.42	2.74	0.68	12	15	8	12	2.9
10	8.331	1.62	1.68	0.06	2.95	2.79	0.16	12	15	8	13	2.9
20	8.331	1.61	1.90	0.29	2.51	2.72	0.21	11	15	5	9	3.0

$(220)^* = (220) \pm k$  with  $k = 0.62$ . This  $(002)^*$  has a purely magnetic origin in the spinel structure, and the spatial ordering of the transverse spins may give rise to the  $(002)^*$  superlattice reflection [149] as predicted in the Yafet–Kittel (YK) model [150–152]. The magnetic moments below  $T_S$  have been listed for both the compounds in Table 3.2 and 3.3.

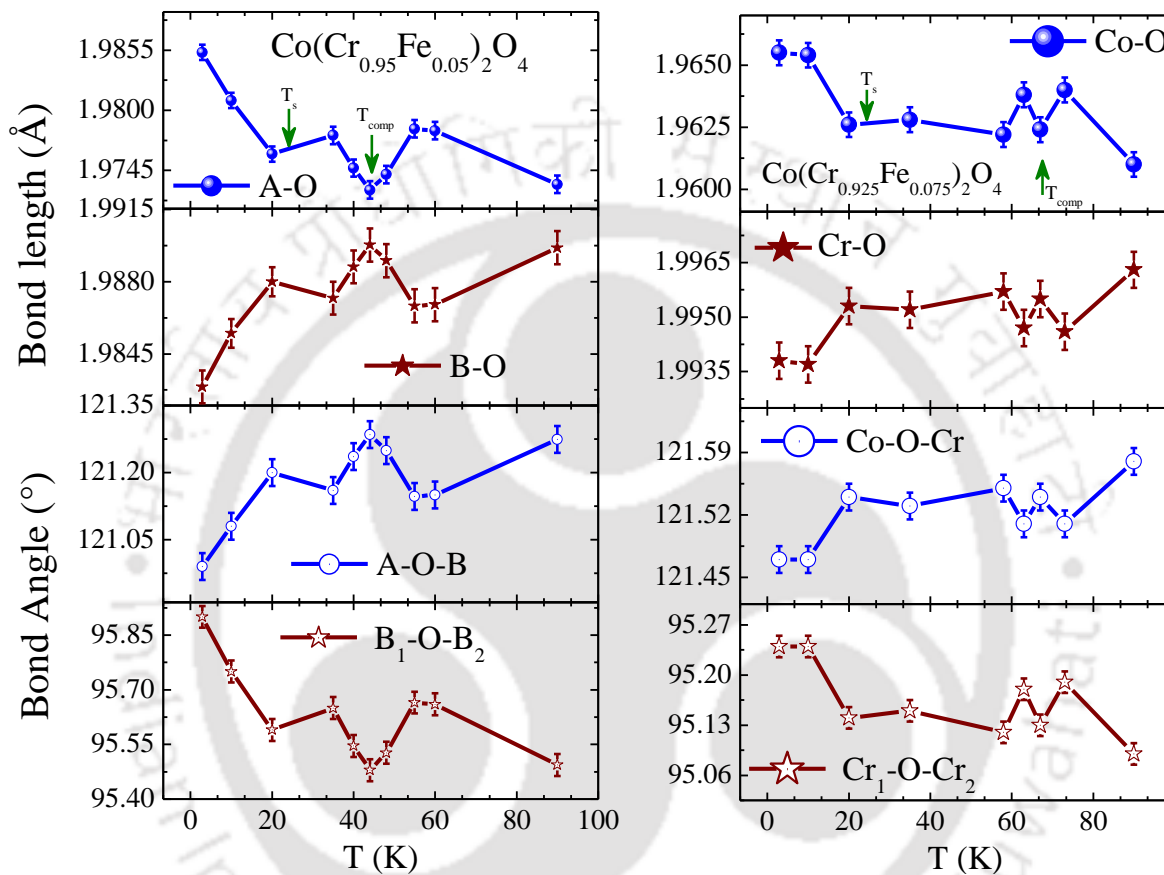


**Figure 3.6** Temperature dependence of the bond lengths A–O and B–O along with the bond angles A–O–B and  $B_1$ –O– $B_2$  in the temperature range 2.9–90 K for both  $\text{Co}(\text{Cr}_{0.95}\text{Fe}_{0.05})_2\text{O}_4$  and  $\text{Co}(\text{Cr}_{0.925}\text{Fe}_{0.075})_2\text{O}_4$ .

Figure 3.6 depicts the plots of the temperature dependence of the bond angles and bond lengths which corresponds to the magnetic superexchange paths in these spinel compounds. As we are substituting Fe for Cr in the B-sites of the spinel compound, one can see these bond parameters such as A–O and B–O bond lengths and corresponding bond angles, i.e. A–O–B and  $B_1$ –O– $B_2$  which show fluctuations across  $T_{\text{comp}}$ . The A–O bond length and  $B_1$ –O– $B_2$  angle is found to increase significantly below the magneto-structural transition temperature ( $T_S$ ), whereas the B–O bond length and A–O–B angles are found to decrease. This indicates that there are magnetically driven distortions in existing tetrahedra and octahedra which consequences in a

correlation between the magnetic ordering and the crystal structure. Fig. 3.7 represents the schematic crystal structure of the pristine  $\text{CoCr}_2\text{O}_4$  for better view of understanding the different bond lengths and bond angles which are calculated from NPD data.

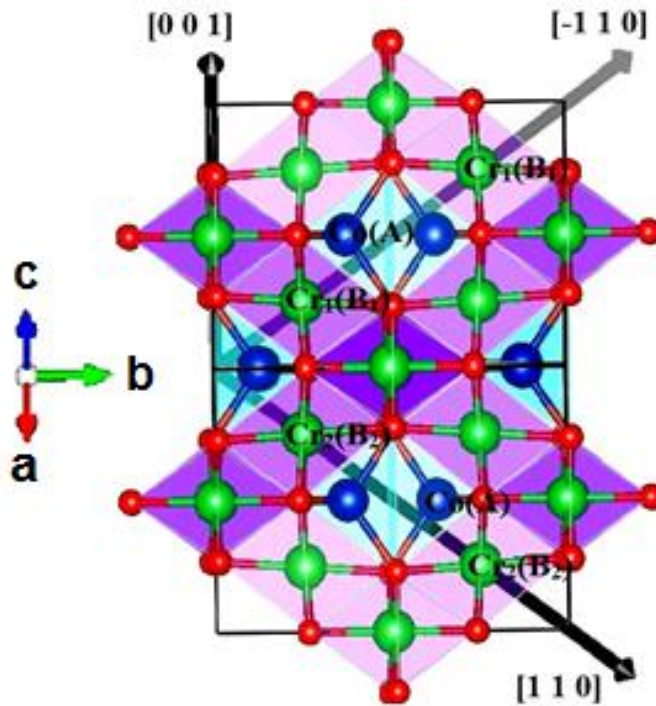


**Figure 3.7** Schematic diagram of the crystal structure of pristine  $\text{CoCr}_2\text{O}_4$  for the better understanding of the different bond parameters in the compound.

Detailed NPD patterns recorded at different temperatures in the range 2.9 – 90 K for both of the Fe substituted  $\text{CoCr}_2\text{O}_4$  samples are shown in Fig. 3.8 [(a) for  $x = 0.05$  and (b) for  $x = 0.075$ ]. On lowering the temperature, it can be seen from the NPD patterns that intensities of lower angle Bragg reflections increase with decreasing temperature. Furthermore, the appearance of two additional broad (not instrumental resolution limited) asymmetric peaks, i.e. the magnetic satellite peaks  $(220)^*$  at scattering vector ( $Q = 4\pi\sin\theta/\lambda$ )  $\sim 1.46 \text{ \AA}^{-1}$  and  $(002)^*$  at  $Q \sim 1.64 \text{ \AA}^{-1}$  suggest the presence of non-collinear spin-spiral orderings at low temperatures below  $T_S$  for both the compounds. As displayed in the insets of Fig. 3.8, it can be observed that the peak intensity of  $(220)^*$  and  $(002)^*$  magnetic reflections increases significantly on lowering the temperature from 20 K to 2.9 K. The A-site and B-site magnetic moments show a clear variation with temperature and their values are much lower than the spin only moment value, confirming the non-collinear magnetic ordering in these compounds. The lower value of the magnetic moment

Neutron Counts (arb. units)

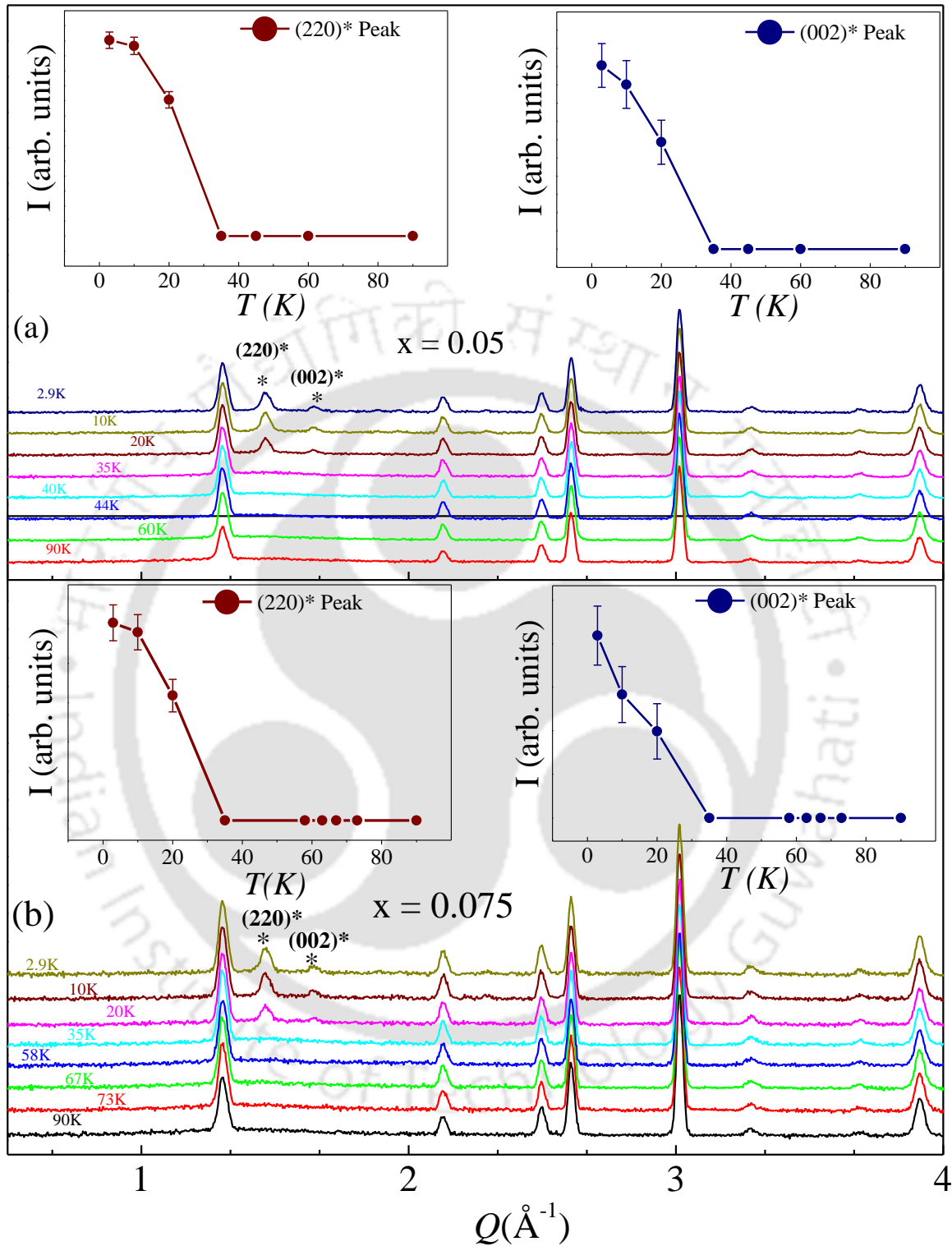


**Figure 3.8** Neutron diffraction patterns measured at various temperatures of (a)  $x = 0.05$  and (b)  $x = 0.075$  samples. The appearance of the  $(220)^*$  and  $(002)^*$  peaks below 35 K is evident. Insets show the temperature variation of the integrated intensity of the satellite peaks  $(220)^*$  and  $(002)^*$ .

on the A-site [see Tables 3.2 and 3.3] indicates the coexistence of disordered finite magnetic clusters within the infinite magnetic network and these disordered magnetic clusters play an important role for the low magnetic moment value [151,153,154]. The observed loss of the B-site magnetic moment suggests the possibility of a canted spin structure at B-site, i.e. the moments are highly non-collinear in these compounds, similar to the parent compound reported by Menyuk et al. [33].

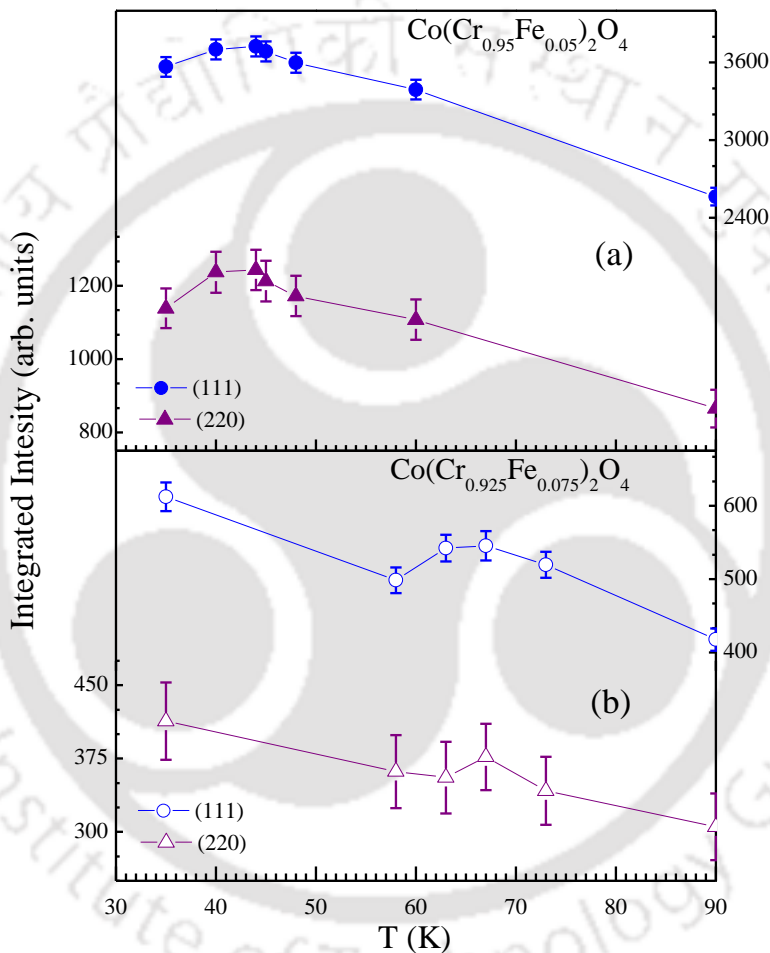


**Figure 3.9** Temperature dependence of the integrated intensity of the (111) and (220) fundamental reflections for both (a)  $\text{Co}(\text{Cr}_{0.95}\text{Fe}_{0.05})_2\text{O}_4$ , and (b)  $\text{Co}(\text{Cr}_{0.925}\text{Fe}_{0.075})_2\text{O}_4$ .

Further, Fig. 3.9 shows the temperature dependent variation of integrated intensity of the fundamental reflections (111) and (220) of  $\text{Co}(\text{Cr}_{0.95}\text{Fe}_{0.05})_2\text{O}_4$  (a) and  $\text{Co}(\text{Cr}_{0.925}\text{Fe}_{0.075})_2\text{O}_4$  (b) calculated from NPD data. Intensity of both the reflections appears to increase up to 30 K, but there is an unusual change around  $T_{\text{comp}} \sim 43.8$  K and 67.8 K for  $\text{Co}(\text{Cr}_{0.95}\text{Fe}_{0.05})_2\text{O}_4$  and  $\text{Co}(\text{Cr}_{0.925}\text{Fe}_{0.075})_2\text{O}_4$ , respectively. It was observed in  $\text{CoCr}_2\text{O}_4$  that magnetic order consists of a

FIM component and a spiral component below the FIM transition temperature. Hence, in this case, it was found that the magnetic moment makes an angle (*cf.* cone angle) with the cone axis in the  $[0\ 0\ 1]$  direction [8,33,155]. In present compounds, where the amount of Fe substitution is minimal, the observed behaviour is similar to that of parent compound. The variation in the magnitude of these spiral components is the primary cause for the variation in the integrated intensity. Hence, this unusual change of integrated intensity around compensation temperature could be the result of the change in the magnitude of the spiral components of the magnetic moments.

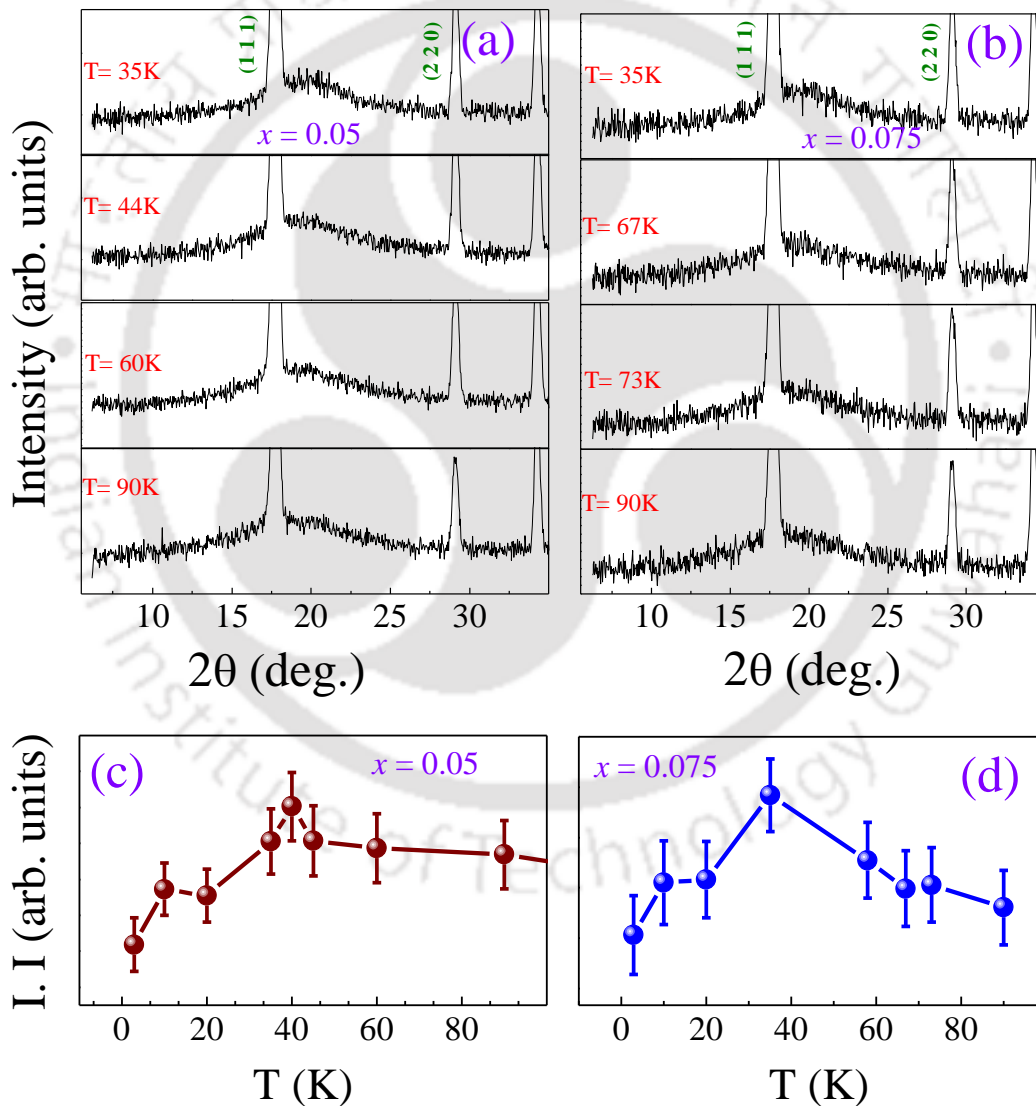


**Figure 3.10** Diffuse signal around the (111) Bragg peak in the neutron diffraction patterns at different temperatures for (a)  $x = 0.05$ , and (b)  $x = 0.075$  (all graphs are plotted in the same scale). Temperature variation of integrated intensity of diffuse scattering are shown of both (c)  $x = 0.05$ , and (d)  $x = 0.075$  compounds.

Fig. 3.10 shows the enlarged portions of the low-angle NPD patterns at different temperatures for both the  $x = 0.05$  and  $0.075$  samples. The patterns at 90 K, i.e. closer to the FIM temperature,  $T_C$  for both of the samples, show the presence of a diffuse signal around the (111) reflection. The presence of this diffuse signal, which is of magnetic origin, indicates the formation of magnetic spin clusters in these compounds. Contributions to the diffraction pattern from these clusters are only limited around the (111) peak in these compounds, and may be due to very sharp form factor dependence [156]. From earlier reports on the magnetic structure study of  $\text{CoCr}_2\text{O}_4$ , it is observed that there is a clear long range FIM ordering along with a short range spin spiral ordering emerging at around 80 K, below  $T_C$  [33]. Further, it seems that the diffused signal started appearing at a higher temperature compared to that of the parent  $\text{CoCr}_2\text{O}_4$  compound. This could be the result of the substituted Fe ions at the Cr site. The presence of this diffuse signal may be due to the finite short range clusters of the transverse spin component coexisting with the infinite long ranged magnetic order in these spinel compounds [151,153,154]. The scattering from these disordered magnetic clusters which are present in these compounds is the origin for these diffuse signals. The variation in diffuse intensity with temperature is shown in Fig. 3.10 (c) and (d). With decreasing temperature, the diffuse scattering intensity increases up to 35–45 K and then decreases, possibly due to the presence of long-range spin-spiral order commencing below  $T_S$  in these compounds. This is an explicit indication of the build-up of a short range correlation of the transverse spin component with temperatures above the spin-spiral transition,  $T_S$ .

In Fig. 3.11, we have shown the temperature dependence of EB field along with the moments corresponding to different sublattices in the spinel structure. EB field defined as,  $H_{EB} = (H_+ + H_-)/2$ , where  $H_+$  and  $H_-$  represent the right and left field values of M-H loop where the net magnetization crosses the  $M = 0$  axis. It can be seen that EB field changes its sign across the  $T_{comp}$  for both the samples. The sign change of the M-H loop shifting across the compensation temperature, which was absent in the pristine  $\text{CoCr}_2\text{O}_4$ , indicates temperature dependency of spin configurations in  $\text{Co}(\text{Cr}_{0.95}\text{Fe}_{0.05})_2\text{O}_4$  and  $\text{Co}(\text{Cr}_{0.925}\text{Fe}_{0.075})_2\text{O}_4$ . Attentively, in the narrow temperature window in the proximity of  $T_{comp}$ , there is a non-monotonic variation in the individual moments of A-site,  $B_1$ -site and  $B_2$ -site which will be discussed later with NPD results. This is indicative of the reorientation of moments due to the underlying spin reorientation

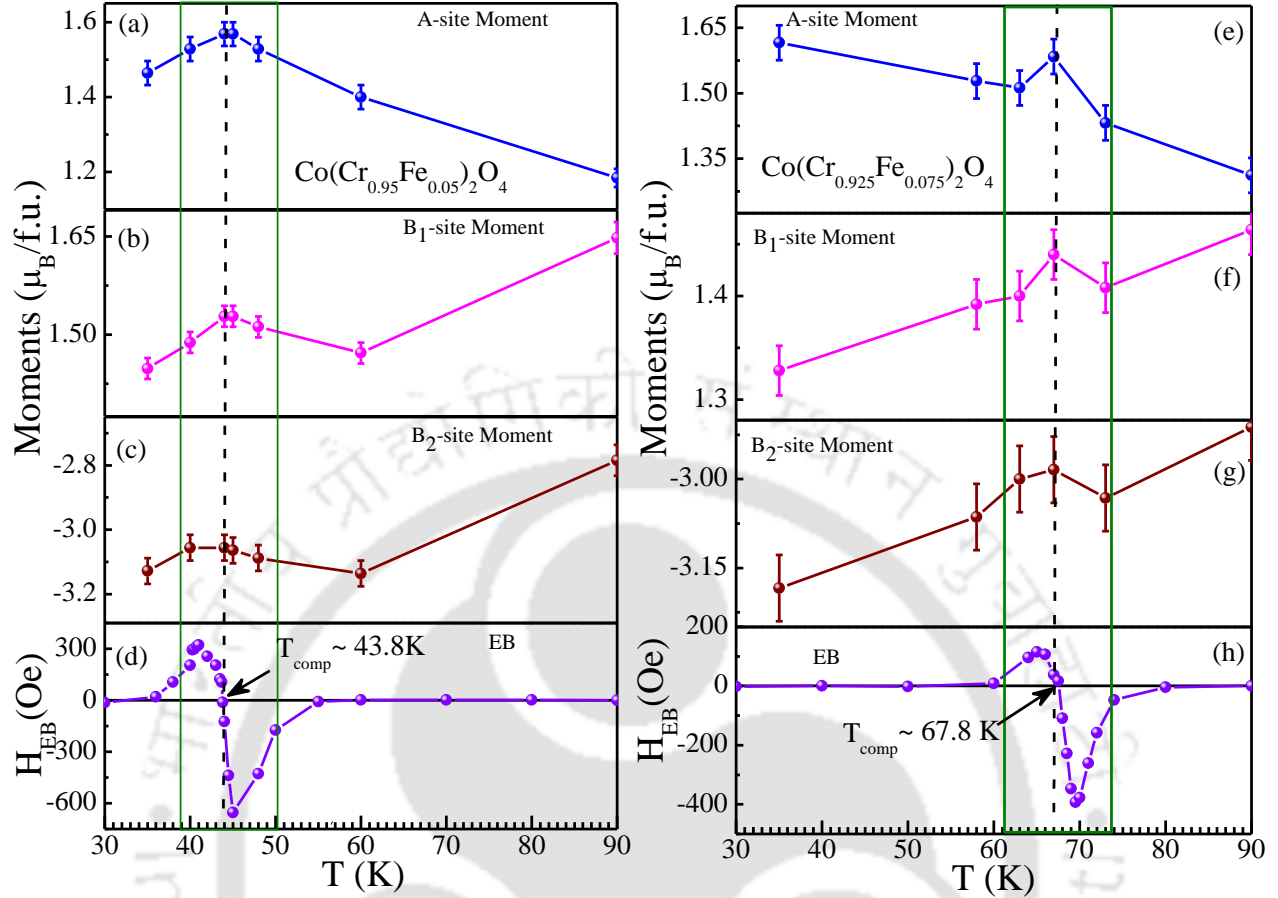


**Figure 3.11** Temperature dependence of different site moments calculated from NPD along with EB field of  $\text{Co}(\text{Cr}_{0.095}\text{Fe}_{0.05})_2\text{O}_4$  (a-d) and  $\text{Co}(\text{Cr}_{0.925}\text{Fe}_{0.075})_2\text{O}_4$  (e-h) compounds.

which was invoked for the explanation of the sign reversal of EB across the compensation temperature [23]. The EB field is present only in the close vicinity of  $T_{\text{comp}}$  and goes to zero as one increases/decreases the temperature beyond this temperature window of  $T_{\text{comp}}$ . Further, from dc-magnetization data we know that ZFC M-T curves do not show any change in the slope (or unusual features) across  $T_{\text{comp}}$  window representative of a spin-glass transition. Moreover, we have not observed any relaxation in this temperature region in the magnetization values. However, we cannot completely rule out the possibility of an appearance of a very thin spin-glass interface between the ferromagnetic and antiferromagnetic clusters. Hence, we do not expect any spin-glass transition responsible for observed EB effect. The pristine compound  $\text{CoCr}_2\text{O}_4$  has a strong spin-lattice coupling [12,13]. With a small amount of Fe substitution, there is no reason that the strength of this spin-lattice coupling will change. Here, we have also observed this strong spin-lattice effect where a non-monotonic change of the spin angle is taking

place around  $T_{\text{comp}}$  as shown in Fig.3.12. So, in other words, the sign change of EB effect is indirectly related to spin-lattice coupling.

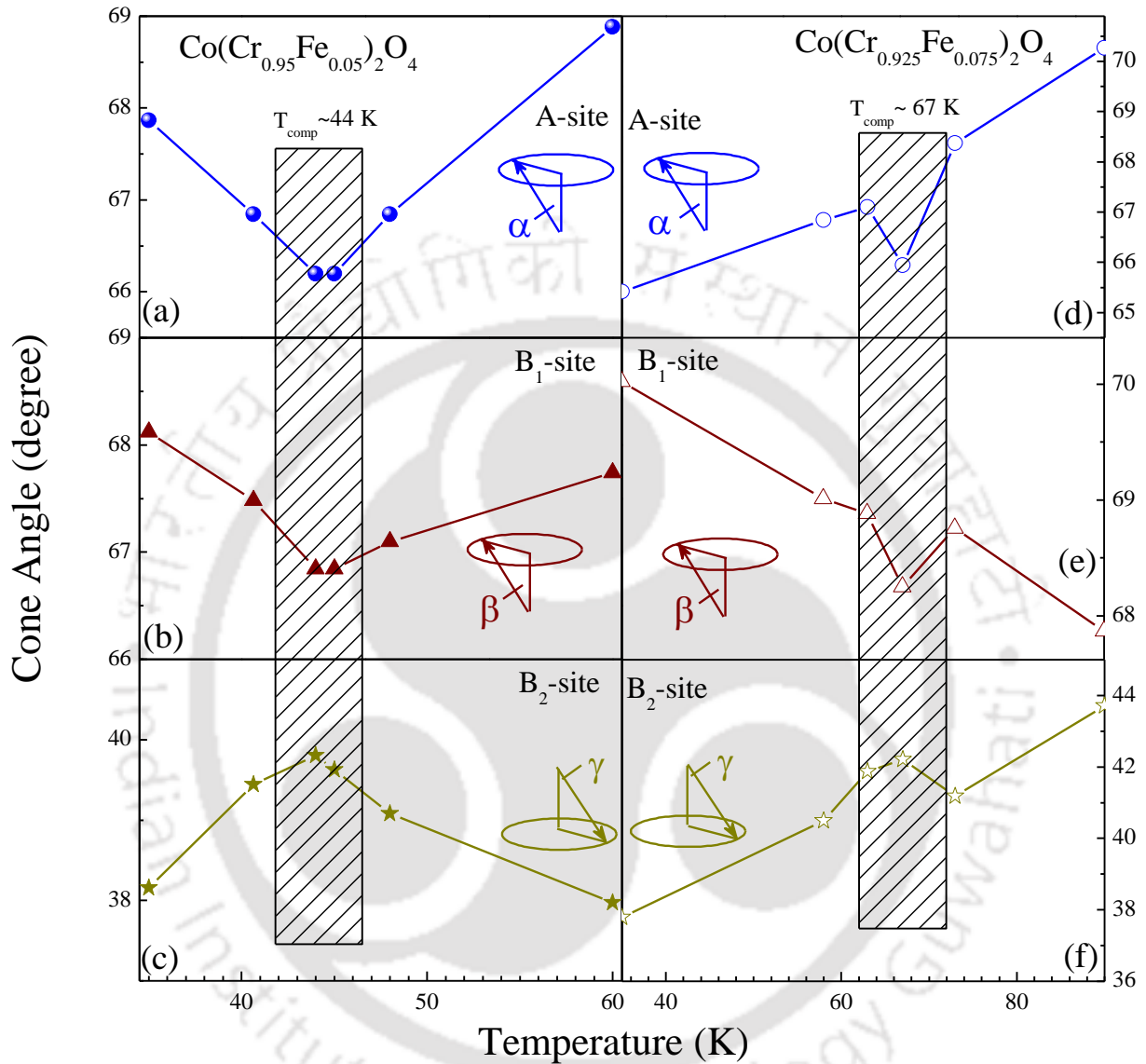


**Figure 3.12** Temperature dependence of cone angles of the different sub-lattices (A,  $B_1$  and  $B_2$ ) of both  $\text{Co}(\text{Cr}_{0.95}\text{Fe}_{0.05})_2\text{O}_4$  (a-c) and  $\text{Co}(\text{Cr}_{0.925}\text{Fe}_{0.075})_2\text{O}_4$  (d-f) samples. Inset shows the ferrimagnetic spin spiral order which points to the  $[001]$  direction similar to that of the  $\text{CoCr}_2\text{O}_4$ .

Six panels of Fig. 3.13 depict the comparison of the temperature dependent spontaneous magnetization obtained from the refinement of the magnetic phase of the ND patterns of  $\text{Co}(\text{Cr}_{0.95}\text{Fe}_{0.05})_2\text{O}_4$  and  $\text{Co}(\text{Cr}_{0.925}\text{Fe}_{0.075})_2\text{O}_4$  samples with that of the bulk magnetization measured experimentally under the applied fields of 0.01 T and 5 T. We can see that, similar to the bulk magnetization, the moments obtained from the ND data also exhibit near zero values at

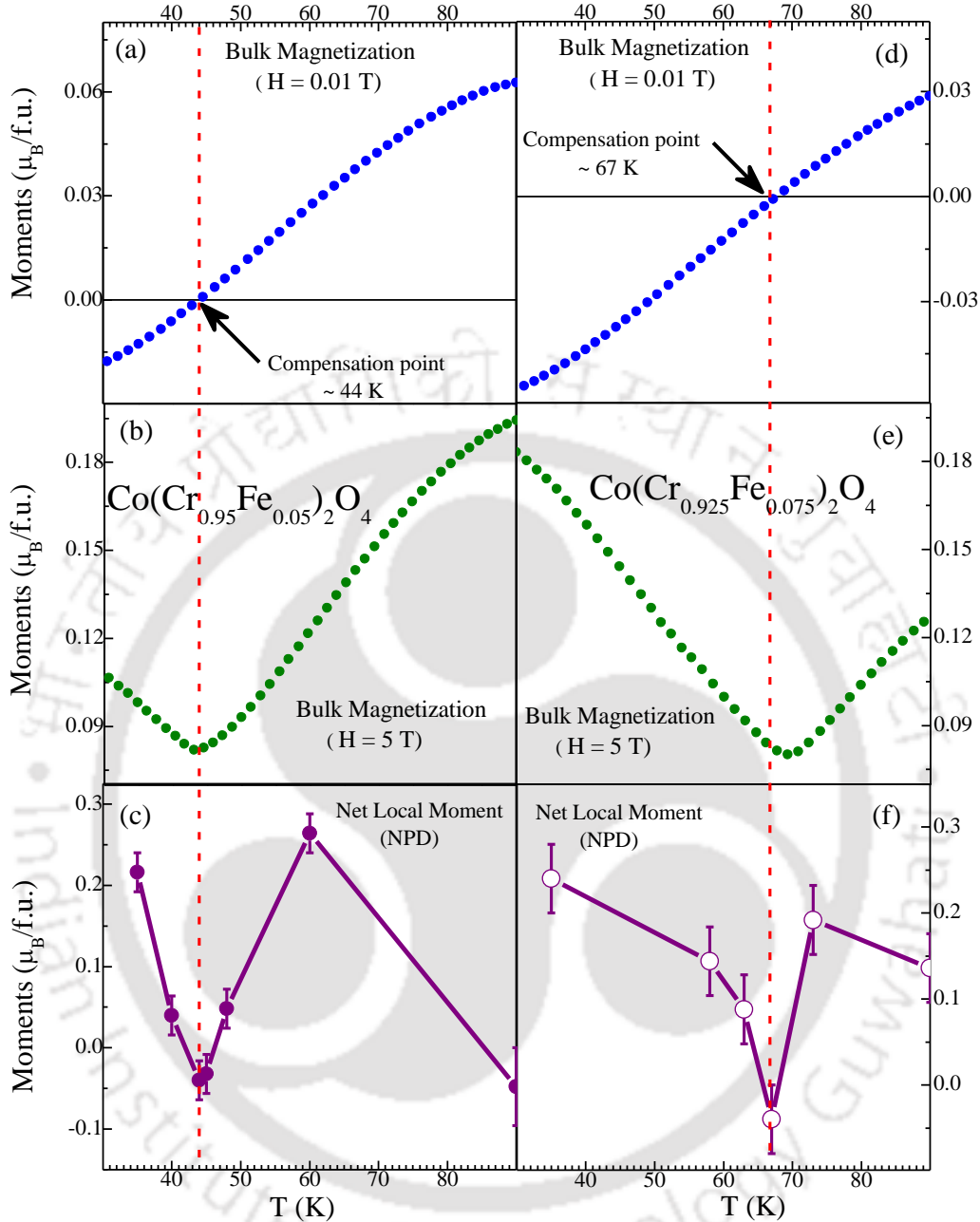


**Figure 3.13** Temperature dependent magnetization  $M(T)$  curves of  $\text{Co}(\text{Cr}_{1-x}\text{Fe}_x)_2\text{O}_4$  ( $x = 0.05$ , left column and  $0.075$ , right column) samples measured under the low field  $0.01$  T [(a) and (d)], high field  $5$  T [(b) and (e)]. (c) and (f) are the net local moments obtained from NPD data.

the compensation points  $T_{\text{comp}} \sim 43.8$  K and  $67.8$  K for  $\text{Co}(\text{Cr}_{0.95}\text{Fe}_{0.05})_2\text{O}_4$  and  $\text{Co}(\text{Cr}_{0.925}\text{Fe}_{0.075})_2\text{O}_4$ , respectively. And remarkably, it can be observed that the behaviour of the spontaneous magnetization across the compensation point is very similar to the bulk magnetization under  $5$  T field. The magnetic moment values obtained from ND experiments are the actual values of the sublattice magnetization (without any external perturbation or excitation,

such as external magnetic field). However, what we observe from the high field magnetization measurement is a rather dynamic experiment, where the external field induces the magnetization in the sample, which is then measured using the magnetometer. The interesting observation we make here is that the net moment observed from ND experiments shows the similar functional form as that observed in magnetization measurements carried out in 5 T field, around the compensation point. From here, it is clear that there is a strong spin-lattice coupling which is influenced by the external field. One more point that is clear from these combined plots is that magnetization obtained from both measurements is of the same order for the compounds. From this plot, it is understood that there are orientations of the moments corresponding to different sublattices, across the compensation point. All these features are not noticed in case of the parent  $\text{CoCr}_2\text{O}_4$  compound.

The left panel of Fig. 3.14 demonstrates the enlarged view of the  $(220)^*$  satellite reflection in the low temperature part from 2.9–20 K. Here, we can see that at 20 K, the peak is symmetrical in nature, but on lowering the temperature to 10 K, it becomes asymmetric, and there is a clear modulation of the peak, which becomes more prominent on further lowering of the temperature down to 2.9 K. The  $Q$ -values of these two modulated satellite peaks at 2.9 K are 1.46 and 1.48  $\text{\AA}^{-1}$ , respectively. At 20 K, the incommensurate propagation vector for the magnetic structure is  $(0.62, 0.62, 0)$  whereas an additional modulation appears with  $Q \sim 1.48 \text{\AA}^{-1}$  around 10 K. However, in contrast to L. J. Chang et al. [18], we find that the  $(220)$  Bragg peak has a substantial contribution from magnetic origins in these compounds. As the temperature is lowered, the magnetic form factor of this  $(220)$  peak increases until 10 K, after which it saturates off. Remarkably, our data on polycrystalline samples trace these features similar to the single crystalline  $\text{CoCr}_2\text{O}_4$ . This transition temperature at 10 K is identical to the lock-in transition temperature observed in the present study of Fe substituted compounds. Furthermore, the increment in the intensity of this IC peak with a decrease in temperature may indicate the unsaturated magnetic configuration in this temperature range, i.e. 2.9–20 K (cf. inset of Fig. 3.8). We have also calculated the correlation length for the  $(220)$  satellite peak at these three temperatures. It is found that the correlation length increases as the temperature is lowered from 20 K to 2.9 K, and becomes maximum ( $\sim 3.4$  nm) at 2.9 K. This correlation length is of the same order as that calculated by Tomiyasu et al. for their pristine single crystal  $\text{CoCr}_2\text{O}_4$  [8]. To

further confirm the feature of the lock-in transition, we performed field cooled cooling (FCC) and field cooled warming (FCW) magnetization as shown in Fig. 3.14 (b). As shown in Fig. 3.14 (c), the enlarged view of magnetization around 10 K shows a clear thermal hysteresis. This hysteresis could be the result of the modulation in the IC spin-spiral phase with  $Q \sim 1.48 \text{ \AA}^{-1}$  around  $T_L$  (10 K).

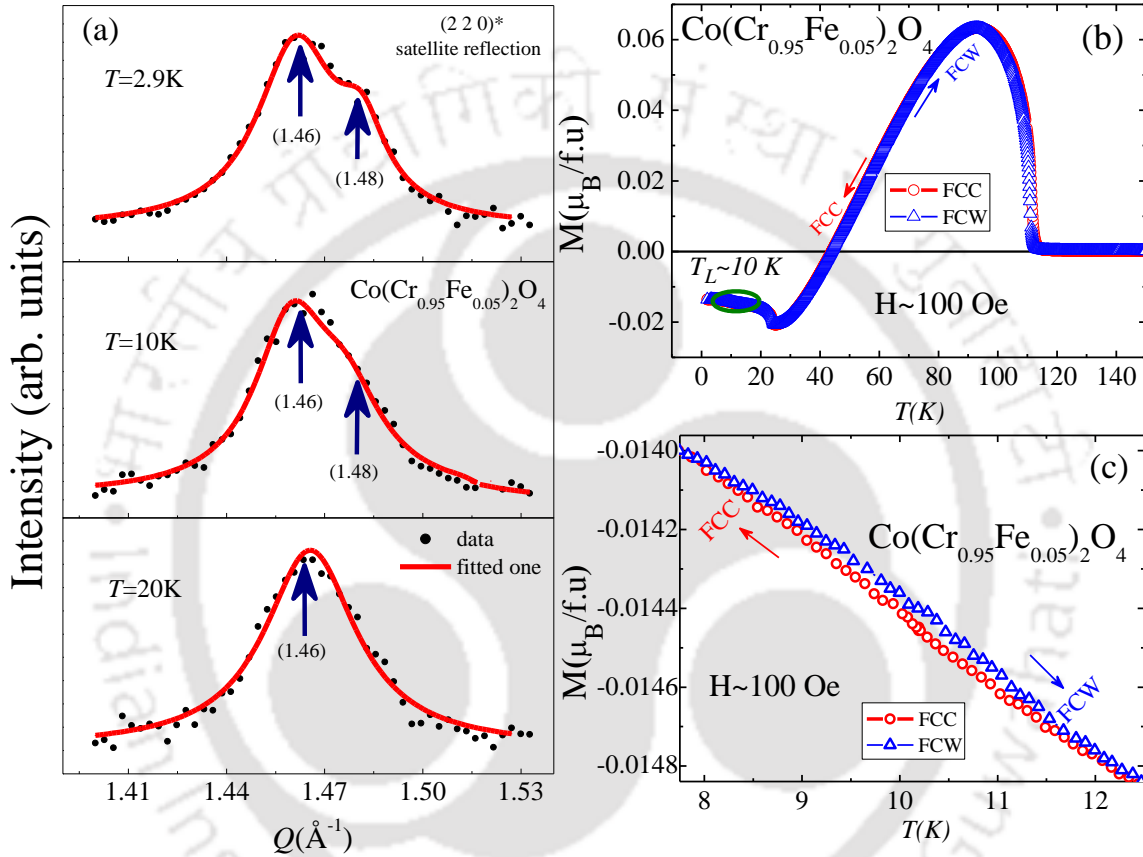


**Figure 3.14** (a) Neutron diffraction spectra showing the modulation of the incommensurate phase for the  $(220)^*$  satellite peak which starts around 10 K. (b) depicts the  $M$ - $T$  data at 100 Oe in the FCC and FCW modes, and (c) shows an enlarged view of the same figure for clear observation of the thermal hysteresis around 10 K.

Thermal variations in the magnetic moments of the A-site (Co) and B-sites (Cr/Fe) as obtained from the NPD data for these compounds are shown in Fig. 3.15. We applied the molecular field model in order to calculate the thermal variations of these magnetic moments. For simplicity, we assumed that these spinel compounds have two sublattices A and B whose spins are anti-parallel to each other with different molecular field constants,  $\lambda_{A-A}$ ,  $\lambda_{A-B}$  and  $\lambda_{B-B}$  representing A-A, A-B and B-B exchanges, respectively. The calculation was done by a self-consistent mean-field calculation method using the Brillouin function  $B_J(x)$  with molecular field

constant ( $\lambda$ ). The values of ‘ $J = S$ ’ used in the function  $B_J(x)$  as given below, are modified to include the substitutional effects, i.e.  $S = 0.95 (3/2) + 0.05 (5/2)$  and  $S = 0.925 (3/2) + 0.075 (5/2)$  for  $\text{Co}(\text{Cr}_{0.95}\text{Fe}_{0.05})_2\text{O}_4$  and  $\text{Co}(\text{Cr}_{0.925}\text{Fe}_{0.075})_2\text{O}_4$ , respectively. Hence, the expressions used for the calculations are [157]:

$$M_A = M_A^{\text{sat}} B_J [g\mu_B S (\lambda_{B-B} M_A - \lambda_{A-B} M_B) / k_B T] \quad (3.1)$$

$$M_B = M_B^{\text{sat}} B_J [g\mu_B S (-\lambda_{A-B} M_A + \lambda_{A-A} M_B) / k_B T] \quad (3.2)$$

Where  $M_A^{\text{sat}}$  and  $M_B^{\text{sat}}$  are the saturated A-site and B-site moments respectively,  $k_B$  is Boltzmann’s constant and  $T$  is the temperature. The best fit of the above formula to the NPD data provides the molecular field constants,  $\lambda_{A-A}$ ,  $\lambda_{A-B}$  and  $\lambda_{B-B}$  which are given in Table 3.4. Furthermore, the Néel transition temperature ( $T_C$ ) and the compensation temperature ( $T_{\text{comp}}$ ) using these molecular field constants,  $\lambda_{A-A}$ ,  $\lambda_{A-B}$  and  $\lambda_{B-B}$  are also shown in the same table. Molecular field calculations are the simplest theoretical model to calculate various magnetization parameters. It has its own limitations in including some corrections when compared to the experiments, such as NPD in the present case. In spite of these, there is good agreement between the parameters obtained from MFC and NPD for these compounds. For both the  $x = 0.05$  and  $x = 0.075$  compounds, there is no change in occupation of the tetrahedral site, as it is parallel only by the Co atoms. Therefore we do not expect different  $\lambda_{A-A}$ , which is also found from our calculation. Here, we have substituted the Fe into the octahedral site and therefore, as the Fe concentration increases in the octahedral site (from  $x = 0.05$  to  $0.075$ ), there is an increment in  $\lambda_{B-B}$ , which suggests that the molecular field between Cr–Fe is stronger than pure Cr–Cr.  $\lambda_{A-B}$  or  $\lambda_{B-A}$  represent the molecular field constants for the A–B interactions, and as the concentration of Fe increases,  $\lambda_{A-B}$  decreases, which suggests that the strength of the Co–Fe molecular field is less than that of the Co–Cr molecular field in the given compounds.

Table 3.4 The calculated molecular field constants,  $\lambda$  from molecular field calculations for both the compounds with  $T_{\text{comp}}$  and  $T_C$  are shown here:

$\text{Co}(\text{Cr}_{1-x}\text{Fe}_x)_2\text{O}_4$	$\lambda_{A-A}$ ( $T/\mu_B$ )	$\lambda_{A-B}$ ( $T/\mu_B$ )	$\lambda_{B-A}$ ( $T/\mu_B$ )	$\lambda_{B-B}$ ( $T/\mu_B$ )	$T_{\text{comp}}^{\text{MFC}}$	$T_{\text{comp}}^{\text{Exp}}$	$T_C^{\text{MFC}}$	$T_C^{\text{MFC}}$
$x = 0.05$	50.07	32.08	33.05	47.65	~93	~44	~130	~110
$x = 0.075$	50.40	29.06	29.10	49.87	~123	~67	~160	~118

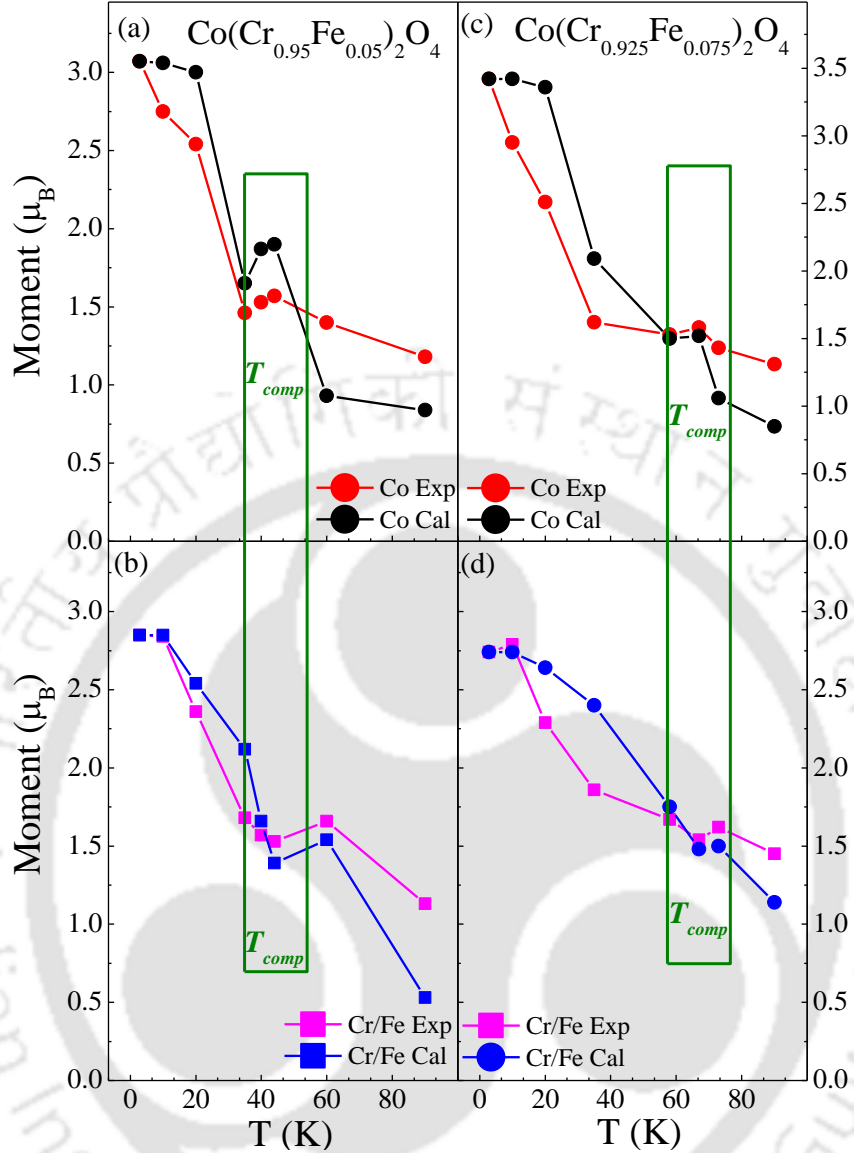


**Figure 3.15** Temperature dependent variation of different site moments from NPD data along with the Brillouin function fit of both  $\text{Co}(\text{Cr}_{0.95}\text{Fe}_{0.05})_2\text{O}_4$  (a,b) and  $\text{Co}(\text{Cr}_{0.925}\text{Fe}_{0.075})_2\text{O}_4$  (c,d).

Further, we have investigated the magnetocaloric properties in the same compound to expose the technological importance. Fig. 3.16 (a) & (c) shows the isothermal magnetization hysteresis (M–H) curve (First quadrant) measured in various temperature ranges of (a) 34–56 K and (c) 102–120 K (with step size of  $T = 2$  K), with an applied field ranges from 1kOe to 90 kOe. We have observed the interesting magnetic transitions as  $T_{\text{comp}}$  (~44 K) and  $T_{\text{C}}$  (~114 K) from bulk dc-magnetization data; therefore these are the respective temperature regions of interest to explore the MCE in  $\text{Co}(\text{Cr}_{0.95}\text{Fe}_{0.05})_2\text{O}_4$ . Hence, we have investigated the MCE behavior in  $\text{Co}(\text{Cr}_{0.90}\text{Fe}_{0.05})_2\text{O}_4$  in the temperature regimes of 34-56 K (around  $T_{\text{comp}}$ ) and in 102 -

120 K (around  $T_C$ ). We have calculated the change in magnetic entropy ( $-\Delta S_M$ ) using isothermal M-H curves [Fig. 3.15 (a) & (c)] across the magnetic transitions. The field sweeping is done from 0 to 90 kOe and again back to 0. During this protocol, the sample was first cooled to 10 K (i.e. below transition temperatures) and then heated back to near its  $T_{comp}$  without overshooting. M-H curve was measured at that temperature, and after the completion of the measurement, the sample was again cooled to 10 K. This time the sample was heated to a temperature 2 K higher than the last measurement temperature without any overshoot, and then, another M-H curve was measured. This method was repeated for all the M-H curves taken within the temperatures between 34 K and 56 K (across the  $T_{comp}$ ) and also between 102 K and 120 K (across the  $T_C$ ).

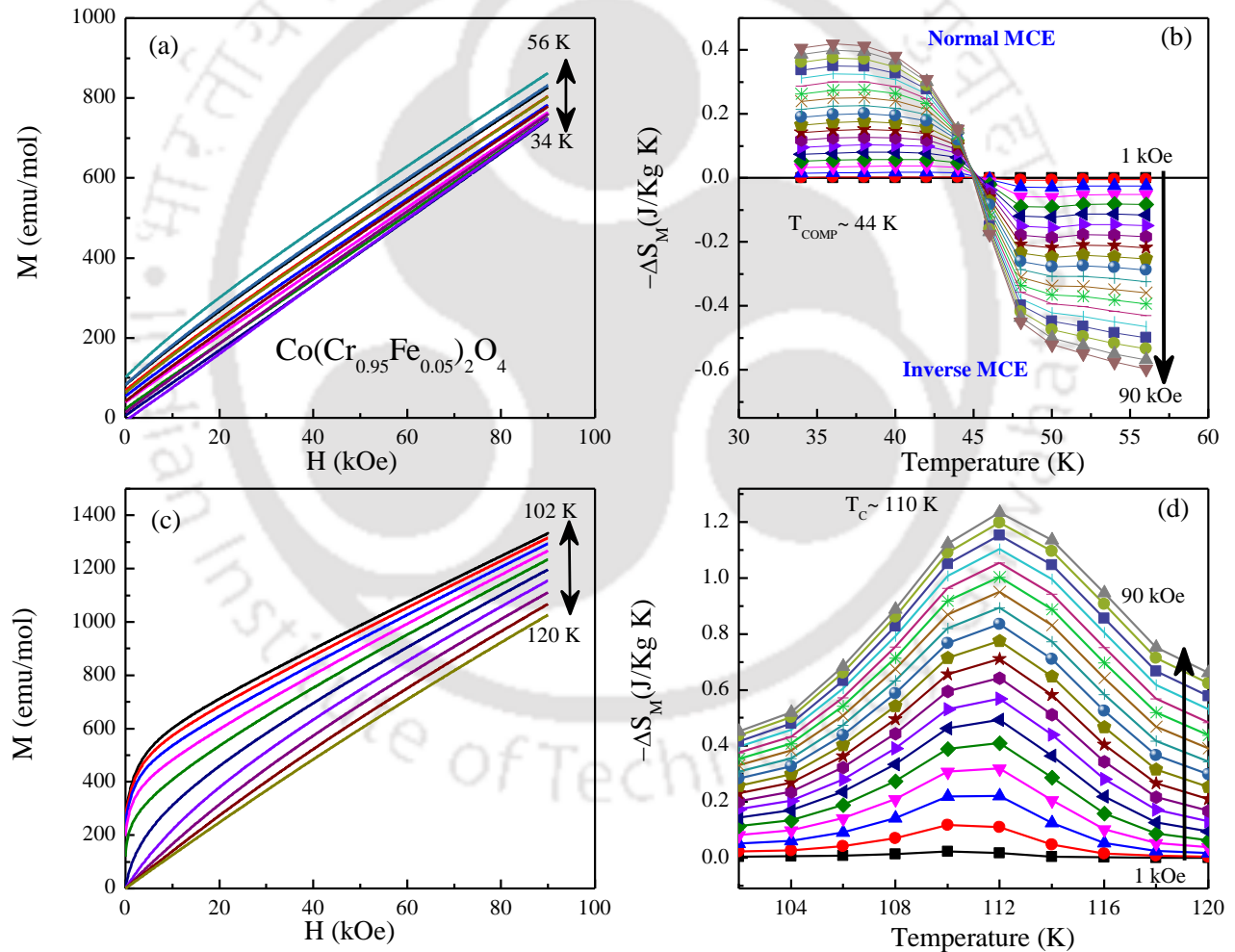


**Figure 3.16** Magnetic field ( $H$ ) dependence of the magnetization ( $M$ ) of  $\text{Co}(\text{Cr}_{0.95}\text{Mn}_{0.05})_2\text{O}_4$  at different temperatures regions, (a) 34-56 K, (c) 102-120 K, (b) calculated temperature-dependent magnetic entropy change ( $-\Delta S_M$ ) around  $T_{comp}$  and (d) around FIM transition temperature  $T_C$  in the various magnetic fields changes (1 kOe–90 kOe).

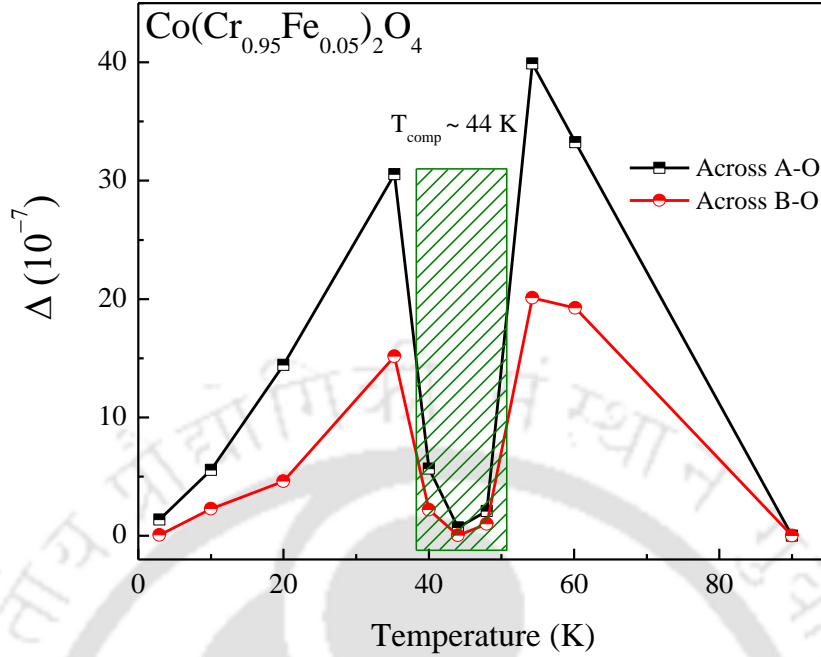


**Figure 3.17** The variation of the distortion ( $\Delta$ ) as a function of temperature along two different paths, i.e. A-O and B-O of  $\text{Co}(\text{Cr}_{0.95}\text{Fe}_{0.05})_2\text{O}_4$ .

Here,  $\Delta S_M$  has been calculated from the isothermal M-H curves using Maxwell's relations [158]:

$$\Delta S_M(T, H) = \int_0^H \left( \frac{\partial M}{\partial T} \right)_H dH \quad (3.3)$$

One of the interesting observations from these plots of  $-\Delta S_M$  for such compound is that there is a sign change in  $-\Delta S_M$  exactly at compensation temperature. Along with earlier discussed magneto-elastic coupling, Fig. 3.17 represents such signatures around  $T_{\text{comp}}$  by calculating the distortion ( $\Delta$ ) in bond parameters where  $\Delta = \left[ \frac{d_T - d_{90}}{d_{90}} \right]^2$ , where  $d_T$  and  $d_{90}$  are the bond lengths at different temperature  $T$  and at 90 K, respectively. Here, we have shown the consequence of the magnetic compensation on the magnetocaloric properties of  $\text{Co}(\text{Cr}_{0.95}\text{Fe}_{0.05})_2\text{O}_4$  compound. A maximum value of  $-\Delta S_M$  observed is  $1.2 \text{ J kg}^{-1} \text{ K}^{-1}$  along with relative cooling power (RCP) of  $13 \text{ J kg}^{-1}$  which is analogous to the other oxide compounds [158–160]. Such finding of sign change across  $T_{\text{comp}}$  in  $-\Delta S_M$  is very attractive as it opens a new opportunity in magnetic materials where both normal as well as inverse MCE effect persists in a single phase compound.

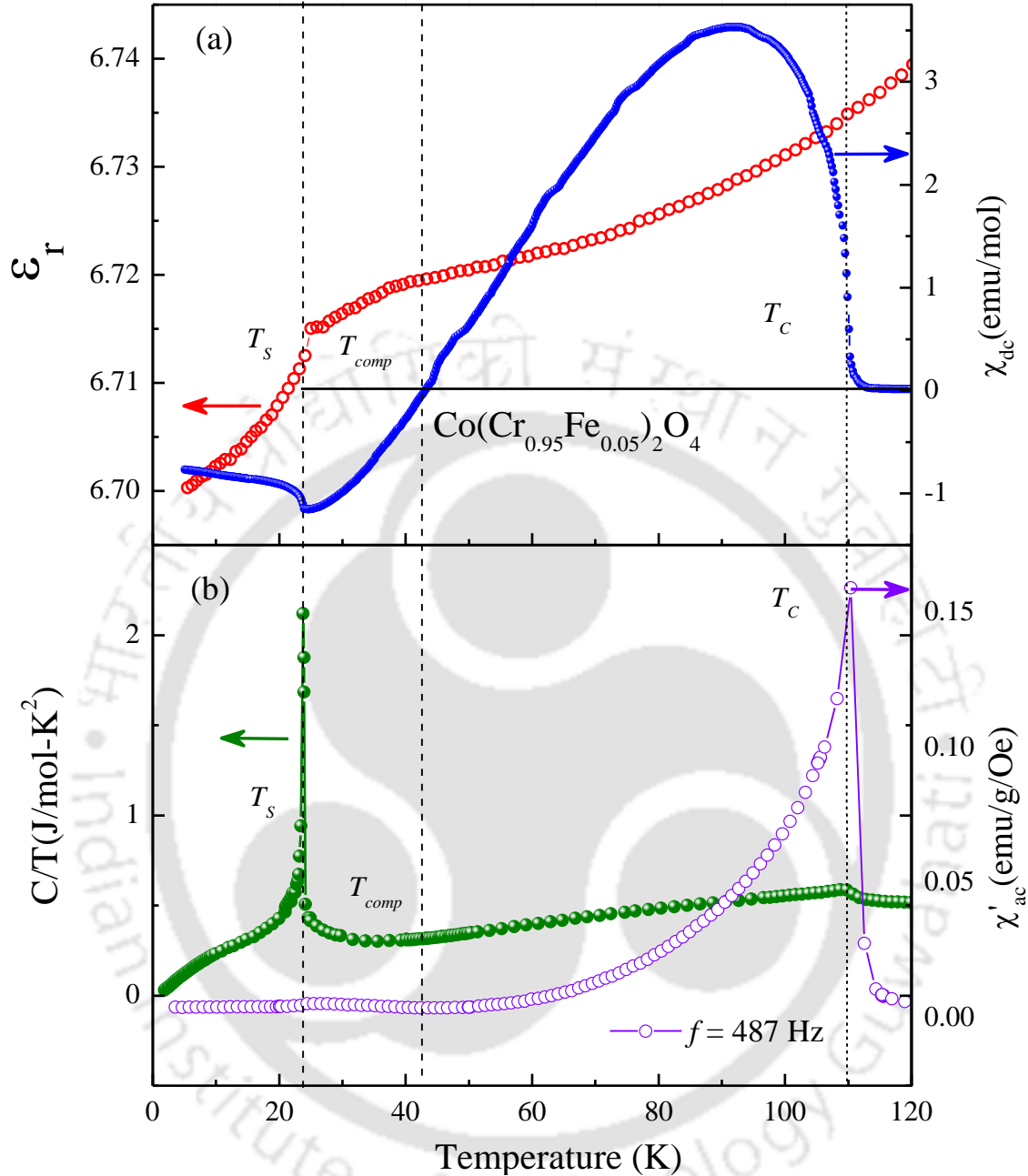


**Figure 3.18** Temperature dependence of (a) dielectric constant at 100 kHz (left y-axis), dc-magnetic susceptibility (right y-axis), (b) specific heat divided by temperature ( $C/T$ ) (left y-axis) and ac-magnetic susceptibility (right y-axis) with  $f = 487$  Hz of  $\text{Co}(\text{Cr}_{0.95}\text{Fe}_{0.05})_2\text{O}_4$ .

### 3.3.5 Dielectric/magneto-dielectric and Pyroelectric Properties

Fig. 3.18 presents the results of dc-susceptibility ( $\chi_{dc}$ ) and dielectric permittivity ( $\epsilon_r$ ) [cf. Fig. 3.18 (a)]; ac-susceptibility ( $\chi_{ac}$ ) and specific heat ( $C_p$ ) [cf. Fig. 3.18 (b)] to depict the correlation between the features of magnetic ordering and dielectric permittivity in

Co(Cr<sub>0.95</sub>Fe<sub>0.05</sub>)<sub>2</sub>O<sub>4</sub>. The dc-susceptibility was obtained in the FC mode under the applied field of 100 Oe. It clearly reveals the collinear FIM transition at  $T_C \sim 110$  K followed by another peak at 24 K which is related to the magnetostructural transition ( $T_S$ ) [161]. We further observed that magnetization changes sign at the compensation temperature,  $T_{\text{comp}} \sim 44$  K. The anomaly at 24 K corresponds to a non-collinear spiral magnetic transition similar to the parent compound CoCr<sub>2</sub>O<sub>4</sub>, as revealed by the neutron diffraction measurements [8,33,161]. It is interesting to note that dc changes its sign across  $T_{\text{comp}}$  which was not observed in pristine compound CoCr<sub>2</sub>O<sub>4</sub>. The above magnetic transitions ( $T_C$ ,  $T_{\text{comp}}$  and  $T_S$ ) are corroborated from  $\chi_{\text{ac}}$  measurements. The temperature dependence of  $\epsilon_r$  measured at  $f = 100$  kHz during the warm-up mode is depicted in Fig. 3.18 (a). The anomaly at  $T \sim 24$  K is related to the transformation of a collinear spin configuration to another incommensurate spin spiral configuration. A clear change in the slope of  $\epsilon_r$  is observed at  $T_{\text{comp}}$ . However, there is no visible sharp change in the  $\epsilon_r(T)$  curve at  $T_C \sim 110$  K. The specific heat data without any applied magnetic field shows a sharp and large transition, reminiscent of first order nature at  $T \sim 24$  K which corresponds to the magneto-structural transition ( $T_S$ ) observed in  $\chi_{\text{dc}}$ . Such  $\lambda$ -shape transition observed at  $T_C \sim 110$  K in  $C_P$  data corresponds to the FIM ordering in the sample. In the parent compound CoCr<sub>2</sub>O<sub>4</sub>, it is generally accepted that the ferroelectric (FE) ordering is compatible with the spiral ordering at  $T_S$ .

The present section deals with the dielectric behavior of the studied compounds. The highly insulating nature of these compounds fulfills the essential requirement to address the changes in dielectric constant ( $\epsilon_r$ ) to its intrinsic properties. Fig. 3.19 (a) shows the temperature dependent complex dielectric permittivity ( $\epsilon_r$ ) with different frequencies (5 kHz–100 kHz) of Co(Cr<sub>0.95</sub>Fe<sub>0.05</sub>)<sub>2</sub>O<sub>4</sub>. Moreover, the value of  $\tan\delta$  (loss) is also very small consistently in the temperature range (8–300 K) as shown in the Fig. 3.18 (b), which confirms the virtuous quality of the sample. We observe no visible sharp change both in  $\epsilon_r$  and in  $\tan\delta$  around  $T_C$  ( $\sim 110$  K). However, a feeble and gradual increase in the value of  $\epsilon_r$ , is observed after  $T_C$ . With further lowering in temperature, a broad hump is observed around  $T_{\text{comp}}$  followed by a very sharp change in  $\epsilon_r$  at  $T_S$  ( $\sim 24$  K). After 150 K, we observe a continuous increase in dielectric constant. Such observation is attributed to the increase in electrical conduction in the system, rather than a global ferroelectric transition.

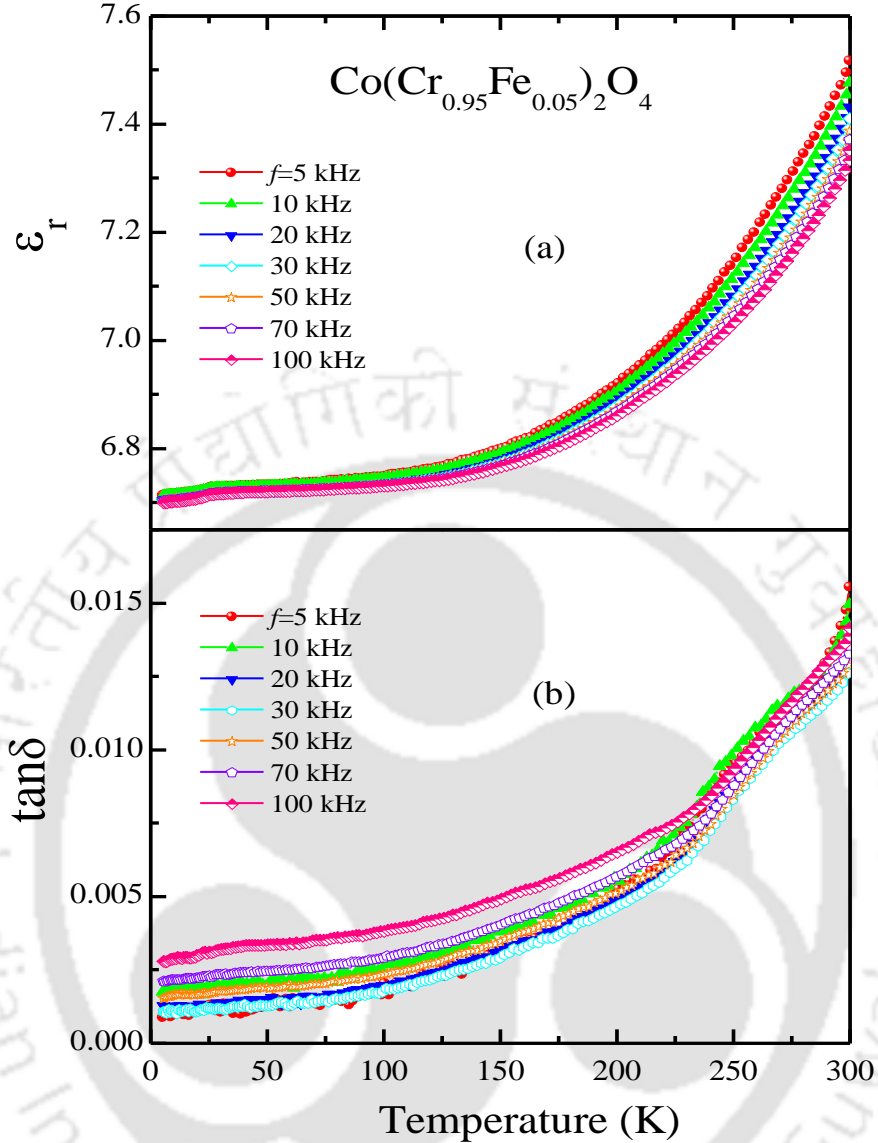


**Figure 3.19** (a) and (b) show temperature dependence of dielectric permittivity ( $\epsilon_r$ ) and  $\tan\delta$  (loss) measured at the different frequencies (5kHz-100kHz) respectively for  $\text{Co}(\text{Cr}_{0.95}\text{Fe}_{0.05})_2\text{O}_4$ .

Fig. 3.20 (a) depicts the frequency dependence of dielectric constant at low temperature. We do not observe noticeable change at  $T_S$  even when the frequency changes by a factor of 20, which rules out any type of electrical glassiness associated with this transition. In addition, it is worth mentioning that there is no frequency dependence of the broad hump around  $T = 40$  K. Fig. 3.20 (b) is the plot of the differences of dielectric constant ( $\epsilon_f$ ) at two extreme frequencies (5 kHz and 100 kHz) as a function of temperature. We observe two clear dips in dielectric constant at  $T = 10$  K and  $T = 40$  K along with a sharp peak at  $T_S$ . The dip at 10 K can be correlated with the lock-in transition ( $T_L$ ) reported in the literature [161]. Furthermore, the dip around  $T_{\text{comp}}$  is

reflected very clearly in  $\epsilon_f$  vs T plot. Although the spin-current model provides a mechanism of correlating electric dipole dynamics with that of the magnetic spin dynamics but further investigations are needed for complete understanding of such dynamical magnetoelectrical phenomena.

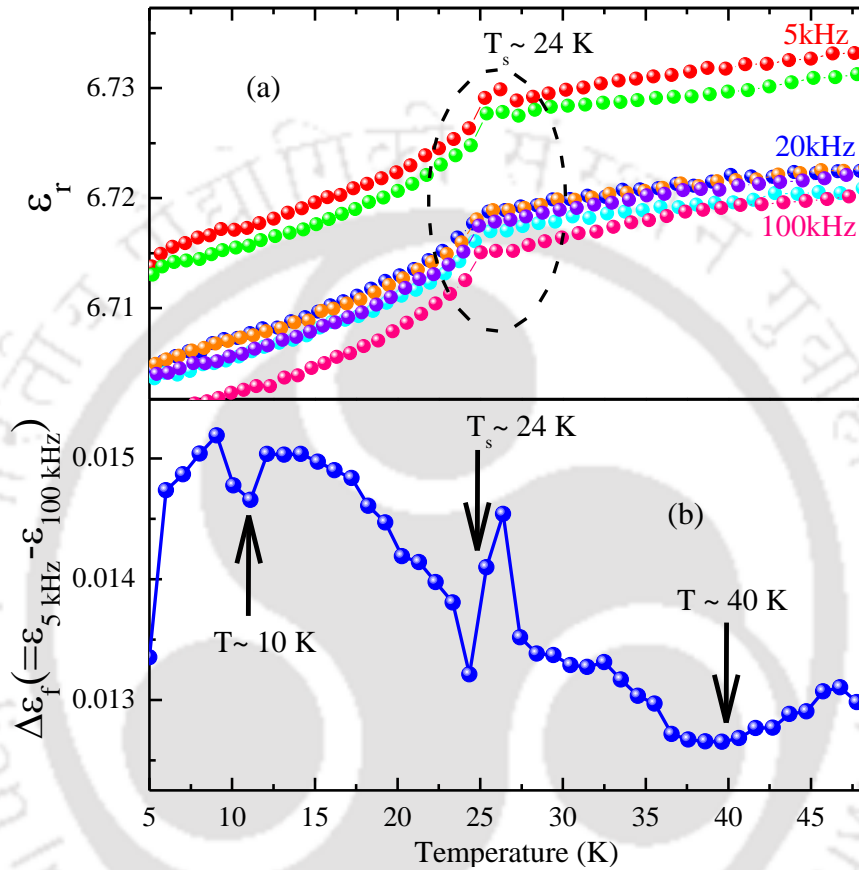


**Figure 3.20** (a) depicts the enlarged view of temperature dependent dielectric permittivity ( $\epsilon_r$ ) at different frequencies (5kHz-100kHz) of  $\text{Co}(\text{Cr}_{0.95}\text{Fe}_{0.05})_2\text{O}_4$ , and (b) shows the plot of the differences of dielectric constant ( $\Delta\epsilon_f$ ) at two extreme frequencies (5 kHz and 100 kHz) as a function of temperature in the same temperature range.

In order to address the magnetodielectric (MD) behavior across the magnetic transitions (especially across  $T_{\text{comp}}$ ),  $\Delta\epsilon_H$  or  $\Delta\epsilon_T$  was measured with 100 kHz frequency as a function of magnetic field (H) at different temperatures for both  $\text{Co}(\text{Cr}_{0.95}\text{Fe}_{0.05})_2\text{O}_4$  and  $\text{Co}(\text{Cr}_{0.925}\text{Fe}_{0.075})_2\text{O}_4$ . These results are shown in Fig. 3.21 in the form of MD effect or  $\Delta\epsilon_r$  vs H, where the magnitude of MD effect in the present case is analogous with the reported value for other magnetoelectric materials in literature [133,139]. The above observed results clearly reveal that there are qualitative changes in the MD behavior at different temperatures. In particular,

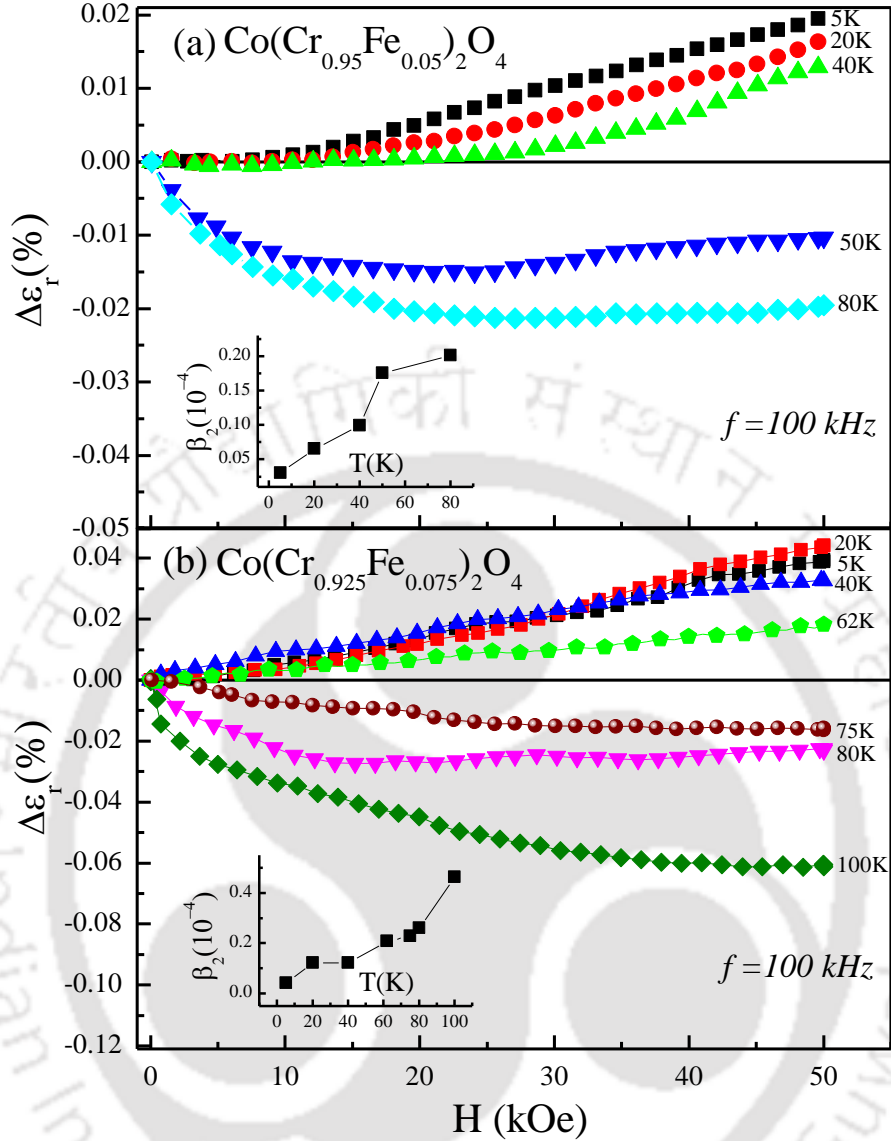


**Figure 3.21** Magnetic field dependent isothermal magnetodielectric data MD i.e.  $\Delta\epsilon_H = [(\epsilon_H - \epsilon_{H=0})/\epsilon_{H=0}]$  measured at different temperatures with 100 kHz frequency of (a)  $\text{Co}(\text{Cr}_{0.95}\text{Fe}_{0.05})_2\text{O}_4$ , and (b)  $\text{Co}(\text{Cr}_{0.925}\text{Fe}_{0.075})_2\text{O}_4$ ; respective insets show the coefficient of quadratic term ( $\beta_2$ ) as a function of temperature. (For more details about fitting, see the text.)

there is a sign change of MD effect for different temperature regions, like  $T < T_{\text{comp}}$  and  $T > T_{\text{comp}}$ . From literature, we found that such observed MD vs  $H$  behavior suggests the presence of a higher-order ME coupling effect in these systems (mostly quadratic at higher  $H$ ). The sign of MD depends on the temperature and magnetic field and can be explained by using the simple phenomenological model given by Katsufuji et al. [162]. Further, we have fitted the MD results by using the combination of linear and quadratic terms of  $H$ , i.e.  $\text{MD} \sim (\beta_1 H + \beta_2 H^2)$ . The coefficient of fitting parameter of the quadratic term ( $\beta_2$ ) is found to increase with the increase in

temperature for both the samples as shown in the insets of Fig. 3.21 (a) and (b). This is in contrast with the result obtained in other oxides where, there was a distinct change in sign of  $\beta_2$  across various magnetic ordering regimes [133,163]. It is possibly due to the different MD coupling in the unlike magnetic regimes (AFM and FM). However, in our compounds the magnetodielectric coupling does not change substantially as entire region has FIM correlation below  $T_C$ . This perfectly explains the positive value of  $\beta_2$  throughout the temperature domain. Hence, the sign change of MD and  $\beta_2$  arises from different underline physics in these compounds which will be discussed later.

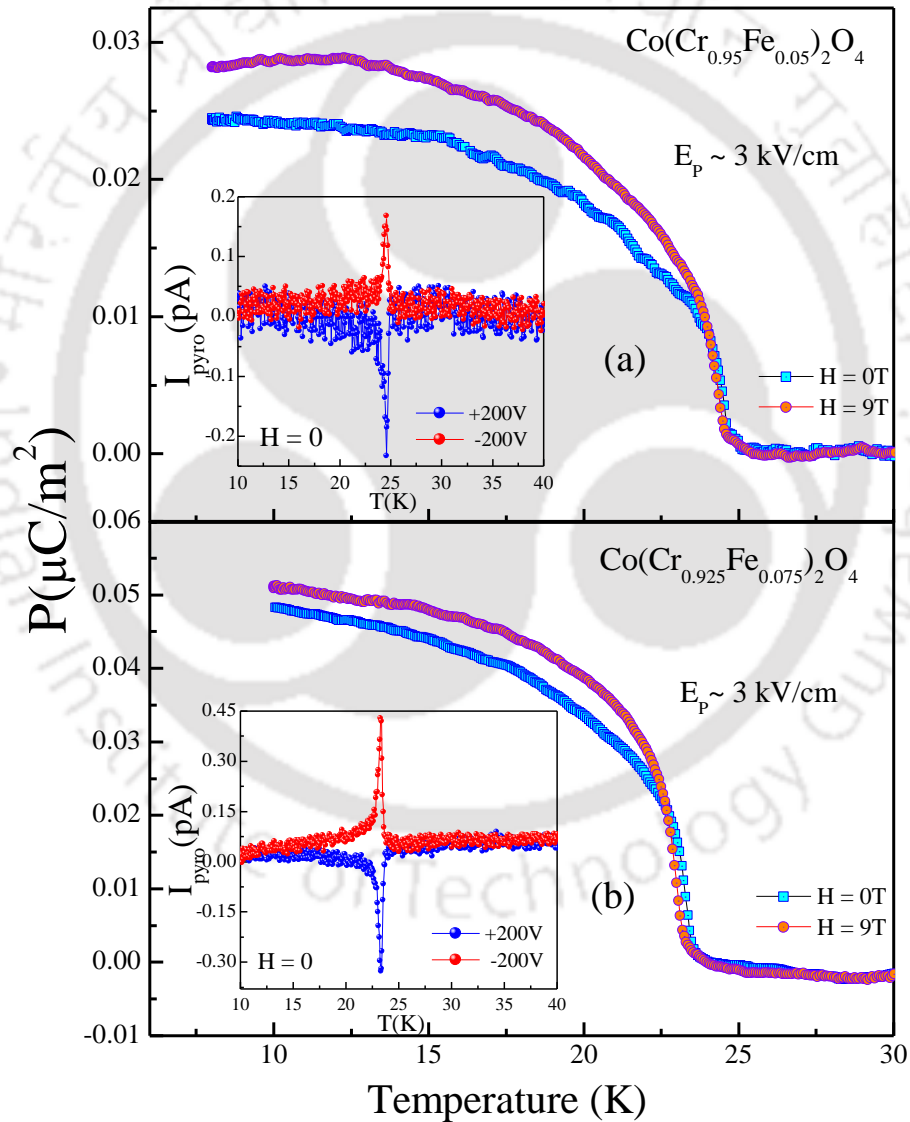


**Figure 3.22** Temperature dependence of electric polarization ( $P$ ) obtained from pyroelectric current measurements for  $\text{Co}(\text{Cr}_{0.95}\text{Fe}_{0.05})_2\text{O}_4$  (a) and  $\text{Co}(\text{Cr}_{0.925}\text{Fe}_{0.075})_2\text{O}_4$  (b). The insets show the corresponding temperature dependent pyroelectric current data, which is measured with an applied voltage of 200 V in the absence of external magnetic field.

Further, we have carried out Pyroelectric current measurements for the study of electric Polarization (P) behavior which clearly address ME coupling in these compounds. Main panels of Fig. 3.22 depict the results of these pyroelectric measurements i.e. temperature dependence of polarization for both  $\text{Co}(\text{Cr}_{0.95}\text{Fe}_{0.05})_2\text{O}_4$  (a) and  $\text{Co}(\text{Cr}_{0.925}\text{Fe}_{0.075})_2\text{O}_4$  (b) compounds. The pyroelectric current is also shown in the insets of respective plots. The pyroelectric current exhibits a sharp peak at respective  $T_S$  of these samples for both polarity of applied electric field ( $E \sim 3 \text{ kV/cm}$ ). This sharpness of the pyroelectric peak attributes to the first order nature of the transition which collaborates with the specific heat data. The strategic finding of this experiment is that the electric polarization sets just below  $T_S$  of respective compounds. Electric P changes slowly with increasing temperature and decreases sharply at  $T_S$ , following which it becomes temperature independent at above  $T_S$ . The sign of P is changed by reversing the poling electric field which is very clear from the pyroelectric current plots. It has also been observed that value of P increases about 12% (in case of 5% Fe substitution) with the application of external magnetic field ( $H = 9 \text{ T}$ ) at the lowest temperature, which proves the existence of ME coupling in these compounds. Such ME coupling is also observed in other compounds [162,164,165]. All these results prove that these compounds have polar behavior which can be tuned with the application of external magnetic field. It will be worthwhile to recollect the point that the transition at  $T_S$  is associated with the transformation of conical spiral magnetic ordering to an incommensurate spin-spiral ordering. It is surprising that only when the spin-spiral wave vector is incommensurate, a noticeable magnitude of polarization or ferroelectricity is generated. The present studied systems are type-II multiferroic, where the ferroelectricity is the by-product of change (improper ferroelectric) in the magnetic structure [100].

The above dielectric and pyroelectric results indicate that there is a strong coupling between the magnetic moments and electric dipoles in both  $\text{Co}(\text{Cr}_{0.95}\text{Fe}_{0.05})_2\text{O}_4$  and  $\text{Co}(\text{Cr}_{0.925}\text{Fe}_{0.075})_2\text{O}_4$  compounds. In addition to it, the MD results indicate that the strong coupling in magnetic moments with that of the electric dipoles exists within the collinear FIM region. This is illustrated by the change in sign of MD effect in the vicinity of the compensation temperature. The MD effect is positive below  $T_{\text{comp}}$  and negative above  $T_{\text{comp}}$ . From neutron diffraction experiments, it has been observed that there is a change in spin configuration around compensation point [161,166] which could be seen by the change in cone angles (that is, spin canting) of the spins of all different sub-lattices of the spinel structure. From the above results,

one can argue out that the explanation about the sign change of MD effect has to be strongly coupled to the change in spin configuration around  $T_{\text{comp}}$ .

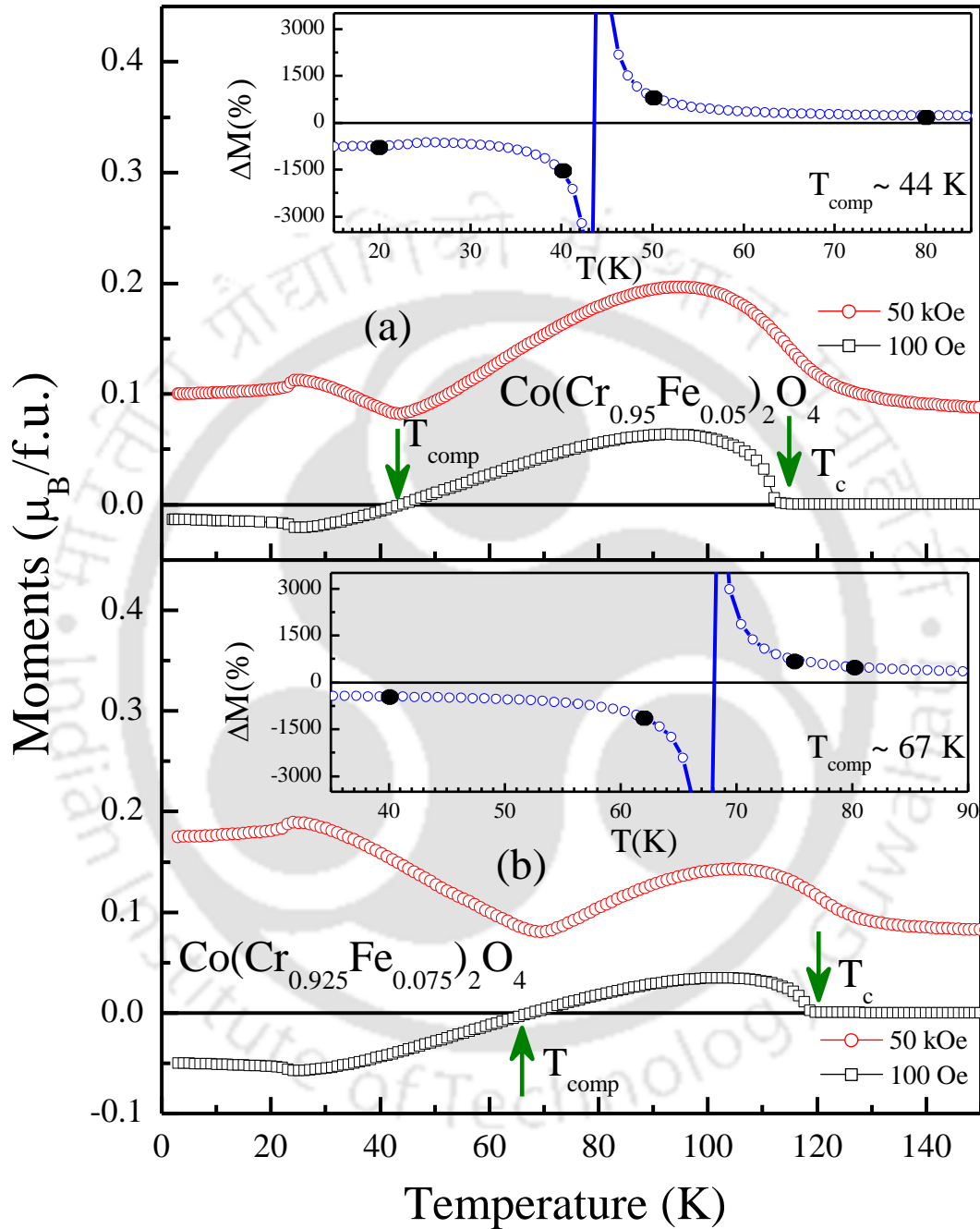


**Figure 3.23** Temperature dependent magnetization of (a)  $\text{Co}(\text{Cr}_{0.95}\text{Fe}_{0.05})_2\text{O}_4$  and (b)  $\text{Co}(\text{Cr}_{0.925}\text{Fe}_{0.075})_2\text{O}_4$  samples in FC mode with two different applied magnetic fields, i.e. 100 Oe and 50 kOe. Insets of both (a) and (b) show the sign change of  $\Delta M [= (M_{H=50\text{kOe}} - M_{H=100\text{Oe}}) / M_{H=100\text{Oe}}]$  around compensation temperature for  $\text{Co}(\text{Cr}_{0.95}\text{Fe}_{0.05})_2\text{O}_4$  and  $\text{Co}(\text{Cr}_{0.925}\text{Fe}_{0.075})_2\text{O}_4$ , respectively. Black circles in insets represent the respective temperatures where MD effect is shown.

Main panels (a) and (b) of Fig. 3.23 depict the temperature dependent FC magnetization data in the presence of low magnetic field (100 Oe) and high magnetic field (50 kOe) for both the compounds  $\text{Co}(\text{Cr}_{0.95}\text{Fe}_{0.05})_2\text{O}_4$  and  $\text{Co}(\text{Cr}_{0.925}\text{Fe}_{0.075})_2\text{O}_4$ , respectively. We observe a compensation temperature in case of 100 Oe field whereas there is a strong dip exactly at  $T_{\text{comp}}$  for 50 kOe field. This change in magnetization data is associated with the re-orientations of a part of the spin moment with that of the crystal lattice. NPD results have already revealed a non-monotonic variation in the cone angles of the spins of Co and (Cr/Fe) across  $T_{\text{comp}}$  [166]. Further, insets of Fig. 3.23 (a) and (b) show that change in magnetization i.e.  $\Delta M [= (M_{H=50\text{kOe}} - M_{H=100\text{Oe}})/M_{H=100\text{Oe}}]$  for both the samples. The sign change in  $\Delta M$  across  $T_{\text{comp}}$  reflects an intrinsic readjustment of the spin configuration as demonstrated by neutron experiments. As anticipated earlier, the mechanism which is responsible for sign change of MD effect is the identical one which is responsible for the sign change in  $\Delta M$ .

For quantitative explanation of sign change of MD effect and  $\Delta M$  in  $\text{Co}(\text{Cr}_{0.95}\text{Fe}_{0.05})_2\text{O}_4$  and  $\text{Co}(\text{Cr}_{0.925}\text{Fe}_{0.075})_2\text{O}_4$  around compensation temperature in collinear FIM region, we resort to the phenomenological model of Landau to deduce the expression for the magnetodielectric permittivity. After assuming the fact that magnetic moment and electric polarization are coupled in such realistic non-collinear magnets, the total free energy for such systems can be written in the following form [167],

$$F(M, P) = aM^2 + bM^4 - MH + cP^2 + dP^4 - PE + eM^2P^2 \quad (3.4)$$

Where  $M$ ,  $P$ ,  $H$  and  $E$  are magnetization, polarization, magnetic field and electric fields, respectively and  $a$ ,  $b$ ,  $c$ ,  $d$  and  $e$  are temperature dependent coefficients. From equation (3.4), one can deduce the dielectric permittivity by performing second-order derivative of total free energy with respect to polarization  $P$ , i.e.  $1/\epsilon = \partial^2 F / \partial P^2$ . Because  $P$  is very small, we are neglecting the higher order terms in  $P$  i.e.  $P^4$  and finally has the mathematical expression for magnetodielectric permittivity in the following form:

$$1/\epsilon = 2c + eM^2 \quad (3.5)$$

From equation (3.5), it is clearly seen that magnetodielectric permittivity ( $\epsilon_H$ ) is inversely related to square of magnetization ( $M^2$ ). According to this equation, if  $M(H)$  increases with the application of the external magnetic field relative to the magnetization at zero field

M ( $H \sim 0$ ) i.e.  $M(H)/M(0) > 1$  (i.e.  $[\Delta M = (M(H) - M(0))/M(0)]$  is positive) then from above equation, we can infer that  $\varepsilon(H)/\varepsilon(0) < 1$  (i.e.  $[\varepsilon(H) - \varepsilon(0)]$  is negative). On the other hand, if the value of  $M(H)/M(0) < 1$  (i.e.  $[\Delta M = (M(H) - M(0))/M(0)]$  is negative) then it results  $\varepsilon(H)/\varepsilon(0) > 1$  (i.e.  $[\varepsilon(H) - \varepsilon(0)]$  is positive). The insets of the Fig. 3.23 claim a sign change in  $\Delta M$  across the  $T_{comp}$ . This can be explained in another way, by differentiating equation (2), where one has the relation,  $-\Delta\varepsilon/\varepsilon^2 = 4eM \times \Delta M$ , which is nothing but  $-\Delta\varepsilon \propto M \times \Delta M$ . This relation demands that MD behavior should also change sign across  $T_{comp}$  if there is sign change in the quantity  $(M \Delta M)$ , which is in agreement with the results obtained in our experiment (*cf.* Fig. 3.21).

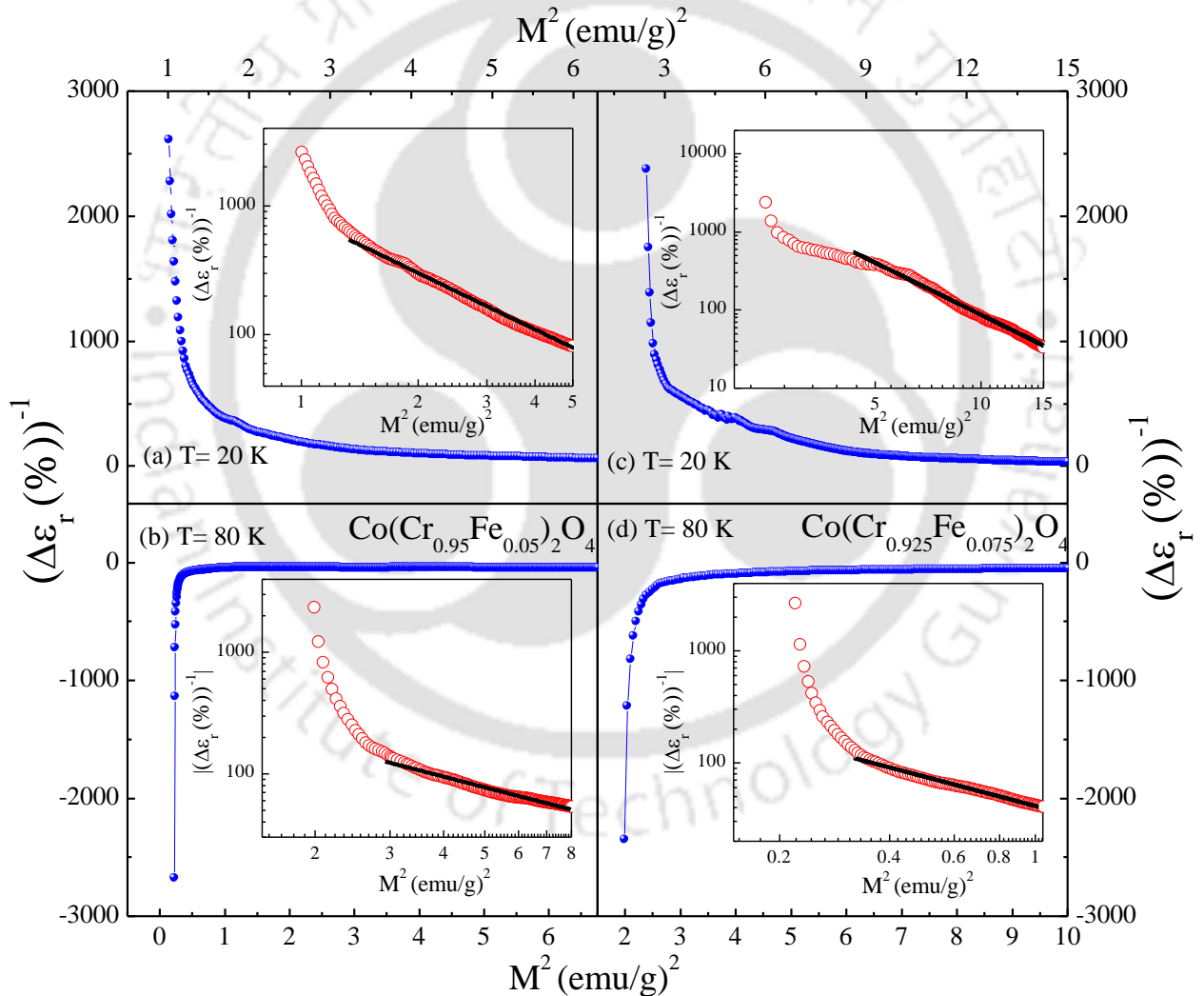


**Figure 3.24** Plots of Inverse  $\Delta\varepsilon_r$  with the square of magnetization ( $M^2$ ) of  $\text{Co}(\text{Cr}_{0.95}\text{Fe}_{0.05})_2\text{O}_4$  (a, b) and  $\text{Co}(\text{Cr}_{0.925}\text{Fe}_{0.075})_2\text{O}_4$  (c, d) at 20 K and 80 K, respectively. Respective insets show the linear variation with the square of magnetization in log scale measured at 20 K ( $T < T_{comp}$ ) and 80 K ( $T > T_{comp}$ ).

Table 3.5 Parameter ( $\gamma$ ) extracted from the fits in Fig. 3.24 by using eq. (3.6) for both  $\text{Co}(\text{Cr}_{0.95}\text{Fe}_{0.05})_2\text{O}_4$  and  $\text{Co}(\text{Cr}_{0.925}\text{Fe}_{0.075})_2\text{O}_4$  compounds at different temperatures are given as:

$\text{Co}(\text{Cr}_{0.95}\text{Fe}_{0.05})_2\text{O}_4$		$\text{Co}(\text{Cr}_{0.925}\text{Fe}_{0.075})_2\text{O}_4$	
T(K)	Slope ( $\gamma$ )	T(K)	Slope( $\gamma$ )
20	1.46	20	1.54
40	1.61	40	1.14
50	0.91	80	0.86
80	0.81	100	0.94

For our polycrystalline samples, the magnetic domains are randomly oriented in zero applied fields, resulting in a zero average magnetization. Thus  $\varepsilon(0)$  is a constant value. Hence changes in the value of MD effect, i.e.  $\Delta\varepsilon_H \left[ = \frac{\varepsilon_H - \varepsilon_{H=0}}{\varepsilon_{H=0}} \right]$  arise only from the changes of the value of  $\varepsilon(H)$ . So equation (3.4) can be retold as the value of MD effect is a decreasing function of  $M^2$ . To examine the effect of ME coupling from Landau phenomenological theory, the MD effect and the magnetization data are reported in the form of  $1/\Delta\varepsilon_H$  vs  $M^2$  in Fig. 3.24. The temperatures 20 K and 80 K are so chosen that one is below  $T_{\text{comp}}$  and other is above  $T_{\text{comp}}$  respectively, in both the samples. As required from above model, we observed that the sign of  $1/\Delta\varepsilon_H$  is different at two different temperatures. The  $M^2$  dependence of the MD value can be re-expressed in the form of the scaling function given as,

$$\log|1/\Delta\varepsilon_H| = \alpha + \gamma \log M^2 \quad (3.6)$$

This equation fits well to the data as shown in the insets of the Fig. 3.24. The Value of slope ( $\gamma$ ) hovers around 1 [see table. 3.5] which is consistent with the mean-field phenomenological theory. These results lead to the conclusion that the ME effect is attributed to the coupling term  $P^2M^2$  in the thermo-dynamical potential of the model.

### 3.4 Summary

In conclusion for this chapter, we have investigated the detailed structural and magnetic and dielectric/magnetodielectric and ferroelectric properties of Fe substituted magnetically compensated compounds of  $\text{CoCr}_2\text{O}_4$ , i.e.  $\text{Co}(\text{Cr}_{1-x}\text{Fe}_x)_2\text{O}_4$  ( $x = 0.05, 0.075$ ). These studied samples were synthesized in polycrystalline form by standard solid state reaction method. Magnetic properties have been studied in great details through dc and ac-magnetization

measurements. There is an increase in the FIM transition with Fe substitution. It has been observed that minimal Fe substitution gives rise to all the fascinating properties of negative magnetization and sign change of EB across respective  $T_{\text{comp}}$ . Further, detailed temperature and field dependent dielectric and pyroelectric properties show the signature of multiferrocity which includes the sign change in magneto-dielectric (MD) behavior across respective  $T_{\text{comp}}$ , for the first time in such multiferroic compounds. Temperature dependent NPD experiments were performed for understanding of the real microscopic origin of these emerging properties such as negative magnetization, sign change in EB, sign change in MD behavior and sign change in magnetocaloric effect. Long range FIM ordering is observed at  $T_C$  for both the samples. The local magnetic moments and the crystalline structure show a non-monotonic variation across  $T_{\text{comp}}$ . Sign change in EB field across the compensation temperature is correlated with the magneto-structural effects revealed from the neutron data. This class of materials provides a platform to study the competition between the crystalline energy and the Zeeman energy, which is reflected in the sign change of the exchange bias. A clear transition into incommensurate spin-spiral phase across  $T_S$  has been also observed but at a lower temperature compared to  $\text{CoCr}_2\text{O}_4$ . Moreover, below  $T_L$ , an additional incommensurate modulation in the magnetic structure is observed in these Fe substituted compounds. We have also carried out molecular field calculations for moments on different sites, which are best fitted to the moments extracted from the NPD experiment.

---

### *Studies on $\text{Co}(\text{Cr}_{1-x}\text{Mn}_x)_2\text{O}_4$ ( $x = 0.0-0.3$ )*

---

#### **4.1 Introduction**

In the previous chapter, we have noticed that the substitution of 'Fe' for Cr-site in  $\text{CoCr}_2\text{O}_4$  influences its magnetic properties due to its different magnetic structures compared to the pristine  $\text{CoCr}_2\text{O}_4$ . NPD experiments described that the 'Fe' substitution which leads to the negative magnetization and sign change of EB across the  $T_{\text{comp}}$ , gives rise to unusual magnetic structures around  $T_{\text{comp}}$ . Further, it is very clear that 'Fe' substitution in  $\text{CoCr}_2\text{O}_4$  influences the magnetic structure of pristine  $\text{CoCr}_2\text{O}_4$  which is responsible for observing EB effect. In addition, it is appreciable to see the influence of  $\text{Mn}^{3+}$  substitutions for 'Cr' on the magnetic properties of  $\text{CoCr}_2\text{O}_4$ . Having similar ionic radii and different magnetic moment with that of Cr in  $\text{CoCr}_2\text{O}_4$ , one can look for interesting as well as different magnetic properties and magnetic structure of these Mn substituted  $\text{CoCr}_2\text{O}_4$  compounds. There are few reports on multilayers of collinear FM and noncollinear AFM materials where unusual temperature dependent EB effect is noticed [168,169]. EB effect has also been observed in the non-collinear spin structure within a single phase bulk material [170] [96]. Hence, it is indispensable to validate the surfacing of EB across  $T_{\text{comp}}$  in the framework of oxide systems with noncollinear spin-spiral such as  $\text{Co}(\text{Cr}_{1-x}\text{Mn}_x)_2\text{O}_4$  compounds.

In this chapter, we have invoked Mn substitution for 'Cr'-site to design the compensated state in  $\text{CoCr}_2\text{O}_4$ . As,  $\text{Mn}^{3+}$ - ions having larger magnetic moment compared to  $\text{Cr}^{3+}$ - ions hence it would be useful to enrich magnetic interactions among A and B-sites of the spinel structure. Low temperature neutron powder diffraction (NPD) experiment has also been carried out for the better understanding of such interesting magnetic properties of compensated compounds. Here, we report preparation, structural, temperature and magnetic field dependent magnetization, the study of EB effects and magnetic structures determination through NPD.

## 4.2 Experimental Details

Polycrystalline samples of  $\text{Co}(\text{Cr}_{1-x}\text{Mn}_x)_2\text{O}_4$  ( $x = 0.0-0.3$ ) were prepared in the single phase by employing standard solid state reaction method by using high purity ( $\geq 99.6\%$ ) binary oxides  $\text{Co}_3\text{O}_4$ ,  $\text{Cr}_2\text{O}_3$  and  $\text{MnO}_2$ . Structural characterization of the sample is conducted by recording room temperature XRD patterns on powdered samples by utilizing  $\text{Cu-K}\alpha$  ( $\lambda = 1.5406 \text{ \AA}$ ) radiation in Rigaku X-ray diffractometer (model : TTRAX III). Temperature dependent neutron powder diffraction experiments were carried out on the high resolution powder diffractometer (FCD-PD3) at beam line TT-1015 at Dhruva reactor using neutrons of wavelengths  $1.48 \text{ \AA}$  [124]. Magnetization measurements on polycrystalline samples are performed using both commercial SQUID-VSM (Model S-VSM Quantum Design, Inc.) and Physical Property Measurement System with VSM option (PPMS-VSM, Quantum Design Inc.) in the temperature range from 2 to 300 K with magnetic field range from 0 to 9 T. In addition, AC susceptibility was also measured using PPMS with ACMS option.

## 4.3 Results and Discussions

### 4.3.1 X-Ray Diffraction

Fig. 4.1 depict the observed and fitted powder XRD patterns of  $\text{CoCr}_2\text{O}_4$  (a),  $\text{Co}(\text{Cr}_{0.73}\text{Mn}_{0.27})_2\text{O}_4$  (b) and  $\text{Co}(\text{Cr}_{0.70}\text{Mn}_{0.30})_2\text{O}_4$  (c) compounds by using Rietveld refinement method using the FullProf program. We can see the goodness of fit of the data in terms of the non-scattered difference curve (the blue one) between experimental and fitted patterns having low  $\chi^2$  value around 1.5. From the above plot, it is very clear that all the observed peaks of both the Mn substituted samples adopt normal cubic spinel crystal structure with  $Fd\bar{3}m$  space group similar to  $\text{CoCr}_2\text{O}_4$ . From here one can see that the prepared samples are in a single phase without any trace of impurities. The extracted lattice parameter ( $a$ ), cell volume ( $V$ ) and important bond lengths and bond angles along which the superexchange paths take place are listed in the given Table 4.1. The oxygen coordinates correspond to the  $32e$  Wyckoff positions are found to be (0.26, 0.26, 0.26). From the table, it is very clear that lattice parameter ' $a$ ' and unit cell volume ' $V$ ' increase for Mn substituted compounds. Bond angle between the Co(A) and Cr/Mn(B), i.e. A-O-B (deg) found to be unchanged with Mn substitution and found to be

around 121(deg). Similarly, the angle between the B-site ions, i.e. Cr–O–Cr/Mn (deg) or B–O–B is found to be around 94 (deg) in both parent as well as in the 30% Mn substituted sample. It can be seen that A–O and B–O Bond lengths also change nominally with Mn substitution for Cr-site in  $\text{CoCr}_2\text{O}_4$ . The structural changes are nominal with substituted Mn ions, except expansion in the unit cell. The expansion in lattice parameter or cell volume could be understood in terms of the difference between the ionic sizes of  $\text{Mn}^{3+}$  (0.645 Å) and  $\text{Cr}^{3+}$  (0.615 Å) in octahedral environment [143].

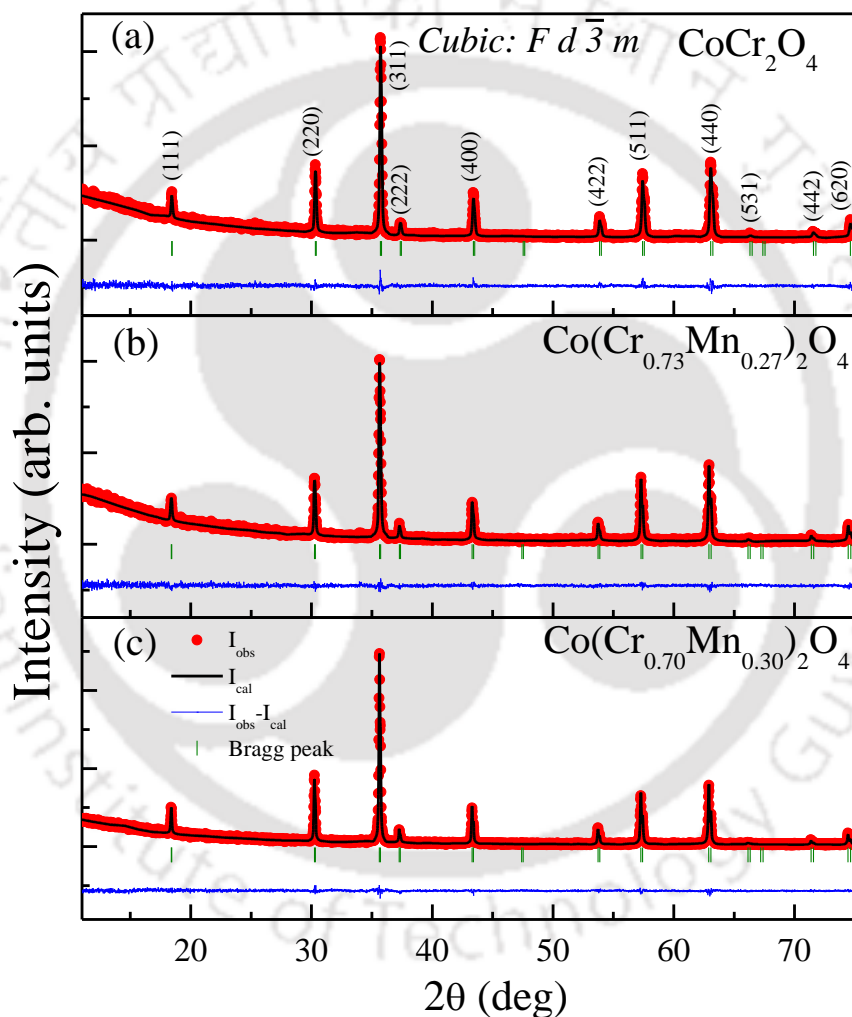


**Figure 4.1** Observed and fitted powder X-ray diffraction patterns of (a)  $\text{CoCr}_2\text{O}_4$ , (b)  $\text{Co}(\text{Cr}_{0.73}\text{Mn}_{0.27})_2\text{O}_4$ , and (c)  $\text{Co}(\text{Cr}_{0.70}\text{Mn}_{0.30})_2\text{O}_4$  compounds by Rietveld refinement method using the FullProf program.

### 4.3.2 Temperature and Field Dependent Magnetic Properties

Fig. 4.2 depicts the temperature dependent magnetization (M-T) curves of  $\text{Co}(\text{Cr}_{1-x}\text{Mn}_x)_2\text{O}_4$  ( $x \leq 0.30$ ) samples measured in ZFC and FC modes with the applied magnetic

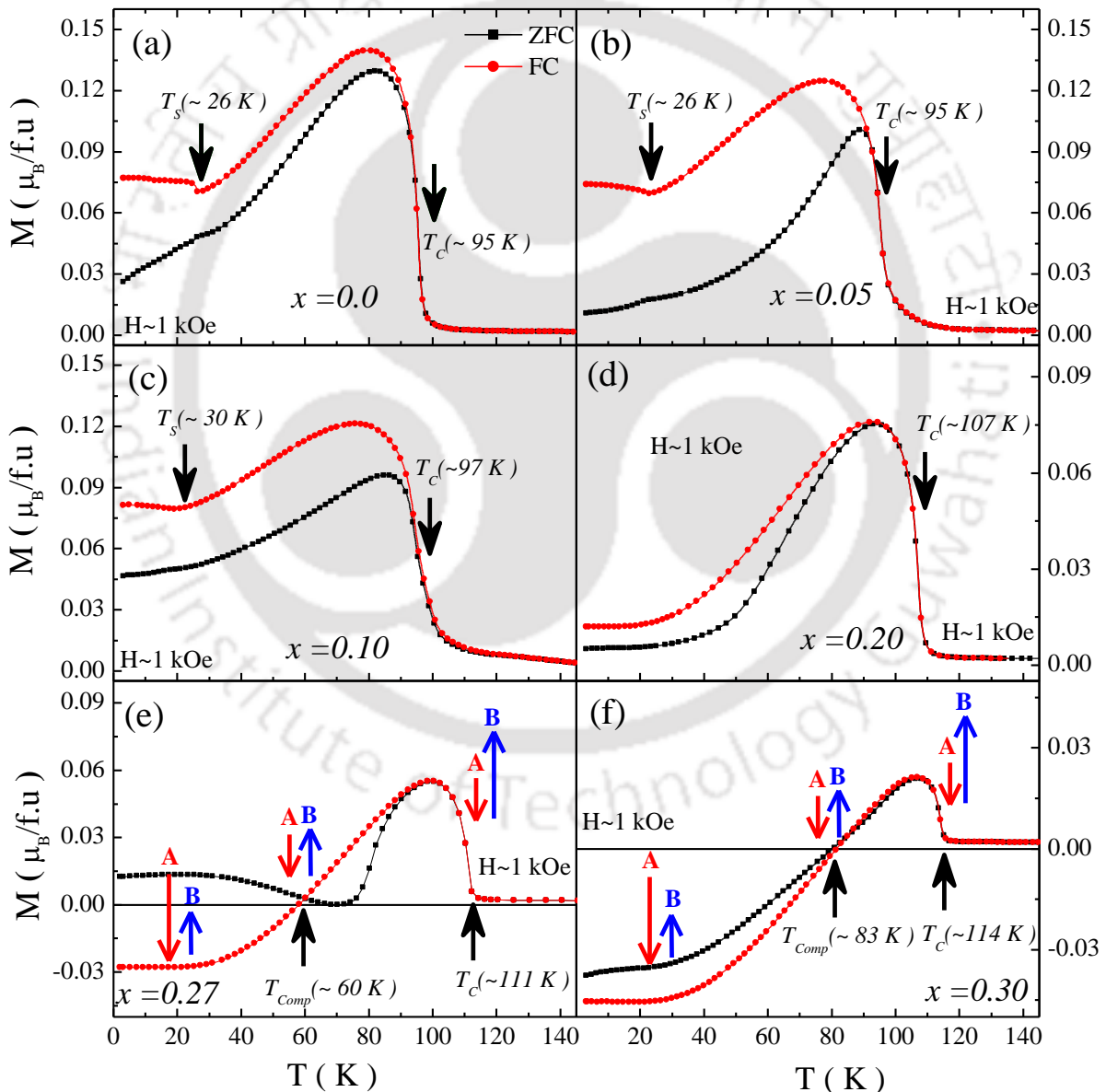
field of  $H \sim 1$  kOe. It is observed that with lowering in temperature from the paramagnetic region, all the compounds exhibit a long range collinear FIM ordering around their respective transition temperatures ( $T_C$ ). Further, we have observed an increase in  $T_C$  with an increase in Mn substitution in  $\text{CoCr}_2\text{O}_4$ . Such observed enhancement in the FIM transition temperature is due to the strong

Table 4.1 Structural parameters, selected bond distances and bond angles from the Rietveld refinement of X-ray powder diffraction patterns for  $\text{Co}(\text{Cr}_{1-x}\text{Mn}_x)_2\text{O}_4$  ( $x = 0.0$  and  $0.30$ ) samples at room temperature.

$\text{Co}(\text{Cr}_{1-x}\text{Mn}_x)_2\text{O}_4$	$x = 0.00$	$x = 0.30$
Crystal Symmetry	Cubic	Cubic
Space Group	$Fd\bar{3}m$	$Fd\bar{3}m$
$a = b = c$ (Å)	8.3328(1)	8.3519(3)
$V$ (Å <sup>3</sup> )	578.59(1)	582.57(4)
$\langle\text{A-O}\rangle$ (Å)	1.947(1)	1.956(1)
$\langle\text{B-O}\rangle$ (Å)	2.004(1)	2.006(1)
$\angle\text{A-O-B}$ (deg)	121.90(2)	121.82(1)
$\angle\text{B-O-B}$ (deg)	94.6(2)	94.8(2)
GOF ( $\chi^2$ )	3.6	3.5

magnetic interactions between A-site ( $\text{Co}^{2+}$ ) and B-sites ( $\text{Cr}^{3+}/\text{Mn}^{3+}$ ) compared to that of the only  $\text{Cr}^{3+}$  at B-sites in the parent  $\text{CoCr}_2\text{O}_4$ . As, there is difference in magnetic moments of different sublattices compare to parent compound, interesting magnetic properties have been noticed. In case of  $x = 0.27$  and  $0.30$  samples, we observed that below respective  $T_C$ , the magnetization show a crossover of  $M = 0$  axis at temperature [i.e. compensation temperature ( $T_{\text{comp}}$ )]  $T \sim 60$  K and  $\sim 83$  K, respectively. Such magnetically compensated state is observed only for  $\text{Co}(\text{Cr}_{0.73}\text{Mn}_{0.27})_2\text{O}_4$  and  $\text{Co}(\text{Cr}_{0.70}\text{Mn}_{0.30})_2\text{O}_4$  compounds among prepared samples. The finding of magnetically compensated state in these compounds indicates the significant influence of ‘Mn’ substitution on the magnetic properties or magnetic exchange interactions between different sublattices of pristine  $\text{CoCr}_2\text{O}_4$ . One can explain this state of magnetic compensation in terms of different temperature dependence of sub-lattices (A and B) magnetization in these FIM compounds. These FIM compounds are having two different sublattices A ( $\text{Co}^{2+}$ ) and B ( $\text{Cr}^{3+}/\text{Mn}^{3+}$ ) which are anti-parallel to each other. We assume that the substitution of 27% and 30% Mn at B-sites makes the magnetic spin of A-site and B-site anti-parallel and parallel to the direction of applied magnetic field. Below ordering temperature, the parallel spins (i.e. B-site) to

the field dominate over the A-site spins which are antiparallel to the field. But with further lowering in temperature, these anti-parallel A-site spins grow up and becomes equal in magnitude to the B-site spin magnetic moment at compensation point and the temperature is known as compensation temperature as  $T = T_{\text{comp}}$ . After this  $T_{\text{comp}}$ , these anti-parallel spins further continue to grow and dominate over the B-site spins and one finds the phenomenon of negative magnetization/magnetization reversal [171]. The present magnetic anisotropy in these systems plays an important role for observing such negative magnetization by holding these antiparallel spins to the applied field direction.



**Figure 4.2** (a) - (f) Temperature dependent dc-magnetization of  $\text{Co}(\text{Cr}_{1-x}\text{Mn}_x)_2\text{O}_4$  ( $x = 0.0 - 0.30$ ) under ZFC and FC modes with the applied field of  $H \sim 1$  kOe.

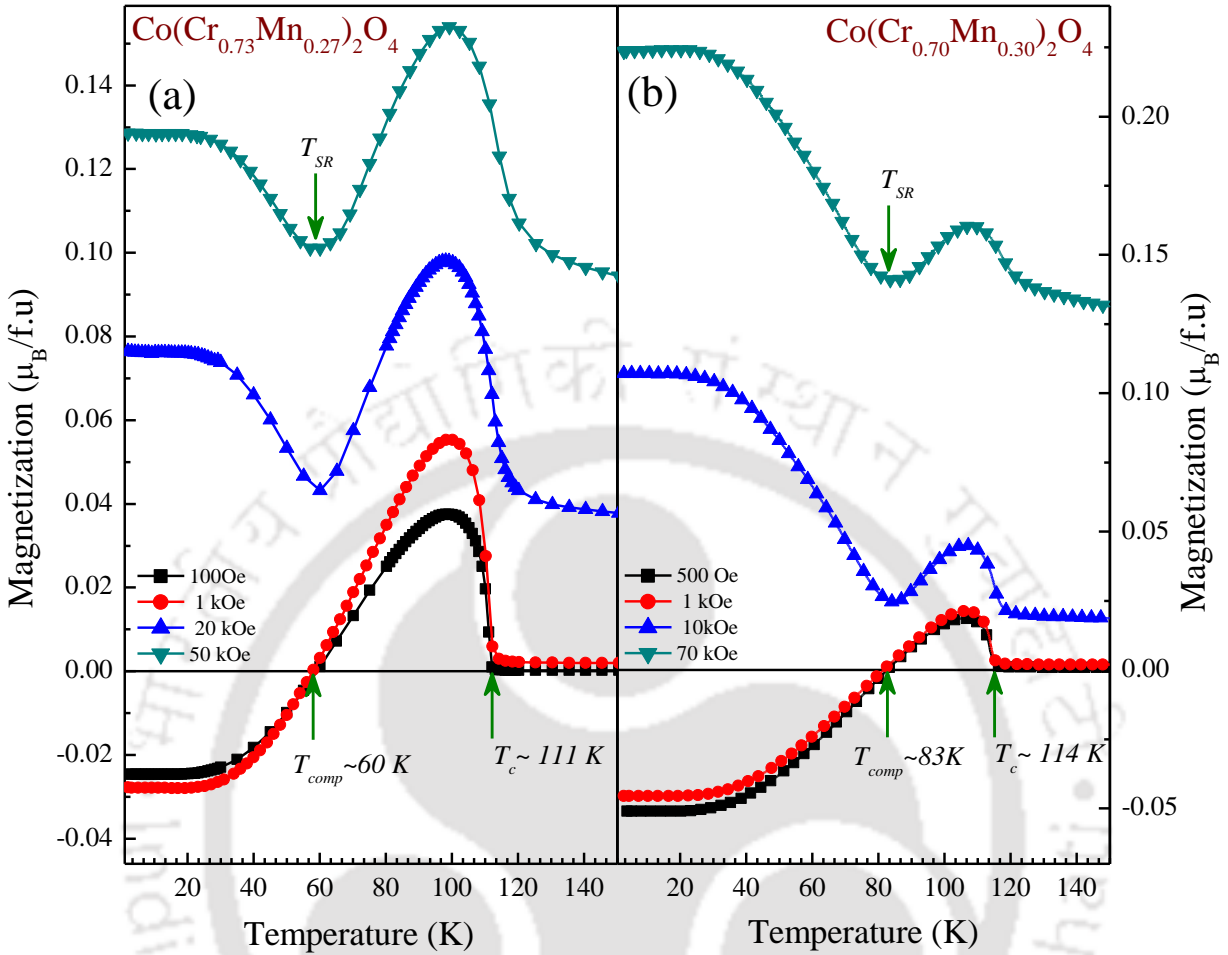


**Figure 4.3** Temperature dependent magnetization of (a)  $\text{Co}(\text{Cr}_{0.73}\text{Mn}_{0.27})_2\text{O}_4$ , and (b)  $\text{Co}(\text{Cr}_{0.70}\text{Mn}_{0.30})_2\text{O}_4$  measured in FC mode under various applied fields ranging from 100 Oe to 70 kOe. Here  $T_c$ ,  $T_{\text{comp}}$  and  $T_{\text{SR}}$  denote ferrimagnetic transition, compensation temperature and field induced spin reorientation transition temperatures, respectively.

Further, we have performed the temperature dependent magnetization in the presence of different applied magnetic fields to study the detailed behavior of magnetic transitions observed in these compensated samples:  $\text{Co}(\text{Cr}_{0.73}\text{Mn}_{0.27})_2\text{O}_4$  and  $\text{Co}(\text{Cr}_{0.70}\text{Mn}_{0.30})_2\text{O}_4$  compounds. Fig. 4.3 depicts the FC M-T curves under the application of various magnetic fields ranging from 500 Oe to 70 kOe. From these plots, it can be seen that magnetization curves exhibit a negative magnetization below  $T_{\text{comp}}$  under low applied field (for  $H = 100\text{--}1\text{ kOe}$ ). For high applied fields (i.e. for  $H \sim 10\text{ kOe}$ ), M-T curve shows a dip exactly at  $T_{\text{comp}}$ , where magnetization again switches back to positive value. This turnover or reorientation of spins exactly at compensation point which takes place under the high applied field is known as spin-reorientation transition, i.e.  $T_{\text{SR}}$  [172]. Interestingly, it has also been noticed that with the increase in the applied field, this

transition at  $T_{SR}$  slightly broaden but not vanishes even under the large applied field of 70 kOe which conveys that such field induced transition is very robust in nature. In addition to it,  $T_C$  also becomes broaden with the strength of the applied magnetic field.

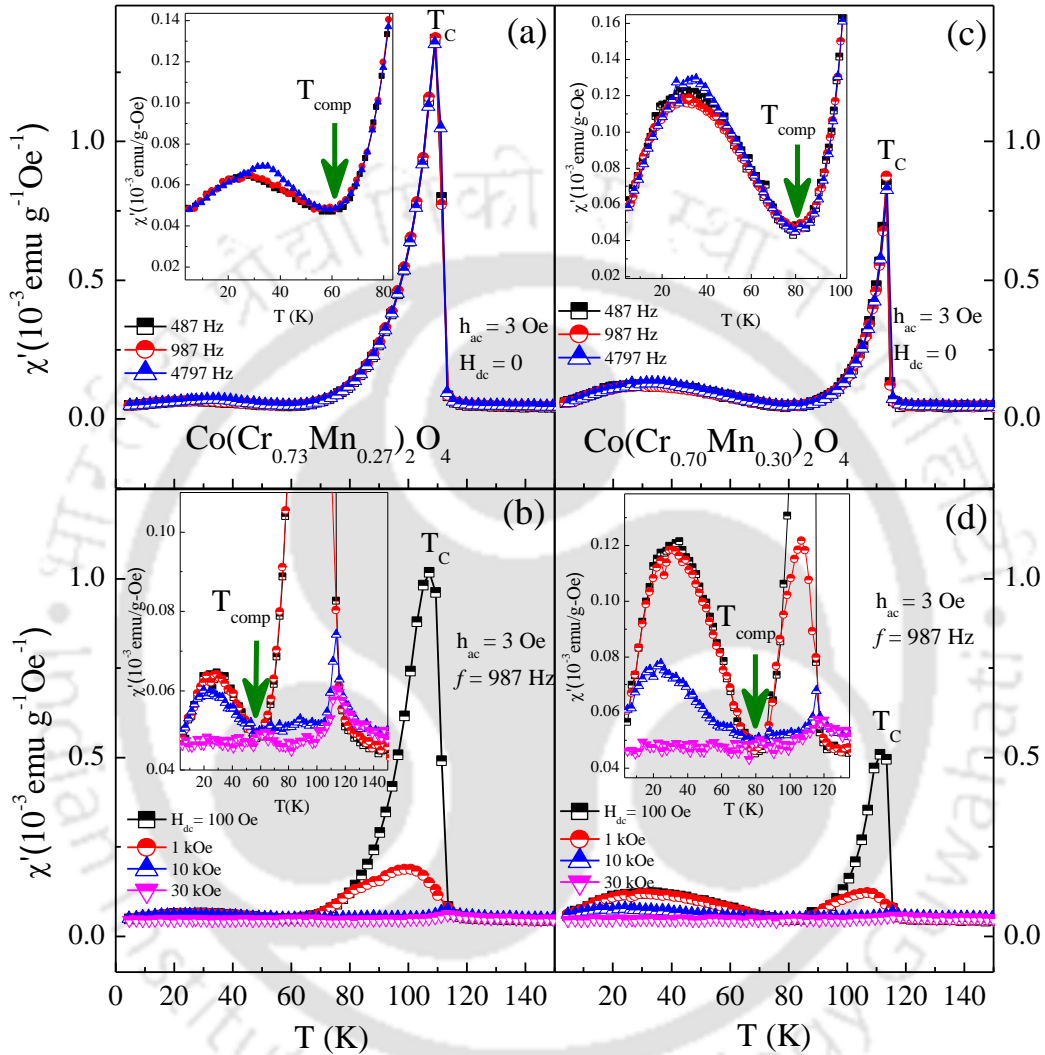


**Figure 4.4** Temperature dependence of ac-magnetic susceptibility measured at various frequencies under zero dc-bias field with  $h_{ac} = 3 \text{ Oe}$  of (a)  $\text{Co}(\text{Cr}_{0.73}\text{Mn}_{0.27})_2\text{O}_4$ , and (c)  $\text{Co}(\text{Cr}_{0.70}\text{Mn}_{0.30})_2\text{O}_4$ . (b) and (d) depict the effect of applied magnetic field for  $f = 987 \text{ Hz}$  for  $\text{Co}(\text{Cr}_{0.73}\text{Mn}_{0.27})_2\text{O}_4$  and  $\text{Co}(\text{Cr}_{0.70}\text{Mn}_{0.30})_2\text{O}_4$  respectively. Respective insets show the enlarged view around  $T_{comp}$ .

We have also performed ac-magnetization measurements for  $x = 0.27$  and  $0.30$  samples. Fig. 4.4 shows the temperature dependent ac-magnetic susceptibility ( $\chi_{ac}$ ) measured frequencies under warming condition using different frequencies and under different applied magnetic fields for both the samples. Four panels, i.e. [(a),(b)] and [(c),(d)] represent the real part of ac-magnetic susceptibility ( $\chi'$ ) with  $h_{ac}=3 \text{ Oe}$ ,  $H_{dc}=0$  and with different applied magnetic field for

Co(Cr<sub>0.73</sub>Mn<sub>0.27</sub>)<sub>2</sub>O<sub>4</sub> and Co(Cr<sub>0.70</sub>Mn<sub>0.30</sub>)<sub>2</sub>O<sub>4</sub>, respectively. For both the samples, there is a large peak representing a long range FIM ordering at  $T_C = 111$  K and 114 K, respectively (cf. Fig. 4.4 (a) and (c)). Further, we have observed a strong dip exactly at respective  $T_{\text{comp}}$  for these compounds [insets of Fig. 4.4 (a) and 4(c)]. From these susceptibility measurements at different frequencies with  $H_{\text{dc}} = 0$ , we ruled out the possibility of glassy nature of the samples as there are no signatures of spin glass in both these compounds. Further, in case of applied magnetic field at a constant frequency (987 Hz), we noticed that these observed transitions are becoming less prominent with the increase in applied field which indicates that effect of the applied magnetic field on existing spin configuration present in these systems.

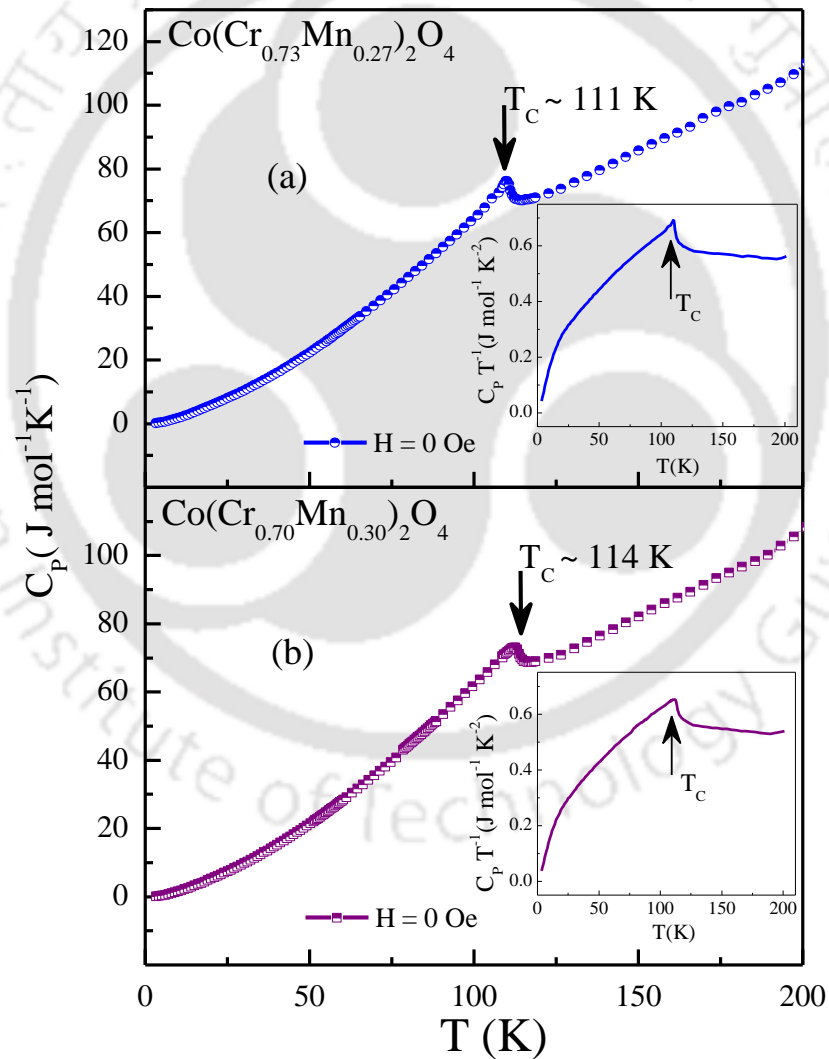


**Figure 4.5** Main panels of (a) and (b) depict the temperature dependent specific heat  $C_p(T)$  of  $\text{Co}(\text{Cr}_{0.73}\text{Mn}_{0.27})_2\text{O}_4$  and  $\text{Co}(\text{Cr}_{0.70}\text{Mn}_{0.30})_2\text{O}_4$  samples measured in zero field, respectively. Insets of (a) and (b) show the respective  $C_p(T)/T$  vs  $T$  plot across  $T_C$  for better clarity of the transitions.

Further, the plots of the temperature dependence of specific heats  $C_P(T)$  and  $C_P(T)/T$  (as in insets) of both  $\text{Co}(\text{Cr}_{0.73}\text{Mn}_{0.27})_2\text{O}_4$  and  $\text{Co}(\text{Cr}_{0.70}\text{Mn}_{0.30})_2\text{O}_4$  compounds measured in the absence of magnetic field are shown in Fig. 4.5. These measurements were performed at smaller temperature intervals around transition temperature regions. We observed a single peak in  $C_P$  versus  $T$  plot, at  $T_C = 111$  K and 114 K for  $\text{Co}(\text{Cr}_{0.73}\text{Mn}_{0.27})_2\text{O}_4$  and  $\text{Co}(\text{Cr}_{0.70}\text{Mn}_{0.30})_2\text{O}_4$  compounds, respectively. Such lambda type shape of the peak observed around  $T_C$  shows the FIM ordering in these samples.

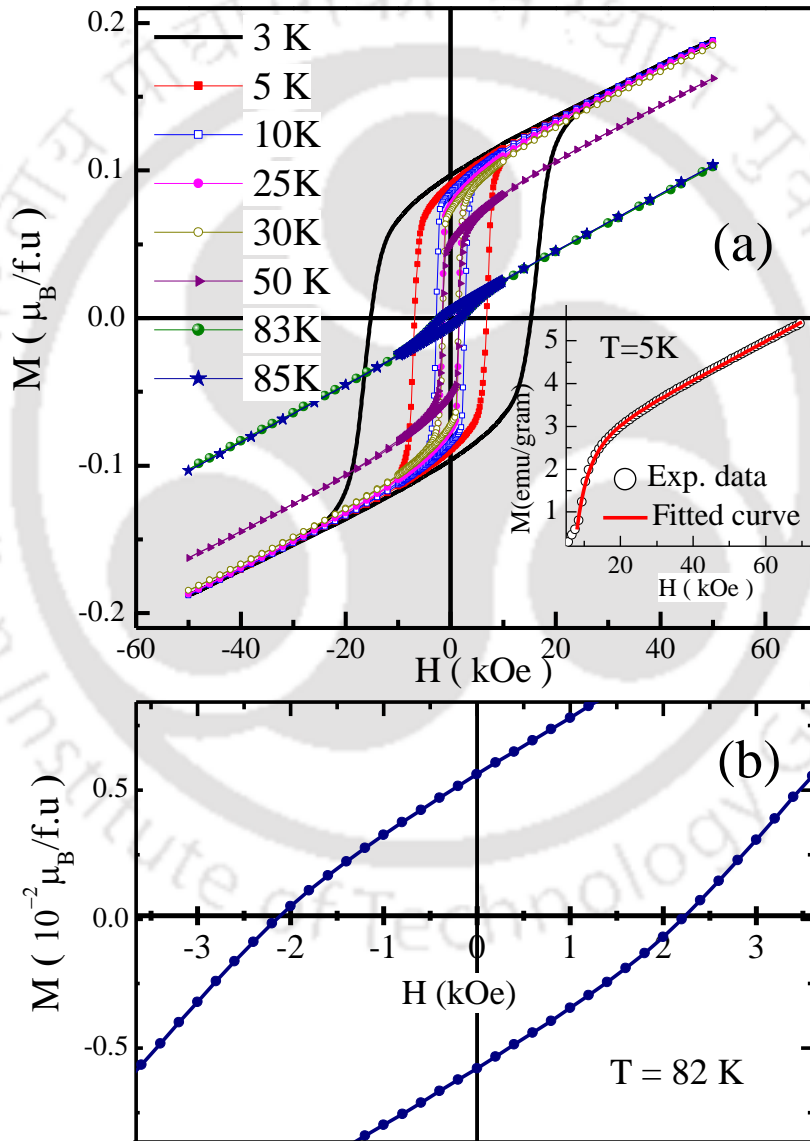


**Figure 4.6** (a) FC M-H loops of  $\text{Co}(\text{Cr}_{0.7}\text{Mn}_{0.3})_2\text{O}_4$  sample at different temperatures under FC condition with  $H = 70$  kOe. (b) depicts an enlarged view of the FC M-H loop at 82 K. Inset of (a) shows the experimental and fitted initial magnetization curve at 5 K.

### 4.3.3 Exchange Bias Effect

Main panel of Fig. 4.6 (a) depicts the field cooled magnetization (FC M-H) loops of  $\text{Co}(\text{Cr}_{0.7}\text{Mn}_{0.3})_2\text{O}_4$  sample recorded at different temperatures under the cooling field of 70 kOe. To record these FC M-H loops the sample was initially cooled in a field of 70 kOe from paramagnetic state to the temperature at which we need to record the M-H loop, and thereafter the field was ramped between 50 kOe. This entire process was repeated to record M-H loops at each temperature. We can see that the loop at 3 K exhibit unusual coercivity in the order of 15.6 kOe which is considerably large in the frame work of oxide compounds. Generally, the anisotropy and spin canting or non-collinear magnetic structure leads to large coercivity in the magnetic systems. In order to assess the rough value of the magnetic anisotropy in the system the initial magnetization curve has been fitted to the equation  $M = M_S \left(1 - \frac{a}{H} - \frac{b}{H^2}\right) + \chi H$ ;  $b = 4 K_1^2/15M_S^2$  and  $H_A = 2K_1/M_S$ , here  $M_S$  is saturation magnetization,  $a$ ,  $b$  are free-parameters,  $K_1$  is anisotropy constant, is the high-field susceptibility and  $H_A$  is the anisotropy field [173,174]. As shown in the inset of the Fig. 4.6 (a) the best fit to the experimental data yields the anisotropy ( $H_A$ ) to be roughly 38(1) kOe. This large value of magnetic anisotropy may results in the large coercivity in the sample at low temperature. Further, in this sample the hysteresis loops are measured such that the maximum applied field (50 kOe)  $> H_A$ . It can be noticed that the behavior of the loop changes drastically on increasing the temperature to compensation point. The loops up to 50 K exhibit typical ferrimagnetic behavior, with decrement in the width of loop. But, the loops in the close vicinity of  $T_{\text{comp}}$  show typical antiferromagnetic trend. Further, a decrease in the magnetization has also been noticed. Fig. 4.6 (b) shows the enlarged FC M-H loop at 82 K i.e. just below the  $T_{\text{comp}}$ . We can see a tiny shift in the loop towards the positive field axis.

For these FC M-H loops we define the effective coercive field,  $H_C^{\text{eff}} = \frac{(H_+ + H_-)}{2}$ , and the EB field, i.e. measure of the amount asymmetry in the loops along the field axis as  $H_{\text{EB}} = -\left(\frac{H_+ - H_-}{2}\right)$ , where  $H_+$  and  $H_-$  represent the right and left field values of M-H loop where the net magnetization crosses the  $M = 0$  axis. The temperature dependence of  $H_C^{\text{eff}}$  is plotted in the main panels of Fig. 4.7 (a). It can be noticed that  $H_C^{\text{eff}}$  falls very sharply on increasing the temperature from 3 K to 10 K. Thereafter it almost saturates up to 50 K and then shows a small upturn just below  $T_{\text{comp}}$  then show minima at  $T_{\text{comp}}$ . As shown in the inset of Fig. 4.7 (a)  $H_C^{\text{eff}}$  is found follow exponentially decaying function. The decrease in anisotropy could be the reason behind the sharp

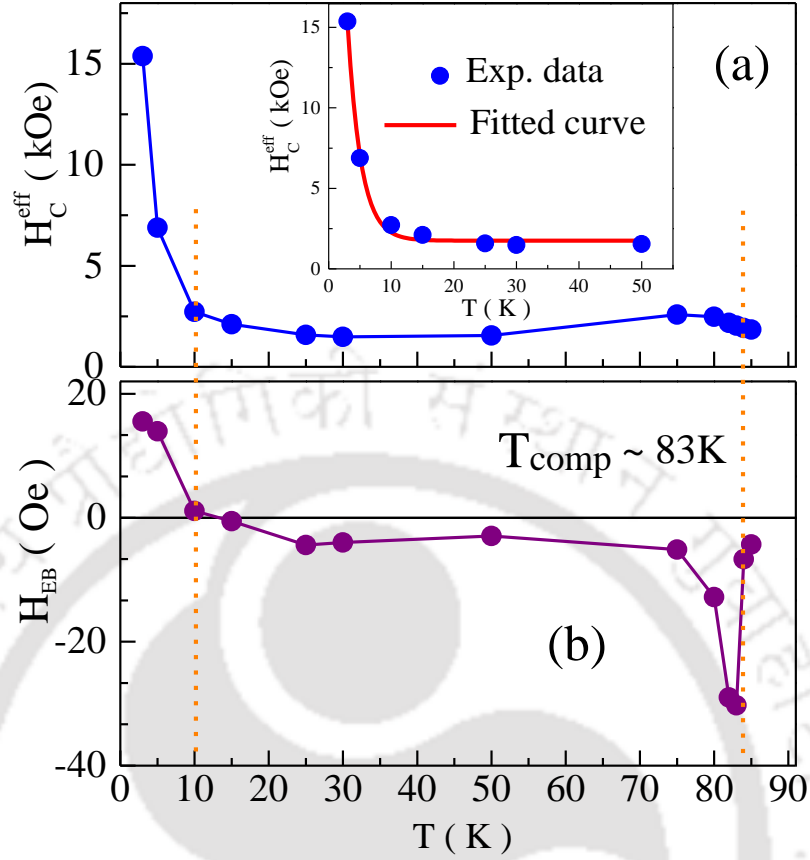


**Figure 4.7** Temperature dependence of (a) effective coercive field  $H_C^{eff}$  and (b) EB field  $H_{EB}$  in  $Co(Cr_{0.7}Mn_{0.3})_2O_4$  compound. Inset of (a) is experimental and fitted temperature dependent  $H_C^{eff}$  plot in  $3 K \leq T \leq 50 K$  range.

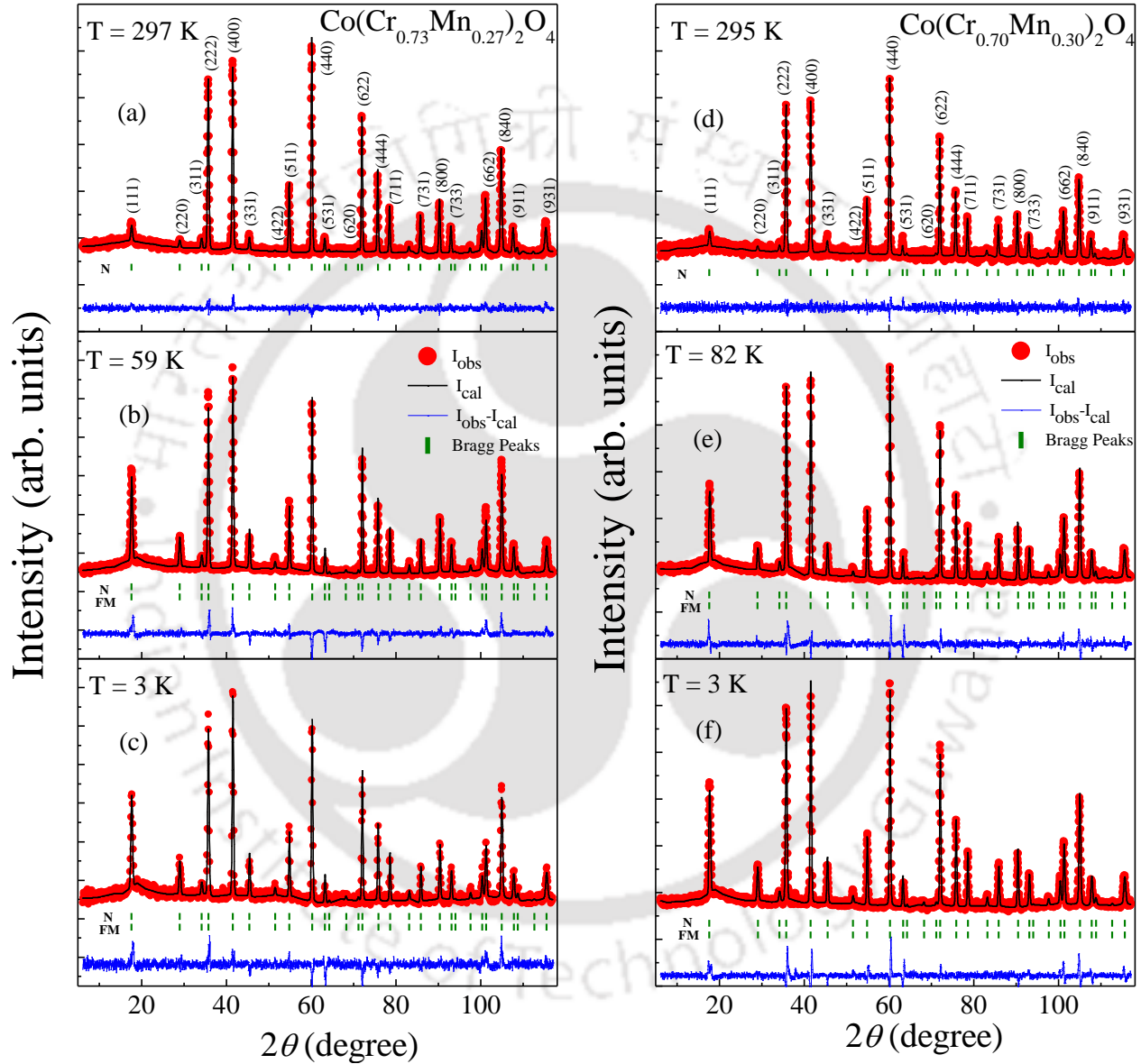
fall of  $H_C^{eff}$  as a function of temperature. As shown in Fig. 4.7 (b)  $H_{EB}$  exhibits considerable value below 10 K as well as in the vicinity of the compensation point. The small rise in the EB below 10 K could be the resultant of the large anisotropy (as evidenced in  $H_C^{eff}$ ) that leads to exchange coupling similar to the conventional EB systems. Further, the observation of EB again only in the vicinity of  $T_{comp}$  could be ascribed to the spin reorientation as observed  $Nd_{0.75}Ho_{0.25}Al_2$  and  $Co(Cr_{0.95}Fe_{0.05})_2O_4$  [23,26]. In addition, the exchange coupling between the nearly compensated moments and that of FIM clusters is also present there [130]. The small enhancement in  $H_C^{eff}$  in the vicinity of  $T_{comp}$  confirms the development of exchange coupling between the nearly compensated moments and that of ferromagnetic clusters. At the intermediate temperature, i.e.  $10 K \geq T < T_{comp}$  neither the spin reorientation nor the anisotropy contributes to the EB field as a result we might have observed negligible values of EB. This could be the possible reason behind the observed temperature dependence of EB around the compensation point. Analogous to our

compound where features like glassiness or phase separation are absent, the only other alloys or intermetallic compounds which shows a sign change in EB across  $T_{\text{comp}}$ , are  $R_{1-x}\text{Gd}_x\text{Al}_2$ ,  $\text{Nd}_{0.75}\text{Ho}_{0.25}\text{Al}_2$  and  $\text{Sm}_{0.975}\text{Gd}_{0.025}\text{Cu}_4\text{Pd}$  [26,146,175]. However, there are some other reports of single phase homogenous Heusler alloys [130] and charge ordered manganites [97] where one observes the large value of EB, but there are no such reports on sign reversal of EB across  $T_{\text{comp}}$ .

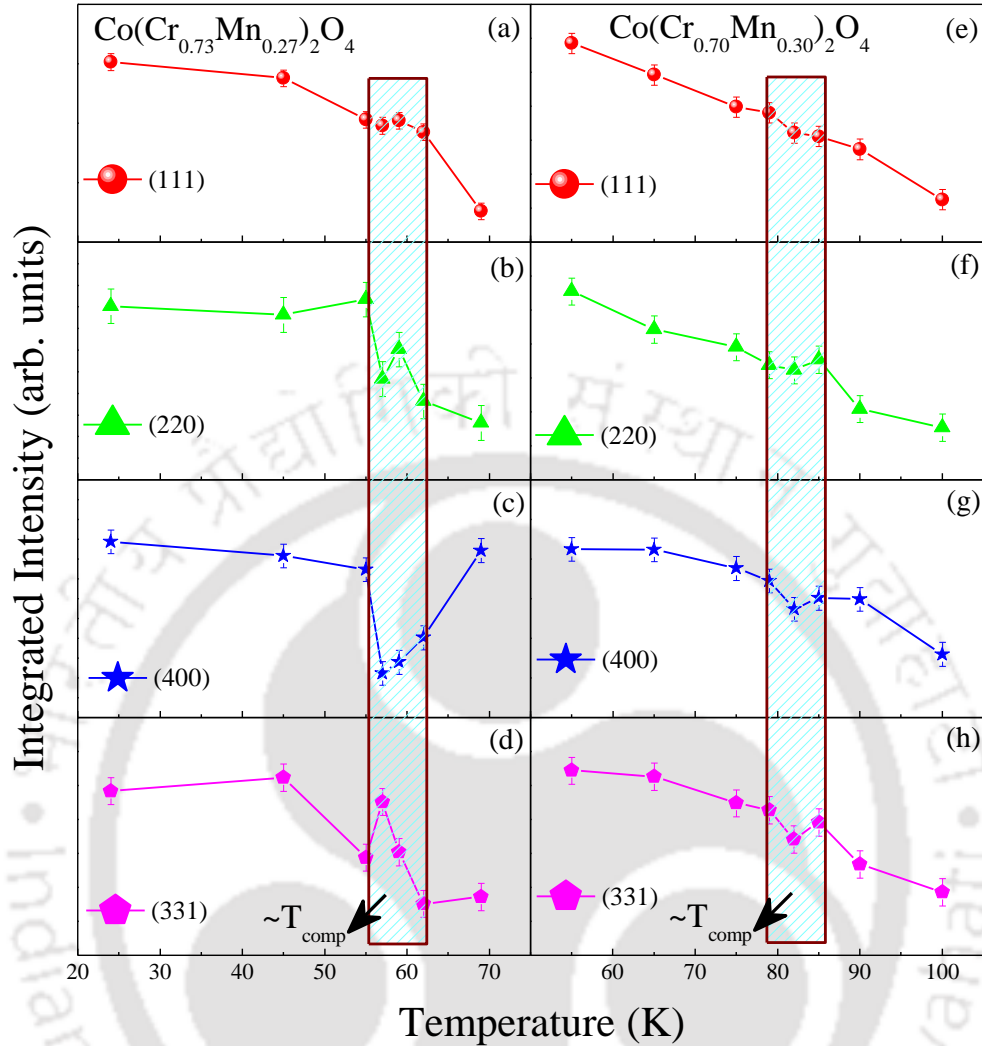
#### ***4.3.4 Temperature Dependent Neutron Powder Diffraction Studies***

In order to see the detailed behavior of negative magnetization and exchange bias, we carried out temperature dependent NPD experiments on  $\text{Co}(\text{Cr}_{0.73}\text{Mn}_{0.27})_2\text{O}_4$  and  $\text{Co}(\text{Cr}_{0.70}\text{Mn}_{0.30})_2\text{O}_4$ . Room temperature chemical structures have been confirmed by performing XRD experiments on these polycrystalline samples of  $\text{Co}(\text{Cr}_{1-x}\text{Mn}_x)_2\text{O}_4$  ( $x \leq 0.30$ ). Fig. 4.8 shows the NPD patterns of  $\text{Co}(\text{Cr}_{0.73}\text{Mn}_{0.27})_2\text{O}_4$  and  $\text{Co}(\text{Cr}_{0.70}\text{Mn}_{0.30})_2\text{O}_4$  together with Rietveld refinement fitting at different temperatures (295 - 3 K) in  $2\theta$ -range 6-120°. The observed patterns are fitted well with a cubic spinel phase having space group:  $Fd\bar{3}m$  (227) till lowest measuring temperature (3 K). In order to study the changes in the nuclear and magnetic structures as a function of temperature, the NPD patterns have been measured at various temperatures ranging from a paramagnetic state to magnetically ordered states till 3 K. It is observed that the experimental data is well fitted to the cubic spinel structure with  $Fd\bar{3}m$  space group, without any impurities till the lowest measuring temperature. The increase of some nuclear Bragg peaks is observed due to the FIM ordering of moments below  $T_C$ , pointed towards the appearance of FM order with propagation vector  $k = [0\ 0\ 0]$ . In order to follow the temperature dependent behavior of the FM components, Rietveld refinement was carried out for temperature range of 3–100 K. Hence, in the magnetically ordered state, in addition to nuclear reflections, we have determined the propagation vector for magnetic reflections using the program K-Search, which is also a part of the FullProf suite program [147]. For FM/FIM systems,  $k$  is always  $[0\ 0\ 0]$  since superstructure reflections are absent. It was found to satisfy the Bragg conditions for all FIM peaks at all temperatures. Further, one can also notice that there is no satellite peak even at 3 K, as a signature of magneto-structural transition ( $T_S$ ) which was present in case of pristine  $\text{CoCr}_2\text{O}_4$  and Fe substituted  $\text{CoCr}_2\text{O}_4$  [16,161]. The absence of  $T_S$  shows that the higher substitution of ‘Mn’ for Cr-site in  $\text{CoCr}_2\text{O}_4$  affects the magnetic ordering strongly and suppresses

$T_S$ . This absence of  $T_S$  in the Mn substituted  $\text{CoCr}_2\text{O}_4$  samples is due to the absence of long range conical spin-spiral ordering which was present in  $\text{CoCr}_2\text{O}_4$ . Hence, one notices the absence of such transformation from collinear FIM state to a conical spin-spiral state in these compensated samples. However, for small amount of Mn substitution,  $T_S$  is present.



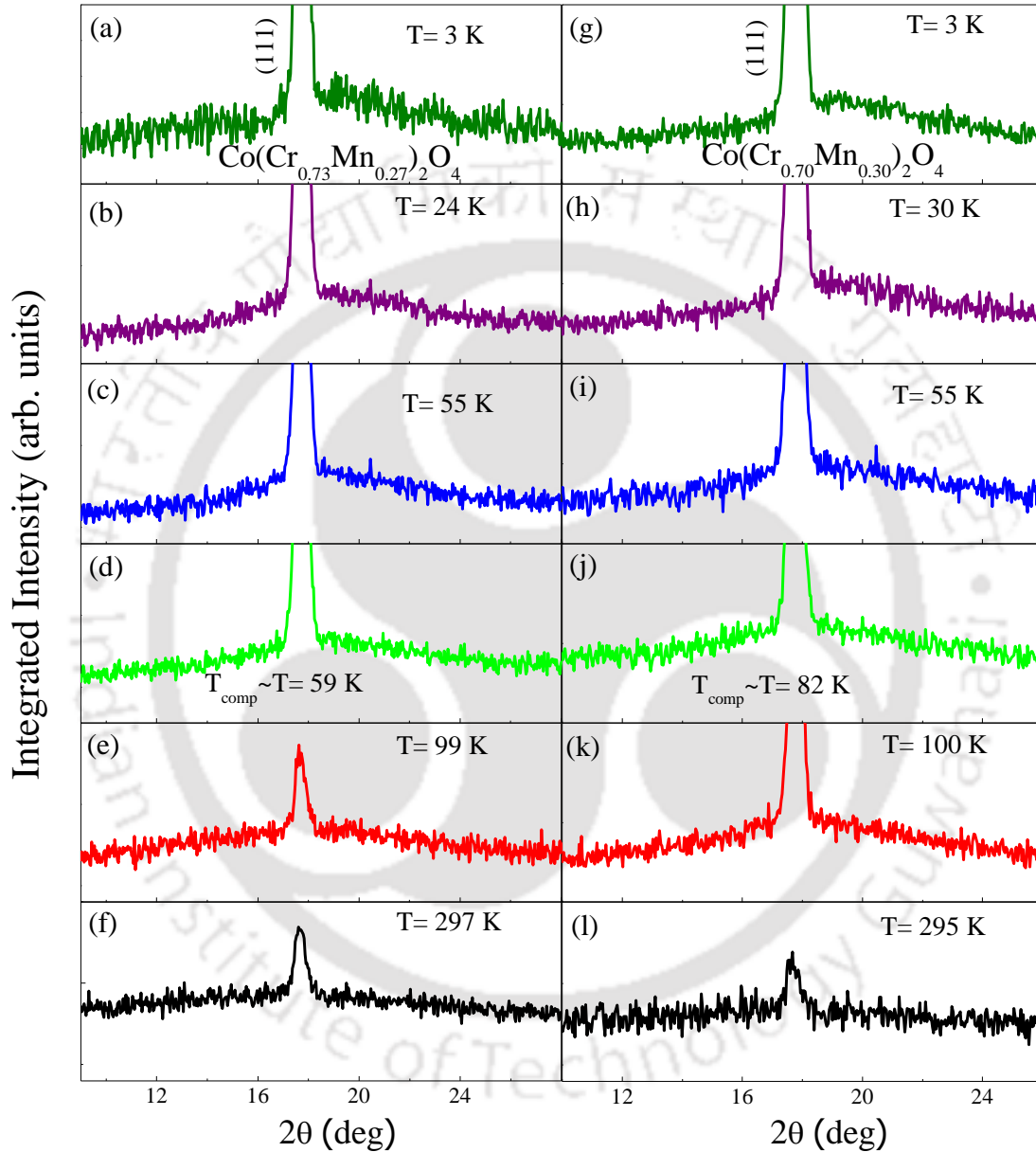
**Figure 4.8** Left panel (a-c) shows the Rietveld refinement of NPD patterns recorded in zero field at  $T = 297$  K, 59 K and 3 K, respectively, for  $\text{Co}(\text{Cr}_{0.73}\text{Mn}_{0.27})_2\text{O}_4$ . Similarly, right panel (a-c) depicts NPD patterns recorded in zero field at  $T = 295$  K, 82 K and 3K, respectively for  $\text{Co}(\text{Cr}_{0.70}\text{Mn}_{0.30})_2\text{O}_4$ . NPD patterns near room temperature (297 K and 295 K) are refined using a structural phase (indicated by the first row of vertical tick marks) whereas another FM phase (second row) is also included in refinement for temperature below  $T_C$ .



**Figure 4.9** Temperature dependence of the integrated intensity of the (111), (220), (400) and (331) fundamental Bragg reflections for  $\text{Co}(\text{Cr}_{0.73}\text{Mn}_{0.27})_2\text{O}_4$  (a-d) and for  $\text{Co}(\text{Cr}_{0.70}\text{Mn}_{0.30})_2\text{O}_4$  (e-h).

Fig. 4.9 illustrates the temperature dependence of the integrated intensity of the (111), (220), (400) and (331) fundamental Bragg reflections for  $\text{Co}(\text{Cr}_{0.73}\text{Mn}_{0.27})_2\text{O}_4$  and  $\text{Co}(\text{Cr}_{0.70}\text{Mn}_{0.30})_2\text{O}_4$ , respectively which are calculated from temperature dependent NPD patterns. We have noticed that there is an unusual change in the integrated intensity plots for the Bragg reflections (111), (220), (400) and (331) in both the compounds. Recently, it was reported that similar to pristine  $\text{CoCr}_2\text{O}_4$ , other transition metal substituted  $\text{CoCr}_2\text{O}_4$ , also possesses a short-range conical spin-spiral components along with the long range FIM ordering below  $T_C$  [161]. Similar to these reports, we also found that there exists a combined ordering of FIM components along with spin-spiral components below  $T_C$  in  $\text{Co}(\text{Cr}_{0.73}\text{Mn}_{0.27})_2\text{O}_4$  and  $\text{Co}(\text{Cr}_{0.70}\text{Mn}_{0.30})_2\text{O}_4$  samples. The variation in the magnitude of these spin-spiral components is

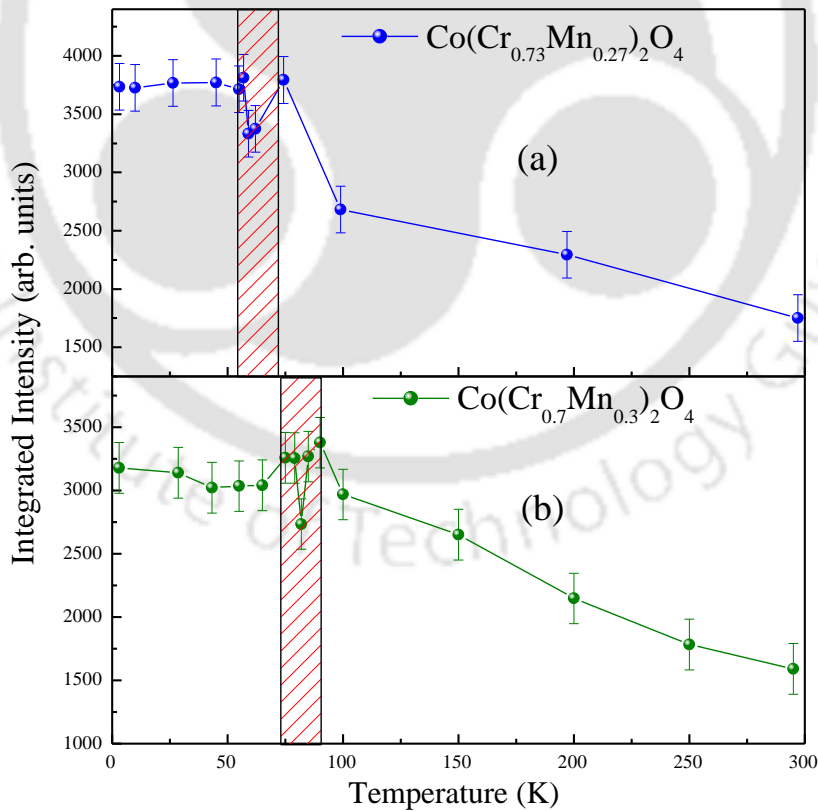
the prime source for the observed variation in the integrated intensity. Such change in the magnitude of the spiral components of the magnetic moments (i.e. the cone angles) could be the reason for the observed modulation in integrated intensity around respective  $T_{\text{comp}}$ .



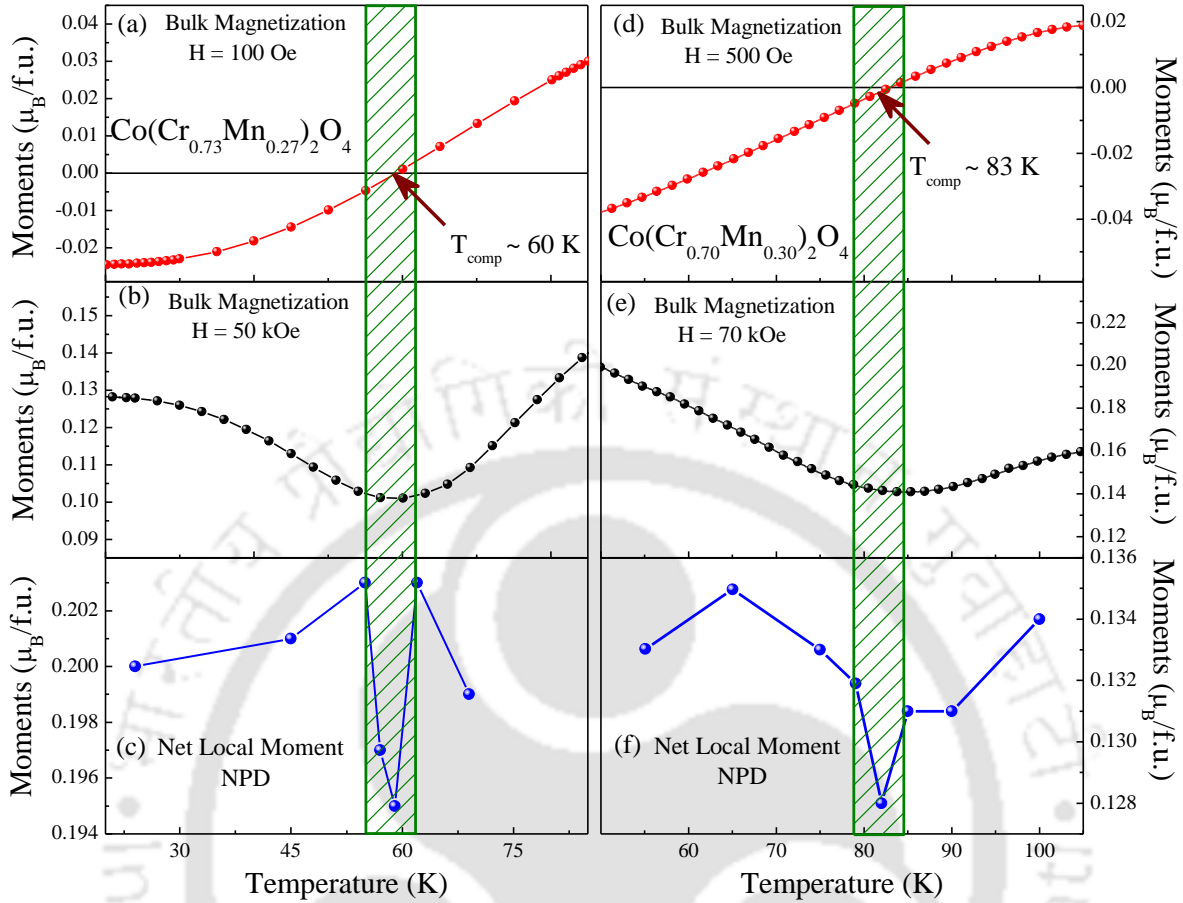
**Figure 4.10** Diffuse signal around the (111) Bragg peak in the neutron diffraction patterns at different temperatures for  $\text{Co}(\text{Cr}_{0.73}\text{Mn}_{0.27})_2\text{O}_4$  (a-f) and  $\text{Co}(\text{Cr}_{0.70}\text{Mn}_{0.30})_2\text{O}_4$  (g-l) (all graphs are plotted in the same scale).

Fig. 4.10 depicts the enlarged view of the low-angle NPD patterns at several temperatures for both  $\text{Co}(\text{Cr}_{0.73}\text{Mn}_{0.27})_2\text{O}_4$  and  $\text{Co}(\text{Cr}_{0.70}\text{Mn}_{0.30})_2\text{O}_4$  compounds. One can see that the patterns around 100 K, which is near to the ordering temperatures of both the samples, have some

presence of a diffuse signal around the (111) Bragg-reflection which were absent in room temperature NPD patterns. These diffuse signals stipulate the presence of magnetic spin clusters in these compounds [151,153]. Further, it is noticed that this diffused signal originating from magnetic spin clusters is limited around the (111) reflection. In case of parent  $\text{CoCr}_2\text{O}_4$  compound, it is revealed from NPD experiments that below  $T_C$ , both long range ferrimagnetic ordering and a short range spiral ordering coexists [8,16]. Compared to  $\text{CoCr}_2\text{O}_4$ , we have noticed that diffused signal started appearing at a higher temperature which could be because of Mn substitution. In Fig.4.11, the temperature dependence of these diffuse signal intensity is shown for both  $x = 0.27$  (a) and  $0.30$  (b) samples, respectively. With lowering in temperature, the diffuse signal intensity increases but there are non-monotonic changes around the respective  $T_{\text{comp}}$  of the compounds which may be due to competition between the spins of both sublattices which are responsible for the compensated state. Hence, the indication of such short range correlation of the transverse spin components which are present till 3 K give a clue that the spin-spiral transition,  $T_S$  could exists at much lower temperature compared to  $\text{CoCr}_2\text{O}_4$ .

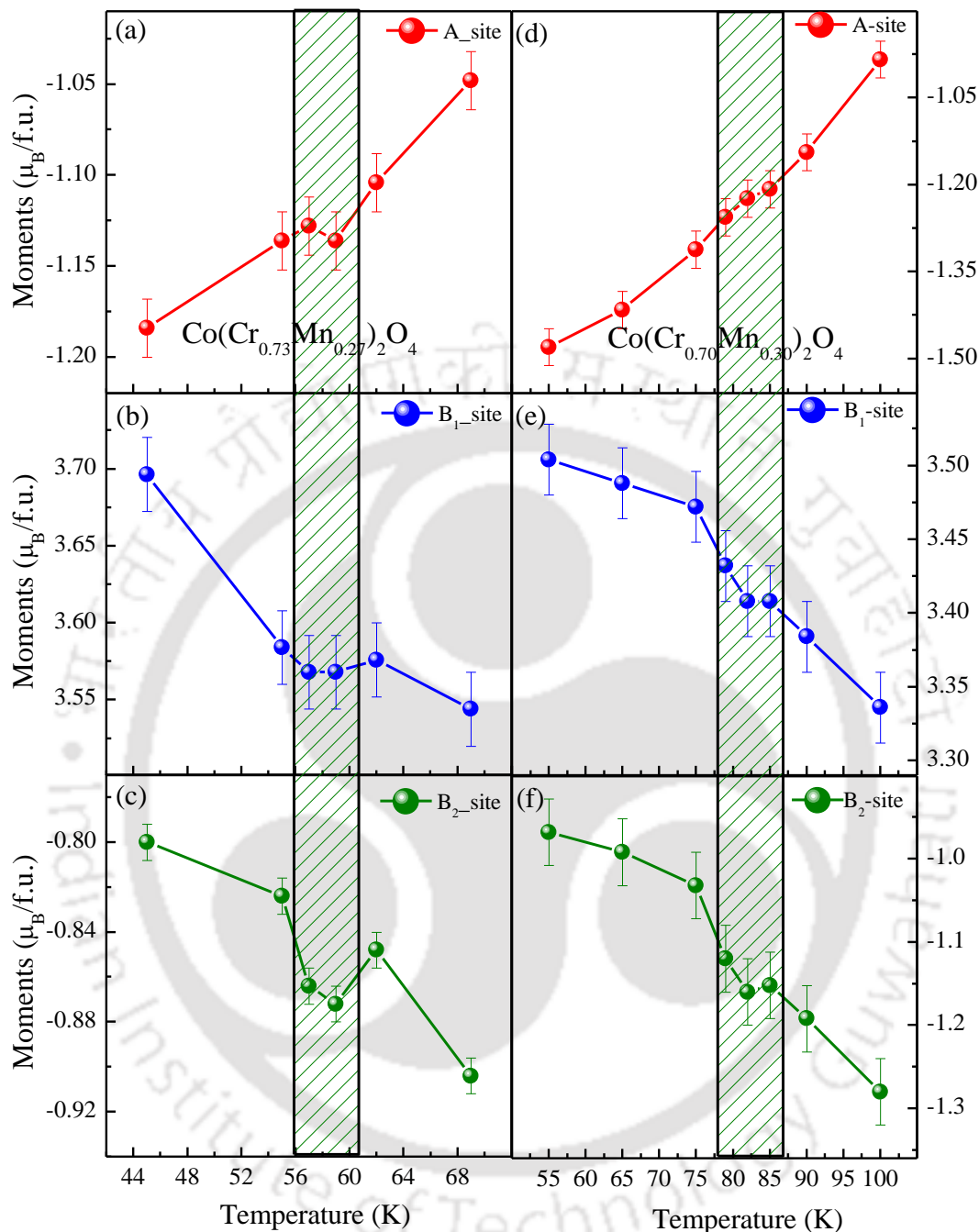


**Figure 4.11** Temperature variation of integrated intensity of diffuse signal around (111) Bragg peak for both  $\text{Co}(\text{Cr}_{0.73}\text{Mn}_{0.27})_2\text{O}_4$  (a) and  $\text{Co}(\text{Cr}_{0.7}\text{Mn}_{0.3})_2\text{O}_4$  (b) compounds.



**Figure 4.12** Temperature dependent magnetization  $M(T)$  curves of  $\text{Co}(\text{Cr}_{0.73}\text{Mn}_{0.27})_2\text{O}_4$  (Left panel) and  $\text{Co}(\text{Cr}_{0.70}\text{Mn}_{0.30})_2\text{O}_4$  (right panel) samples measured under low field (a)&(d) and under high field (b)&(e). In last (c)&(f) show the net local moments obtained from NPD data of both the samples  $\text{Co}(\text{Cr}_{0.73}\text{Mn}_{0.27})_2\text{O}_4$  and  $\text{Co}(\text{Cr}_{0.70}\text{Mn}_{0.30})_2\text{O}_4$  respectively.

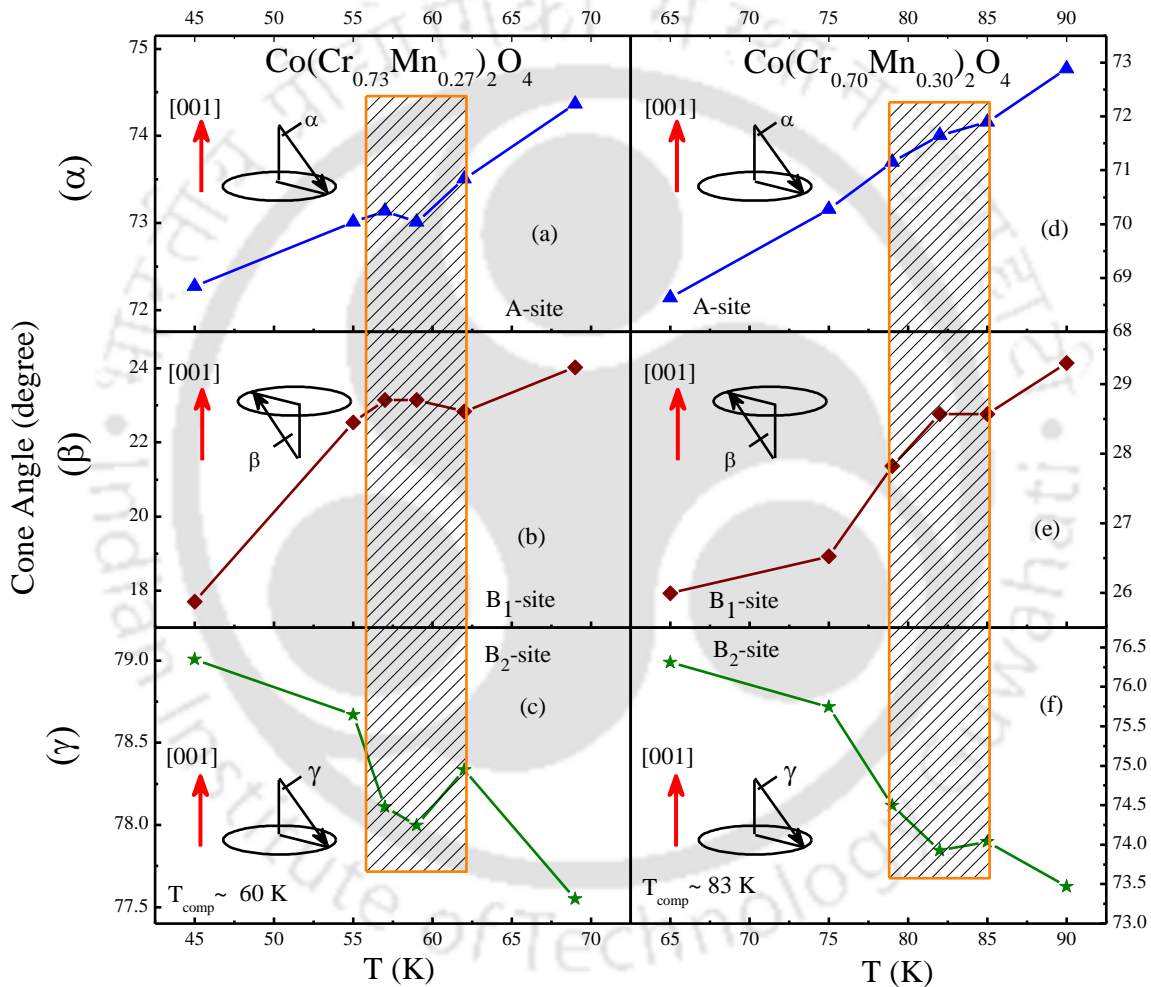
Now, we will discuss the results obtained from the NPD experiments along with the bulk-magnetization measurements. Fig. 4.12 shows a comparative plot of the bulk dc-magnetization measured under the different applied fields with that of temperature dependent spontaneous magnetization obtained from the refinement of the magnetic phase of the NPD patterns of  $\text{Co}(\text{Cr}_{0.73}\text{Mn}_{0.27})_2\text{O}_4$  and  $\text{Co}(\text{Cr}_{0.70}\text{Mn}_{0.30})_2\text{O}_4$  compounds. From here, one can see that similar to the bulk magnetization, the moments obtained from the magnetic phase refinement of NPD data also exhibit the same order of magnitude of magnetization at the compensation points  $T_{\text{comp}} = 60$  K and 82 K for  $\text{Co}(\text{Cr}_{0.73}\text{Mn}_{0.27})_2\text{O}_4$  and  $\text{Co}(\text{Cr}_{0.70}\text{Mn}_{0.30})_2\text{O}_4$ , respectively. Interestingly, it can also be noticed that the behavior of the spontaneous magnetization calculated from NPD data across the compensation point has the similar functional form as the bulk magnetization



**Figure 4.13** Temperature dependence of different site moments (i.e. A, B<sub>1</sub> and B<sub>2</sub>) of both the compounds; (a-c)  $\text{Co}(\text{Cr}_{0.73}\text{Mn}_{0.27})_2\text{O}_4$ , and (d-f)  $\text{Co}(\text{Cr}_{0.70}\text{Mn}_{0.30})_2\text{O}_4$ .

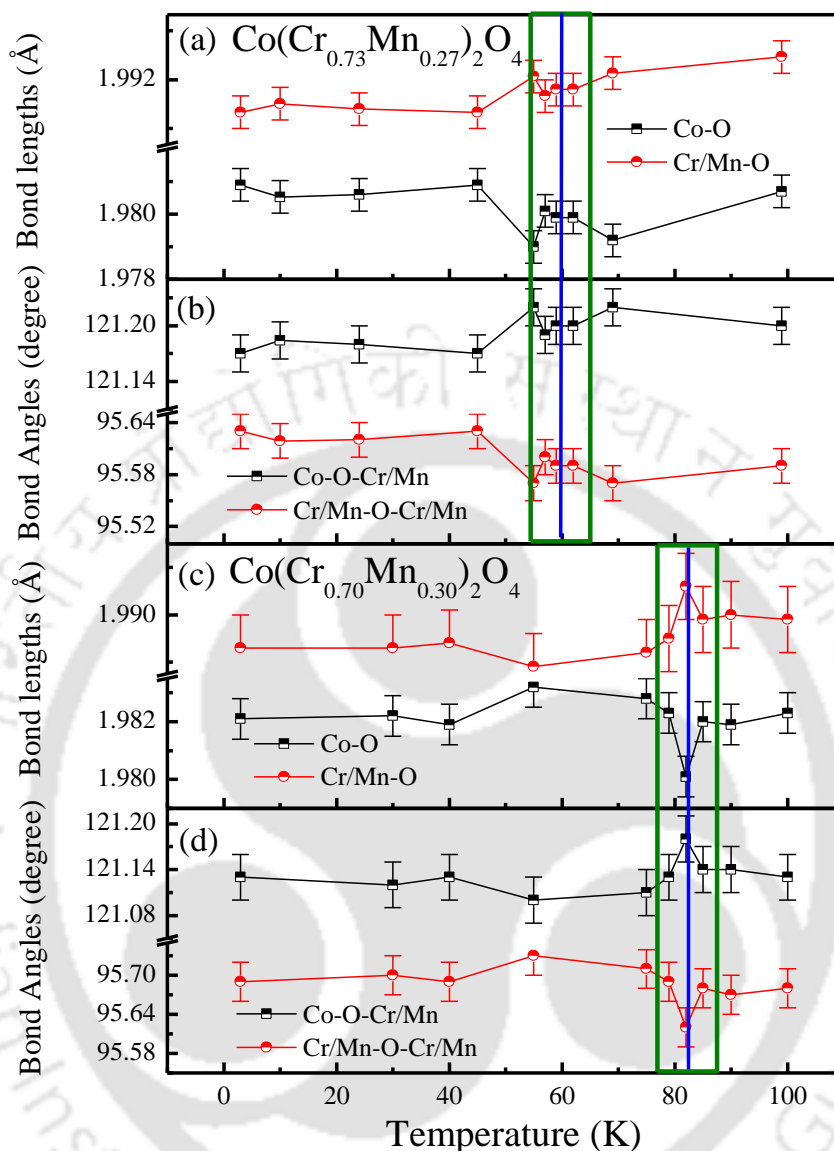
under the application of high magnetic field of 50 kOe or 70 kOe. This observed magnetization behavior validates that there is a strong spin-lattice coupling presents in these systems which is influenced by the application of the external field. From here, it is clear that there are different orientations of magnetic spins corresponding to different sub-lattices around magnetic compensation state. Hence, one observes these respective compensation temperatures form bulk

magnetization data and verified the change in magnetic spin configuration across  $T_{\text{comp}}$  through NPD experiments. It should be noticed that all these interesting features like magnetic compensation, were absent in  $\text{CoCr}_2\text{O}_4$ . We have further calculated the different site-moments for both these samples from NPD data as shown in Fig. 4.13. Noticeable non-monotonic changes in different site magnetic moments around the respective compensation temperatures for these compounds implies the real understanding of magnetic structure which is responsible to attaining the state of magnetic compensation.



**Figure 4.14** Temperature dependence of cone angles ( $\alpha$ ), ( $\beta$ ) and ( $\gamma$ ) of sublattices A,  $B_1$  and  $B_2$  of (a-c)  $\text{Co}(\text{Cr}_{0.73}\text{Mn}_{0.27})_2\text{O}_4$  and (d-f)  $\text{Co}(\text{Cr}_{0.70}\text{Mn}_{0.30})_2\text{O}_4$ , respectively. Insets show the cone angles representing conical spin-spiral ordering pointing to the [001] direction.

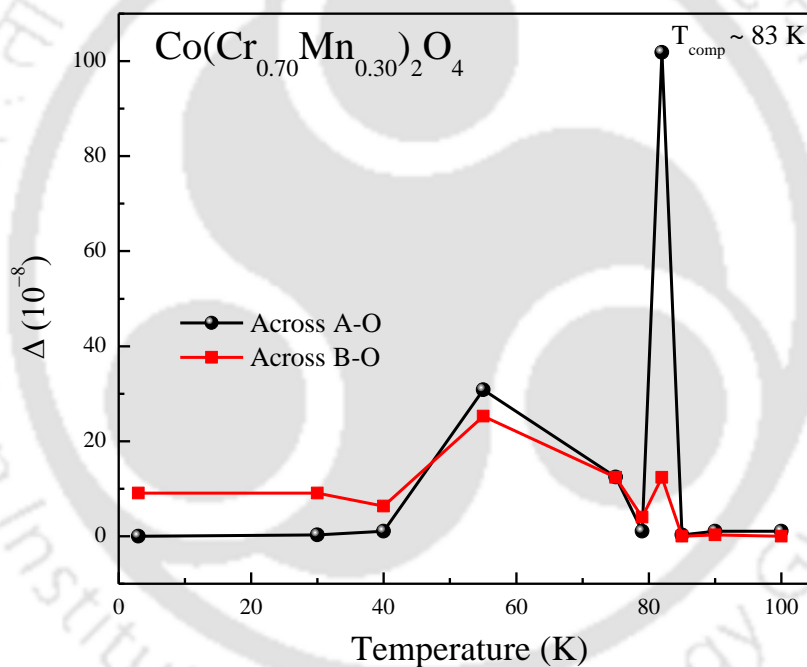
Fig. 4.14 depicts the change in the cone angles ( $\alpha$ ,  $\beta$  and  $\gamma$ ) of different sites (A,  $B_1$  and  $B_2$ ) as a function of temperature for both  $\text{Co}(\text{Cr}_{0.73}\text{Mn}_{0.27})_2\text{O}_4$  (a-c) and  $\text{Co}(\text{Cr}_{0.70}\text{Mn}_{0.30})_2\text{O}_4$  (d-f) compounds which attains a complicated conical spin-spiral ordering. Similar to the parent



**Figure 4.15** The temperature dependence of the bond lengths Co-O (A-O) and Cr/Mn-O (B-O) along with the bond angles Co-O-Cr/Mn (A-O-B) and Cr/Mn-O-Cr/Mn (B-O-B) for  $\text{Co}(\text{Cr}_{0.73}\text{Mn}_{0.27})_2\text{O}_4$  [(a) & (b)] and  $\text{Co}(\text{Cr}_{0.70}\text{Mn}_{0.30})_2\text{O}_4$  [(c) & (d)] compounds.

$\text{CoCr}_2\text{O}_4$ , the magnetic spiral configuration made a cone angle with the [0 0 1] direction. There may be a change in the crystalline parameters which result in a change in the cone angles of the spin configurations of all the sub-lattices. Hence, it is remarkable to observe a variation of the cone angles across the compensation temperature in these Mn substituted compounds. The most interesting finding regarding the magnetic structure of these samples is that the magnetic spin of A-site has become anti-parallel to the [001] direction which was earlier parallel to [001] in the case of pristine  $\text{CoCr}_2\text{O}_4$ . This could be explained in terms of the reasonable changes in the

magnitude of the magnetic moments of different sublattices by substituting 27% and 30 % of Mn for Cr in  $\text{CoCr}_2\text{O}_4$ . This is the favorable spin configuration for these Mn substituted compounds for achieving the state of magnetic compensation. Further, from the magnetic structure of these samples, one can understand the reason of small value of EB in  $\text{Co}(\text{Cr}_{0.70}\text{Mn}_{0.30})_2\text{O}_4$  (cf. Fig. 4.7). Compared to earlier studied EB in Fe substituted  $\text{CoCr}_2\text{O}_4$  samples, the A-site spins becomes parallel to that of  $B_2$ -site in these Mn substituted samples which is unfavorable to achieve the similar EB effect. It should be noted that to get a large EB, the favorable condition was that A and  $B_2$  sites should be anti-parallel to each other [166]. Further, the possible reason for a minimal EB arises from the coupling of  $B_1$  and  $B_2$  sites which are anti-parallel. But the exchange coupling among B-sites is not strong enough to gives rise to a large EB in the compound.



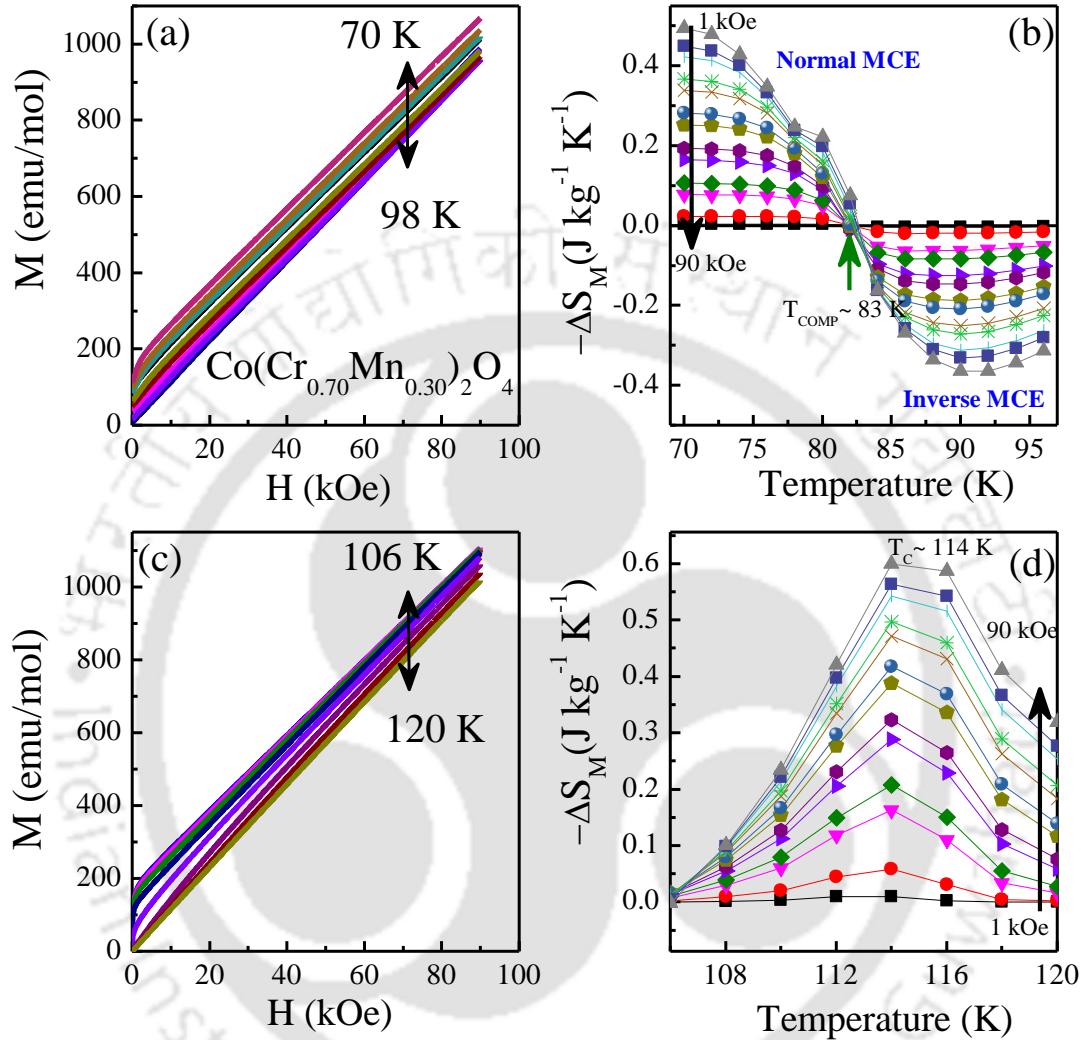
**Figure 4.16** The variation of the distortion ( $\Delta$ ) as a function of temperature along two different paths, i.e. A-O and B-O of  $\text{Co}(\text{Cr}_{0.70}\text{Mn}_{0.30})_2\text{O}_4$ .

Fig. 4.15 represents the temperature dependence of the structural parameters such as bond lengths and bond angles which are calculated from NPD data. These calculated bond lengths and bond angles correspond to magnetic super-exchange paths in both  $\text{Co}(\text{Cr}_{0.73}\text{Mn}_{0.27})_2\text{O}_4$  and  $\text{Co}(\text{Cr}_{0.70}\text{Mn}_{0.30})_2\text{O}_4$  which are important to know the possible exchange interactions present in these systems. From this figure, one can see that all the calculated bond parameters, i.e. Co-O (A-O) and Cr/Mn-O (B-O) bond lengths with Co-O-Cr/Mn (A-O-B) and Cr/Mn-O-Mn/Cr (B-O-

B) bond angles have modulations around the respective  $T_{\text{comp}}$  of both the samples. Such modulation in bond lengths and bond angles around magnetic compensation temperature indicates the magnetically driven distortions in different interstitial sites, i.e., tetrahedral A-site and octahedral B-sites of this spinel structure. Hence, such observations around  $T_{\text{comp}}$  gives raise a clue for a correlation between crystalline and magnetic structures in these compounds. Further, observed magnetic compensates state at  $T_{\text{comp}}$  is correlated with noticeable structural distortions in bond parameters of both  $\text{Co}(\text{Cr}_{0.73}\text{Mn}_{0.27})_2\text{O}_4$  and  $\text{Co}(\text{Cr}_{0.70}\text{Mn}_{0.30})_2\text{O}_4$ . In addition, One can calculate the present distortion ( $\Delta$ ) in these compounds which is defined as:  $\Delta = \left[ \frac{d_T - d_{100}}{d_{100}} \right]^2$ , where  $d_T$  and  $d_{100}$  are the bond lengths at different temperature  $T$  and at 100 K, respectively. For  $\text{Co}(\text{Cr}_{0.70}\text{Mn}_{0.30})_2\text{O}_4$ , the variation of the calculated distortion along both A-O and B-O path as a function of temperature is shown in Fig. 4.16. We observed that there is a negligible distortion occur at the low temperature as well as at high temperatures but a large jump exactly at compensation temperature ( $\sim 83$  K) is noticed in such distortion which indicates a large magneto-structural coupling in the compound.

Because of such intrinsic magnetization induced distortion ( $\Delta$ ) across  $T_{\text{comp}}$ , which in other words produces a magneto-elastic effect, it would be worthwhile to study the MCE in this temperature region. Fig. 4.17 (a) & (c) show the isothermal magnetization hysteresis (M–H) curves (First quadrant) measured in various temperature ranges of (a) 70–98 K and (c) 106–120 K (with  $\Delta T = 2$  K), with an applied field ranges from 1koe to 90 kOe. We have noticed the interesting magnetic transitions of  $T_{\text{comp}}$  ( $\sim 83$  K) and  $T_C$  ( $\sim 114$  K) from bulk dc-magnetization data; therefore these are the respective temperature regions of interest to explore the MCE behavior. Hence, we have investigated the MCE behavior in  $\text{Co}(\text{Cr}_{0.70}\text{Mn}_{0.30})_2\text{O}_4$  in the temperature regimes of 70–98 K (around  $T_{\text{comp}}$ ) and in 102–120 K (around  $T_C$ ). We have calculated the change in magnetic entropy ( $-\Delta S_M$ ) using isothermal M-H curves [Fig. 4.17 (a) & (c)] across the magnetic transitions. The field sweeping is done from 0 to 90 kOe and again back to 0. During this protocol, the sample was first cooled to 10 K (i.e. below transition temperatures) and then heated back to a particular temperature around  $T_{\text{comp}}$  without overshooting. M-H curve was measured at that temperature, and after the completion of the measurement, the sample was again cooled to 10 K. This time the sample was heated to a temperature 2 K higher than the last measurement temperature, and then, another M-H curve was

measured. This method was repeated for all the M-H curves taken within the temperatures between 70 K and 98 K (across the  $T_{\text{comp}}$ ) and also between 106 K and 120 K (across the  $T_C$ ).



**Figure 4.17** Magnetic field ( $H$ ) dependence of the magnetization ( $M$ ) for  $\text{Co}(\text{Cr}_{0.70}\text{Mn}_{0.30})_2\text{O}_4$  at different temperatures regions, 70-98 K (a) and 106-120 K (c) and calculated temperature-dependent magnetic entropy change ( $-\Delta S_M$ ) around  $T_{\text{comp}}$  (b) and around FIM transition temperature  $T_C$  (d) under various magnetic fields changes (1 kOe- 90 kOe).

Here,  $\Delta S_M$  has been calculated from the isothermal M-H curves using the Maxwell's relations [158]:

$$\Delta S_M(T,H) = \int_0^H \left( \frac{\partial M}{\partial T} \right)_H dH \quad (4.1)$$

One of the interesting observations from these plots of  $-\Delta S_M$  for this magnetically compensated compound is that there is a sign change in  $-\Delta S_M$  exactly at  $T_{\text{comp}}$ . From earlier discussed magneto-structural coupling along with the ordering of different magnetic species around  $T_{\text{comp}}$ , we have shown the consequence of the magnetic compensation on the magnetocaloric properties of  $\text{Co}(\text{Cr}_{0.70}\text{Mn}_{0.30})_2\text{O}_4$  compound. This is the key finding in this study of MCE effect in this compound which has state of magnetic compensation. A maximum value of  $-\Delta S_M$  observed is  $0.6 \text{ J kg}^{-1} \text{ K}^{-1}$  which results in a relative cooling power (RCP) of  $5.89 \text{ J kg}^{-1}$  which is near to the same order as observed in other oxides [158–160]. Such finding of sign change in  $-\Delta S_M$  across  $T_{\text{comp}}$  is very attractive as it opens a new opportunity in magnetic materials where both normal as well as inverse MCE effect persists in a single phase compound. The sign change in MCE effect is in the proximity of liquid nitrogen temperature but one can tune this temperature by other transition metal ion substitution in similar materials for practical application of magnetic compensation in the area of solid state refrigeration devices [171,176].

In addition, we modelled the temperature dependence of the different site moments for both the compounds by using the molecular-field theory according to which the magnetic moment should follow the following temperature dependence [177]:

$$\mu = \mu_0 B_J(x) \quad (4.2)$$

With,  $x = \left(\frac{3J}{J+1} \frac{T_C}{T} \frac{\mu}{\mu_0}\right)$  where  $\mu$  and  $\mu_0$  are the magnetic moments at temperature  $T$  and at  $0 \text{ K}$  and  $J$  is the total angular momentum of the system.  $B_J$  is the Brillouin function. As shown in Fig. 4.18, we have fitted the Eq. (4.2) for both the samples. Further, we have also calculated the molecular field constants ( $l$ ) from these modelled fitting;  $\lambda_A \sim 100 \text{ T}/\mu_B$ ,  $122 \text{ T}/\mu_B$  and  $\lambda_B \sim 92 \text{ T}/\mu_B$ ,  $97 \text{ T}/\mu_B$  for  $\text{Co}(\text{Cr}_{0.73}\text{Mn}_{0.27})_2\text{O}_4$  and  $\text{Co}(\text{Cr}_{0.70}\text{Mn}_{0.30})_2\text{O}_4$ , respectively which matches with similar systems [161]. It is noticed that strength of molecular field constants increases with Mn substitution. One can observe that the variation of moments deviates from the mean field behavior around respective compensation temperatures shown by a rectangular box in the Fig. 4.18. This implies that the underlying crystal structure has a strong influence to the magnetic spin configuration which results in the deviation from the Brillouin function. Hence, it confirms the presence of a strong magneto-elastic coupling in these Mn substituted compensated compounds of  $\text{CoCr}_2\text{O}_4$ .

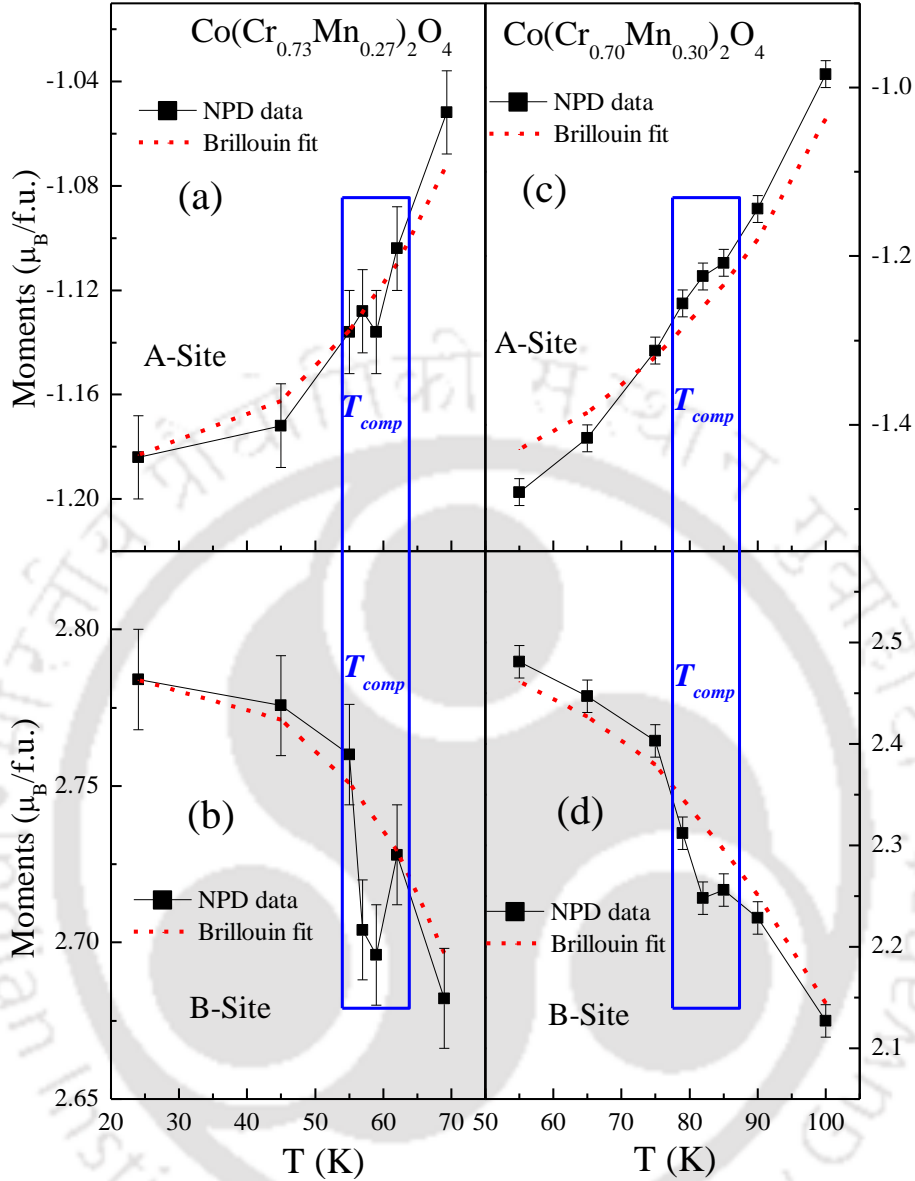


**Figure 4.18** Temperature dependent variation of different site moments along with the fit for the Brillouin function of both  $\text{Co}(\text{Cr}_{0.73}\text{Mn}_{0.27})_2\text{O}_4$  (a-b) and  $\text{Co}(\text{Cr}_{0.70}\text{Mn}_{0.30})_2\text{O}_4$  (c-d).

#### 4.4 Summary

To conclude, we have presented the detailed investigations of structural and magnetic properties through XRD, temperature and field dependent dc and ac-magnetization measurements and performing temperature dependent NPD experiments on  $\text{Co}(\text{Cr}_{1-x}\text{Mn}_x)_2\text{O}_4$  ( $x \leq 0.30$ ). Such Mn substitution with  $x = 0.27$  and  $0.30$  for Cr-site in  $\text{CoCr}_2\text{O}_4$  drive the system to magnetic compensation state at  $T = T_{\text{comp}}$  under low applied fields below which negative

magnetization has been observed in both the compounds. Further, such magnetization reversal is turnout to be in the form of field induced spin reorientation transition at the respective compensation temperature. Temperature dependent NPD experiments reveal that spin reorientations of different sublattice sites play a crucial role to attain the observed magnetic transitions in these compounds. The exchange bias like behavior observed below 10 K, and in the close vicinity of compensation point, has been discussed in the context of large anisotropy (as evidenced in the  $H_C^{\text{eff}}$ ) and spin reorientation. NPD experiments reveal the reason for getting such minimal EB field in Mn substitution case which is different from the Fe case. Observation of short range spiral ordering till lowest measuring temperature (3 K), reveals the absence of spin-spiral transition which was present in the parent  $\text{CoCr}_2\text{O}_4$  and also in lower Mn substituted samples. Change in crystalline parameters (i.e. bond lengths and bond angles) across respective  $T_{\text{comp}}$  also reveals the correlation between chemical structure and the present magnetic spin configuration around that temperature window. We also observed a sign change of  $-\Delta S_M$  across the  $T_{\text{comp}}$  where one can have both normal and inverse MCE in single phase compounds. For further detailed investigation of this sign change in  $-\Delta S_M$ , single crystal neutron scattering experiment under thermodynamical variables such as pressure (P) and field (H) is highly desirable.

## Studies on $\text{Co}_{1-x}\text{Cu}_x\text{Cr}_2\text{O}_4$ ( $x = 0.00 - 0.20$ )

### 5.1 Introduction

We have noticed that the substitution of ‘Fe & Mn’ for B (Cr)-site in  $\text{CoCr}_2\text{O}_4$  influences its magnetic structure and gives rise to interesting magnetic properties which were absent in the pristine  $\text{CoCr}_2\text{O}_4$  [161,166]. NPD experiments described that the ‘Fe’ substitution which leads to the magnetization reversal and sign change of EB field across  $T_{\text{comp}}$ , gives rise to the modulations in the magnetic structures around  $T_{\text{comp}}$ . The explanation of the observed  $T_S$  and transformation of magnetic structure around  $T_L$  could be made by performing NPD experiments at different temperatures in Fe substituted samples. In case of Mn substituted samples, there are some dissimilarity with respect to the magnetic structures of  $\text{CoCr}_2\text{O}_4$  and  $\text{Co}(\text{Cr}_{1-x}\text{Fe}_x)_2\text{O}_4$  ( $x = 0.05 - 0.075$ ) compounds. Hence, the observed magnetic properties are also different which is explained well through both bulk magnetization measurements and temperature dependent NPD experiments.

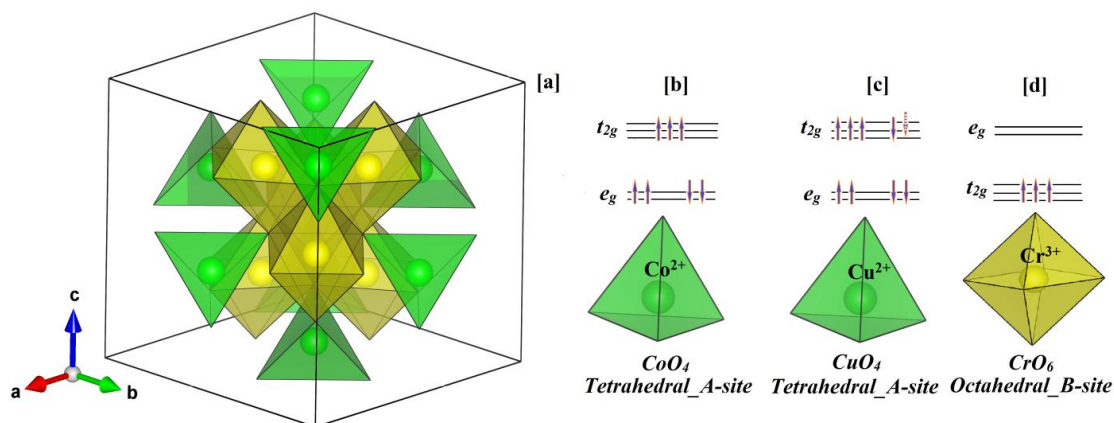


**Figure 5.1** (a) An example of the linkage of  $\text{CoO}_4/\text{CuO}_4$  tetrahedral A-site through a  $\text{CrO}_6$  octahedral B-site. Schematic representation of enlarged view of  $\text{CoO}_4$  (b) &  $\text{CuO}_4$  (c) tetrahedron and  $\text{CrO}_6$  octahedron (d) with electronic configurations of constituent  $\text{Co}^{2+}$ ,  $\text{Cu}^{2+}$  and  $\text{Cr}^{3+}$  ions, respectively. The dotted spin arrow in case of  $\text{CuO}_4$  shows the degeneracy present in the  $t_{2g}$  orbitals. Oxygen atoms are omitted for a clear view.

With the motivation of Fe and Mn substitution, we want to study the effect of transition metal ion substitution on A (Co)-site of the  $\text{CoCr}_2\text{O}_4$ . For this study, we have chosen the ‘Cu’ with the same valence state of ‘Co’ (i.e.  $\text{Co}^{2+}$ ) which has nearly similar ionic radii but different

magnetic moment in comparison to  $\text{Co}^{2+}$ . Present chapter deals with the synthesis, structural, temperature and magnetic field dependent magnetization, EB effects and detailed study of magnetic structures by temperature dependent NPD experiments of  $\text{Co}_{1-x}\text{Cu}_x\text{Cr}_2\text{O}_4$  ( $x = 0.0-0.20$ ). Fig. 5.1 depicts the crystal structure of pristine  $\text{CoCr}_2\text{O}_4$  along with electronic configuration of constituent  $\text{Co}^{2+}$ ,  $\text{Cu}^{2+}$  and  $\text{Cr}^{3+}$  ions in different crystal field environments.

## 5.2 Experimental Details

Polycrystalline samples of  $\text{Co}_{1-x}\text{Cu}_x\text{Cr}_2\text{O}_4$  ( $x = 0.0-0.20$ ) were prepared by standard solid state reaction method. Stoichiometric amounts of the constituent oxides ( $\text{Co}_3\text{O}_4$ ,  $\text{Cr}_2\text{O}_3$  and  $\text{CuO}$ ) with high purity ( $\geq 99.6\%$ ) were initially mixed using an agate mortar pestle. These mixed powders were pressed into cylindrical pellets of diameter  $\sim 10$  mm using a hydraulic press with a maximum load of 5 tons per  $\text{cm}^2$  and placed in a platinum crucible. All the pellets were finally sintered at  $1200^\circ\text{C}$  for 24 h in air with intermediate grinding and pre-sintering. The structural characterization was performed using a Rigaku x-ray diffractometer (model TTRAX III) with  $\text{Cu-K}\alpha$  radiation ( $\lambda = 1.54056 \text{ \AA}$ ). Temperature dependent NPD measurements were carried out on finely ground powders of magnetically compensated  $\text{Co}_{0.8}\text{Cu}_{0.2}\text{Cr}_2\text{O}_4$  sample packed in a vanadium container at the UGC-DAE CSR beam line at Dhruva reactor using a focusing crystal based powder diffractometer (FCD-PD3). Closed cycle refrigerator (CCR) was used to cool the samples from room temperature to 3 K. The NPD patterns were recorded using an array of linear PSDs. Neutrons at a wavelength of  $1.48 \text{ \AA}$  were used in the measurements [124]. Bulk dc magnetization measurements were performed using a SQUID based magnetometer from Quantum Design with temperature capabilities of 2–320 K and magnetic field (H) up to  $\pm 70$  kOe along with ac-magnetic susceptibility measurements from PPMS with ACMS option. The temperature dependent heat capacity data [ $C_p(T)$ ] was recorded by means of a physical property measurement system (PPMS) from Quantum Design.

## 5.3 Results and Discussions

### 5.3.1 X-ray Diffraction

Room temperature XRD pattern of the polycrystalline sample of  $\text{Co}_{1-x}\text{Cu}_x\text{Cr}_2\text{O}_4$  ( $x = 0.0-0.20$ ) was analyzed by Rietveld refinement using the FullProf program [147]. Fig. 5.2 shows the

typical XRD pattern of prepared compounds. This analysis reveals that all the patterns are consistent with the standard cubic spinel structure with  $Fd\bar{3}m$  (No. 227) space group, without any trace of impurities. The lattice parameter is found to be  $a = 8.328(1) \text{ \AA}$  which is slightly smaller than the lattice parameter of pristine  $\text{CoCr}_2\text{O}_4$  ( $a = 8.333 \text{ \AA}$ ) [16]. Such minimal variation in the lattice parameter is generally due to the difference in the ionic radii of the  $\text{Co}^{2+}$  ( $0.58 \text{ \AA}$ ) and  $\text{Cu}^{2+}$  ( $0.57 \text{ \AA}$ ) in tetrahedral coordination [ref shanno radii]. Even though  $\text{Cu}^{2+}$  is a Jahn–Teller (JT) active ion and occupies tetrahedral A-site which can induce a structural transition from cubic to other lower symmetry structure, but there is no structural transition is observed at room temperature for Cu substituted  $\text{CoCr}_2\text{O}_4$  compounds.

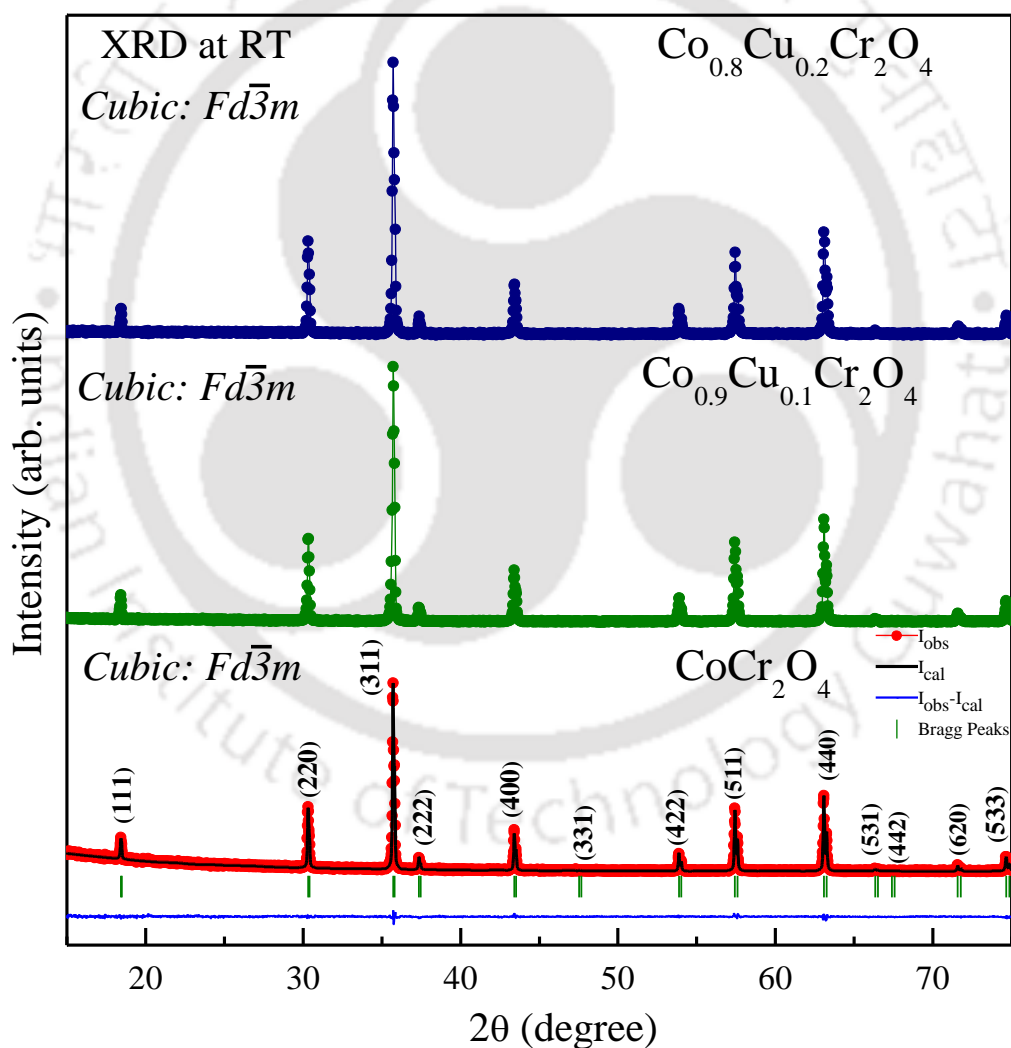


**Figure 5.2** Room temperature X-ray diffraction patterns of  $\text{Co}_{1-x}\text{Cu}_x\text{Cr}_2\text{O}_4$  ( $x = 0.0-0.20$ ) polycrystalline compound with Rietveld refinement showing that all compounds are in single phase with cubic  $Fd\bar{3}m$  space group.

### 5.3.2 Temperature and Field Dependent Magnetic Properties

Fig. 5.3 shows the temperature dependence of dc-magnetization ( $M$ - $T$ ) curves for polycrystalline  $\text{Co}_{1-x}\text{Cu}_x\text{Cr}_2\text{O}_4$  ( $x = 0.0-0.20$ ) compounds both in ZFC and FC modes under the applied field of  $H = 1$  kOe. We have observed that FIM transition  $T_C$  is decreased with Cu substitution which is simply due to the weakening of magnetic exchange interactions between A and B-sites. Further, one can notice that negative magnetization is taking place below  $T_{\text{comp}} \sim 52$  K in 20% Cu substituted sample (i.e.  $\text{Co}_{0.8}\text{Cu}_{0.2}\text{Cr}_2\text{O}_4$ ). As we are interested in the state of magnetic compensation, we moved further with this compensated sample for more detailed study in terms of both bulk dc and ac-magnetization and temperature dependent NPD experiments.

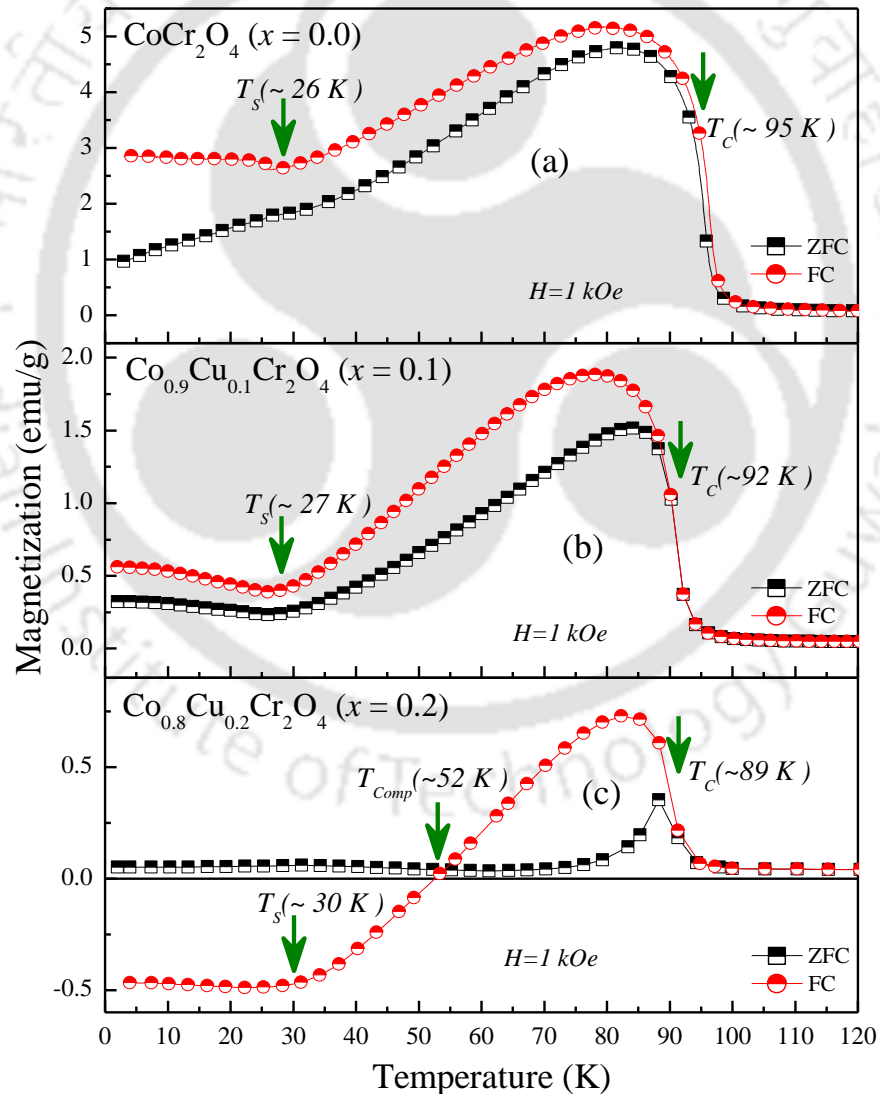


**Figure 5.3** Temperature dependent dc-magnetization of  $\text{Co}_{1-x}\text{Cu}_x\text{Cr}_2\text{O}_4$  ( $x = 0.0-0.20$ ) under ZFC and FC conditions with the applied field of  $H \sim 1$  kOe.

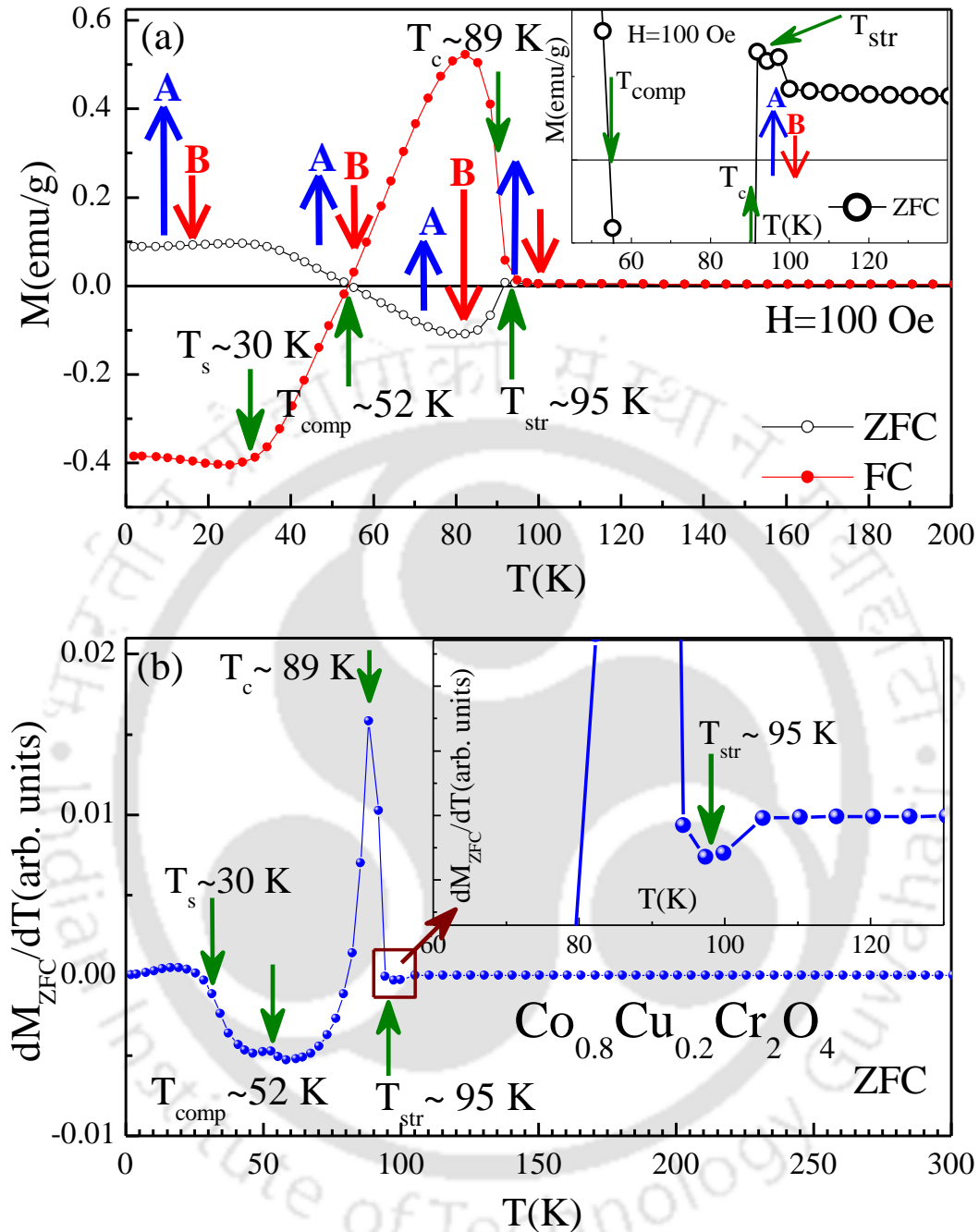


**Figure 5.4** (a) Temperature dependent magnetization for  $\text{Co}_{0.8}\text{Cu}_{0.2}\text{Cr}_2\text{O}_4$  at  $H = 100$  Oe under both the ZFC and FC conditions, and (b) shows the  $dM_{\text{ZFC}}/dT$  plot of the same sample. Insets show the enlarged portion of the plot where another transition ( $T_{\text{str}} \sim 95$  K) can be seen clearly. Arrows represent the different magnetic transitions in the sample.

Fig. 5.4 (a) shows the temperature dependent dc-magnetization ( $M$ - $T$ ) curves of the  $\text{Co}_{0.8}\text{Cu}_{0.2}\text{Cr}_2\text{O}_4$  compound in ZFC and FC states under low the applied field of  $H = 100$  Oe and Fig. 5.4 (b) demonstrates the first order derivative of the magnetization curve in ZFC protocol,

( $dM_{ZFC}/dT$ ) versus temperature plot where all the transitions are observed more evidently. The main panel of this figure depicts that the onset of FIM ordering temperature occurs at 100 K, and the long range FIM ordering completes by  $T_C \sim 89$  K. Within this window of temperature (100–89 K) where the compound undergoes a long range FIM ordering, we observe a small peak (named as  $T_{str} \sim 95$  K) in ZFC magnetization data which can be attributed to a magneto-structural transition. This is related to the structural distortion of the crystal lattice which shall be discussed later. With further lowering of the temperature, we observed the compensation temperature at  $T_{comp} \sim 52$  K. The signature of long range spin-spiral transition which was earlier observed in parent  $CoCr_2O_4$  [8,16] and Fe substituted  $CoCr_2O_4$  [161] compounds, is found to occur at  $T_S \sim 30$  K.

The FIM ordering in the present spinel compound results in a non-collinear spiral configuration below  $T_C$ . To avoid complexity in the spin configurations, we shall confine ourselves only to the longitudinal spin components (both A and B sublattices) along the direction of applied magnetic field and present discussion deals with these molds. In Fig. 5.4 (a), the spin component of A-sublattice is represented in blue color, whereas the spin component of the entire B-sublattices is represented in red color. At very low temperature, the data depicts that the ZFC magnetization is positive. Hence, we can infer that the magnitude of the longitudinal A-site moment which is parallel to the applied magnetic field is larger than the magnitude of the longitudinal B-site moment which is anti-parallel to the applied magnetic field [16]. With increase in temperature, it reaches a compensated state at  $T \sim 52$  K where magnitudes of spin moments of both sublattices exactly cancel each other resulting in a zero magnetic moment. With further increase in temperature, we find the magnitude of the longitudinal B-site moment which is anti-parallel to the applied magnetic field is larger than the magnitude of the longitudinal A-site moment which is parallel to the applied magnetic field, resulting in the negative magnetization. Close to the FIM ordering temperature, we find that magnitude of longitudinal spin moments in both the sublattices becomes comparable, resulting in the decrease in the magnitude of the net magnetization. But an interesting fact is that the net magnetization becomes positive before reaching the paramagnetic state. In this region, the longitudinal magnetic moment of A-site is larger than that of the resultant B-site [see inset of the Fig. 5.4 (a)] which is due to the internal reorientation of the magnetic moments. The crystalline structural distortion can be held responsible for this internal reorientation of magnetic moments.

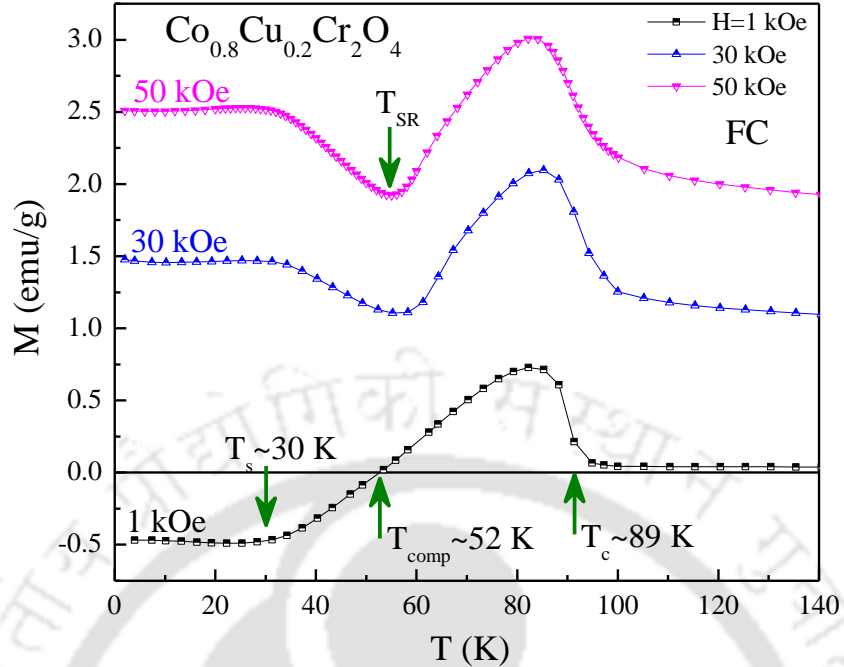


**Figure 5.5** Temperature dependent dc-magnetization of  $\text{Co}_{0.8}\text{Cu}_{0.2}\text{Cr}_2\text{O}_4$  sample measured in FC mode for different applied fields (1 kOe, 30 kOe and 50 kOe).

The isothermal FC magnetization data resembles a classical ferrimagnet. Below  $T_{\text{comp}}$ , the magnitude of B-site moment is larger than that of the A-site magnetic moment whereas above  $T_{\text{comp}}$ , the magnitude of A-site moment is larger than that of the B-site magnetic moment. Fig. 5.5 depicts the isothermal FC magnetization of the  $\text{Co}_{0.8}\text{Cu}_{0.2}\text{Cr}_2\text{O}_4$  compound under different applied fields. This plot shows how gradually the FC curve changes with increasing applied field from 1 kOe to 50 kOe. It is noticeable that under low field, i.e. 1 kOe, FC curve exhibits magnetization reversal below the  $T_{\text{comp}}$ , while with the increase in the field, magnetization shows a turnover exactly at  $T_{\text{comp}}$ . Further, it has also been observed that this field induced transition of  $\text{Co}_{0.8}\text{Cu}_{0.2}\text{Cr}_2\text{O}_4$  does not change with temperature under the large field of 50 kOe.

The temperature dependence of the ac-magnetic susceptibility ( $\chi'$ ) was measured using different frequencies  $f = 487, 987$  and  $4797$  Hz with  $h_{\text{ac}} = 3$  Oe &  $H_{\text{dc}} = 0$  Oe which is shown in Fig. 5.6. It has been observed that there are two different peaks in the close vicinity of ordering temperature, one at  $T_{\text{str}} = 95$  K and another one is at  $T_{\text{C}} \sim 89$  K which corroborate with dc-magnetization measurements in ZFC protocol discussed in the previous section. The presence of a large peak around 89 K indicates the long range FIM ordering in  $\text{Co}_{0.8}\text{Cu}_{0.2}\text{Cr}_2\text{O}_4$ . In addition,

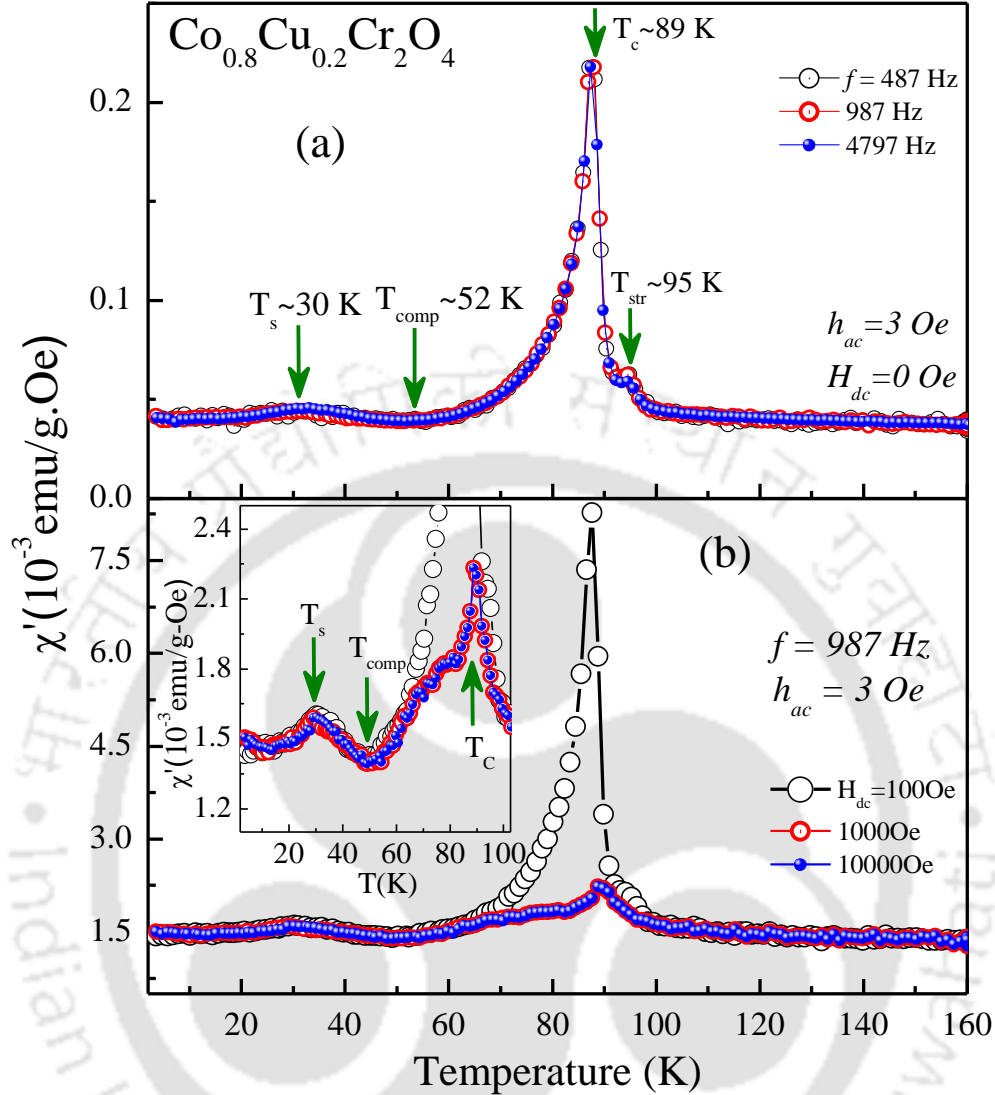


**Figure 5.6** (a) Temperature dependence of ac-magnetic susceptibility of  $\text{Co}_{0.8}\text{Cu}_{0.2}\text{Cr}_2\text{O}_4$  recorded at various frequencies, 487 Hz, 987 Hz and 4797 Hz under zero dc-bias field with  $h_{ac} = 3$  Oe. (b) shows the effect of applied magnetic field for  $f = 987$  Hz of the same sample. Inset shows the enlarged view around magnetic transitions.

we observe a small peak around  $T \sim 95$  K which could be related to the structural transition present in the system (will discuss in following section). The main peak representing long-ranged FIM transition at 89 K is frequency independent and, therefore, ruling out the possibility of glassy nature of the transition. All magnetic transitions present in dc magnetization measurements also have their signatures in the ac susceptibility ( $\chi_{ac}$ ) curve, shown in Fig. 5.6 (a). Further, Fig. 5.6 (b) depicts the temperature dependence of  $\chi_{ac}'$  with  $h_{ac} = 3$  Oe superimposed with various dc fields  $H_{dc} = 100$  Oe, 1 kOe and 10 kOe. From here, one can see that the main large peak around FIM transition is suppressed with the increase in  $H_{dc}$ . Interestingly the small

peak around 95 K disappears or merges to a single peak. Moreover, a very clear down turn exactly at  $T_{\text{comp}}$  can be seen both in absence and presence of applied dc field. This signature of  $T_{\text{comp}}$  is unaffected with the increase in dc field till 10 kOe. In order to resolve the nature of low temperature magnetic ordering present in this system, experimental tools, such as neutron diffraction is very much essential, and have, therefore, been performed to get a clear understanding of magnetic ordering at the microscopic level.

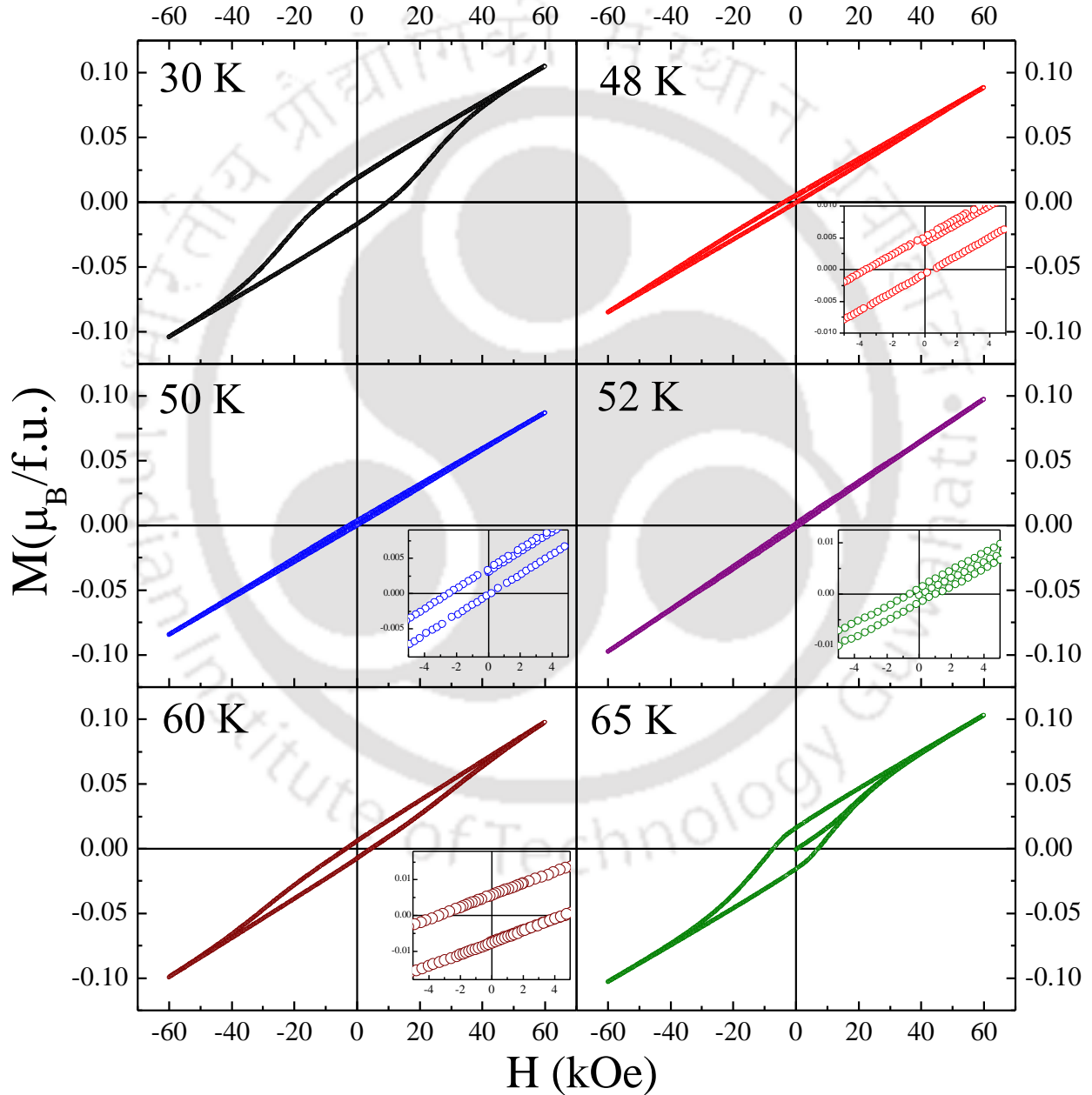


**Figure 5.7** The magnetization ( $M$ ) versus field ( $H$ ) hysteresis loops of  $\text{Co}_{0.8}\text{Cu}_{0.2}\text{Cr}_2\text{O}_4$  are shown at selected temperatures in the vicinity of compensation temperature. The respective insets show the enlarged view of  $M$ - $H$  loops near origin showing the asymmetry in the loops.

### 5.3.3 Exchange Bias Effect

Hysteresis loop (M-H) measurements of  $\text{Co}_{0.8}\text{Cu}_{0.2}\text{Cr}_2\text{O}_4$  were performed at selected temperatures between 3 and 100 K in the magnetic field range of  $-60$  to  $+60$  kOe. These measurements were done in the similar protocol as done in the earlier chapters. Fig. 5.7 shows the hysteresis loops, at six selected temperatures (especially in the vicinity of  $T_{\text{comp}}$ ) which favor the FIM behavior in the compound. All respective insets depict the enlarged view of the loops for a clear view to notice the asymmetry in the M-H loops measured at the different temperature in the vicinity of magnetic compensation.

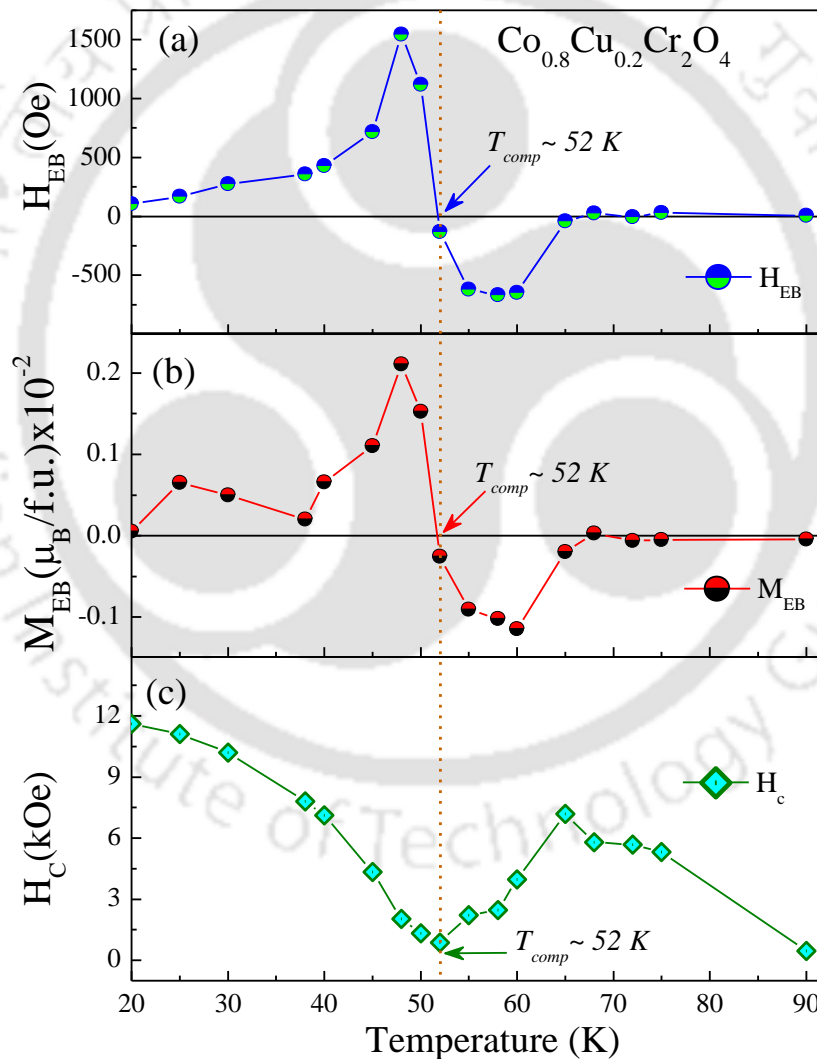


**Figure 5.8** The temperature variation of exchange bias field; (a)  $H_{\text{EB}}(T)$ , (b)  $M_{\text{EB}}(T)$ , and (c) coercive field  $H_{\text{c}}(T)$  in  $\text{Co}_{0.8}\text{Cu}_{0.2}\text{Cr}_2\text{O}_4$ . The lines connecting the data points are visual guides.

The standard definition of EB field which is calculated in terms of the loop shifting along the field direction i.e.  $H_{EB} = -(H_+ + H_-)/2$ , where  $H_+$  and  $H_-$  are magnetic field values at  $M = 0$ , similarly the  $M_{EB} = (M_+ + M_-)/2$  for the magnetization at  $H = 0$  and coercivity can be calculated as  $H_C = (H_+ - H_-)/2$ . Fig. 5.8 depicts the  $H_{EB}$  (a),  $M_{EB}$  (b) and  $H_C$  (c) of  $Co_{0.8}Cu_{0.2}Cr_2O_4$ . We have noticed that, below 10 K, all the M-H data appear like minor loops; thus, magnitudes of  $H_{EB}$ ,  $M_{EB}$  and  $H_C$  will not be worth to present. Interestingly, one can see that there is a sign change both in the  $H_{EB}$  and  $M_{EB}$  across  $T_{comp} \sim 52$  K. The value of the  $H_{EB}$  in this system is about  $\sim 1400$  Oe, which is analogous to the values in the rare earth alloys. From Fig. 5.8(c), it is observed that  $H_C(T)$  collapses dramatically to zero at  $T_{comp}$  in the temperature window ( $\Delta T$ ) of  $40 < T < 65$  K. Fe substituted polycrystalline  $CoCr_2O_4$  also perceived the similar behavior of  $H_{EB}(T)$  and  $H_C(T)$  in the vicinity of  $T_{comp}$  [166,172].

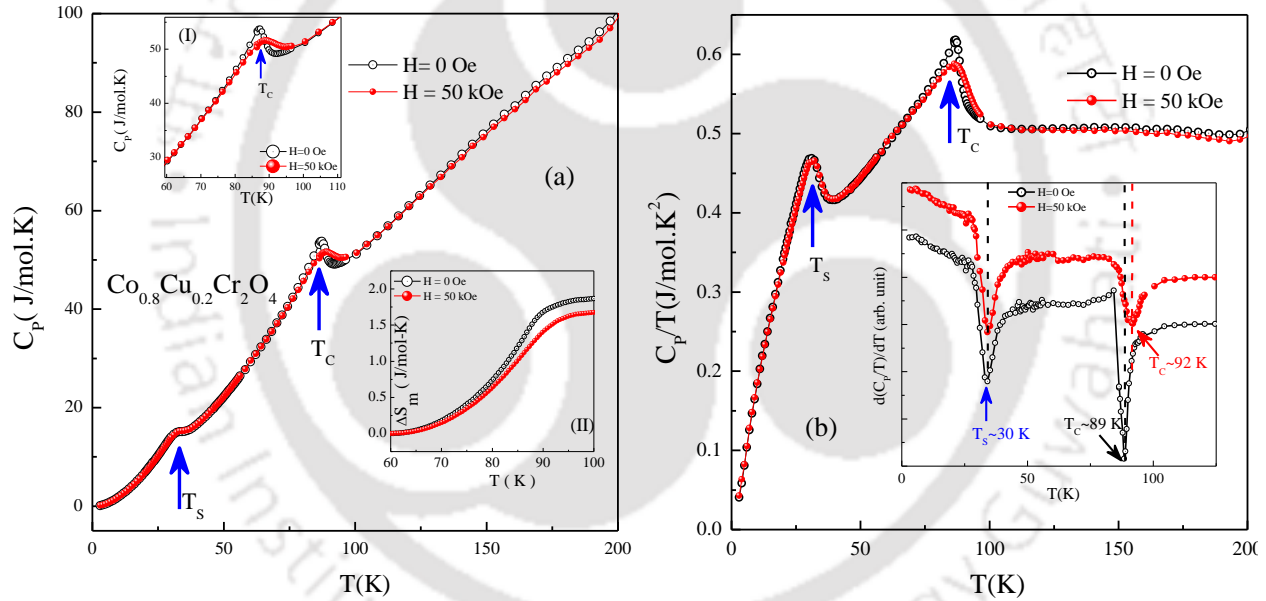


**Figure 5.9** The main panel of (a) shows the temperature dependent specific heat  $C_p(T)$  of  $Co_{0.8}Cu_{0.2}Cr_2O_4$  sample measured with  $H = 0$  Oe and 50 kOe. Insets (I) and (II) show the enlarged view across  $T_c$  and magnetic entropy  $\Delta S_m(T)$  across the  $T_c$ , respectively. Main panel of (b) shows the  $C_p(T)/T$  with the first order derivative in the inset.

The plots of the temperature dependence of specific heat  $C_p(T)$  and  $C_p(T)/T$  of  $Co_{0.8}Cu_{0.2}Cr_2O_4$  measured under  $H = 0$  Oe and 50 kOe are shown as the main panel of Fig. 5.9 (a) and (b), respectively. Measurements were done at smaller temperature intervals around transition temperature regions. At  $H = 0$  Oe, two peaks in  $C_p$  versus  $T$  are observed, at  $T_S = 30$  K and at  $T_C \sim 89$  K. A lambda type peak observed around  $T_C$  represents the FIM transition in the

compound. Another peak which is weak, like a shoulder at around  $T_S = 30$  K, represents spin-spiral transition in the sample. In applied field of 50 kOe, the peak at  $T_C$  clearly smears and shifts towards higher temperatures (see inset of Fig. 5.9 (b)). Interestingly, another peak at  $T_S$  is unaffected with the application of large field,  $H = 50$  kOe. Inset (II) of Fig. 5.9 (a) demonstrates the temperature dependence of change in magnetic entropy,  $\Delta S_m(T)_H = (C_p(T)/T)dT$ . One can see that  $\Delta S_m(T)$  decreases with increase in the applied field. As there is always lattice contribution to total  $C_p(T)$ , we have, therefore, plotted temperature dependence of  $C_p(T)/T$  in Fig. 5.9 (b) to get a clear picture of the magnetic ordering. Inset of Fig. 5.9 (b) shows the clear shifting of  $T_C$  towards higher temperature. This shifting of  $T_C$  towards higher temperature could be due to the application of applied field which makes possible the unstable spin configuration around  $T_C$  transform to a stable one. This is also confirmed from the entropy calculation which shows that  $\Delta S_m(T)_{H=50 \text{ kOe}} < \Delta S_m(T)_{H=0 \text{ kOe}}$  [cf. inset of Fig. 5.9 (a)].

### 5.3.4 Temperature Dependent Neutron Powder Diffraction Studies

The structural and magnetic phases of  $\text{Co}_{0.8}\text{Cu}_{0.2}\text{Cr}_2\text{O}_4$  are identified by performing temperature dependent NPD experiments. NPD patterns have been measured in zero fields at various temperatures between 300–3 K which covers paramagnetic state to magnetically ordered states across  $T_C$ ,  $T_{\text{comp}}$  and  $T_S$ . Fig. 5.10 shows the Rietveld refinement of the NPD patterns recorded at 300 K (paramagnetic state), at 51 K (close to  $T_{\text{comp}}$ ) and at 3 K (below  $T_S$ ) for  $\text{Co}_{0.8}\text{Cu}_{0.2}\text{Cr}_2\text{O}_4$  using the FULLPROF program [147]. The temperature dependencies of the different magnetic Bragg peaks intensity of  $\text{Co}_{0.8}\text{Cu}_{0.2}\text{Cr}_2\text{O}_4$  are plotted in Fig. 5.11 which clearly shows that magnetic ordering starts around 90 K. Interestingly, we have also found that there is a non-monotonic variation in the calculated integrated intensity of magnetic reflections in the vicinity of  $T_{\text{comp}}$ . For low temperature NPD data ( $T = 3\text{--}20$  K), we have done magnetic symmetry analysis using the program BasIreps for the magnetic atoms on different sites for different propagation vector ( $k$ ) which has given the best fitted values for magnetic structures refinement between 3–20 K NPD data. Above  $T = 20$  K, or for the temperature  $T = 45\text{--}90$  K, we have FIM ordering with propagation vector  $k = [0 \ 0 \ 0]$  in addition to the nuclear phases. From bulk dc-magnetization measurements, we know that  $\text{Co}_{0.8}\text{Cu}_{0.2}\text{Cr}_2\text{O}_4$  is paramagnetic above 90 K, hence only the nuclear (crystallographic) phase was included in the refinement for

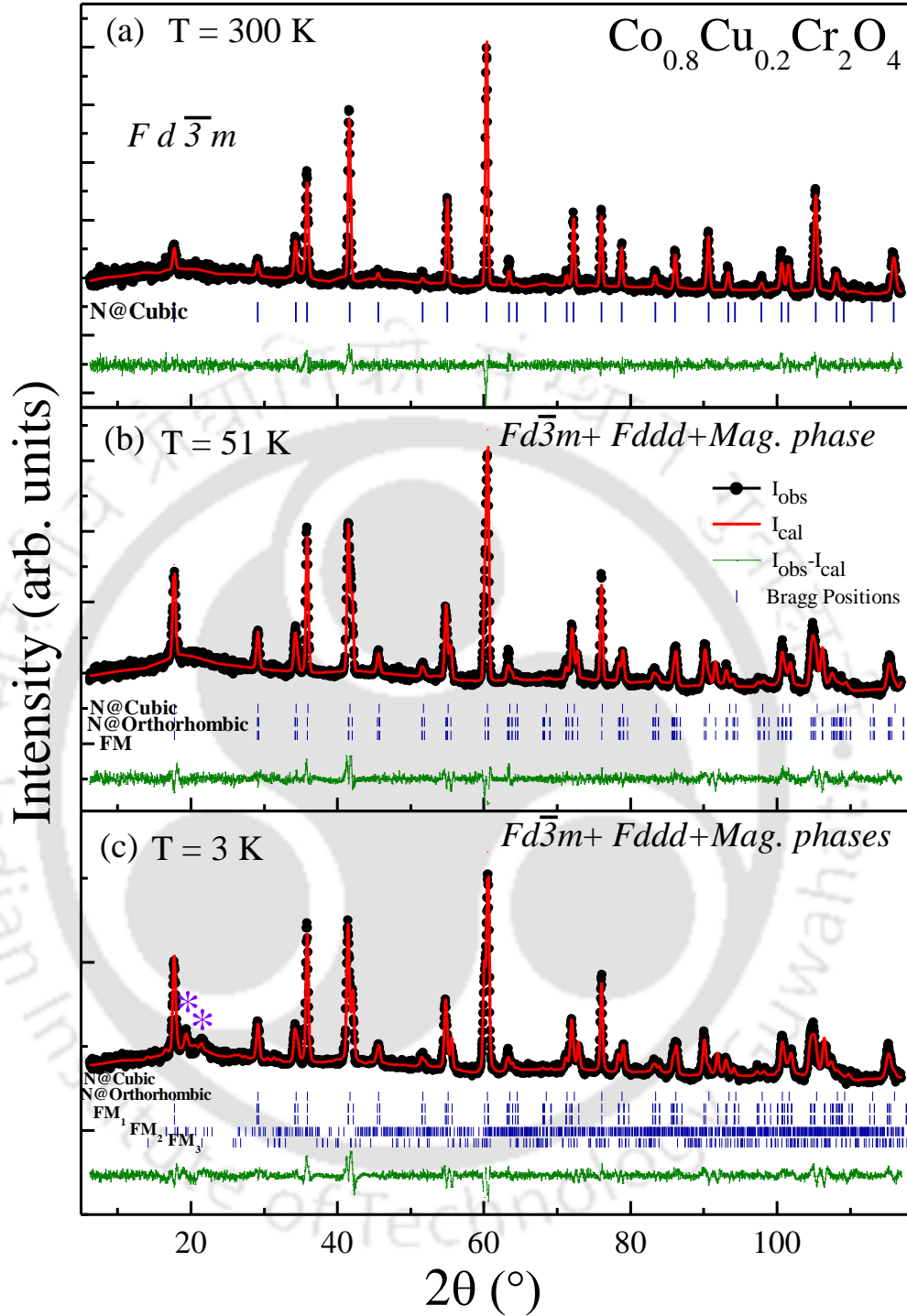


**Figure 5.10** Temperature dependent NPD patterns with Rietveld refinement in zero field at (a)  $T = 300 \text{ K}$ , (b)  $51 \text{ K}$  and (c)  $3 \text{ K}$  of  $\text{Co}_{0.8}\text{Cu}_{0.2}\text{Cr}_2\text{O}_4$ . NPD pattern at room temperature ( $300 \text{ K}$ ) is refined using a structural phase (indicated by the first row of vertical tick marks) whereas for  $51 \text{ K}$  another structural phase along with FM phase (second row and third row) is also included in the refinement. NPD patterns at  $3 \text{ K}$  include additional incommensurate (IC) phase along with all these phases in the refinement.

NPD data above 90 K. Fig. 5.10 (a) shows that NPD pattern at 300 K with nuclear reflections and well fitted to the normal cubic spinel structure. There is FIM ordering at 52 K (close to the state of magnetic compensation) which can be clearly seen from Fig. 5.10 (b) with quite enhancement in the magnetic spin magnitude representing by lower angle Bragg peaks. In addition, Fig. 5.10 (c) depicts the emergence of new satellite peaks at much lower temperatures (3 K) with IC magnetic phases which start below  $T_S$ . Pictorial representation of temperature dependent magnetic structure of  $\text{Co}_{0.8}\text{Cu}_{0.2}\text{Cr}_2\text{O}_4$  is shown in Fig. 5.12.

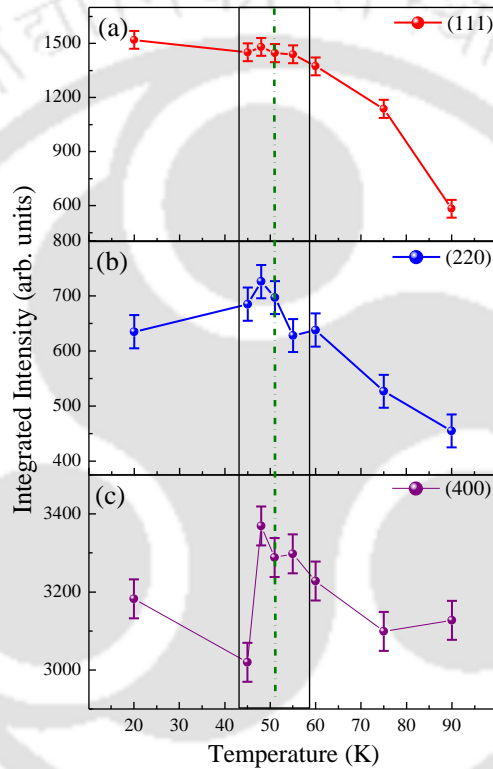


**Figure 5.11** Temperature dependence of the integrated intensity of the fundamental reflections for  $\text{Co}_{0.8}\text{Cu}_{0.2}\text{Cr}_2\text{O}_4$ .

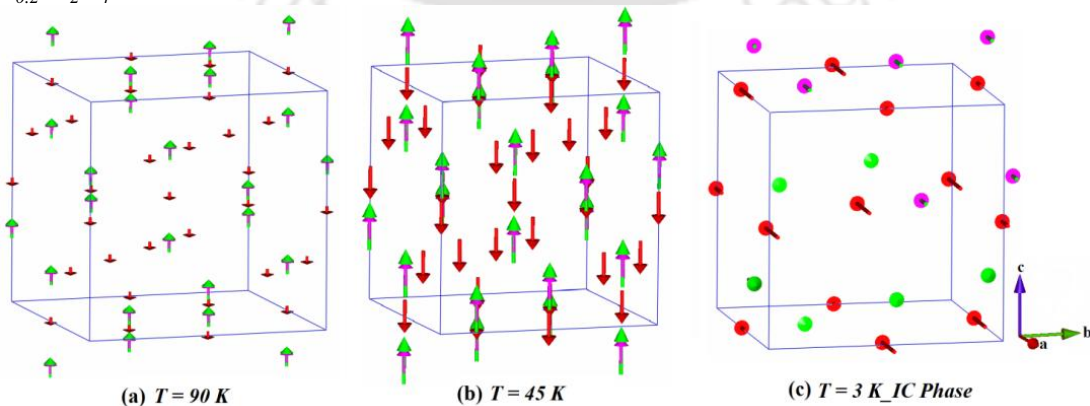


**Figure 5.12** Low temperature magnetic structure of  $\text{Co}_{0.8}\text{Cu}_{0.2}\text{Cr}_2\text{O}_4$  at (a) 90 K, (b) 45 K, and (c) 3 K.

In order to understand the observed distortion at 95 K from dc-magnetization, temperature dependent NPD experiment is extremely helpful. The structural distortion can be experimentally determined through the technique of neutron scattering at different temperatures along with the magnetic structure of the compound. Here, NPD patterns were recorded on  $\text{Co}_{0.8}\text{Cu}_{0.2}\text{Cr}_2\text{O}_4$  sample at 200 K (paramagnetic state) and 90 K (close to FIM transition). Fig. 5.13 (a) depicts the NPD pattern at 200 K which is refined perfectly with the cubic spinel structure without including any addition phase. The cell parameters, the position of oxygen atoms and occupancies are refined and pattern is perfectly fitted with cubic structure as shown Table 5.1. No impurity reflections were observed in the pattern which indicates that the sample is prepared in single phase. But, on lowering of temperature to 90 K, distortion in some higher order Bragg reflections (such as (800) reflection) was observed in the NPD pattern [Fig. 5.13 (b)] which gives rise to the possibility of a structural distortion present in the system. There is no obvious structural phase transition observed at 200 K in NPD data and the symmetry is perfectly cubic, as shown in Fig. 5.13 (a). The similarity in the tetrahedral ionic radii of  $\text{Co}^{2+}$  and  $\text{Cu}^{2+}$  ions allows the prepared compound,  $\text{Co}_{0.8}\text{Cu}_{0.2}\text{Cr}_2\text{O}_4$  to maintain cubic symmetry at room temperature. At low temperature (90 K), we have observed a phase co-existence of both cubic ( $Fd\bar{3}m$ ) and orthorhombic ( $Fddd$ ) nuclear phases along with the magnetic phase, as shown in Fig. 5.13 (b). Regarding structural distortion or phase-coexistence around magnetic ordering temperature, we observe that, there is no peak splitting of (800) reflection at 200 K but at low temperature (90 K), Bragg peak splitting of the (800) reflection is deconvoluted into contributions from both  $Fd\bar{3}m$  and  $Fddd$  phases (as shown in Fig. 5.13 (c) & (d)). Nearly 32% of cubic and 68% of orthorhombic phase fractions coexist in the 90 K nuclear structure of  $\text{Co}_{0.8}\text{Cu}_{0.2}\text{Cr}_2\text{O}_4$ . With further lowering in temperature, the  $Fddd$  phase fraction increases to ~88% at 3 K. The observed phase coexistence over a wide temperature range in present work may arise due to the one of the possibilities that the cubic phase goes quickly to orthorhombic phase via the tetragonal one within a very narrow temperature range. Hence, the presence of stress and the strain due to the quick transformation in the sample which was not relaxed, leading to the phase coexistence over wide temperature range. Similar phase co-existence over relatively wide temperature range has also been observed in other spinels [178]. The crystalline parameters such as lattice constants, atomic site positions, and occupancies etc. along with the values of fitting parameters are presented in Table 5.2.

Table 5.1 Refined parameters of  $\text{Co}_{0.8}\text{Cu}_{0.2}\text{Cr}_2\text{O}_4$  from NPD pattern at 200 K.

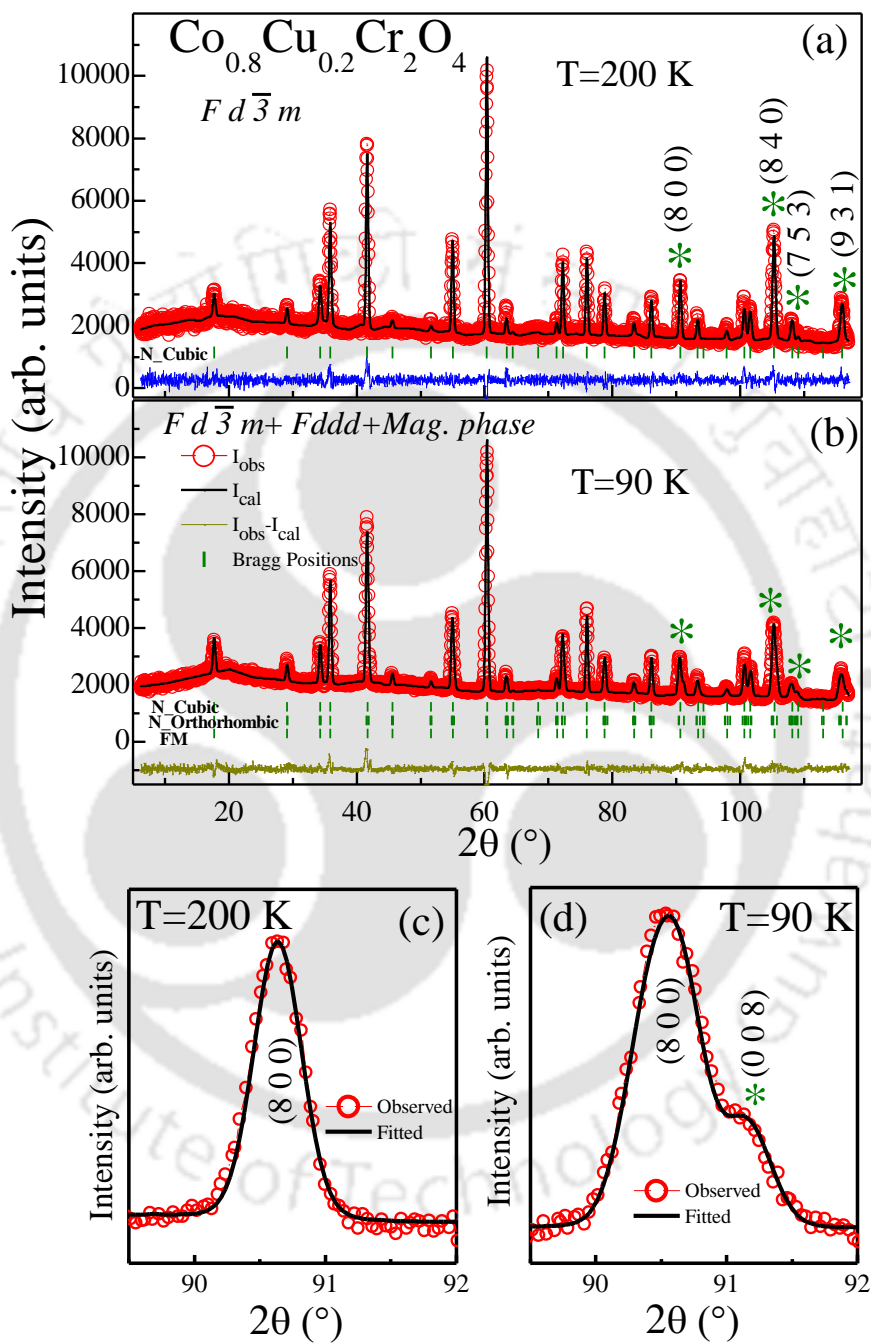
Atoms	Site	<i>x</i>	<i>y</i>	<i>z</i>	Site occu.
Co	8a	0.125	0.125	0.125	0.796(2)
Cu	8a	0.125	0.125	0.125	0.194(2)
Cr	16d	0.5	0.5	0.5	1.021(1)
O	32e	0.262(1)	0.262(1)	0.262(1)	0.999(1)

Table 5.2 Crystallographic information and Rietveld profile reliability factors for  $\text{Co}_{0.8}\text{Cu}_{0.2}\text{Cr}_2\text{O}_4$  from NPD pattern at 200 K and 90 K.

Parameters	T = 200 K	T = 90 K
Crystal Symmetry	Cubic	Cubic(I) + Orthorhombic(II)
Space Group	$Fd\bar{3}m$	$Fd\bar{3}m + Fddd$
Phase Fraction	100%	32% [I]+68% [II]
a (Å)	8.3262(2)	8.3242(7) [I], 8.3400(7) [II]
b (Å)	8.3262(2)	8.3483(7) [II]
c (Å)	8.3262(2)	8.2890(7) [II]
c/a	1	0.994
V (Å <sup>3</sup> )	577.22(1)	577.03(1)[I], 576.95 (1) [II]
Theta Range	6–120°	6–120°
Bragg R-factor	6.0	6.3 & 6.9
Magnetic R-factor	0	9.2
GOF ( $\chi^2$ )	3.6	3.5

For the low temperature case (i.e.  $T < 200$  K), the structure distortion from cubic to orthorhombic is observed at  $T \sim 90$  K. With further lowering in temperature this orthorhombic phase is starting to dominate over cubic phase which is depicted in Fig. 5.14 In case of temperature  $T \geq 200$  K, there is no obvious structural phase transition observed and symmetry is cubic. These different patterns were well described by the jumble of space groups  $Fd\bar{3}m$  and  $Fddd$ . This is observed that there is cubic-orthorhombic structural phase transition instead of cubic-tetragonal-orthorhombic sequence upon decreasing the temperature which is very common. For  $T = 90$  K, although the phase transition related peaks splitting is not much, the peak splitting of (800) at 90 K is very clear which was absent at  $T \geq 200$  K. The non-monotonic change in phase fractions of this compound around compensation temperature (as shown in Fig. 5.14) is corroborating with the magnetic structure around  $T_{\text{comp}}$ . The temperature dependent anomaly at  $\sim 52$  K is strong on both integrated intensities and phase fractions; hence a correlation between the crystal and magnetic structure is suggested around magnetic compensation in  $\text{Co}_{0.8}\text{Cu}_{0.2}\text{Cr}_2\text{O}_4$ . It is possible that the anomalies in the bulk magnetization measurements

originate from the transition/crossover to the different ground state of  $t_{2g}$  orbitals in the tetrahedral environment due to the structural transition/distortion.



**Figure 5.13** NPD patterns of  $\text{Co}_{0.8}\text{Cu}_{0.2}\text{Cr}_2\text{O}_4$  measured at (a) 200 K, and (b) 90 K with Rietveld refinement. The enlarged view of the (800) Bragg reflections of these NPD patterns have been shown at (c) 200 K, and (d) 90 K. The stars indicate the distorted peaks in the patterns.

Pristine compound  $\text{CoCr}_2\text{O}_4$ , does not show any structural phase co-existence/transition due to the absence of Jahn-Teller active ion with orbital degree of freedom at tetrahedral A-site.  $\text{CoCr}_2\text{O}_4$  is perfectly cubic till low temperature with complex non-collinear magnetic ordering with two magnetic sub lattices, namely A and B [12–14]. From the recent developments in Fe substituted  $\text{CoCr}_2\text{O}_4$  compound [24, 27], it has been observed that there is no crystalline structural phase transition close to the FIM transition. From this observation, it is very clear that substitution of the Jahn-Teller active  $\text{Cu}^{2+}$ -ions gives rise to the observed structural phase distortion in  $\text{Co}_{0.8}\text{Cu}_{0.2}\text{Cr}_2\text{O}_4$ . The weakening of the overall strength of magnetic interactions is attributed to the lower spin of  $\text{Cu}^{2+}$  ( $3d^9$ )  $S = 1/2$  compared to  $\text{Co}^{2+}$  ( $3d^7$ )  $S = 3/2$ . The higher spin of  $\text{Co}^{2+}$  contributes to stronger magnetic interactions in parent  $\text{CoCr}_2\text{O}_4$ . The onset of magnetic ordering in  $\text{Co}_{0.8}\text{Cu}_{0.2}\text{Cr}_2\text{O}_4$  occurs at lower temperature compared to  $\text{CoCr}_2\text{O}_4$  due to the dilution of A-site spins. From NPD, it is clear that the substituted  $\text{Cu}^{2+}$  -ions occupy only the A site of the spinel, and the compound has the normal spinel structure with the formula  $[\text{Co}^{2+}\text{Cu}^{2+}][\text{Cr}^{3+}]_2\text{O}_4$ . A cubic and orthorhombic phase co-existence has been observed at 90 K from NPD data which matches with the  $T_C \sim 89$  K of magnetization data. The spin-Jahn-Teller distortion observed in  $\text{Co}_{0.8}\text{Cu}_{0.2}\text{Cr}_2\text{O}_4$  is illustrated by the splitting of the (8 0 0) reflection to another (0 0 8) peak at 90 K [see Fig. 5.13 (c) and (d)]. This Jahn-Teller effect also has strong impact on the (8 4 0) and (9 3 1) Bragg peaks which attests the presence of orthorhombic phase in the compound. The observed phase coexistence of cubic and orthorhombic phases at 90 K also authenticates the transition at  $T_{\text{str}}$  observed from both the dc and ac magnetic measurements (see Fig. 5.5 and 5.6). The importance of this structural transition is that it possibly bypasses the tetragonal ( $I4_1/amd$ ) structure observed in another spinel compound e.g.  $\text{CuCr}_2\text{O}_4$ .

This lowering in the symmetry (from cubic to orthorhombic) occurs due to the Jahn-Teller active  $\text{Cu}^{2+}$  -ions present in the compound. Due to Jahn-Teller effect, these ions lower their energy to get equal stabilization by spontaneous deformation of their perfect tetrahedral or octahedral environment to orthorhombic symmetry. Kanamori's theory explains the relation between the local distortions and cooperative effect due to tetrahedral Jahn-Teller cations [6]. We know that the ground orbital level at the tetrahedral environment is doubly degenerate  $e_g$  levels, whereas excited state is triply degenerate  $t_{2g}$  orbital level. In present compound where  $\text{Cu}^{2+}$ -ion at A-site (tetrahedral environment), has nine 3d electrons so the configuration

introduced by this element will be:  $(e_g)^4$  and  $(t_{2g})^5$ . This configuration, which is degenerated with respect to the  $t_{2g}$  orbital, results to produce a distortion such that  $d_{xy}$  has more energy than  $d_{yz}$  and  $d_{zx}$ . This resulting distortion also affects the eg orbitals where the  $d_z^2$  orbital has the lower energy than  $d_{x^2-y^2}$  orbital. In the present compound where  $\text{Co}^{2+}$  and substituted  $\text{Cu}^{2+}$  ions are located at tetrahedral site, two normal distortion modes ( $Q_2$  and  $Q_3$ ) are then given by [179–182]:

$$Q_2 = \frac{1}{L\sqrt{2}} (\delta X - \delta Y) \quad (5.1)$$

$$Q_3 = \frac{1}{L\sqrt{6}} (2\delta Z - \delta X - \delta Y) \quad (5.2)$$

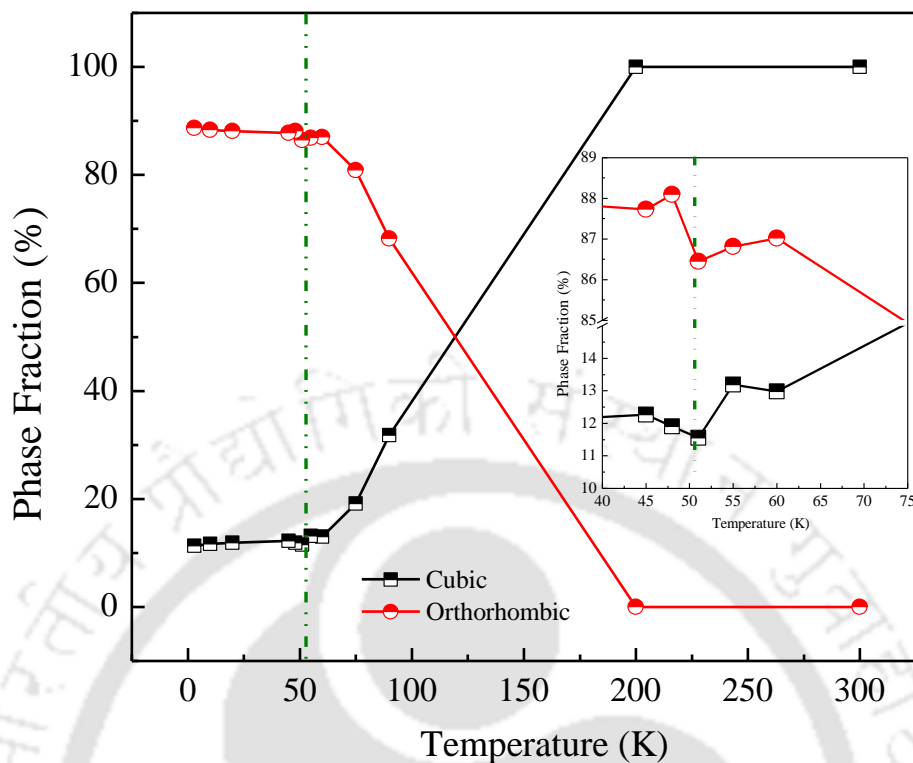
Where L is the cube length, and  $\delta X$ ,  $\delta Y$  and  $\delta Z$  are the modulations of the cube dimensions. Just for the simplification of the above equations, one can introduce the polar coordinate representation of  $Q_2$  and  $Q_3$  such as [3,6]:

$$Q_2 = Q \sin \theta \quad (5.3)$$

$$Q_3 = Q \cos \theta \quad (5.4)$$

Now with these simplified equations, one can illustrate the relation between  $\theta$  and the deformation described by it. It reveals that the directions  $\theta = 0, 2\pi/3$  and  $4\pi/3$  have elongations along the  $z, x$  and  $y$  axes, respectively whereas  $\theta = \pi/3, \pi$  and  $5\pi/3$  have contractions along the  $y, z$  and  $x$  axes, respectively. The observed distortions along the above mentioned angles correspond to the tetragonal distortion whereas the intermediate angles between these directions correspond to orthorhombic distortions [6]. In the present study, we found  $\theta = (\pi - 7.34^\circ)$  with an error of  $0.07^\circ$  which lies in the domain of orthorhombic distortions and satisfies the explanation of observed distortion in  $\text{Co}_{0.8}\text{Cu}_{0.2}\text{Cr}_2\text{O}_4$ .

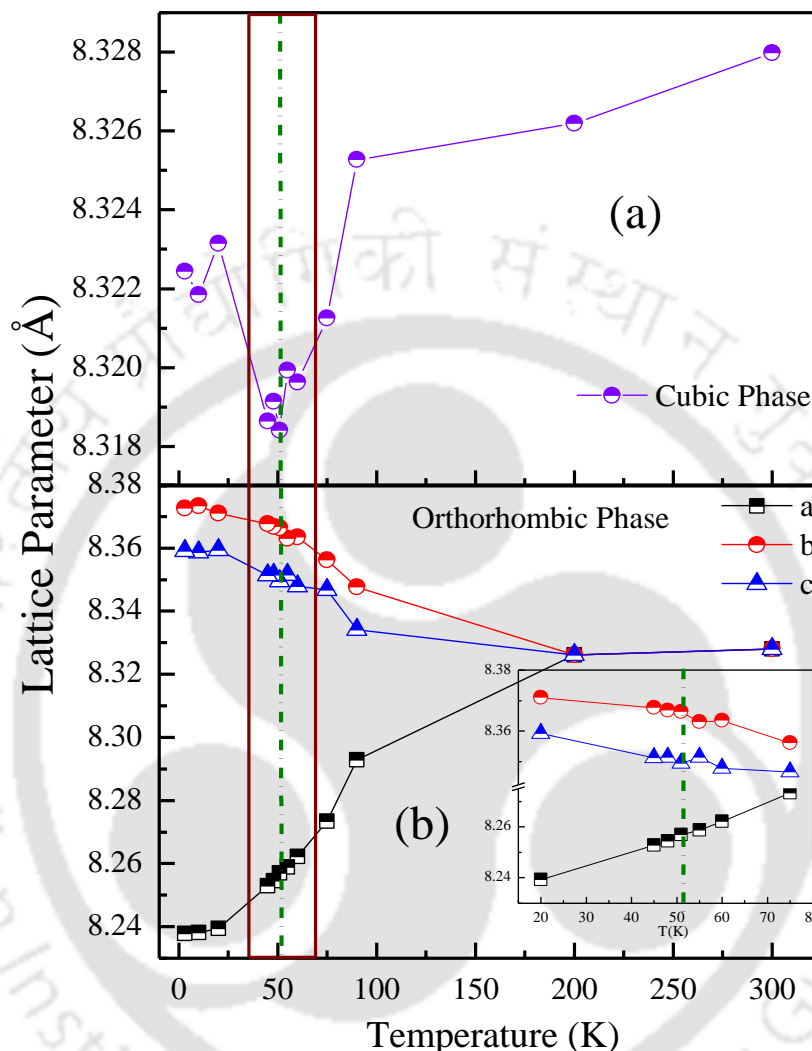
Further, as there is phase co-existence of cubic and orthorhombic phases as single cubic lattice constant 'a' changes into three independent orthorhombic lattice parameters (a, b and c) below  $T = 200$  K [Fig. 5.15 (a) and (b)]. Interestingly, it is observed that cubic lattice constant decreases gradually with temperature, but there is a sharp dip at  $T_{\text{comp}}$ . These lattice parameters of  $Fddd$  phase also have minimal anomaly at  $T_{\text{comp}}$ . Although the structural distortions of  $\text{Co}_{0.8}\text{Cu}_{0.2}\text{Cr}_2\text{O}_4$  occur primarily due to the Jahn-Teller activity of tetrahedral substitution of



**Figure 5.14** The temperature dependence of phase fraction of both the phases (cubic and orthorhombic) present in  $\text{Co}_{0.8}\text{Cu}_{0.2}\text{Cr}_2\text{O}_4$ . The green dashed line at  $T \sim 52$  K displays an unusual structural phase fraction around  $T_{\text{comp}}$ . The inset shows an enlarged view of such unusual anomaly around  $T \sim 52$  K.

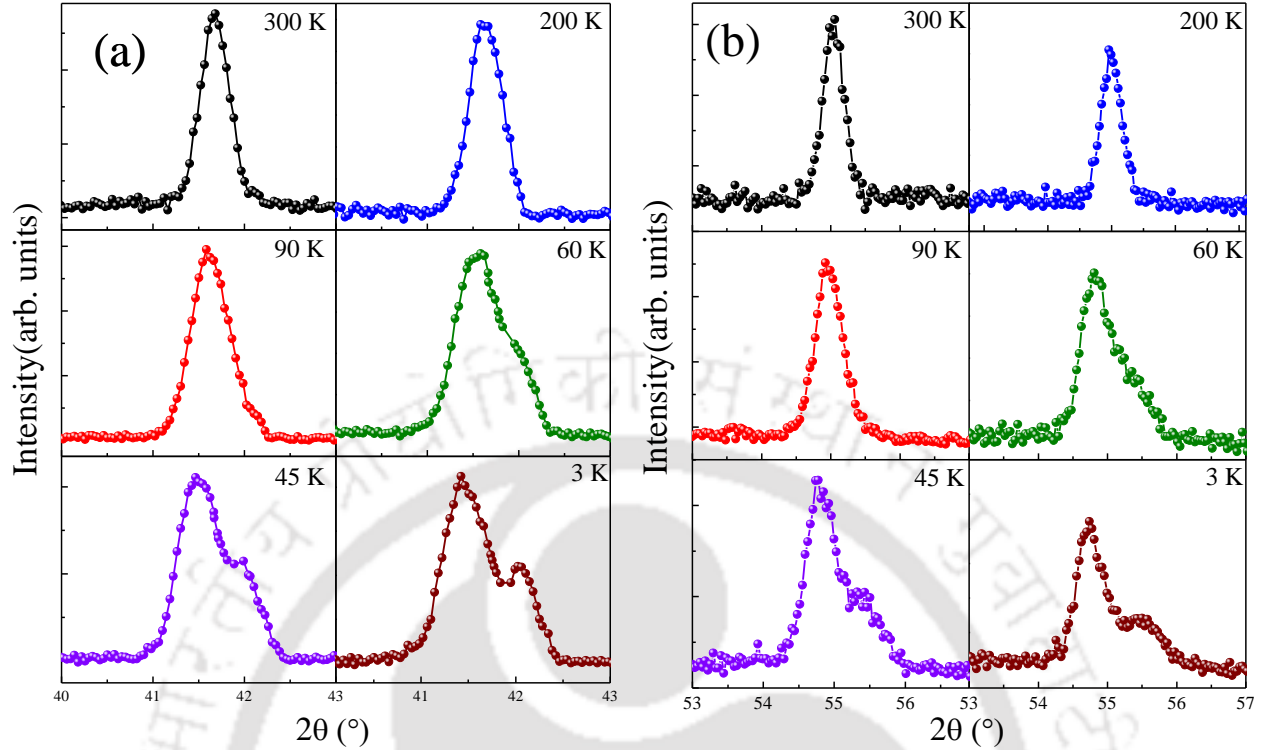
$\text{Cu}^{2+}$ , there is a distinct difference in the distortions observed in  $\text{Co}_{0.8}\text{Cu}_{0.2}\text{Cr}_2\text{O}_4$  compared to the spinel  $\text{CuCr}_2\text{O}_4$  where A-site is fully occupied with  $\text{Cu}^{2+}$ . In case of  $\text{CuCr}_2\text{O}_4$  the existing Jahn-Teller distortions involve a cubic  $Fd\bar{3}m$  to tetragonal  $I_{41}/amd$  lattice distortion which is different from  $\text{Co}_{0.8}\text{Cu}_{0.2}\text{Cr}_2\text{O}_4$  [72]. It has also been reported that there is another structural distortion in  $\text{CuCr}_2\text{O}_4$  from tetragonal  $I_{41}/amd$  to orthorhombic  $Fddd$  symmetry which is derived due to the magnetostructural coupling present in the system [183]. In the present system, we have observed a cubic  $Fd\bar{3}m$  to orthorhombic  $Fddd$  distortion, possibly bypassing the tetragonal  $I_{41}/amd$  structure observed in  $\text{CuCr}_2\text{O}_4$ . Moreover, there was no correlation between the existing lattice distortions with that of the onset of magnetic ordering which has been observed in present case of  $\text{Co}_{0.8}\text{Cu}_{0.2}\text{Cr}_2\text{O}_4$ . The modest connectivity between A-site  $\text{CuO}_4$  tetrahedra along with  $\text{CoO}_4$  could be the reason for the different character of distortion in  $\text{Co}_{0.8}\text{Cu}_{0.2}\text{Cr}_2\text{O}_4$  compared to  $\text{CuCr}_2\text{O}_4$ . The partial Cu substitution (i.e. 20%) which dilutes the A-site of spinel structure  $\text{CoCr}_2\text{O}_4$  and results in randomly distributed  $\text{CuO}_4$  tetrahedra among  $\text{CoO}_4$  which gives rise to the average distortions in all three axes ( $x$ ,  $y$  and  $z$ ) of the cubic unit cell and hence system adopt

orthorhombic ( $Fddd$ ) symmetry in case of  $\text{Co}_{0.8}\text{Cu}_{0.2}\text{Cr}_2\text{O}_4$ . There are some reports in literature where a similar cubic  $Fd\bar{3}m$  to orthorhombic  $Fddd$  lattice distortion has been observed.



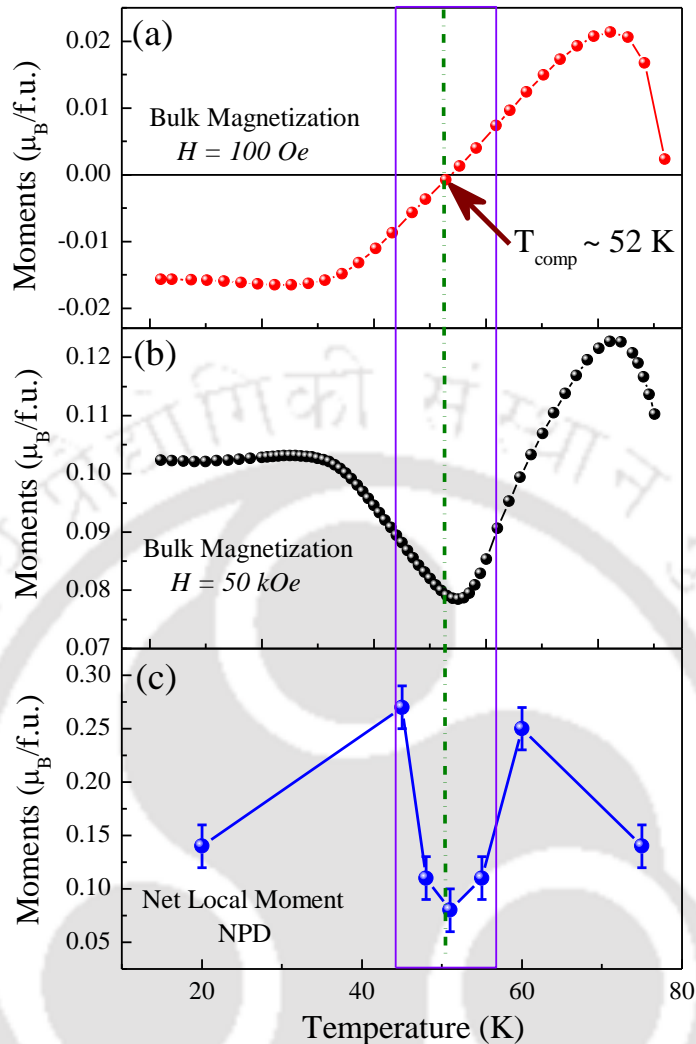
**Figure 5.15** Variation in lattice parameter as a function of temperature in  $\text{Co}_{0.8}\text{Cu}_{0.2}\text{Cr}_2\text{O}_4$ . (a) Cubic lattice constant shows a dip around  $T_{comp} \sim 52$  K, and (b) also depicts the non-monotonic change in lattice parameters (a, b and c) of the orthorhombic phase around same  $T_{comp}$ .

To further demonstrate the structural distortion, the temperature dependence of the (400) and (511) Bragg peaks of NPD patterns is depicted in Fig.5.16. The single (400) and (511) peak start to split into two peaks at  $T = 90$  K (where coexistence starts between cubic and orthorhombic phases). Such deconvolution in these Bragg peaks becomes more and more prominent with decrease in temperature. This stronger splitting with lowering the temperature, also validate the dominance of orthorhombic phase on cubic phase with the decrease in temperature.



**Figure 5.16** The temperature dependence of the different Bragg peaks; (a) (400), and (b) (511) of  $\text{Co}_{0.8}\text{Cu}_{0.2}\text{Cr}_2\text{O}_4$  at different temperatures.

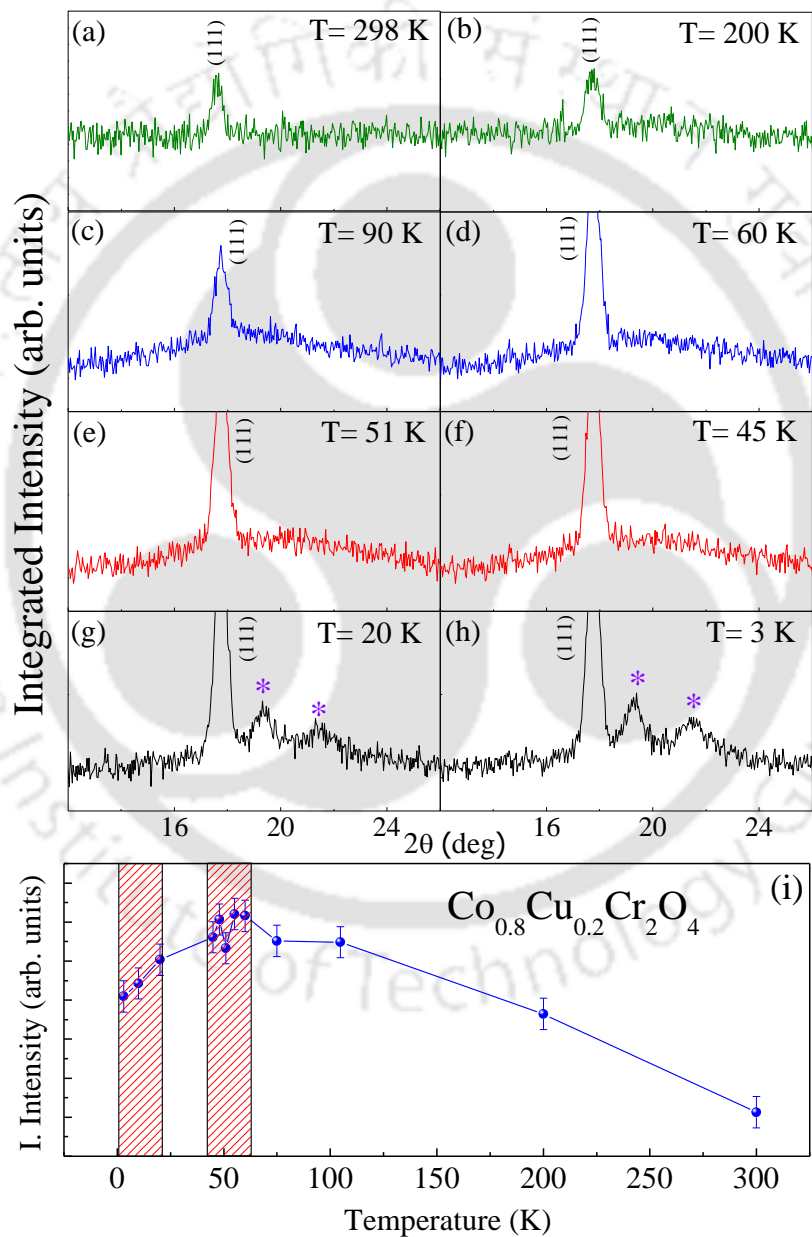
Fig. 5.17 depicts the comparison of the bulk magnetization measured under low applied field of  $H = 100$  Oe and high field of 50 kOe with that of temperature dependent spontaneous magnetization obtained from the refinement of the magnetic phases of the NPD patterns of  $\text{Co}_{0.8}\text{Cu}_{0.2}\text{Cr}_2\text{O}_4$ . Both the bulk magnetization and the local moments obtained from the NPD experiment, exhibit a clear down turn at the compensation points  $T_{\text{comp}} \sim 52$  K. Interestingly, we observed that the net moment observed from NPD experiments shows the similar functional form as that observed in bulk magnetization measurements carried out in 50 kOe field, around the compensation point. Further, the non-monotonic change in unit cell parameters, both the phases, in the vicinity of  $T_{\text{comp}}$  shows that there is a strong spin-lattice coupling present in the system. It can be understood that corresponding to different sublattices (i.e. A and B) and due to different substitution in these sublattices, different magnetic spins orientations take place in the vicinity of compensation point which gives rise to the strong spin-lattice coupling. All these interesting observations were absent in  $\text{CoCr}_2\text{O}_4$  as there was no magnetic compensation.



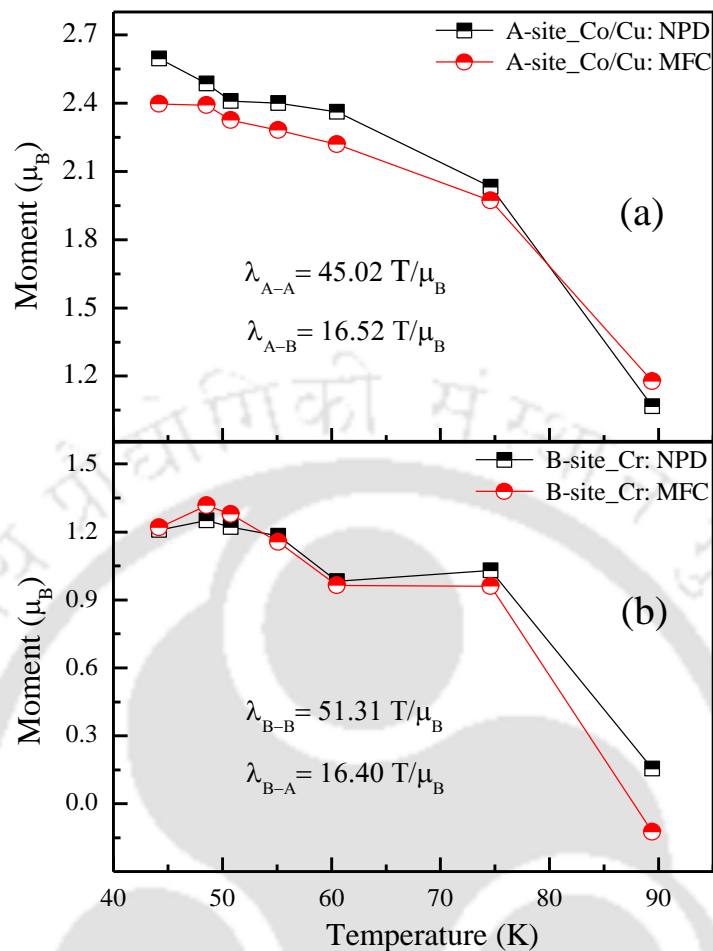
**Figure 5.17** Temperature dependent magnetization  $M(T)$  curves of  $\text{Co}_{0.8}\text{Cu}_{0.2}\text{Cr}_2\text{O}_4$  measured under low field (a) 100 Oe, and (b) high field 50 kOe. Net local moments obtained from NPD data are shown in (c).

Fig. 5.18 shows the enlarged portions of the low-angle NPD patterns at several temperatures for  $\text{Co}_{0.8}\text{Cu}_{0.2}\text{Cr}_2\text{O}_4$ . The patterns at 90 K, i.e. closer to the FIM transition temperature,  $T_C \sim 89 \text{ K}$ , shows the presence of a diffuse signal around the (111) reflection. The presence of such diffuse signal, which is of magnetic origin, indicates the formation of magnetic spin clusters in the compounds [151,153,154]. Further, it is found that these diffused signals which induce short-range correlation among magnetic clusters contribute to the diffraction pattern only around the low angle range, i.e. around (111) peak. In case of  $\text{CoCr}_2\text{O}_4$ , it is reported that a short range spin spiral ordering emerges around  $\sim 80 \text{ K}$ , below  $T_C$  [16] whereas in this Cu substituted sample, one can see this short range correlation has activated at a higher temperature (i.e. 90 K) compared to that of the parent compound. The presence of this diffuse signal may be

due to the finite short range clusters of the transverse spin component coexisting with the finite long ranged magnetic order in these spinel compounds [151,153]. The scattering from these disordered magnetic clusters which are present in these compounds is the origin for these diffuse signals. There is a variation in the intensity of these diffused signals with temperature. This is an explicit indication of the build-up of a short range correlation of the transverse spin component with temperatures above the spin-spiral transition,  $T_s$ .



**Figure 5.18** (a-h) Diffuse signals around the (111) Bragg peak in the neutron diffraction patterns at different temperatures of  $\text{Co}_{0.8}\text{Cu}_{0.2}\text{Cr}_2\text{O}_4$  (all graphs are plotted in the same scale). The integrated intensity of these humps is shown in (i).



**Figure 5.19** Temperature dependence of the observed magnetic moments of A (Co/Cu) and B (Cr) sites from the NPD data and calculated moments from the molecular field calculation (MFC) of  $\text{Co}_{0.8}\text{Cu}_{0.2}\text{Cr}_2\text{O}_4$ .

Thermal variations in the magnetic moments of the A-site (Co/Cu) and B-sites (Cr) for  $\text{Co}_{0.8}\text{Cu}_{0.2}\text{Cr}_2\text{O}_4$  as calculated from the NPD are depicted in Fig. 5.19 (black rectangles). Further, we applied the molecular field model in order to calculate the thermal variations of these magnetic moments. We assumed that these spinel compounds have two sub-lattices A and B whose spins are anti-parallel to each other with different molecular field constants,  $\lambda_{A-A}$ ,  $\lambda_{A-B}$  or  $\lambda_{B-A}$  and  $\lambda_{B-B}$  representing A–A, A–B and B–B exchanges, respectively. The calculation was done by a self-consistent mean- field calculation method using the Brillouin function  $B_J(x)$  along with the above molecular field constant ( $\lambda$ ). The values of ‘J=S’ used in the function  $B_J(x)$  as given below, are modified to include the substitutional effects, i.e.,  $S = 0.8 \times (3/2) + 0.2 \times (1/2)$ . Hence, the expressions used for the calculations are [157]:

$$M_A = M_A^{\text{sat}} B_J [g\mu_B S(\lambda_{B-B} M_A - \lambda_{A-B} M_B) / k_B T] \quad (5.5)$$

$$M_B = M_B^{\text{sat}} B_J [g\mu_B S(-\lambda_{A-B} M_A + \lambda_{A-A} M_B) / k_B T] \quad (5.6)$$

where  $M_A^{\text{sat}}$  and  $M_B^{\text{sat}}$  are the saturated A-site and B-site moments respectively,  $k_B$  is Boltzmann's constant and  $T$  is the temperature. The best fit of the above formula to the NPD data provides the molecular field constants,  $\lambda_{A-A}$ ,  $\lambda_{A-B}$  or  $\lambda_{B-A}$  and  $\lambda_{B-B}$  which are shown in Fig. 5.19 (a) and (b). Furthermore, the FIM transition temperature ( $T_C$ ) and the compensation temperature ( $T_{\text{comp}}$ ) using these molecular field constants,  $\lambda_{A-A}$ ,  $\lambda_{A-B}$  or  $\lambda_{B-A}$  and  $\lambda_{B-B}$  are found to be  $T_C = 192$  K and  $T_{\text{comp}} = 176$  K which are in good comparison to the experimental value of  $T_C = 89$  K and  $T_{\text{comp}} = 52$  K, respectively. Molecular field calculations are the simplest theoretical model to calculate various magnetization parameters. It has its own limitations in including some corrections when compared to the experiments, such as NPD in the present case. In spite of these, there is good agreement between the parameters obtained from MFC and NPD for  $\text{Co}_{0.8}\text{Cu}_{0.2}\text{Cr}_2\text{O}_4$ .

Further, with this magnetically compensated  $\text{Co}_{0.8}\text{Cu}_{0.2}\text{Cr}_2\text{O}_4$  which has both positive as well as negative magnetization in a single phase material, we have investigated the magnetocaloric properties in this compound. Temperature dependent NPD experiments reveal that there exists a magneto-elastic coupling in the proximity of  $T_{\text{comp}}$ . We have observed the interesting magnetic transitions as  $T_S$ ,  $T_{\text{comp}}$  and  $T_C$  from bulk dc-magnetization data; therefore these are the respective temperature regions of interest to explore the MCE behavior in  $\text{Co}_{0.8}\text{Cu}_{0.2}\text{Cr}_2\text{O}_4$ . Hence, we have investigated the MCE behavior in the temperature regimes of 24–60 K (in the range of  $T_S$  &  $T_{\text{comp}}$ ) and in 80–100 K (around  $T_C$ ). Fig. 5.20 shows the calculated change in magnetic entropy ( $-\Delta S_M$ ) using isothermal M-H curves across the magnetic transitions. Here,  $\Delta S_M$  has been calculated using Maxwell's relations [158]:

$$\Delta S_M(T, H) = \int_0^H \left( \frac{\partial M}{\partial T} \right)_H dH \quad (5.7)$$

As shown in Fig. 5.20, the interesting observations from this study is the sign change in  $-\Delta S_M$  exactly at compensation point. From NPD measurements we have observed that the compound exhibits strong magneto-elastic coupling around  $T_{\text{comp}}$  (*cf.* Fig. 5.21) which could be the reason for this sign change in  $-\Delta S_M$  across  $T_{\text{comp}}$ . We have shown the consequence of the magnetic

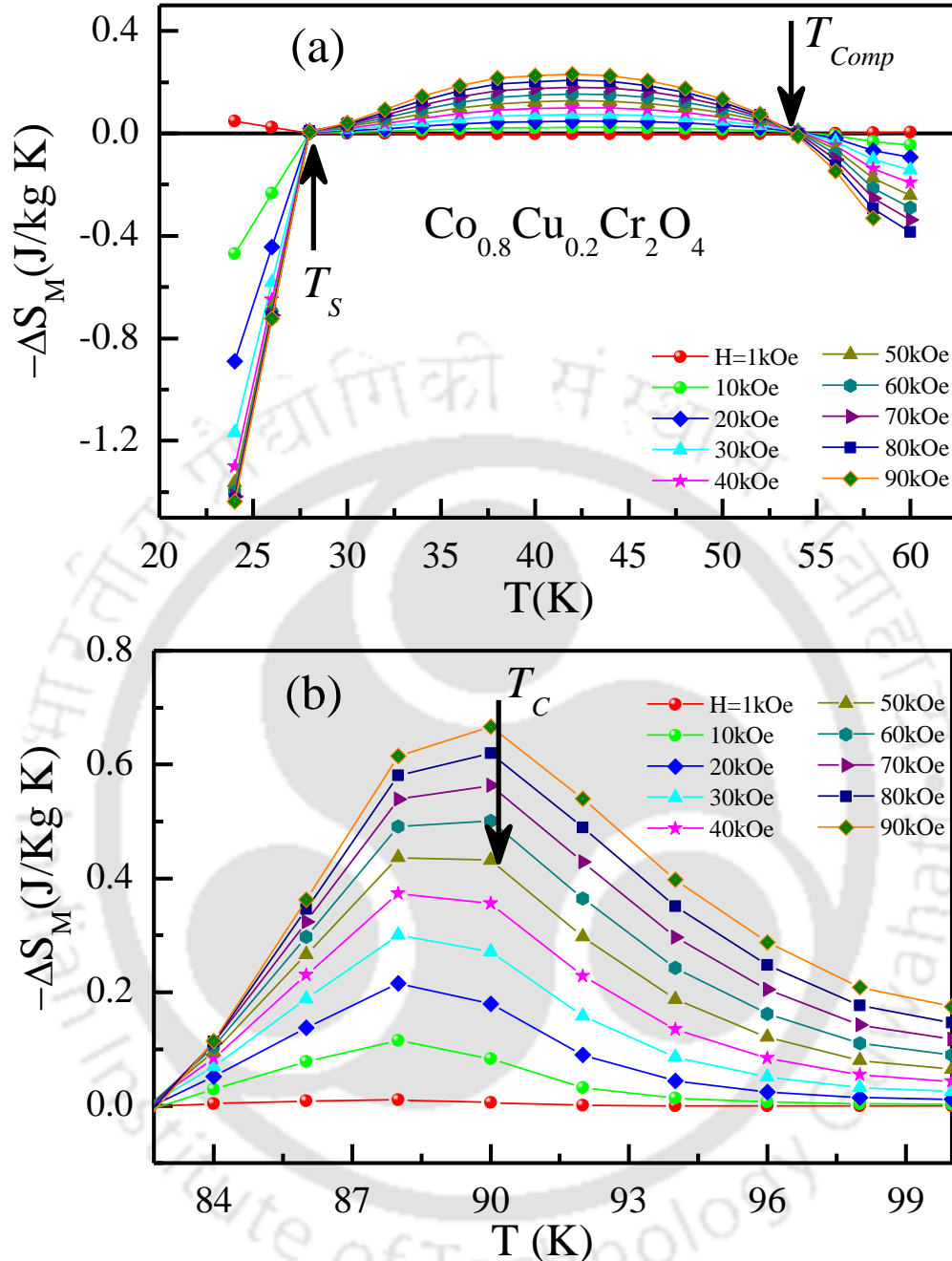


**Figure 5.20** Temperature dependent magnetic entropy change ( $-\Delta S_M$ ) around (a)  $T_S$  and  $T_{comp}$ , and (b) around  $T_C$  for  $\text{Co}_{0.8}\text{Cu}_{0.2}\text{Cr}_2\text{O}_4$ .

compensation on the magnetocaloric properties. This is the key finding in this study of MCE effect in this magnetically compensated compound. A maximum value of  $-\Delta S_M$  observed is  $0.65 \text{ J kg}^{-1} \text{ K}^{-1}$ . Such finding of sign change across  $T_{comp}$  in  $-\Delta S_M$  is very attractive as it opens a new opportunity in magnetic materials where both normal as well as inverse MCE effect persists in a single phase compound.

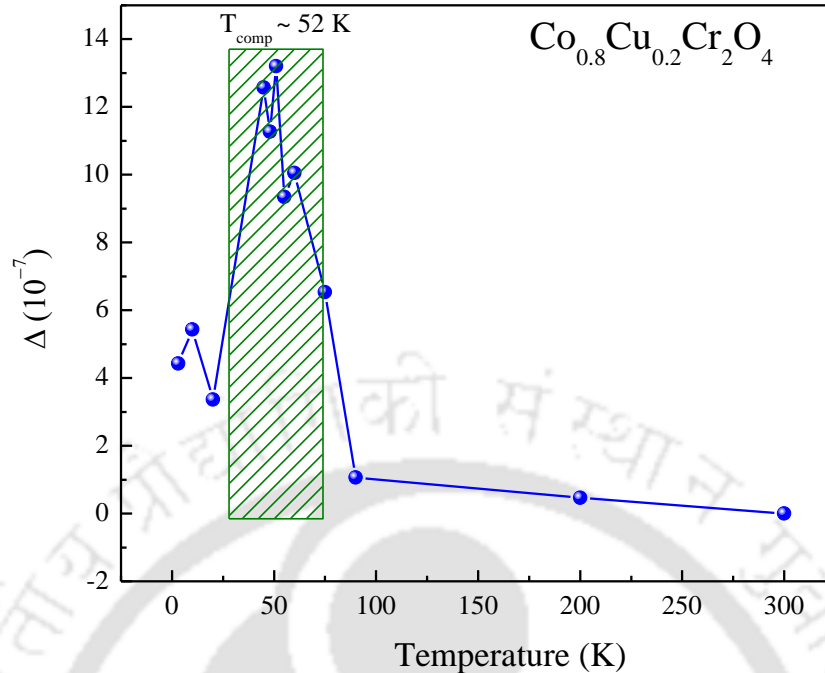


**Figure 5.21** Observed distortion ( $\Delta$ ) in lattice constant of cubic phase of  $\text{Co}_{0.8}\text{Cu}_{0.2}\text{Cr}_2\text{O}_4$  as a function of temperature with clear anomaly around  $T_{\text{comp}}$ .

## 5.4 Summary

In conclusion for present chapter, we have investigated the detailed structural and magnetic properties of Cu substituted polycrystalline compounds i.e.  $\text{Co}_{1-x}\text{Cu}_x\text{Cr}_2\text{O}_4$  ( $x = 0.00-0.20$ ). Magnetic properties have been studied through temperature and field dependent bulk dc and ac-magnetization measurements. The substitution of  $\text{Cu}^{2+}$  for  $\text{Co}^{2+}$  reduces the paramagnetic to collinear FIM transition temperature,  $T_C$ , which is likely due to the weakening of magnetic interactions between A and B-site ions in these Cu substituted compounds compared to that of  $\text{CoCr}_2\text{O}_4$ . In addition, negative magnetization and sign change of EB and MCE across  $T_{\text{comp}}$  is also observed in 20% Cu substituted sample i.e.  $\text{Co}_{0.8}\text{Cu}_{0.2}\text{Cr}_2\text{O}_4$ . Temperature dependent NPD experiments were performed for an understanding of the real microscopic origin negative magnetization, sign change in EB and sign change in MCE. The substitution of Jahn-Teller active  $\text{Cu}^{2+}$  ion gives rise to the structural distortion with a phase co-existence of cubic and orthorhombic at temperature  $T_{\text{str}} = 95$  K just above the  $T_C$  in this compound. The observation of this  $T_{\text{str}}$  close to  $T_C$  is likely due to the long-range nature of magnetic interaction which is held responsible for distortion present in the system. A notable

point is that such cubic to orthorhombic distortion possibly bypasses the tetragonal one which is one of the new findings in such compounds. NPD data reveals that magnetic moments and the crystalline structure show a nonmonotonic variation around  $T_{\text{comp}}$ . Sign change in exchange bias and MCE across  $T_{\text{comp}}$  is correlated with the magneto-structural effects revealed from the neutron data. We have also carried out molecular field calculations for moments on different sites, which are best fitted to the moments extracted from the NPD experiment.



---

### *Summary and Conclusions*

---

From the experimental work carried out for this thesis, the results obtained from three different and distinct substitution effects at both Co and Cr-sites in  $\text{CoCr}_2\text{O}_4$  may be summarized as follows. The present thesis is based on the studies of different magnetic structure which are responsible for different magnetic properties in compensated substituted compounds of  $\text{CoCr}_2\text{O}_4$ . Detailed investigations of structural and magnetic properties on (i)  $\text{Co}(\text{Cr}_{1-x}\text{Fe}_x)_2\text{O}_4$  ( $x = 0.00-0.075$ ), (ii)  $\text{Co}(\text{Cr}_{1-x}\text{Mn}_x)_2\text{O}_4$  ( $x = 0.00-0.30$ ) and (iii)  $\text{Co}_{1-x}\text{Cu}_x\text{Cr}_2\text{O}_4$  ( $x = 0.00-0.20$ ) are reported. Structural analysis of these polycrystalline compounds shows that substituted compounds of Fe and Mn retains the cubic phase till the lowest measuring temperature (i.e. 3 K) whereas a structural distortion is observed in case of Cu (20%) substituted sample. Bulk dc and ac magnetization and heat-capacity measurements have revealed many interesting magnetic properties including negative magnetization, sign change in exchange bias field and sign change in MCE across compensation temperature. Temperature dependent NPD experiments have been performed on the compensated substituted compounds which provide a detailed magnetic structure responsible for observed fascinating magnetic properties of these compounds. Summarizing the key results of the thesis, we concluded this chapter with some future guidelines.

Minimal substitution (i.e. 5% and 7.5%) of  $\text{Fe}^{3+}$ -ions for  $\text{Cr}^{3+}$  (B-site) in  $\text{CoCr}_2\text{O}_4$  systematically enhances the FIM transition temperature possibly due to the strengthening of superexchange interactions between different sites of the spinel structure. But magneto-structural transition ( $T_S$ ) is not affected much as compared to  $\text{CoCr}_2\text{O}_4$  in these Fe substituted samples. One of the interesting findings of this small amount of Fe substitution, is the occurrence of negative magnetization which was absent in case of  $\text{CoCr}_2\text{O}_4$ . Further such magnetization reversal below compensation temperature which occurs under small applied fields changes to a field induced transition at  $T_{\text{comp}}$  upon increasing the strength of the applied field. EB studies on these compensated samples have revealed that there is a sign change in EB field across respective  $T_{\text{comp}}$  in these compounds. We have also observed the sign change in magneto-caloric effect (MCE) across the  $T_{\text{comp}}$  which is due to the presence of strong magneto-elastic

coupling present over there in the close vicinity of magnetically compensated state. In addition, detailed temperature and field dependent dielectric and pyroelectric properties show the signature of multiferroicity which includes the sign change in magneto-dielectric (MD) behavior across respective  $T_{\text{comp}}$ , for the first time in such multiferroic compounds.

Temperature dependent NPD experiments were performed for an understanding of the real microscopic origin of these emerging properties such as negative magnetization, sign change in EB, sign change in MD behavior and also a sign change in MCE. Long range FIM ordering is observed below  $T_C$  for both the samples. The local magnetic moments and the crystalline parameter show a nonmonotonic variation across the compensation temperature. Sign change in exchange bias across this compensation temperature is correlated with the magneto-elastic effects revealed by the neutron data. This class of materials provides a platform to study the competition between the crystalline energy and the Zeeman energy, which is reflected in the sign change of the exchange bias. A clear transition into incommensurate spin-spiral phase across  $T_S$ , has also been observed but at a lower temperature compared to  $\text{CoCr}_2\text{O}_4$ . Moreover, below  $T_L$ , an additional incommensurate modulation in the magnetic structure is observed in these compounds.

Having the interesting results with minimal Fe substitution in  $\text{CoCr}_2\text{O}_4$ , we have chosen other transition metal ions (i.e.  $\text{Mn}^{3+}$ ) with nearly similar ionic size but different magnetic moments compared to that of the  $\text{Cr}^{3+}$  in  $\text{CoCr}_2\text{O}_4$ . We have presented the detailed investigations of structural and magnetic properties through XRD, temperature and field dependent dc and ac-magnetization and by performing temperature dependent NPD experiments on  $\text{Co}(\text{Cr}_{1-x}\text{Mn}_x)_2\text{O}_4$  ( $x = 0.00-0.30$ ). In case of Mn substitution, we have observed that  $x = 0.27$  and  $0.30$  in  $\text{Co}(\text{Cr}_{1-x}\text{Mn}_x)_2\text{O}_4$  drive the system to magnetic compensation state at  $T = T_{\text{comp}}$  under low applied fields below which negative magnetization has been observed. Further, such magnetization reversal is turnout to be in the form of field induced spin reorientation transition across the respective  $T_{\text{comp}}$ . Temperature dependent NPD experiments revealed that spin reorientations of different sublattices play a crucial role to attain the observed magnetic transitions. The exchange bias like behavior observed below 10 K, and in the close vicinity of compensation point has been discussed in the context of large anisotropy and spin reorientation. NPD results provided the understanding of such minimal exchange bias in these compounds which is different from that of

the Fe substitution case. Further, observation of short range spiral ordering till lowest measuring temperature (3 K), revealed the absence of spin-spiral transition which was present in  $\text{CoCr}_2\text{O}_4$  and also in the less Mn substituted samples. Change in crystalline parameters (i.e. bond lengths and bond angles) across respective  $T_{\text{comp}}$  also revealed the correlation between chemical structure and the present magnetic spin configuration around that temperature window. We also observed a sign change of  $-\Delta S_M$  across the  $T_{\text{comp}}$  where one can have both normal and inverse MCE in single phase compounds.

Next, with above conclusions of 'Fe' and 'Mn' substitution at B-site of  $\text{CoCr}_2\text{O}_4$ , I have moved to the A-site substitution with  $\text{Cu}^{2+}$ -ions in place of  $\text{Co}^{2+}$  in  $\text{CoCr}_2\text{O}_4$ . We have investigated the detailed structural, and magnetic properties of Cu substituted polycrystalline compounds, i.e.  $\text{Co}_{1-x}\text{Cu}_x\text{Cr}_2\text{O}_4$  ( $x = 0.00-0.20$ ). Magnetic properties have been studied through temperature and field dependent bulk dc and ac-magnetization and heat-capacity measurements. The substitution of  $\text{Cu}^{2+}$  for  $\text{Co}^{2+}$  reduces the paramagnetic to collinear FIM transition temperature,  $T_C$ , which is likely due to the weakening of magnetic interactions between A and B-sites ions in these Cu substituted compounds compare to  $\text{CoCr}_2\text{O}_4$ . In addition, negative magnetization and sign change of EB and MCE across  $T_{\text{comp}}$  is also observed in 20% Cu substituted sample, i.e.  $\text{Co}_{0.8}\text{Cu}_{0.2}\text{Cr}_2\text{O}_4$ . The substitution of Jahn-Teller active  $\text{Cu}^{2+}$  ion gives rise to the structural distortion with a phase co-existence of cubic and orthorhombic at temperature  $T_{\text{str}} = 95$  K just above the  $T_C$  in  $\text{Co}_{0.8}\text{Cu}_{0.2}\text{Cr}_2\text{O}_4$ . The observation of this  $T_{\text{str}}$  near  $T_C$  is likely due to the long-range nature of magnetic interaction which is held responsible for distortion present in the system. The notable point is that this cubic to orthorhombic distortion possibly bypasses the tetragonal one. This is one of the new findings in such compounds. NPD data reveals that magnetic moments and the crystalline structure show a nonmonotonic variation around  $T_{\text{comp}}$ . Sign change in exchange bias and MCE across  $T_{\text{comp}}$  is correlated with the magneto-elastic effects revealed by the neutron data. We have also carried out molecular field calculations for moments on different sites, which are best fitted to the moments extracted from the NPD experiment.

These all interesting findings of compensated substituted samples of  $\text{CoCr}_2\text{O}_4$  adds the additional degree of freedom to the multi-functionally of the system which has great potential applications.

## ***Future Scope***

Present thesis has explored the magnetic structure determination of compensated substituted compounds of spinel  $\text{CoCr}_2\text{O}_4$ . Below listed are some remarks and one can provide possible extensions of the current thesis work as:

- To perform the dielectric/magnetodielectric measurements to discover the multiferroicity at different temperature regimes having both collinear as well as non-collinear magnetic ordering.
- One can grow the single crystals of these substituted samples, and after performing neutron scattering experiments, one can draw the conclusions for observed magnetic properties by magnetic structure analysis.
- To perform the electronic band-structure calculations using density function theory and make a comparative study with the experimental results obtained from the optical measurements (in UV-Vis-NIR regime).
- To synthesize the thin-films or nanostructure of these substituted samples for a systematic comparative study of their structural, optical and magnetic properties with their bulk counterpart.

## References:

- [1] S.-H. Lee, C. Broholm, W. Ratcliff, G. Gasparovic, Q. Huang, T.H. Kim, S.-W. Cheong, *Nature*. 418 (2002) 856–858.
- [2] J.D. Dunitz, L.E. Orgel, *J. Phys. Chem. Solids*. 3 (1957) 20–29.
- [3] J. Kanamori, *J. Appl. Phys.* 31 (1960) S14–S23.
- [4] A. Wold, R.J. Arnott, E. Whipple, J.B. Goodenough, *J. Appl. Phys.* 34 (1963) 1085–1086.
- [5] D.W. Bruce, *Functional Oxides - Google Books*, 2010.
- [6] M. Kataoka, J. Kanamori, *J. Phys. Soc. Japan*. 32 (1972) 113–134.
- [7] M. Reehuis, M. Tovar, D.M. Többens, P. Pattison, A. Hoser, B. Lake, *Phys. Rev. B*. 91 (2015) 24407.
- [8] K. Tomiyasu, J. Fukunaga, H. Suzuki, *Phys. Rev. B*. 70 (2004) 214434.
- [9] J. Zhu, Q. Gao, *Microporous Mesoporous Mater.* 124 (2009) 144–152.
- [10] S. Thota, A. Kumar, J. Kumar, *Mater. Sci. Eng. B*. 164 (2009) 30–37.
- [11] V.G. Harris, A. Geiler, Y. Chen, S.D. Yoon, M. Wu, A. Yang, Z. Chen, P. He, P. V Parimi, X. Zuo, C.E. Patton, M. Abe, O. Acher, C. Vittoria, *J. Magn. Magn. Mater.* 321 (2009) 2035–2047.
- [12] Y.J. Choi, J. Okamoto, D.J. Huang, K.S. Chao, H.J. Lin, C.T. Chen, M. van Veenendaal, T.A. Kaplan, S.-W. Cheong, *Phys. Rev. Lett.* 102 (2009) 67601.
- [13] Y. Yamasaki, S. Miyasaka, Y. Kaneko, J.-P. He, T. Arima, Y. Tokura, *Phys. Rev. Lett.* 96 (2006) 207204.
- [14] G. Lawes, B. Melot, K. Page, C. Ederer, M.A. Hayward, T. Proffen, R. Seshadri, *Phys. Rev. B*. 74 (2006) 24413.
- [15] V. Tsurkan, S. Zherlitsyn, S. Yasin, V. Felea, Y. Skourski, J. Deisenhofer, H.-A.K. von Nidda, J. Wosnitzer, A. Loidl, *Phys. Rev. Lett.* 110 (2013) 115502.
- [16] N. Menyuk, K. Dwight, A. Wold, *J. Phys.* 25 (1964) 528–536.
- [17] S. Funahashi, Y. Morii, H.R. Child, *J. Appl. Phys.* 61 (1987) 4114–4116.
- [18] L.J. Chang, D.J. Huang, W.-H. Li, S.-W. Cheong, W. Ratcliff, J.W. Lynn, *J. Phys. Condens. Matter*. 21 (2009) 456008.
- [19] H. Katsura, N. Nagaosa, A. V. Balatsky, *Phys. Rev. Lett.* 95 (2005) 57205.
- [20] B.C. Melot, J.E. Drewes, R. Seshadri, E.M. Stoudenmire, A.P. Ramirez, *J. Phys. Condens. Matter*. 21 (2009) 216007.
- [21] L. Neel, *Ann. Phys. Paris*. 3 (1948) 137–198.
- [22] C. Tsang, R.E. Fontana, T. Lin, D.E. Heim, V.S. Speriosu, B.A. Gurney, M.L. Williams, *IEEE Trans. Magn.* 30 (1994) 3801–3806.
- [23] R. Padam, S. Pandya, S. Ravi, A.K. Nigam, S. Ramakrishnan, A.K. Grover, D. Pal, *Appl. Phys. Lett.* 102 (2013) 0–4.
- [24] J. Sharma, K.G. Suresh, *Appl. Phys. Lett.* 106 (2015) 72405.
- [25] B.M. Wang, Y. Liu, P. Ren, B. Xia, K.B. Ruan, J.B. Yi, J. Ding, X.G. Li, L. Wang, *Phys. Rev. Lett.* 106 (2011) 77203.
- [26] P.D. Kulkarni, A. Thamizhavel, V.C. Rakhecha, A.K. Nigam, P.L. Paulose, S. Ramakrishnan, A.K. Grover, *Epl*. 86 (2009) 47003.
- [27] J.C.S. Kools, *IEEE Trans. Magn.* 32 (1996) 3165–3184.
- [28] J. Nogués, I.K. Schuller, *J. Magn. Magn. Mater.* 192 (1999) 203–232.
- [29] Y. Tang, Y. Sun, Z. Cheng, *Phys. Rev. B*. 73 (2006) 174419.
- [30] S. Urazhdin, P. Tabor, W.-L. Lim, *Phys. Rev. B*. 78 (2008) 52403.
- [31] I. Kim, Y.S. Oh, Y. Liu, S.H. Chun, J.-S. Lee, K.-T. Ko, J.-H. Park, J.-H. Chung, K.H. Kim, *Appl. Phys. Lett.* 94 (2009) 42505.
- [32] A. V Pronin, M. Uhlarz, R. Beyer, T. Fischer, J. Wosnitzer, B.P. Gorshunov, G.A. Komandin, A.S. Prokhorov, M. Dressel, A.A. Bush, V.I. Torgashev, *Phys. Rev. B*. 85 (2012).
- [33] N. Menyuk, K. Dwight, D.G. Wickham, *Phys. Rev. Lett.* 4 (1960) 119–120.

- [34] T. V. Chandrasekhar Rao, P. Raj, S.M. Yusur, L.M. Rao, A. Sathyamoorthy, V.C. Sahni, *Philos. Mag. B.* 74 (1996) 275–291.
- [35] K.R. Rao, *Pramana - J. Phys.* 63 (2004) 5–14.
- [36] J. v. Lier, G. Koel, W. v. Gestel, L. Postma, J. Gerkema, F. Gorter, W. Druyvesteyn, *IEEE Trans. Magn.* 12 (1976) 716–718.
- [37] C. Tsang, M. Pinarbasi, H. Santini, E. Marinero, P. Arnett, R. Olson, R. Hsiao, M. Williams, R. Payne, R. Wang, J. Moore, B. Gurney, T. Lin, R. Fontana, *IEEE Trans. Magn.* 35 (1999) 689–694.
- [38] S. Gangopadhyay, K. Subramanian, P. Ryan, A. Mack, E. Murdock, M.L. Covault, E. Yan, E. Champion, G.J. Tamopolsky, Y.C. Feng, Z. Zhang, D.Q. Chen, S.D. Harkness, R.Y. Ranjan, G.C. Rauch, H.J. Richter, *J. Appl. Phys.* 87 (2000) 5407.
- [39] C.H. Tsang, R.E. Fontana, T. Lin, D.E. Heim, B.A. Gurney, M.L. Williams, *IBM J. Res. Dev.* 42 (1998) 103–116.
- [40] S. Stringari, R.R. Wilson, *Rend. Lincei.* 11 (2000) 115–136.
- [41] Ching Tsang, Tsann Lin, S. MacDonald, M. Pinarbasi, N. Robertson, H. Santini, M. Doerner, T. Reith, Lang Vo, T. Diola, P. Arnett, *IEEE Trans. Magn.* 33 (1997) 2866–2871.
- [42] C. Kittel, Wiley, 2005.
- [43] V. Wadhawan, CRC Press, 2014.
- [44] B. Dieny, V.S. Speriosu, S.S.P. Parkin, B.A. Gurney, D.R. Wilhoit, D. Mauri, *Phys. Rev. B.* 43 (1991) 1297–1300.
- [45] R.E. Newnham, J.J. Kramer, W.A. Schulze, L.E. Cross, *J. Appl. Phys.* 49 (1978) 6088–6091.
- [46] D.C. Kim, S.K. Ihm, *Environ. Sci. Technol.* 35 (2001) 222–6.
- [47] W. Schiessl, W. Potzel, H. Karzel, M. Steiner, G.M. Kalvius, A. Martin, M.K. Krause, I. Halevy, J. Gal, W. Schäfer, G. Will, M. Hillberg, R. Wäppling, *Phys. Rev. B.* 53 (1996) 9143–9152.
- [48] J. Zhang, J. Liang, Y. Zhu, D. Wei, L. Fan, Y. Qian, *J. Mater. Chem. A.* 2 (2014) 2728.
- [49] M.M. Vopson, *Crit. Rev. Solid State Mater. Sci.* 40 (2015) 223–250.
- [50] C.N.R. Rao, B. Raveau, Wiley-VCH, 1998.
- [51] S.-W. Cheong, M. Mostovoy, *Nat. Mater.* 6 (2007) 13–20.
- [52] S. Thota, B. Prasad, J. Kumar, *Mater. Sci. Eng. B.* 167 (2010) 153–160.
- [53] W.H. Bragg, *Dublin Philos. Mag. J. Sci.* 30 (1915) 305–315.
- [54] S. NISHIKAWA, *Proc. Tokyo Math. Soc. 2nd Ser.* 8 (1915) 199–209\_1.
- [55] G.A. Sawatzky, F. Van Der Woude, A.H. Morrish, *Phys. Rev.* 187 (1969) 747–757.
- [56] D. Peddis, N. Yaacoub, M. Ferretti, A. Martinelli, G. Piccaluga, A. Musinu, C. Cannas, G. Navarra, J.M. Greneche, D. Fiorani, *J. Phys. Condens. Matter.* 23 (2011) 426004.
- [57] M. Harris, *Nature.* 399 (1999) 311–312.
- [58] E.A. Goremychkin, R. Osborn, B.D. Rainford, R.T. Macaluso, D.T. Adroja, M. Koza, *Nat. Phys.* 4 (2008) 766–770.
- [59] H.T. Diep, WORLD SCIENTIFIC, 2013.
- [60] L. Balents, *Nature.* 464 (2010) 199–208.
- [61] T.A. Kaplan, N. Menyuk, *Philos. Mag.* 87 (2007) 3711–3785.
- [62] G.J. MacDougall, D. Gout, J.L. Zarestky, G. Ehlers, A. Podlesnyak, M.A. McGuire, D. Mandrus, S.E. Nagler, *Proc. Natl. Acad. Sci. U. S. A.* 108 (2011) 15693–8.
- [63] B. Roy, A. Pandey, Q. Zhang, T.W. Heitmann, D. Vaknin, D.C. Johnston, Y. Furukawa, *Phys. Rev. B.* 88 (2013) 174415.
- [64] N. Tristan, J. Hemberger, A. Krimmel, H.-A. Krug von Nidda, V. Tsurkan, A. Loidl, *Phys. Rev. B.* 72 (2005) 174404.
- [65] O. Zaharko, A. Cervellino, V. Tsurkan, N.B. Christensen, A. Loidl, *Phys. Rev. B.* 81 (2010) 64416.
- [66] D.H. Lyons, T.A. Kaplan, K. Dwight, N. Menyuk, *Phys. Rev.* 126 (1962) 540–555.
- [67] D. Kamenskyi, H. Engelkamp, T. Fischer, M. Uhlarz, J. Wosnitzer, B.P. Gorshunov, G.A. Komandin, A.S. Prokhorov, M. Dressel, A.A. Bush, V.I. Torgashev, A. V. Pronin, *Phys. Rev. B.* 87 (2013) 134423.

- [68] S. Blundell, Oxford University Press, 2001.
- [69] W. Moffitt, C.J. Ballhausen, *Annu. Rev. Phys. Chem.* 7 (1956) 107–136.
- [70] B.N. Figgis, M.A. Hitchman, Wiley-VCH, 2000.
- [71] H.A. Jahn, E. Teller, *Proc. R. Soc. A Math. Phys. Eng. Sci.* 161 (1937) 220–235.
- [72] M.R. Suchomel, D.P. Shoemaker, L. Ribaud, M.C. Kemei, R. Seshadri, *Phys. Rev. B.* 86 (2012) 54406.
- [73] Z.-G. Yé, O. Crottaz, F. Vaudano, F. Kubel, P. Tissot, H. Schmid, *Ferroelectrics.* 162 (1994) 103–118.
- [74] A.M. Balagurov, I.A. Bobrikov, M.S. Maschenko, D. Sangaa, V.G. Simkin, *Crystallogr. Reports.* 58 (2013) 710–717.
- [75] E.W. Gorter, J.A. Schulkes, *Phys. Rev.* 90 (1953) 487–488.
- [76] A. Kumar, S.M. Yusuf, L. Keller, J. V. Yakhmi, *Phys. Rev. Lett.* 101 (2008) 1–4.
- [77] S. Ohkoshi, Y. Abe, A. Fujishima, K. Hashimoto, *Phys. Rev. Lett.* 82 (1999) 1285–1288.
- [78] H. Kageyama, D.I. Khomskii, R.Z. Levitin, A.N. Vasil'ev, *Phys. Rev. B.* 67 (2003) 224422.
- [79] W.H. Meiklejohn, C.P. Bean, *Phys. Rev.* 102 (1956) 1413–1414.
- [80] W.H. Meiklejohn, C.P. Bean, *Phys. Rev.* 105 (1957) 904–913.
- [81] S. Giri, M. Patra, S. Majumdar, *J. Phys. Condens. Matter.* 23 (2011).
- [82] D.C. Worledge, D.W. Abraham, *Appl. Phys. Lett.* 82 (2003) 4522–4524.
- [83] S. Kaka, S.E. Russek, *Appl. Phys. Lett.* 80 (2002) 2958–2960.
- [84] B. Warot-Fonrose, C. Gatel, L. Calmels, V. Serin, E. Snoeck, S. Cherifi, *J. Appl. Phys.* 107 (2010) 09D301.
- [85] Y.K. Zheng, K.B. Li, J.J. Qiu, G.C. Han, Z.B. Guo, B.Y. Zong, L.H. An, P. Luo, Z.Y. Liu, Y.H. Wu, *IEEE Trans. Magn.* 40 (2004) 2248–2250.
- [86] J.-E. Wegrowe, A. Comment, Y. Jaccard, J.-P. Ansermet, N.M. Dempsey, J.-P. Nozières, *Phys. Rev. B.* 61 (2000) 12216–12220.
- [87] R.H. Koch, G. Grinstein, G.A. Keefe, Y. Lu, P.L. Trouilloud, W.J. Gallagher, S.S.P. Parkin, *Phys. Rev. Lett.* 84 (2000) 5419–5422.
- [88] J. Sort, J. Nogués, X. Amils, S. Suriñach, J.S. Muñoz, M.D. Baró, *Appl. Phys. Lett.* 75 (1999) 3177.
- [89] J. Sort, S. Suriñach, J.S. Muñoz, M.D. Baró, J. Nogués, G. Chouteau, V. Skumryev, G.C. Hadjipanayis, *Phys. Rev. B.* 65 (2002) 174420.
- [90] J. Sort, J. Nogués, S. Suriñach, J.S. Muñoz, M.D. Baró, E. Chappel, F. Dupont, G. Chouteau, *Appl. Phys. Lett.* 79 (2001) 1142–1144.
- [91] W.H. Meiklejohn, *J. Appl. Phys.* 33 (1962) 1328–1335.
- [92] D. Niebieskikwiat, M.B. Salamon, *Phys. Rev. B.* 72 (2005) 174422.
- [93] Y. Tang, Y. Sun, Z. Cheng, *Phys. Rev. B.* 73 (2006) 174419.
- [94] M. Thakur, M. Patra, S. Majumdar, S. Giri, *J. Alloys Compd.* 480 (2009) 193–197.
- [95] S. Das, M. Patra, S. Majumdar, S. Giri, *J. Alloys Compd.* 488 (2009) 27–30.
- [96] K. Yoshii, *Appl. Phys. Lett.* 99 (2011) 142501.
- [97] F. Hong, Z. Cheng, J. Wang, X. Wang, S. Dou, *Appl. Phys. Lett.* 101 (2012) 102411.
- [98] R.P. Singh, C. V. Tomy, A.K. Grover, *Appl. Phys. Lett.* 97 (2010) 182505.
- [99] J. Nogués, D. Lederman, T.J. Moran, I.K. Schuller, *Phys. Rev. Lett.* 76 (1996) 4624–4627.
- [100] D. Khomskii, *Physics (College. Park. Md.)* 2 (2009) 20.
- [101] X. He, Y. Wang, N. Wu, A.N. Caruso, E. Vescovo, K.D. Belashchenko, P.A. Dowben, C. Binek, *Nat. Mater.* 9 (2010) 579–585.
- [102] W. Eerenstein, N.D. Mathur, J.F. Scott, *Nature.* 442 (2006) 759–765.
- [103] C.-W. Nan, M.I. Bichurin, S. Dong, D. Viehland, G. Srinivasan, *J. Appl. Phys.* 103 (2008) 31101.
- [104] V. Skumryev, V. Laukhin, I. Fina, X. Martí, F. Sánchez, M. Gospodinov, J. Fontcuberta, *Phys. Rev. Lett.* 106 (2011) 57206.
- [105] S.M. Wu, S.A. Cybart, P. Yu, M.D. Rossell, J.X. Zhang, R. Ramesh, R.C. Dynes, *Nat. Mater.* 9 (2010) 756–761.

- [106] S.M. Wu, S.A. Cybart, D. Yi, J.M. Parker, R. Ramesh, R.C. Dynes, *Phys. Rev. Lett.* 110 (2013) 67202.
- [107] M. Fiebig, *J. Phys. D: Appl. Phys.* 38 (2005) R123–R152.
- [108] L.C. Chapon, G.R. Blake, M.J. Gutmann, S. Park, N. Hur, P.G. Radaelli, S.-W. Cheong, *Phys. Rev. Lett.* 93 (2004) 177402.
- [109] C. Lu, S. Dong, Z. Xia, H. Luo, Z. Yan, H. Wang, Z. Tian, S. Yuan, T. Wu, J. Liu, *Sci. Rep.* 3 (2013) 3374.
- [110] T. Kimura, T. Goto, H. Shintani, K. Ishizaka, others, *Nature*. 426 (2003) 55.
- [111] K. Singh, A. Maignan, C. Simon, C. Martin, *Appl. Phys. Lett.* 99 (2011) 172903.
- [112] S. Yang, H.X. Bao, D.Z. Xue, C. Zhou, J.H. Gao, Y. Wang, J.Q. Wang, X.P. Song, Z.B. Sun, X.B. Ren, K. Otsuka, *J. Phys. D: Appl. Phys.* 45 (2012) 0–5.
- [113] C. Ederer, M. Komelj, *Phys. Rev. B.* 76 (2007) 64409.
- [114] A.R. West, *Solid state chemistry and its applications.*
- [115] H.M. Rietveld, *IUCr, urn:issn:0021-8898.* 2 (1969) 65–71.
- [116] J. Rodríguez-Carvajal, *Phys. B Condens. Matter.* 192 (1993) 55–69.
- [117] A. Boulouf, D. Louër, *IUCr, J. Appl. Crystallogr.* 37 (2004) 724–731.
- [118] W. Marshall and S. W. Lovesey, Clarendon Press. (1971).
- [119] G.E. Bacon, Clarendon Press, 1975.
- [120] Y.A. Izyumov, V.E. Naish, R.P. Ozerov, Springer US, 1991.
- [121] G.L. Squires, Cambridge University Press, 2012.
- [122] A. Furrer, J. Mesot, T. Strässle, *WORLD SCIENTIFIC*, 2009.
- [123] T. Chatterji, Elsevier, 2006.
- [124] V. Siruguri, P.D. Babu, M. Gupta, A. V. Pimpale, P.S. Goyal, *Pramana.* 71 (2008) 1197–1202.
- [125] J.C. Lashley, M.F. Hundley, A. Migliori, J.L. Sarrao, P.G. Pagliuso, T.W. Darling, M. Jaime, J.C. Cooley, W.L. Hults, L. Morales, D.J. Thoma, J.L. Smith, J. Boerio-Goates, B.F. Woodfield, G.R. Stewart, R.A. Fisher, N.E. Phillips, *Cryogenics (Guildf).* 43 (2003) 369–378.
- [126] E. Dachs, A. Benisek, *Cryogenics (Guildf).* 51 (2011) 460–464.
- [127] J.S. Hwang, K.J. Lin, C. Tien, *Rev. Sci. Instrum.* 68 (1998) 94.
- [128] M. Gibert, P. Zubko, R. Scherwitzl, J. Íñiguez, J.-M. Triscone, *Nat. Mater.* 11 (2012) 195–198.
- [129] J. Mao, Y. Sui, X. Zhang, X. Wang, Y. Su, Z. Liu, Y. Wang, R. Zhu, Y. Wang, W. Liu, X. Liu, *Solid State Commun.* 151 (2011) 1982–1985.
- [130] A.K. Nayak, M. Nicklas, S. Chadov, P. Khuntia, C. Shekhar, A. Kalache, M. Baenitz, Y. Skourski, V.K. Guduru, A. Puri, U. Zeitler, J.M.D. Coey, C. Felser, *Nat. Mater.* 14 (2015) 679–684.
- [131] H.S. Nair, T. Chatterji, A.M. Strydom, *Appl. Phys. Lett.* 106 (2015) 22407.
- [132] T. Basu, V.V.R. Kishore, S. Gohil, K. Singh, N. Mohapatra, S. Bhattacharjee, B. Gonde, N.P. Lalla, P. Mahadevan, S. Ghosh, others, *Sci. Rep.* 4 (2014).
- [133] S. Sharma, T. Basu, A. Shahee, K. Singh, N.P. Lalla, E. V Sampathkumaran, *Phys. Rev. B.* 90 (2014) 144426.
- [134] C.N.R. Rao, A. Sundaresan, R. Saha, *J. Phys. Chem. Lett.* 3 (2012) 2237–2246.
- [135] T. Katsufuji, S. Mori, M. Masaki, Y. Moritomo, N. Yamamoto, H. Takagi, *Phys. Rev. B.* 64 (2001) 104419.
- [136] T. Kimura, S. Kawamoto, I. Yamada, M. Azuma, M. Takano, Y. Tokura, *Phys. Rev. B.* 67 (2003) 180401.
- [137] H. Takei, T. Suzuki, T. Katsufuji, *Appl. Phys. Lett.* 91 (2007) 72506.
- [138] T. Suzuki, M. Katsumura, K. Taniguchi, T. Arima, T. Katsufuji, Orbital ordering and magnetic field effect in MnV<sub>2</sub>O<sub>4</sub>, *Phys. Rev. Lett.* 98 (2007) 127203.
- [139] N. Mufti, A.A. Nugroho, G.R. Blake, T.T.M. Palstra, *J. Phys. Condens. Matter.* 22 (2010) 75902.
- [140] N.E. Rajeevan, P.P. Pradyumn, R. Kumar, D.K. Shukla, S. Kumar, A.K. Singh, S. Patnaik, S.K. Arora, I. V. Shvets, *Appl. Phys. Lett.* 92 (2008) 102910.
- [141] D.I. Khomskii, *J. Magn. Magn. Mater.* 306 (2006) 1–8.
- [142] S.-W. Cheong, M. Mostovoy, *Nat. Mater.* 6 (2007) 13–20.

- [143] B.Y.R.D. Shannon, M. H, N.H. Baur, O.H. Gibbs, M. Eu, V. Cu, Acta , (1976).
- [144] S. Venkatesh, U. Vaidya, V.C. Rakhecha, S. Ramakrishnan, A.K. Grover, J. Phys. Condens. Matter. 22 (2010) 496002.
- [145] P.K. Manna, S.M. Yusuf, R. Shukla, A.K. Tyagi, Appl. Phys. Lett. 96 (2010) 242508.
- [146] P.D. Kulkarni, S.K. Dhar, A. Provino, P. Manfrinetti, A.K. Grover, Phys. Rev. B. 82 (2010) 144411.
- [147] J. Rodríguez-Carvajal, Phys. B Condens. Matter. 192 (1993) 55–69.
- [148] B.H. Toby, Powder Diffr. 21 (2006) 67–70.
- [149] B. Roy, A. Pandey, Q. Zhang, T.W. Heitmann, D. Vaknin, D.C. Johnston, Y. Furukawa, Phys. Rev. B. 88 (2013) 174415.
- [150] Y. Yafet, C. Kittel, Phys. Rev. 87 (1952) 290.
- [151] R. Chakravarthy, L.M. Rao, S.K. Paranjpe, S.K. Kulshreshtha, S.B. Roy, Phys. Rev. B. 43 (1991) 6031.
- [152] N.S.S. Murthy, M.G. Natera, S.I. Youssef, R.J. Begum, C.M. Srivastava, Phys. Rev. 181 (1969) 969.
- [153] S.M. Yunus, J.A. Fernandez-Baca, M.A. Asgar, F.U. Ahmed, J. Alloys Compd. 298 (2000) 9–17.
- [154] S.M. Yunus, H. Yamauchi, A.K.M. Zakaria, N. Igawa, A. Hoshikawa, Y. Haga, Y. Ishii, J. Alloys Compd. 455 (2008) 98–105.
- [155] D.E. Cox, W.J. Takei, G. Shirane, J. Phys. Chem. Solids. 24 (1963) 405–423.
- [156] S.K. Paranjpe, R. Chakravarthy, H.S. Bisht, D.K. Kulkarni, Phys. Status Solidi. 98 (1986) K157–K160.
- [157] M. Getzlaff, Springer Berlin Heidelberg, Berlin, Heidelberg, 2008: pp. 47–69.
- [158] A.M. Tishin, Y.I. Spichkin, Institute of Physics Pub, 2003.
- [159] J. Mao, Y. Sui, X. Zhang, Y. Su, X. Wang, Z. Liu, Y. Wang, R. Zhu, Y. Wang, W. Liu, J. Tang, Appl. Phys. Lett. 98 (2011) 192510.
- [160] J. Barman, S. Ravi, J. Magn. Magn. Mater. 426 (2017) 82–88.
- [161] R. Kumar, R. Padam, D. Das, S. Rayaprol, V. Siruguri, D. Pal, RSC Adv. 6 (2016) 93511–93518.
- [162] T. Katsufuji, H. Takagi, Phys. Rev. B. 69 (2004) 64422.
- [163] S.D. Kaushik, S. Rayaprol, J. Saha, N. Mohapatra, V. Siruguri, P.D. Babu, S. Patnaik, E. V. Sampathkumaran, J. Appl. Phys. 108 (2010) 1–6. doi:10.1063/1.3499262.
- [164] T. Basu, K. Singh, E. V Sampathkumaran, J. Phys. Condens. Matter. 25 (2013) 496013.
- [165] G. Sharma, J. Saha, S.D. Kaushik, V. Siruguri, S. Patnaik, Appl. Phys. Lett. 103 (2013) 12903.
- [166] R. Kumar, R. Padam, S. Rayaprol, V. Siruguri, D. Pal, J. Appl. Phys. 119 (2016) 0–6.
- [167] G.A. Smolenskii, I.E. Chupis, Sov. Phys. Usp. 25 (1982) 475.
- [168] Y.F. Tian, J.F. Ding, W.N. Lin, Z.H. Chen, A. David, M. He, W.J. Hu, L. Chen, T. Wu, Sci. Rep. 3 (2013).
- [169] X. Xue, X. Yuan, W. Rui, Q. Xu, B. You, W. Zhang, S. Zhou, J. Du, Eur. Phys. J. B. 86 (2013) 121.
- [170] Z. Li, C. Jing, J. Chen, S. Yuan, S. Cao, J. Zhang, Appl. Phys. Lett. 91 (2007) 1–4.
- [171] A. Kumar, S.M. Yusuf, Phys. Rep. 556 (2015) 1–34.
- [172] R. Padam, S. Pandya, S. Ravi, S. Ramakrishnan, A.K. Nigam, A.K. Grover, D. Pal, J. Phys. Condens. Matter. 29 (2017) 55803.
- [173] S.V. Andreev, M.I. Bartashevich, V.I. Pushkarsky, V.N. Maltsev, L.A. Pamyatnykh, E.N. Tarasov, N.V. Kudrevatykh, T. Goto, J. Alloys Compd. 260 (1997) 196–200.
- [174] M. Patra, M. Thakur, K. De, S. Majumdar, S. Giri, J. Phys. Condens. Matter. 21 (2009) 78002.
- [175] P.D. Kulkarni, S. Venkatesh, A. Thamizhavel, V.C. Rakhecha, S. Ramakrishnan, A.K. Grover, IEEE Trans. Magn. 45 (2009) 2902–2906.
- [176] S.M. Yusuf, A. Kumar, J. V. Yakhmi, Appl. Phys. Lett. 95 (2009) 182506.
- [177] M.I. Darby, Br. J. Appl. Phys. 18 (1967) 1415–1417.
- [178] M.C. Kemei, J.K. Harada, R. Seshadri, M.R. Suchomel, Phys. Rev. B. 90 (2014) 64418.
- [179] S. Ohtani, Y. Watanabe, M. Saito, N. Abe, K. Taniguchi, H. Sagayama, T. Arima, M. Watanabe,

- Y. Noda, *J. Phys. Condens. Matter.* 22 (2010) 176003.
- [180] J. Ma, V.O. Garlea, A. Rondinone, A.A. Aczel, S. Calder, C. dela Cruz, R. Sinclair, W. Tian, S. Chi, A. Kiswandhi, J.S. Brooks, H.D. Zhou, M. Matsuda, Magnetic and structural phase transitions in the spinel compound  $\text{Fe}_{1+x}\text{Cr}_{2-x}\text{O}_4$ , *Phys. Rev. B.* 89 (2014) 134106. doi:10.1103/PhysRevB.89.134106.
- [181] J.H. Van Vleck, The Jahn-Teller Effect and Crystalline Stark Splitting for Clusters of the Form  $\text{XY}_6$ , *J. Chem. Phys.* 7 (1939) 72–84. doi:10.1063/1.1750327.
- [182] U. Opik, M.H.L. Pryce, *Proc. R. Soc. A Math. Phys. Eng. Sci.* 238 (1957) 425–447.
- [183] Z.-G. Yé, O. Crottaz, F. Vaudano, F. Kubel, P. Tissot, H. Schmid, *Ferroelectrics.* 162 (1994) 103–118.



## **Vitae**

Ram Kumar was born on 07<sup>th</sup> October, 1988 in Uttar Pradesh state, India. He obtained his Bachelors and Masters in Physics from Aligarh Muslim University, Aligarh, Uttar Pradesh and also completed Masters in Nanotechnology from same Aligarh Muslim University, Aligarh, Uttar Pradesh. He pursued his doctoral research career with experimental condensed matter physics, at the Department of Physics, IIT Guwahati under the supervision of Prof. Dilip Pal. His current research interests include Multiferroics, Magnetism, Strongly correlated electron systems and Magnetic structure studies of magnetic compounds through neutron scattering experiments.